Investigating Potency and Efficacy of mRNA Lipid Nanoparticle Systems and Targeting Lymph Node

A thesis presented for the degree of

Doctor of Philosophy

from the Institute of Pharmacy and Biomedical Science

at the University of Strathclyde

by

Burcu Binici

Declaration of Authenticity

'This thesis is the result of the author's original research. It has been composed by the author and has not been previously submitted for examination which has led to the award of a degree.'

'The copyright of this thesis belongs to the author under the terms of the United Kingdom Copyright Acts as qualified by University of Strathclyde Regulation 3.50. Due acknowledgement must always be made of the use of any material contained in, or derived from, this thesis.'

Signed: Burcu Binici

Date: 16th May 2024

Acknowledgements

I would like to express my deepest gratitude to my supervisor, Professor Yvonne Perrie, for her invaluable guidance and advice. Her unwavering support throughout my PhD journey has been a constant source of motivation, especially during challenging times. I always felt her support in developing my scientific skills and building my network and collaboration in academia and industry. She made my PhD journey invaluable.

I am very thankful to the Ministry of Higher Education of the Turkish government for the financial support. Without this support, I would not be able to do a PhD in the UK.

I am also very grateful to my second supervisor, Dr Zahra Rattray, for her support, particularly for providing feedback on my papers. Additionally, I want to extend my heartfelt thanks to the postdocs in our group, Dr Muattaz Hussain and Dr Ankita Borah, for their invaluable assistance, especially in my *in vivo* and *in vitro* studies, as well as for helping me think critically about my data and providing valuable ideas. I also want to thank all the colleagues from academia and industry with whom I have collaborated. Their insights have broadened my horizons and enriched our discussions.

My sincere thanks also go to my group members for their help and support. I greatly enjoyed our discussions and knowledge-sharing, which made my experience productive and pleasant. I cannot write everyone's name here as we are a big group, but I truly enjoyed every discussion with everyone. Also, I want to thank Cameron for his help when I started my PhD.

I am deeply indebted to my family for their unwavering support and encouragement. My parents, Ramazan and Hilal, and my sister, Buket, have been my main sources of strength and motivation—a special thanks to my sister for always supporting me and making me laugh.

Finally, I thank my husband, Ridvan Binici, for his endless support. He has always been by my side on the other end of the phone, even across the miles. His love, encouragement, and positivity have been my greatest sources of strength and joy during the toughest times.

Lastly, I thank myself for persevering and believing in my abilities throughout my PhD journey.

University of Strathclyde

Investigating Potency and Efficacy of mRNA Lipid Nanoparticle Systems and Targeting Lymph Node

Burcu Binici

Abstract

mRNA lipid nanoparticle (LNPs) based vaccines played a crucial role in dealing with the COVID-19 pandemic. The primary function of LNPs is to encapsulate and deliver mRNA to the target site, facilitating its release into the cytosol, thereby eliciting an immune response against the antigen transcribed from the mRNA. Despite LNP's first approval in 2018 for delivering siRNA to the liver cells, LNPs face challenges such as endosomal escape, stability, and extrahepatic targeting. The components of LNPs need to be optimised with *in vitro* and *in vivo* studies to address these challenges.

This thesis aimed to investigate the efficiency of mRNA-LNP systems. The study evaluated ionisable lipids such as ALC-0315, SM-102, and Polyethylene glycol (PEG) lipids, including DMG-PEG2k and ALC-0159. From the *in vitro* and *in vivo* studies, SM-102 LNPs were selected as a lead formulation and moved further with testing the ionic strength of the encapsulation buffer. This study showed that the concentration of citrate buffer also had a significant role in transfection efficiency; increasing the ionic strength from 50 mM to 300 mM negatively impacted the transfection efficiency. Additionally, the efficacy of a microfluidic-based rapid mixing method (MF) was evaluated using the Design of Experiment (DoE) approach to reveal the importance of process parameter and their interactions and quadratic effects. Subsequently, an *in vivo* study (using ovalbumin (OVA) mRNA in varying doses) highlighted the sex-specific immune response, irrespective of the protein expression. The final study focused on using biotinylated LNPs to target the lymph node, exploiting the strong interaction between avidin and biotin.

Overall, this thesis provided insight into investigating mRNA-LNP systems, demonstrating potential strategies to enhance the efficacy of mRNA-based vaccines, which is crucial for advancing therapeutic applications.

List of Publications

Binici B, Rattray Z, Schroeder A, Perrie Y. The Role of Biological Sex in Pre-Clinical (Mouse) mRNA Vaccine Studies. Vaccines (Basel). 2024 Mar 7;12(3):282. doi: 10.3390/vaccines12030282. PMID: 38543916; PMCID: PMC10975141.

Binici B, Borah A, Watts A.J, McLoughlin D, Perrie Y. The Impact of Citrate Buffer Molarity in mRNA-LNPs: Insights Beyond General Critical Quality Attributes. Journal: International Journal of Pharmaceutics. 2024 (Accepted)

Binici B, Rattray Z, Zinger A, Yvonne Perrie. Exploring the Impact of Lipid Composition on the Transfection Efficiency of mRNA-LNPs: A combined in vitro and pre-clinical perspective. Journal of Controlled Release. 2024 (Under revision)

Hussain M, **Binici B**, O'Connor L, Perrie Y. Production of mRNA lipid nanoparticles using advanced crossflow micromixing. Journal of Pharmacy and Pharmacology. ISSN 0022-3573 (In Press)

McMillan C, Druschitzb A. Rumbelowb S, Borah, **Binici B**, Rattray Z, Perrie Y, Tailoring Lipid Nanoparticle Dimensions Through, RSC Pharmaceutics, Tailoring lipid nanoparticle dimensions through manufacturing processes. RSC Pharmaceutics. 10.1039/d4pm00128a.

Plant-Hately AJ, **Eryilmaz B**, David CAW, Brain DE, Heaton BJ, Perrie Y, Liptrott NJ. Exposure of the Basophilic Cell Line KU812 to Liposomes Reveals Activation Profiles Associated with Potential Anaphylactic Responses Linked to Physico-Chemical Characteristics. Pharmaceutics. 2022 Nov 15;14(11):2470. doi: 10.3390/pharmaceutics14112470. PMID: 36432660; PMCID: PMC9695975.

Webb C, Ip S, Bathula NV, Popova P, Soriano SKV, Ly HH, **Eryilmaz B**, Nguyen Huu VA, Broadhead R, Rabel M, Villamagna I, Abraham S, Raeesi V, Thomas A, Clarke S, Ramsay EC, Perrie Y, Blakney AK. Current Status and Future Perspectives on MRNA Drug Manufacturing. Mol Pharm. 2022 Apr 4;19(4):1047-1058. doi: 10.1021/acs.molpharmaceut.2c00010. Epub 2022 Mar 3. PMID: 35238565

List of Poster Presentation

Evaluation of Biological Sex on mRNA-Lipid Nanoparticle *in vivo* Expression and Vaccine Potency, 18th Liposome Research Days, June 2024, Glasgow,

Evaluation of Biological Sex on mRNA-Lipid Nanoparticle *in vivo* Expression and Vaccine Potency, CPI 2023, London

Evaluation of mRNA-lipid nanoparticle potency *in vitro* and *in vivo*, CRS 2023, Las Vegas (Top poster award)

Preclinical Evaluation of mRNA-Lipid Nanoparticles, APS 2022, Belfast

The Effect of PEG Density on Lipid Nanoparticle Attributes and *in vivo* and *in vitro* studies, FORGE 2022, Belfast

The impact of Cholesterol Content and PEGylation on liposome attributes prepared by microfluidics, CRS 2021, Virtual

Assessing the effect of cholesterol and PEG content on liposome attributes prepared by Microfluidics, AAPS 2021, Virtual

List of Oral Presentations

The Importance of Biological Sex in the mRNA Vaccine's Pre-Clinical Studies, APS 2024, Huddersfield, UK, 05.09.24

Evaluation of Biological Sex on mRNA-Lipid Nanoparticle *in vivo* Expression and Vaccine potency, 20th Anniversary bioprocess UK Conference 2023 bursary competition, 3-minute flash talk, Brighton, 29.11.2024

SCDT Nanoparticle Health Technologies Research Symposia; The University of Strathclyde; 10.02.2023

New Medicines, Better Medicines, Better use of Medicines; Fulbright 2022, The University of Strathclyde; 20.07.2022

The Role of Formulation in LNPs, Astra Zeneca Workshop on Nanomedicines, The University of Strathclyde; 05.07.2022

In vitro and *in vivo* Evaluation of mRNA-Lipid Nanoparticles, Young Lipid Scientist Award; SCI, London; 15.06.2022

List of Collaboration

The University of Nottingham: Collaboration with Dr Rafal Kopiasz and Prof. Cameron Alexander. This study included injecting mice with the sample from The University of Nottingham, performing IVIS sessions, analysing data and reporting the result. Two IVIS studies were performed.

The University of Liverpool: Collaboration with Dr Alexander Plant-Hately and Dr Neil Liptrott. The samples prepared in our lab were sent to the team at the University of Liverpool. They tested the immunological responses associated with complement activation according to the liposome physicochemical characteristics. The findings from this research were published and can be found in the publications section.

Refeyn: Collaboration with Dr Laura Pala and Ivor Crooks. This company has focused on developing an instrument for particle basis analysis based on mass spectrometry. The instrument was set up in our lab for 2 months. The sample preparation and characterisation with this instrument were performed in this collaboration. The results were reported to the company to aid in developing their technology, allowing them to compare the sample features with those obtained from established particle size analysis instruments.

Collaboration with Prof. Mandy MacLean's group at the University of Strathclyde: The study focused on encapsulating micro-RNA (miRNA) into the LNPs. Samples were prepared and transferred to Dr Hicham Labazi and Gregor Aitchison to be tested *in vitro* and *in vivo*. The study has continued since 03.2022.

Stable Pharma: The study was done confidentially between the University of Strathclyde and Stable Pharma in 2022 for almost a year. The sample preparation, characterisation, and in vitro testing were included at the University of Strathclyde.

University of Cambridge: Dr Thomas Mulroney was assisted with sample preparation. The preparation and calculation of LNPs were demonstrated to support his study.

CMAC-Leon Collaboration: The study included an *in vivo* testing sample. The samples were provided by Ashish Muglikar from our group. The injecting mice, performing the IVIS study, analysing data and reporting the results to the company were done. Also, contributions to writing a manuscript generated with this data were included in the collaboration.

Centillion: Collaboration with the group of Prof. Harris Makatsoris, who is working at King's College London. The Centillion's team receive support in calculating the formulation parameters and preparing LNP-based formulations.

List of Teaching Activities

Demonstrator in MPharm teaching labs at the University of Strathclyde: Being a demonstrator in the MPharm Labs, including pharmacology and chemistry labs during the second semester of 2022, supporting students during practical sessions.

Table of Contents

Figure of Content

Table of Content

Abbreviations

ALC-0159	Methoxypolyethyleneglycoloxy(2000)-N,N-ditetradecylacetamide
ALC-0315	6-((2-hexyldecanoyl)oxy)-N-(6-((2-hexyldecanoyl)oxy)hexyl)-N-(4-hydroxybutyl)hexan-1-aminium
APC	Antigen Presenting Cells
APOE	Apolipoprotein E
AUC	Area Under the Curve
BBD	Box-Behnken Design
C12-200	1,1'-[[2-[4-[2-[[2-[bis(2-hydroxydodecyl)amino]ethyl](2-hydroxydodecyl)amino]ethyl]-1-piperazinyl]ethyl]imino]bis-2-dodecanol
CD	Cluster of Differentiation
Con A	Concanavalin A
COVID-19	Coronavirus disease 2019
CRYO-TEM	Cryogenic Transmission Electron Microscopy
DilC	1,1'-Dioctadecyl-3,3,3',3'-tetramethylindocarbocyanine perchlorate
DiR	1,1-dioctadecyl-3,3,3,3-tetramethylindotricarbocyanine iodide
DLin-DMA	1,2-dilinoleyloxy-N, N-dimethyl-3-aminopropane
DLin-DMA-MC3 (MC3)	(4-(dimethylamino)-butanoic acid, (10Z,13Z)-1-(9Z,12Z)-9,12-octadecadien-1-yl-10,13-nonadecadien-1-yl ester)
DMG-PEG2k	1,2-dimyristoyl-rac-glycero-3-methoxypolyethylene glycol-2000
DMPE-PEG2k	1,2-dimyristoyl-sn-glycero-3-phosphoethanolamine-N-[methoxy(polyethylene glycol)-2000]
DODAP	1,2-dioleoyl-3-dimethylammonium-propane)
DOPE	Dioleoylphosphatidylethanolamine
DOTAP	1,2-dioleoyl-3-trimethylammonium-propane
DOTMA	1,2-di-O-octadecenyl-3-trimethylammonium propane
DSPC	Distearoylphosphatidylcholine
DSPE	1,2-Distearoyl-sn-glycero-3-phosphorylethanolamine
DSPE-PEG2k	1,2-distearoyl-sn-glycero-3-phosphoethanolamine-N-[amino(polyethylene glycol)-2000]
EE	Encapsulation Efficiency
ELISA	Enzyme-Linked Immunosorbent Assay
FDA	Food and Drug Administration

FRR	Flow Rate Ratio
IFN-γ	Interferon Gamma
IgG	Immunoglobulin G
IL 5	Interleukin 5
LDLR	Low-Density Lipoprotein Receptor
LN	Lymph Node
LNP	Lipid Nanoparticle
LSD	Least Significant Difference
MF	Microfluidic
MHC	Major Histocompatibility Complex
MHF	Microfluidic hydrodynamic focusing
mRNA	messenger RNA
MW	Molecular Weight
NA	Nucleic Acid
NP ratio	N-to-P ratio. The ratio of nitrogen (N) in the ionisable/cationic lipid component to the phosphate (P) groups in the mRNA.
NTA	Nanoparticle Tracking Analysis
NC3R	National Centre for the Replacement, Refinement, and Reduction of Animals in Research
PC	Phosphatidylcholine
PDI	Polydispersity Index
PE	Phosphatidylethanolamine
pKa	Acid Dissociation Constant
SARS-CoV-2	Severe Acute Respiratory Syndrome Coronavirus 2
SEM	Scanning Electron Microscopy
SHM	Staggered Herringbone Mixer
SM-102	9-Heptadecanyl 8-{(2-hydroxyethyl)[6-oxo-6-(undecyloxy)hexyl]amino}octanoate
SORT	Selective Organ Targeting
TFF	Total Flow Rate
TFF	Tangential Flow Filtration
Th1	T helper type 1
Th2	T helper type 2
TLR-7	Toll-like receptor 7

TMB	3,3',5,5'-Tetramethylbenzidine

Chapter 1: General Introduction

1.1 Lipid Nanoparticle for Drug Delivery

Lipid-based drug delivery systems were initially developed based on the self-assembly properties of lipids in water. Liposomes (Figure 1.1) are the earliest sub-group of these systems and were developed in the 1960s [1,2]. In 1995, the first liposomal drug product, Doxil®, was approved, encapsulating the chemotherapeutic drug doxorubicin to treat ovarian cancer [3]. Additionally, in 1978, the transfection of mRNA into human cell lines was first established via encapsulating it into lecithin liposomes composed of Phosphatidylcholine (PC) and Phosphatidylethanolamine (PE) [4,5]. A later variation of liposome is lipid nanoparticle (LNP), as shown in Figure 1.1. Liposomes and LNPs are slightly different; liposomes have an aqueous core and bilayer(s), while LNPs have a more electron-dense core and a single lipid layer (Figure 1.1). When it comes to encapsulating larger molecules such as nucleic acids, liposomes may face challenges with encapsulation efficiency (EE) and stability [6]. A transmembrane pH gradient can be exploited to load small molecules into the liposomes. However, this method is not effective for encapsulating negatively charged macromolecules such as mRNA due to their size and negative charge [7]. Encapsulating mRNA into the LNPs is based on charge interaction between mRNA and lipid. It is a self-assembled process using microfluidic systems while encapsulation into the liposomes is based on high-energy dispersion that utilises the thin-film dispersion method [8].
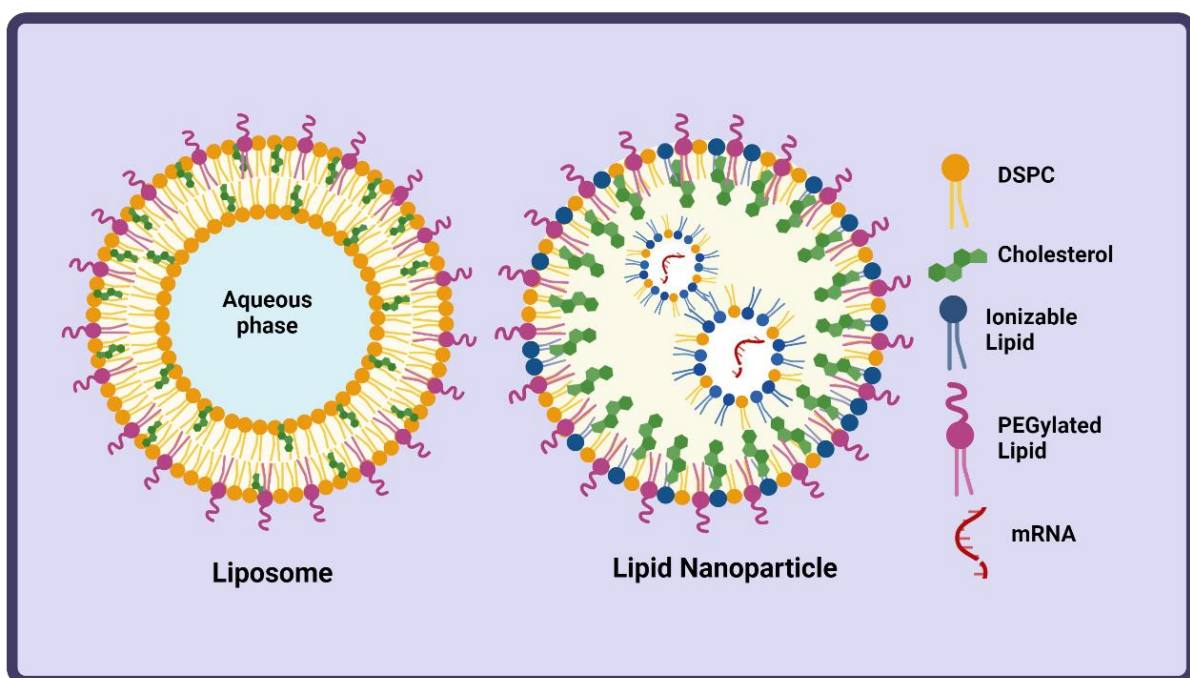
Figure 1.1 *Illustration of liposome and lipid nanoparticle (LNPs), created by Biorender. Liposomes have aqueous cores and bilayer-structured membranes, while LNPs have electron cores and single lipid layer membranes.*

Notwithstanding, liposomes have been used to encapsulate nucleic acids, with a major development being the use of a positively charged lipid, 1,2-di-O-octadecenyl-3-trimethylammonium propane (DOTMA), by Felgner in 1987 [9]. This lipid formed stable unilamellar vesicles alone and with phospholipids. However, *in vivo* studies revealed toxicities and immune system activation related to the cationic lipids [9]. Thus, their applications are limited to *in vitro* delivery, and they are currently in the market as an *in vitro* transfection reagent, Lipofectamine, in combination with dioleoylphosphatidylethanolamine (DOPE) (DOTMA: DOPE) [10]. Despite the limitations of cationic liposomes, early studies have paved the way for the development of ionisable cationic lipids. These lipids introduce a positive charge at the acidic pH and can encapsulate negatively charged nucleic acid, and they become neutrally charged at physiological pH. This is enabled by the lipid head groups having an acid-dissociation constant (pKa) between 6-7. Based on this principle, 1,2-dioleoyl-3-dimethylammonium-propane (DODAP) was developed as the first ionisable lipid; however, DODAP lacked efficient intracellular delivery. Subsequently, 1,2-dilinoleyloxy-N, N-dimethyl-3-aminopropane (DLin-DMA) as an ether analogue of DODAP with linoleic acyl chains was developed to target the hepatocytes to silence a gene using small interfering RNA (siRNA) via intravenous (IV) injection [7]. Further refinements in lipid chemistry led to the development of (4-(dimethylamino)-butanoic acid, (10Z,13Z)-1-(9Z,12Z)-9,12-octadecadien-1-yl-10,13-nonadecadien-1-yl ester) DLin-MC3-DMA (MC3), resulting in improved efficiency of siRNA delivery 3-times compared to DLin-DMA [7]. Eventually, Onpattro (Patisiran®) employing MC3 was approved by the Food and Drug Administration (FDA) in 2018 for the treatment of hereditary transthyretin by silencing transthyretin activity in the liver (Table 1.1). MC3 substantially reduced the dose required for efficient gene silencing [9]. In the design of ionisable lipids, a pKa between 6.2 and 6.4 has been reported as the most effective window for the amine group of the cationic ionisable lipids for the targeting of the hepatocytes via IV injection [7]. In addition to pKa, the saturation level of the acyl chains and ether linkages in the ionisable lipids was reported as another critical factor that needs to be considered when developing ionisable lipids [7].

The breaking point for LNPs came with the COVID-19 pandemic. mRNA-1273 vaccine entered the phase 1 clinical trial 63 days after the Severe Acute Respiratory Syndrome Coronavirus 2 (SARS-CoV-2) sequence was released [11]. This enormous speed was not a surprise as mRNA-

LNP vaccines were already in clinical trials for infectious diseases such as the influenza virus [12]. LNPs are a very versatile platform as they enable the encapsulation of a wide range of mRNA or siRNA with established protocols; namely, existing LNP formulations may allow easy encapsulation of mRNA encoding the desired protein antigen. The COVID-19 pandemic accelerated the approval process of LNPs encapsulating mRNA, which encodes SARS-COVID-19 spike protein. Both Spikevax (mRNA 1273) and Comirnaty (BNT162b2) vaccines showed over 90% efficacy and were approved by the FDA (Table 1.1). Additionally, their safety profile fulfilled the criteria by not interacting with the recipient's nucleus. Moreover, their ease of production and low cost were additional attractive factors.

1.2 The Component of mRNA-LNPs

LNPs can be manufactured using a micromixer that rapidly mixes the lipid phase with the mRNA phase (Figure 1.2). In this process, the lipids (typically dissolved in a solvent such as ethanol) are rapidly mixed with an aqueous phase at low pH, usually around pH 4 (normally containing mRNA). This rapid mixing leads to nanoprecipitation and the formation of LNPs (Figure 1.2). Subsequently, a buffer exchange is conducted to bring the pH to physiological levels and remove ethanol content (Figure 1.2).
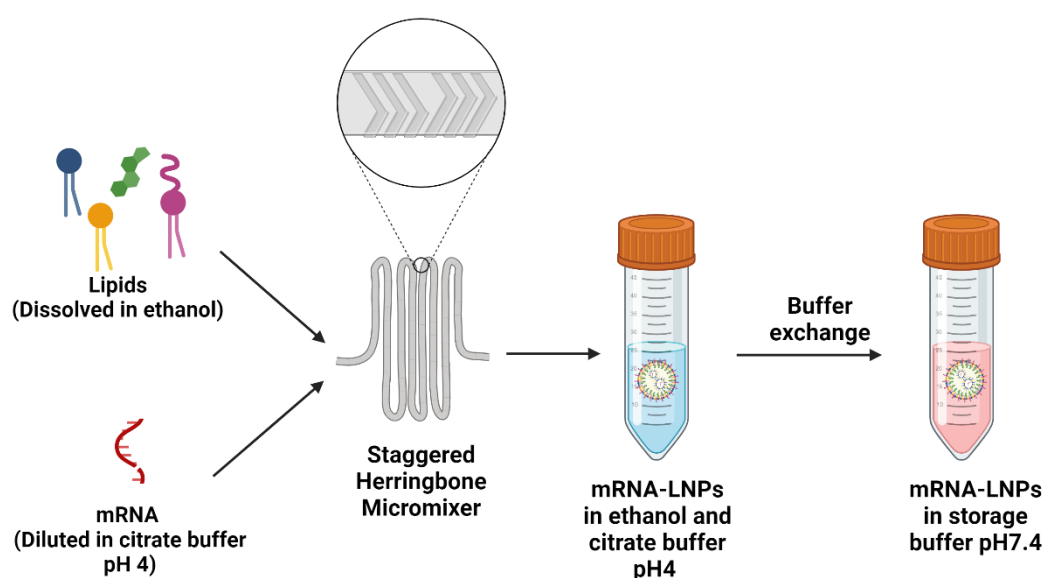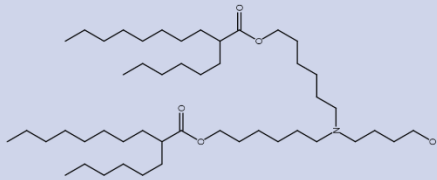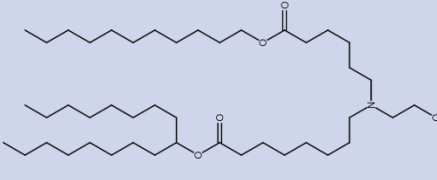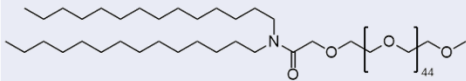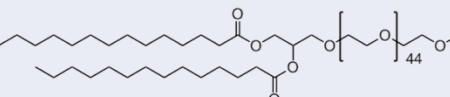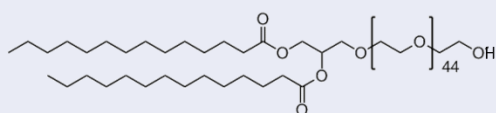
Figure 1.2 *Illustration of production of mRNA lipid nanoparticles. Lipid dissolved in a solvent (usually ethanol) is rapidly mixed with mRNA using a staggered herringbone micromixer. After the self-assembling of LNPs, buffer exchange is performed to remove ethanol and to raise pH to physiological conditions. Figure created by Biorender.*

Table 1.1 *Features of ionisable and PEG lipid structures of three approved RNA-based products. The table prepared was by the source referenced* [13–16]

Category	Pfizer-BioNTech mRNA vaccine	Moderna mRNA vaccine	Patisiran
Name product	BNT162b2; Comirnaty	mRNA-1273; Spikevax	Onpattro
Product dose; route of administration	30 µg mRNA; intramuscular	100 µg mRNA; intramuscular	0.3 mg/kg siRNA; intravenous infusion
product concentration in the vial	100 µg/mL mRNA	200 µg/mL mRNA	2 mg/mL
NP ratio	6	6	3
Storage Buffer	Tris (tromethamine) pH 7–8	Tris (tromethamine) pH 7–8	Potassium phosphate, monobasic, anhydrous Sodium phosphate, dibasic, heptahydrate pH ~ 7
Shelf life of drug product (unopened vials)	2 years when stored at -90 °C to -60 °C	1 year when stored at -50°C to -15°C	27 months (2°C to 8°C , avoid freeze)
LNP Components - Phospholipid: Sterol: Ionisable Lipid: PEGylated lipid (mol%)	DSPC:Chol:ALC-0315:ALC-0159 9.4:42.7:46.3:1.6	DSPC:Chol:SM-102:DMG-mPEG2k 10:38.5:50:1.5	DSPC: Chol:Dlin-MC3-DMA:DMG-C-mPEG2k 10:38.5:50:1.5
pKa of ionisable lipid	6.09	6.75	6.44
Structure of ionisable Lipid			
Structure of PEGylated Lipid			

1.2.1 Lipid Phase

Typically, LNPs are composed of 4 lipids, including structural, helper, ionisable, and PEG lipids (Figure 1.1), and each lipid has the responsibility of encapsulating mRNA and releasing it.

1.2.1.1 Helper Lipids

Helper lipids provide structural support to the LNPs during self-assembly in the production step and help maintain particle integrity during storage. Cholesterol and phospholipids (especially Distearoylphosphatidylcholine (DSPC) and 1,2-Distearoyl-sn-glycero-3-phosphorylethanolamine (DSPE)) are the most used helper lipids in LNP formulations [6]. Cholesterol provides structural integrity and rigidity by filling the gaps between the lipids (Figure 1.3) and driving the lipids to a liquid order phase. When cholesterol is formulated with high transition temperature lipids (e.g., DSPC; 55 ^{0}C), cholesterol increases membrane fluidity by slotting between the hydrophobic tails. On the other hand, cholesterol decreases membrane fluidity for lipids with low transition temperature (for example, DOPC; -40 ^{0}C) by filling the gaps between hydrophobic chains of the lipids, and thus increases the membrane thickness [17]. In both cases, cholesterol helps bring membranes to the liquid order phase (Figure 1.3). Cholesterol can be transferred from the endogenous membrane and accumulate in the particle. Therefore, the amount of cholesterol in typical formulations is maintained close to that of the endogenous membrane, thereby providing equilibrium between the endogenous (30-40%) and exogenous cholesterol, therefore maintaining the structural integrity of the membrane [17]. Moreover, higher cholesterol content generally increases membrane rigidity. However, it could also affect the deprotonation of the ionisable lipids due to forming insoluble cholesterol in the LNP core [18]. Furthermore, cholesterol is likely responsible for the accumulation of LNPs in the liver. ApoE has a high affinity to lipids and binds to the LNP surface in the bloodstream. This binding, influenced by cholesterol content, leads to internalisation by low-density lipoprotein receptors (LDLR), which are primarily found in the liver. Using various cholesterol analogues can drive the selectivity of LNPs in the various cells of the liver. For example, modification of the cholesterol tail via oxidation can promote accumulation in the liver endothelial cells and Kupfer cells instead of the hepatocytes [10]. Also, using different cholesterol analogues can manipulate gene expression and particle morphology. For example, using the β-sterol analogue improved the transfection efficiency 200-fold [19].
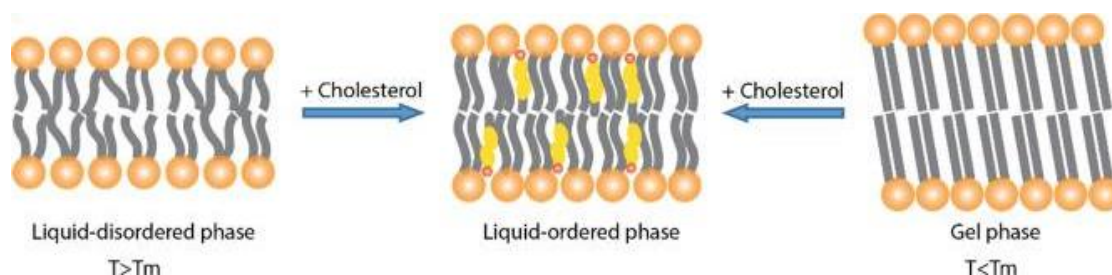
Figure 1.3 *The three different lipid-membrane phases are liquid-disordered, liquid-ordered and gel phase. Cholesterol fills the gaps between the hydrophobic tails when combined with lipids with low transition temperature, increasing bilayer thickness. Also, cholesterol inserts the hydrophobic chain of the lipids with high transition temperature, which increases membrane fluidity and decreases bilayer thickness. The figure is from* [17]

Phospholipids are another structural lipid in LNPs, promoting bilayer formation due to their cylindrical structure. They also contribute to releasing mRNA into the cytosol by disturbing the endosome membrane [6]. PC, a member of phospholipids, is found in mammalian biological membranes. DSPC is the most used phospholipid for the manufacturing of LNPs. DSPC provides stability to LNPs due to the higher melting point (55^0C) associated with the saturated hydrophobic chains. LNPs, including unsaturated PCs such as 1,2-Dioleoyl-sn-glycero-3-phosphocholine (DOPC), are more prone to opsonisation (coating the particles by serum protein to be recognised and internalised by immune cells) due to their low transition temperature resulting in a more fluid lipid membrane at physiological temperature [20]. DSPC is included in all the clinically approved RNA-based LNPs at approximately 10% mol of the total lipids [21–23]. DOPE is another type of phospholipid known as fusogenic lipid due to its inverted cone-shaped structure. When comparing these three phospholipids, the order for stability is DSPC>DOPC>DOPE [20]. However, DOPE has been shown to have a higher transfection efficiency compared to DSPC [24]. Therefore, transfection activity and stability need to be considered when selecting phospholipids.

1.2.1.2 Ionisable Lipids

LNPs are internalised into the cells by endocytosis, and the payload (mRNA) needs to be released from this endosomal vesicle, known as an endosomal escape. This process is critical for transfection efficiency, as the released mRNA will translate into the corresponding protein by the ribosome, which is the ultimate goal. Ionisable lipids play a crucial role in endosomal escape (detailed in section 1.2.1) and encapsulation of mRNA into the LNPs during the production step. The power of ionisable lipids relies on a tertiary amine head group (Chemical

structures in Table 1.1), enabling protonation at an acidic pH and being neutral at the psychological pH. In the design of these lipids, a balance between enabling efficient encapsulation, effective endosomal release, and minimising toxicity at psychological pH must be considered. pKa of the lipids often evaluates this balance (Figure 1.4).
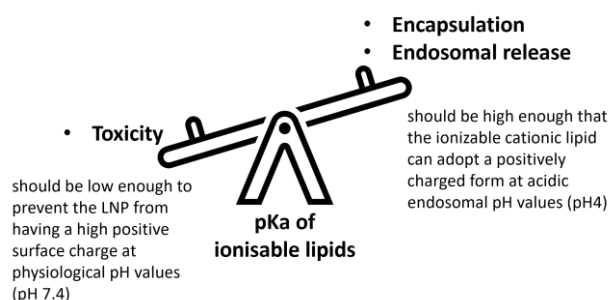
Figure 1.4 *Illustration of optimum pKa of ionisable lipids for an effective endosomal release at pH4 and minimising toxicity at pH 7.4.*

As mentioned, the optimal pKa range of ionisable lipids to elicit an adaptive immune response via the intramuscular route has been defined as 6.6-6.9; however, this decreases to 6.2-6.6 for optimum protein expression via the intravenous route [25]. In this pKa range, the amine group will be positively charged at pH 4, enabling the formation of a complex with negatively charged mRNA, resulting in mRNA-loaded LNP (Figure 1.5). When the pH is increased to physiological conditions during buffer exchange, the particles become neutral in charge, preventing toxicity associated with the positive charge, as cationic particles are known to cause toxicity (Figure 1.5).

Once the LNPs are internalised into the cell by endocytosis, ionisable lipids will again be protonated due to the acidic nature of endosomes (pH4). Then, this positive charge will interact with the negatively charged lipid of the endosomal membrane, making an ion pair (Figure 1.6). This charge interaction will disturb both the LNP and endosomal membranes and, eventually, result in the mRNA being released into the cytosol. However, the optimal pKa range may not always ensure efficient mRNA release, and the geometric shape of the ionisable lipids is another crucial factor. A wider and branched tail, more cone-shaped lipid, disrupts the membrane more, leading to greater endosomal release. As previously mentioned, the development of ionisable lipids was initiated with DODAP. However, a high dose is needed to

reach a therapeutic level *in vivo*, and since then, ionisable lipids have been under development to improve efficiency and biodegradability.
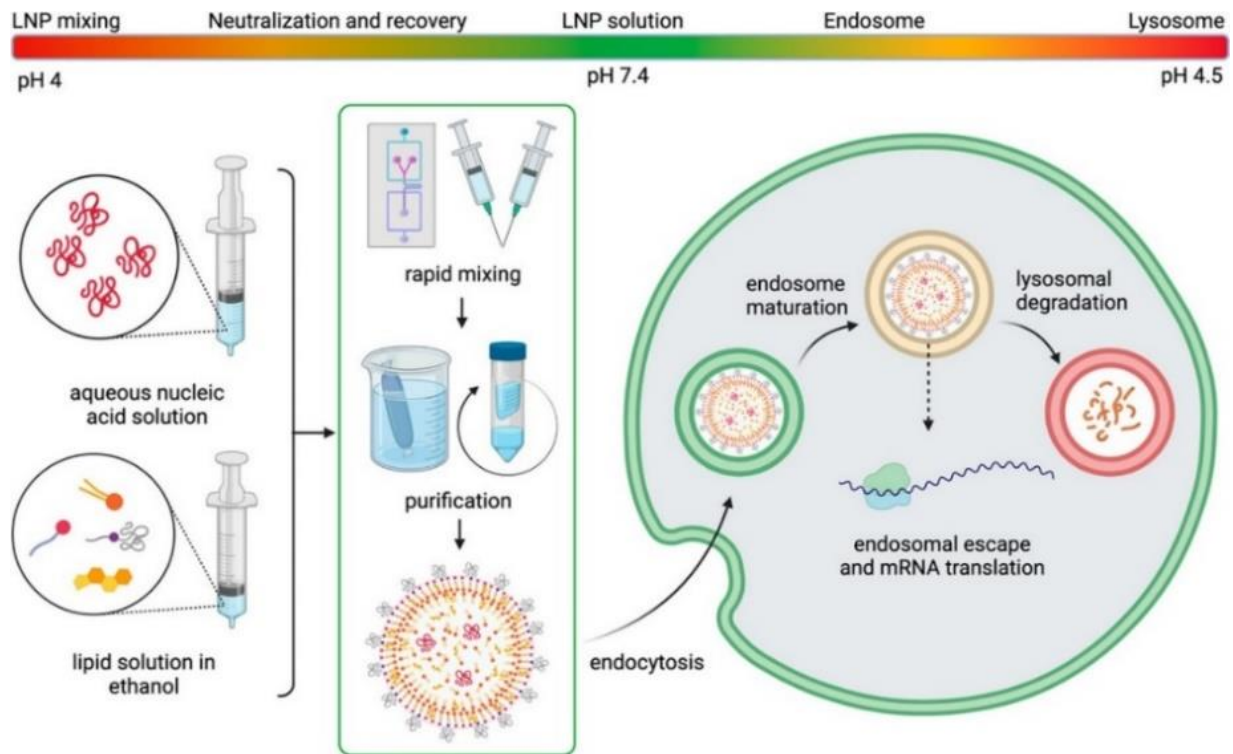
Figure 1.5 *The pH fluctuation through the LNP life cycle from production until the payload is released. At pH4, mRNA forms a complex with ionisable lipids, and then LNPs are neutralised by increasing pH to 7.4. Upon injection and cell uptake, LNPs are internalised by endocytosis, where they encounter the acidic pH of the endosome* [26].

Ionisable lipids can be divided into five groups according to their shape, saturation level and tolerability: unsaturated, multi-tail, polymeric, biodegradable and branched-tail ionisable lipids [27]. The saturation level of the lipid tail substantially affects the ionisable lipid efficiency. Increasing unsaturation levels can lead to greater endosomal release, as the double bonds can disrupt the endosomal membrane more effectively. However, having only unsaturated bonds in the tail is not enough for potential *in vivo* delivery. Multi-tail (3 or more tails) and branched tail (wider structure) are the most dominant factors in releasing mRNA into the cytosol as they can disturb the membrane more effectively. For example, C12-200 has five tails and was initially developed for siRNA delivery. However, it was optimised for mRNA delivery using the Design of Experiments, resulting in improved expression [24]. The branched tail structure has a principle similar to the multi-tail structure and, hence, greater endosomal

escape due to its more cone-shaped morphology. It has been reported that an unsaturated tail is more critical for ionisable lipids with long tails; however, such an effect is less pronounced for multiple short tails [27].
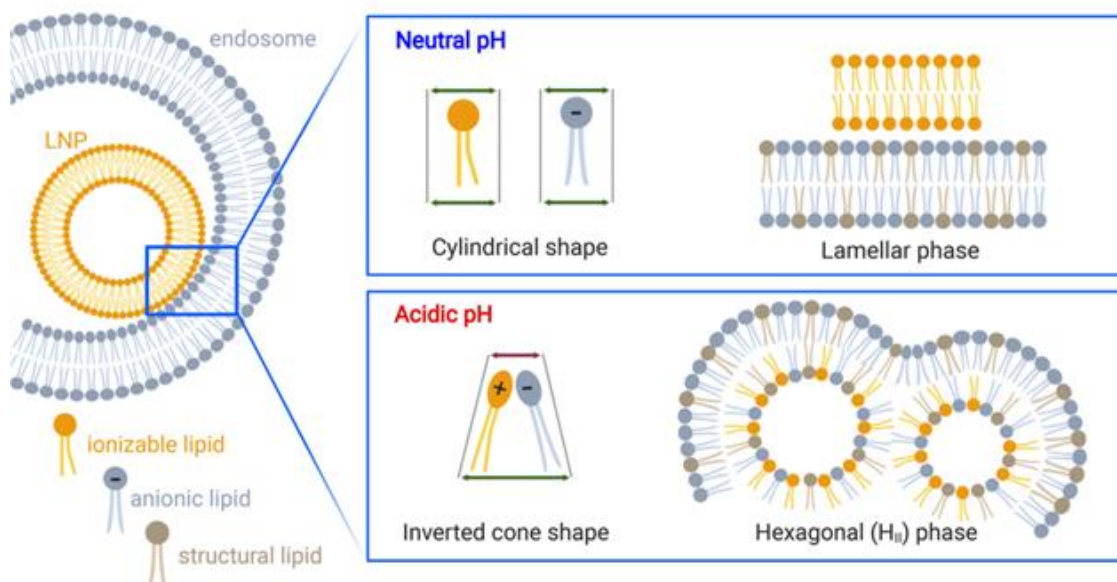
Figure 1.6 *mRNA release into the cytosol based on electrostatic interaction between the endosomal and LNP membrane lipids. Ionisable lipids are ionised at the acidic pH of the endosome and interact with the negatively charged lipids of the endosomal membrane. This ion pair results in an inverted cone shape, disturbing the endosomal membrane and eventually releasing mRNA into the cytosol* [28].

The other group is biodegradable ionisable lipids, especially important for RNA therapeutics requiring multiple doses. However, the degradability of ionisable lipids is limited due to stable backbones. Including ester bonds in the ionisable lipids is a common approach to improve the biodegradability of the ionisable lipids, as the ester bonds are prone to hydrolysis in the tissue and cells. For example, it has been reported that MC3 is less biodegradable than 9-Heptadecanyl 8-{(2-hydroxyethyl)[6-oxo-6-(undecyloxy)hexyl]amino}octanoate (SM-102) (Table 1.1) which has an ester linker group [25]. It is reported that ionisable lipids involving ester bonds have a lower potency than non-degradable analogues due to ease of hydrolysis and faster elimination [27]. Therefore, introducing ester bonds needs to be carefully considered regarding the balance between tolerability and efficiency. Disulfide bonds are another approach to improving biodegradability. However, their synthesis is relatively difficult. Ionisable polymer lipids, including a free amine group on the cationic polymers, have been

investigated. However, the toxicity issue with polymers needs to be considered. When comparing SM-102 and ALC-0315 (Table 1.1) as ionisable lipids used in the Spikevax and Comirnaty COVID mRNA-LNPs vaccines, there are common features: both contain tertiary amine, ester linkers and branched tails. The head group and tail structure are different; ALC-0315 has an amino butanol head group, while SM-102 has aminoethanol, leading to ALC-0315 having a slightly (2C) longer head group. Regarding the tail, ALC-0315 has a more branched tail than SM-102. Moreover, it has been reported that the behaviour of forming bilayer of both lipids differs since ALC-0315 possesses four extremely short tails while SM-102 only has three tails, with one of them being of sufficient length to stabilise the lipid within the lipid layer [29]. Toxicity issues, difficulties in synthesis, and extrahepatic delivery are challenges that must be addressed in future applications of ionisable lipids.

1.2.1.3 PEG lipids

Another lipid component is the PEGylated lipid, which coats the particle surface. It controls particle size during the production step and helps maintain particle stability during storage. PEG chains form a mushroom- or brush-like hydration layer around the particles due to the hydrophilic nature of PEG. This layer provides a physical stearic barrier around the particle, preventing particles from coming too close to each other and aggregating during storage. Also, it reduces nonspecific binding to the blood proteins, preventing opsonisation, which can lead to extending blood circulation time [12]. In vaccination applications, LNPs must be quickly internalised into the cells to release mRNA before clearing from the injection site. However, a longer circulation half-life can be used as a strategy to increase the accumulation of drugs within tumours. Therefore, the use of PEG lipids varies according to the applications. Nonetheless, higher PEG content can cause problems such as diminished cellular uptake and PEG-related allergic reactions [30]. For example, Semple et al. showed that decreasing PEG content (from 10% to 1.4%) showed a 5-fold increase in potency [31]. Thus, the PEG content must be carefully tailored to optimise particle size and stability without hindering cellular uptake. Also, PEG lipids allow surface modification by attaching the ligand to the PEG chain's terminal end. PEG lipids comprise hydrophobic acyl chains, a hydrophilic polar head group, a linker, and a PEG chain. The length of the PEG chain can affect the particle size: larger PEG chains (20-50 kDa) are preferred for small molecules to increase their size and avoid renal clearance, while smaller PEGs (1-5 kDa) are preferred for larger formulations such as

nanoparticles[30]. An increased risk of PEG-related anaphylaxis is associated with higher molecular weight and concentration of PEG. However, a longer PEG chain provides better steric hindrance by minimising unwanted interactions with the biomolecules. mRNA/siRNA-LNP products typically use 2kDa PEG [21–23]. It has been reported that the terminal group of the PEG chain is likely contributing to the level of PEG-related immune response. For example, methoxy-PEG (mPEG) is more immunogenic than hydroxy-PEG, likely because the immune system more readily recognises methoxy's more lipophilic nature than hydroxy end [32]. This can result in loss of activity for mPEG conjugates as they are cleared by the immune system. Regarding the lipid part of PEGylated lipids, the hydrophobic chain's length is essential in terms of the capability of the PEG chain to dissociate from the lipid bilayer. This dissociation rate is an important parameter, as the PEG chain likely hinders cellular uptake due to limiting the interaction between the cellular membrane and particle [33]. The desorption rate of the PEG chain is driven by the quantity and length of hydrophobic chains because the energy required for PEG chain desorption is higher with a greater number of hydrophobic carbon chains [34]. The number of carbon acyl chains affected the desorption rate of the PEG chain, ultimately affecting transfection efficiency [35]. PEG density around the particle surface is also a critical factor. It was shown that increasing PEG content decreased mRNA transfection profile *in vitro* [36,37] and *in vivo* [34,38,39]. Therefore, the quantity and length of the PEG chain and lipid chain must be carefully tailored.

1.2.2 mRNA and Aqueous Phase

Encapsulation buffers refer to the buffer in which mRNA is diluted to prepare the aqueous phase. After forming LNPs, a buffer exchange raises pH to physiological conditions, neutralising the particles (Figure 1.2). Storage buffer refers to the buffer exchanged.

1.2.2.1 Encapsulation Buffer

Compared to the lipid phase, the aqueous phase has received less attention in mRNA-LNP development. The choice of buffer, pH and ionic strength are the key factors in encapsulation buffer when preparing LNPs. Citrate buffer is frequently used as the encapsulation buffer because citric acid minimises the hydrolysis of RNA by chelating the RNase. The pH of this buffer is typically set to 4, according to the Henderson-Hasselbalch equation (Equation 1.1), to protonate the ionisable lipid efficiently.

In this thesis, mRNA encoding firefly luciferase (Fluc mRNA) was used as a model mRNA to assess the *in vitro* and *in vivo* delivery efficiency of LNPs (Figure 1.7). The luminescence light generated from the reaction between substrate (luciferin) and enzyme (expressed protein from luciferase encoding mRNA) is widely used to evaluate the delivery efficiency of LNPs *in vitro* and *in vivo* (Figure 1.7). Additionally, the immunological profile stimulated by mRNA-LNPs was tested using ovalbumin (OVA) mRNA as a model antigen-encoding mRNA.

$$pH = pKa + log\frac{[Tertiary\ amine]}{[Quaternary\ amine]}$$

Equation 1.1

The N-to-P ratio, representing the ratio between lipid and mRNA, is a crucial parameter in LNP formulation. Here, N refers to the molarity of the amine group in ionisable lipids (depending on the number of ionised amine groups at acidic pH), and P refers to that of the phosphate group in nucleotides. This ratio is closely related to EE, particle size, surface charge, morphology, and even toxicity of the particles. [18,40]. For instance, increasing the N/P ratio led to higher transfection efficiency [24,41]. The N/P ratios for Patisiran and both COVID vaccines were 3 and 6, respectively [13].

1.2.2.2 Storage Buffer

Storage buffers are used to store LNPs and play a key role in the stabilisation of LNPs during storage. PBS is the most preferred buffer due to its similarity to physiological conditions; however, it is not ideal for freeze-drying, a dehydration process for long-term storage of LNPs [42]. TRIS buffer, often combined with sucrose or trehalose, which are cryoprotectants, is more suitable for freeze-drying and storage. Initially, the Comirnaty vaccine was formulated with PBS, including potassium chloride and sodium chloride; however, due to notable pH variations that can arise in PBS following freezing, the formulation was later changed to TRIS buffer [43]. Tris-HCl is used because it stabilises nucleic acid molecules.
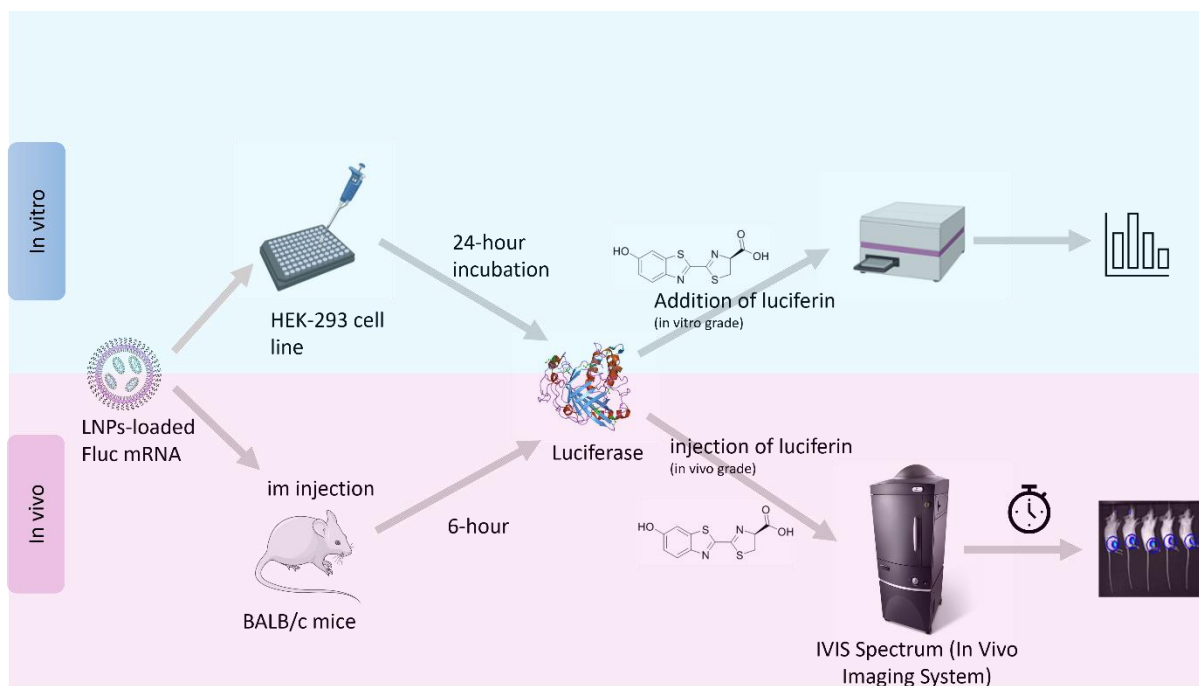
Figure 1.7 *In vitro and in vivo evaluation of the transfection efficiency of LNPs carrying Fluc mRNA. The reaction between Luciferase protein as an enzyme (expressed in vitro and in vivo from Fluc mRNA) and luciferin as substrate generates luminescence light in vitro and in vivo. This light serves as an indicator of the LNPs' delivery efficiency.*

1.1 The Production and Purification of LNPs and Characterisation

1.1.1 Production Method

Implementing traditional methods, such as thin-film hydration or extrusion, for manufacturing LNPs is limited by low encapsulation efficiency, poor reproducibility and scalability, multi-staged and labour-intensive manufacturing [42]. Moreover, these methods were unsuitable for nucleic acids, which are prone to degradation. As a result, in-line T-tube mixing and microfluidic methods, such as Microfluidic hydrodynamic focusing (MHF) and Staggered Herringbone Mixer (SHM), have been developed (Figure 1.8). LNPs are self-formed due to the supersaturation of lipid molecules driven by the rapid increase in the polarity. In other words, hydrophobic lipid chains become less soluble when mixed with the aqueous phase, leading to the nanoprecipitation of the lipids. The main advantage of this rapid mixing process is that it promotes improved controllable physicochemical properties, improved encapsulation efficiency, and ease of scale-up. These three methods each employ rapid-mixing methods. However, their flow mechanism is different due to variations in the 3D structure of the device. T-junction mixing uses the turbulent output flow [42], and it is generally known that decreasing the flow rate increases particle size and results in a higher PDI [43,44]. SHM

leverages the hydrodynamic focusing of the lipid mixture in the solvent by the aqueous phase[42]. Particle size and PDI can be controlled by altering the total flow rate (TFR) and flow rate ratio (FRR), which influence the width of the centre stream. Also, mixer geometry influences these parameters. SHM uses the chaotic advection mixing principle.
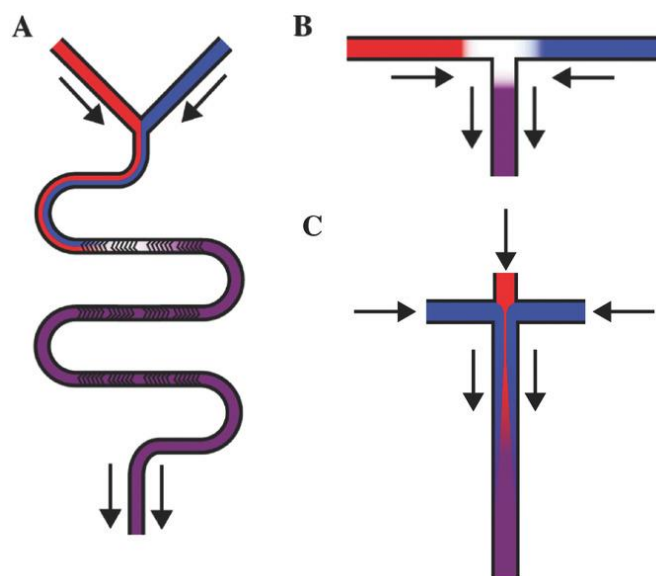
Figure 1.8 *Schematic illustration of new mixing methods: microfluidic mixing using A) a staggered herringbone mixer, B) in-line T-junction mixing, and C) microfluidic hydrodynamic mixing. The aqueous phase is illustrated in blue, the organic phase in red, and the resulting mixture containing particles in purple* [42]*.*

The SHM method offers better control over the mixing process and reduces the mixing time. SHM is a preferred method at the lab scale and can be used on a large scale by parallelising the microfluidic chips. In contrast, T-junction mixing is limited at the lab scale due to the high flow rate required for optimum physicochemical properties. However, this method is employed by companies to manufacture LNP-based mRNA or siRNA products. Overall, these methods provide high encapsulation efficiency, monodispersed particles in a controlled environment, low waste volume, and scalability through parallelisation. However, some drawbacks exist, such as high solvent content after mixing. According to the European and American current guidelines (Ph. Eur. and USP, respectively), the ethanol content is accepted up to 0.5% (v/v). Therefore, this ethanol must be removed using purification methods[42]. Another drawback of this rapid-mixing process is the low solubility of some lipids in ethanol, which can lead to lower lipid concentrations in the LNPs. In this thesis, all LNPs were prepared using SHM.

1.1.2 Purification of LNPs

Various purification methods, including tangential flow filtration (TFF), dialysis, and spin columns, are employed for buffer exchange to remove ethanol content and increase pH to physiological conditions. The spin column protocol uses centrifugal forces to pass particles with a molecular weight (MW) lower than the MW cut-off of the filter through the membrane. Dialysis is based on diffusing the particles through a semi-permeable, generally cellulose, membrane. Tangential flow filtration is based on streaming the flows tangentially across the membrane instead of directly passing through it. TFF is highly scalable for large volumes; however, it is costly and more complex compared to the other methods. Dialysis can handle larger volumes; however, removing the small molecules may be less efficient due to the equilibrium across the membrane. Additionally, working in an RNase-free environment poses challenges, although dialysis is gentle on the sample. Using the spin column is the most straightforward process among the options; nevertheless, it is difficult to scale up, and some lipids may not be compatible with the membrane. For example, 1,2-dioleoyl-3-trimethylammonium-propane (DOTAP)-LNPs could not be centrifuged through the spin column membrane due to the cationic nature of DOTAP.

1.1.3 Critical Quality Parameters

1.1.3.1 Particle Size

Particle size is a critical parameter, as it influences the *in vivo* accumulation, expression, and immunogenicity profile of LNPs [25,42,45,46]. An LNP size below 100 nm is suitable for efficient cellular uptake and transportation to the lymph node [47,48] and is associated with a single-bilayer particle [49]. Releasing mRNA from a single bilayer is likely easier than multilayer particles. The size of LNPs is determined by the self-assembly process, which can be driven by (i) the composition of LNPs, including the cholesterol content, PEG content, N-to-P ratio, lipid concentration, the concentration of encapsulation buffer, the solvent used to dissolve lipids, and (ii) microfluidic parameters such as FRR [2,43,44,50–52]. Particle size can be measured using different techniques, such as dynamic light scattering (DLS), nanoparticle tracking analysis (NTA), scanning electron microscopy (SEM) and others.

DLS is the most established technique for measuring particle size, and it works by evaluating the fluctuations in the intensity of light scattered by particles moving with Brownian motion in a fluid. These fluctuations are correlated to the hydrodynamic diameter of the particles.

The hydrodynamic size of the particles encompasses both the actual particle size and any surrounding layers that impact their motion. Therefore, DLS measured the core LNP size along with the PEG layer around the particles. DLS is the only technique accepted by the FDA as a standard nanoparticle analysis technique [53]. DLS is user-friendly, quick, reproducible, and can measure a broad range of particle concentrations. However, the presence of large particle aggregates can hinder accurate size measurement, and the peak resolution is likely lower compared to single particle analysis techniques such as NTA [54].

1.1.3.2 PDI

In addition to the particle size, the distribution of the size is also another critical factor defined by the polydispersity index (PDI). It ranges from 0.00 (perfectly uniform distribution) to 1.00 (highly polydisperse size populations). It does not have a unit calculated from a two-parameter fit to the correlation data [48]. For most nanoparticles, including LNPs, a PDI below 0.2 is desired. PDI can be measured by using DLS and can be affected by factors such as ionisable lipid content, PEG lipid content, and the manufacturing method used [43,55,56]. Microfluidic manufacturing methods are associated with homogeneous particle size distribution.

1.1.3.3 Zeta Potential

Zeta potential is often confused with surface charge; however, they are slightly different (Figure 1.9). Surface charge refers to the amount of electric charge per unit area between a solid and a liquid. In contrast, the zeta potential quantifies the strength of the electrostatic potential at the shear plane near a particle within a dispersion moving under an electric field. Zeta potential is measured by electrophoretic mobility and indicates the potential difference between the electric double layer (EDL) of electrophoretically mobile particles and the surrounding dispersant layer at the slipping plane [57].

The zeta potential of LNPs is likely driven by the ratio between mRNA to lipid (N-to-P ratio), the charge of the head group of the ionisable lipids and the external buffer used. The zeta potential is crucial for colloidal stability; neutral particles can aggregate, while the charged particles ensure colloidal stability by repulsing each other. Zeta potential over 30 mV or below -30 mV is generally considered sufficient repulsion for stable particle suspension [6]. However, PEGylated LNPs can be excluded from this statement as the PEG chain already provides a stearic barrier. Zeta potential also plays a key role in the *in vivo* accumulation of particles. For instance, it has been reported that positively charged, negatively charged, and neutral

particles are more likely to accumulate in the lungs, spleen, and liver, respectively, upon IV injection [58,59].
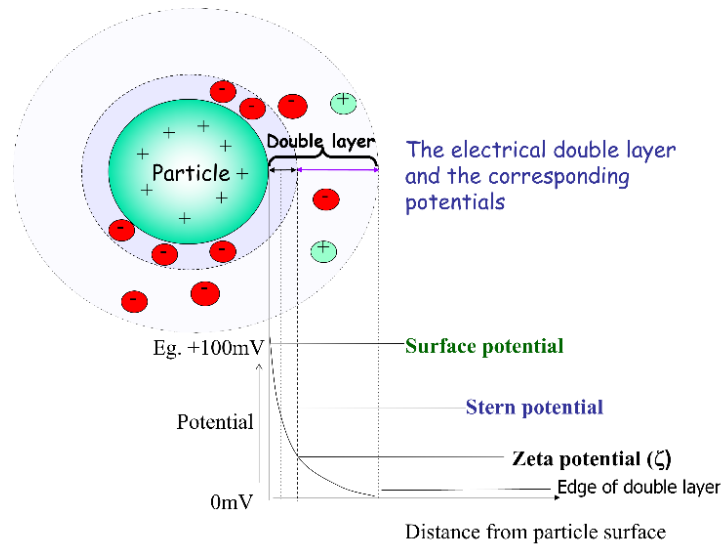
Figure 1.9 *Illustration of zeta potential of the particle. The surface charge represents the total charge of a particle on its surface, while zeta potential measures the electric potential at the slipping plane surrounding the particle, indicating stability in colloidal systems.*

1.1.3.4 Encapsulation Efficiency and Recovery

EE and recovery refer to the proportion of mRNA encapsulated into the LNPs and the total amount of mRNA present, respectively. EE is a critical parameter as naked mRNA is prone to degradation by RNase in the body, resulting in low transfection efficiency [60]. Ribogreen dye, which cannot pass the LNP membrane, is used to measure EE and recovery since it exhibits fluorescence when it binds to the single-stranded mRNA. EE% and recovery% are calculated according to Equation 1.2 and 1.3, respectively.

$$mRNA\ encapsulation\ \% = \frac{Total\ mRNA - Unencapsulated\ mRNA}{Total\ mRNA}\ x\ 100$$

Equation 1.2

$$mRNA\ Recovery\ \% = \frac{Total\ mRNA}{Theoretical\ mRNA}\ x\ 100$$

Equation 1.3

1.2 Mode of action of mRNA-LNPs

This section explains the mode of action of mRNA LNPs following IM injection and their potential to elicit an immune response.

1.2.1 Endosomal Release

After LNPs are taken up by the cells, the endocytic pathway begins. For successful mRNA translation, LNPs must escape the endosome and be released into the cytosol before they are cycled through late endosomes or degraded by lysosomes. There are two main theories regarding endosomal escape.

The first theory, as mentioned above, involves the acidic nature of the endosome. The protonated head group of the ionisable lipids interacts with anionic lipids located on the luminal side of the endosomal membrane (Figure 1.6). This ion pair formation impairs the integrity of the LNPs, releasing the cargo to the cytosol. pKa and the shape of ionisable lipids are well-known factors that influence efficient endosomal release [61]. Moreover, Zheng et al. showed that the topology, namely nanostructure, of mRNA-LNPs is also a critical factor in endosomal release [62]. Cubosome-shaped particles had higher endosomal release than lipoplex and inverse hexagonal structures. Also, a study showed that the endosomal release capability may depend on the transition temperature at which the membrane changes from a bilayer to the hexagonal phase [63]. Cholesterol also plays a crucial role in endosomal escape, promoting the hexagonal phase compared to the lamellar phase [64]. Some studies focused on using cholesterol substitutions, such as β-sterol, to improve the endosomal release [19,65].

Another hypothesis behind endosomal escape is the proton sponge effect (Figure 1.10) though it is not as pronounced as the first mechanism. In this theory, the buffering capacity of LNPs activates the proton pumps in the endosomal membrane ATPase, which pumps protons into the endosome [63,66]. Due to LNPs and excess protons, increasing ionic concentration within the endosome must reach equilibrium, which may involve the diffusion of chloride ions into the endosome. The resulting osmotic pressure causes the endosome to swell, eventually leading to its rupture and the release of the payload into the cytosol. This theory is based on the buffering capacity of ionisable lipids, acidification of the endosome,

and accumulation of the chloride ions within the endosome, leading to the bursting of the endosome and the subsequent release of the contents [63].
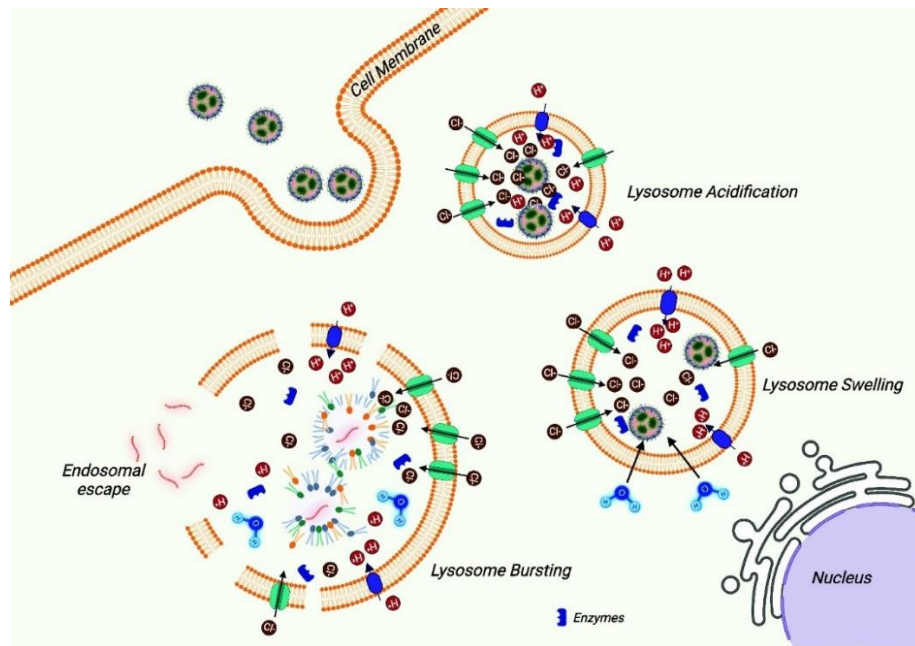
Figure 1.10 *Illustration of the proton-sponge effect. Due to the buffering ability of ionisable lipids, there is a considerable influx of protons by activating the proton pump in endolysosomal compartments. To neutralise the membrane potential, an inflow of chloride ions is triggered, creating an osmotic imbalance followed by water intake. This leads to endolysosomal compartment swelling and eventually bursting, which releases the cargo. Image from ref* [63]*.*

1.2.2 Generating Immune Response

Several routes can happen after mRNA-LNPs are injected; LNPs can be internalised by either non-immune cells, such as muscle cells, or tissue-resident immune cells, such as dendritic cells (DCs) and macrophages [67]. After translating mRNA to the corresponding antigen protein in the non-immune cells, the proteasome degrades the antigen to small peptides (Figure 1.11). These epitopes bind to the major histocompatibility complex (MHC) class I and are then presented on the cell surface. This complex activates cytotoxic T cells expressing CD8, leading to the release of enzymes such as perforin and granzymes to kill the cells [67,68]. In the second case, transfecting the tissue residence immune cells leads to the activation of killer T cells via the same mechanism. Also, the helper T cells expressing CD4 are activated through antigen presentation by the MHC class II complex (Figure 1.11). Once activated, helper T cells release cytokines such as interferon-gamma regulating inflammation and immunity. Also, helper cells activate B cells, which produce antibodies such as Immunoglobulin G (IgG). Another mode of

action occurs when the antigen proteins are recycled to the extracellular compartment or when the antigens appear from the degraded cells. These antigens are taken up by the cells and recognised as an exogenous protein (Figure 1.11). This time, the protein is hydrolysed in the lysosome, and the peptide fragments are loaded onto the MHC class II molecules, leading to the activation of helper T cells. Also, B cells coated with antibodies can be activated directly with this protein released to the extracellular environment (Figure 1.11). Moreover, LNPs can be transported to the neighbouring lymph node through the lymphatic systems and transfect the LN resident cells, such as Antigen Presenting Cells (APCs). This stimulates T and B cells, leading to cellular and humoral immunity [67]. These mechanisms activate humoral immune cells by stimulating B cells and the activation of cellular immunity by stimulating T cells. The advantage of mRNA vaccines is evident here since they stimulate both humoral and cellular immunity [69].

Transfecting the resident cells or moving to the lymph nodes can be influenced by particle size and surface charge. For example, draining particles to the lymph node is mainly driven by particle size; smaller particles are likely moved to the lymph nodes [47]. Additionally, since positively charged particles tend to stay at the injection site and interact with the resident protein, the negatively charged particles move to the LNs. These particles are internalised by multiple mechanisms depending on the type of cells and the properties of the LNPs [10].

1.3 Targeting Strategies with mRNA-LNPs

Targeting strategies are divided into three groups: active targeting, passive targeting, and endogenous targeting (Figure 1.12). Passive targeting is usually affected by the physicochemical properties of particles, such as size and zeta potential, while active targeting is mainly achieved by introducing target-specific ligands, such as antibodies [70]. In endogenous targeting, the biomolecular corona (primarily protein corona) naturally provides particles with a new identity, which may mask the surface's physicochemical properties and affect the targeted delivery of particles [70].

Passive targeting involves the accumulation of particles naturally in specific organs, tissues, and cells. This unintentional localisation of the particles is not dependent on size, morphology, structure, surface, and other physicochemical properties.
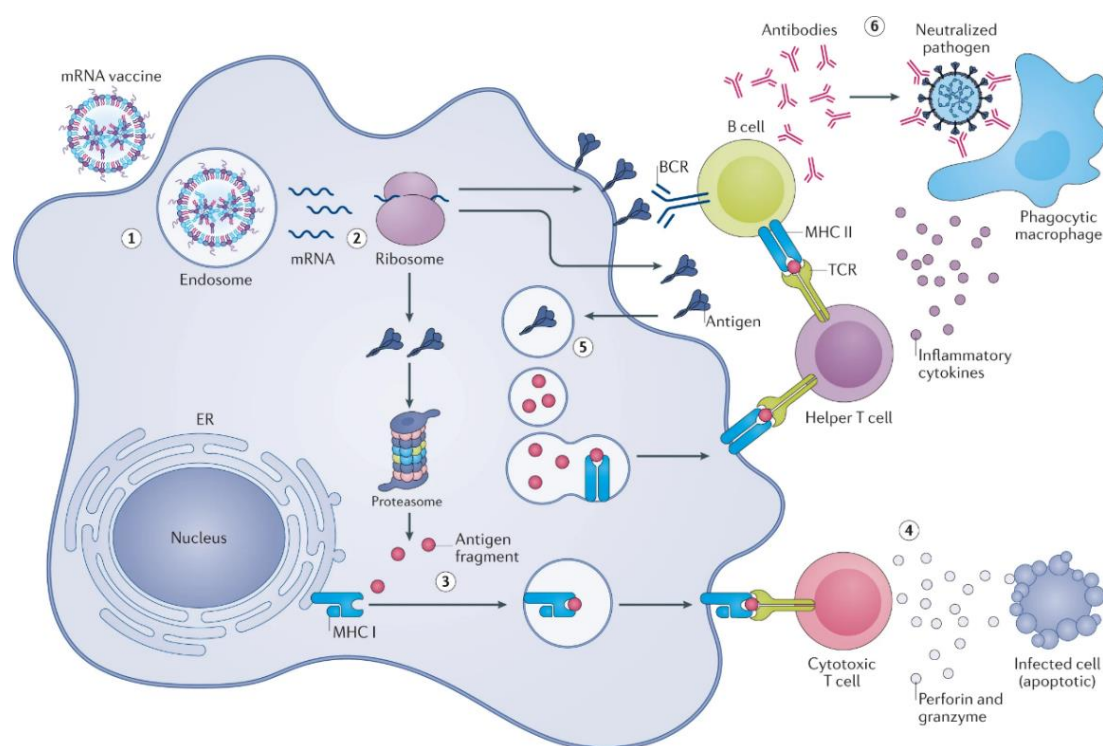
Figure 1.11 1) *Injected mRNA vaccines are endocytosed by antigen-presenting cells. (2) After escaping the endosome and entering the cytosol, mRNA is translated into protein by the ribosome. The translated antigenic protein can stimulate the immune system in several ways. (3) Intracellular antigen is broken down into smaller fragments by the proteasome complex, and the fragments are displayed on the cell surface to cytotoxic T cells by MHC class I proteins. (4) Activated cytotoxic T cells kill infected cells by secreting cytolytic molecules, such as perforin and granzyme. (5) Additionally, cells can take up secreted antigens, degraded inside endosomes and present on the cell surface to helper T cells by MHC class II proteins. (6) Helper T cells facilitate the clearance of circulating pathogens by stimulating B cells to produce neutralising antibodies and by activating phagocytes, such as macrophages, through inflammatory cytokines. BCR, B cell receptor; ER, endoplasmic reticulum; TCR, T cell receptor. The image was taken from* [68]

The anatomical and physiological properties of the target site allow for particle accumulation due to the inherent features of its biological structure (Figure 1.12). The best-known example of passive targeting is Doxil, a doxorubicin liposomal drug product. The large gaps between the endothelial cells of the tumour vascular and the poor lymphatic drainage allow the accumulation of the doxorubicin liposomes at the tumour site instead of in the healthy tissues where endothelial cells have tight junctions. Moreover, lipid components may induce helper T cells and humoral response, which can be considered a kind of passive targeting for vaccine applications [71].

Endogenous targeting uses the endogenous molecules as ligands to direct the particles to the target area (Figure 1.12). This is likely related to the protein corona, the layer of protein adsorbed spontaneously on the particle surface when particles encounter the body proteins. Protein corona can mask targeting ligands, resulting in lost targeting efficiency. However, protein corona can be used as a targeting strategy using the natural way of the biological system. For example, the binding of ApoE around the particle surface (upon desorbing the PEG chain) drives the particles to hepatocytes via binding to Low-density lipoprotein receptor (LDLR). Dillard et al. showed that using additional SORT molecules provides a tropism to a specific organ [58,72]. They created LNPs targeting the liver, spleen, and lung by adding DODAP, PA (an anionic lipid) and DOTAP, respectively. Then, they analysed the serum protein binding to LNPs. The most prevalent proteins in the protein corona of the spleen, liver and lung were ß2-glycoprotein, ApoE and vitronectin, respectively. When considering the close zeta potential of LNPs, the nature of the head group of SORT molecules was likely responsible for this specific binding. Another example is Patisiran, the first approved siRNA-based LNP. LNPs are internalised by ApoE-dependent LDLR receptors after desorbing the PEG chain.

Active targeting is another strategy that enables nanoparticles to be directed to the receptors expressed in the target area (Figure 1.12). LNP surface can be coated by chemical or biological moieties from monoclonal antibodies to small molecules [73]. It is widely explored for oncology applications. Antibody-coated particles can target tumour-specific or tumour-associated antigens. For example, hyaluronic acid binds to CD44, while folate binds to folate receptors expressed in the cancer cells [73]. For instance, targeting mannose receptors abundantly expressed on the immature DCs enhances the ability of DCs to present both MHC class I and II antigens, amplifying the immune response[74]. Adding a ligand at the end of the PEG chain can be easily used as a targeting ligand. However, immune responses related to PEG can limit the concentration of PEG lipids, and hence, less coating can impair targeting potential. Activation of T cells is a good targeting method; however, this can lead to overactivation and exhaustion of T cells[73]. Active targeting is more controllable than passive targeting; however, the complexation of production purification methods is a hurdle for targeting the site actively. Also, the expression of the receptor can vary between patients, cells, and different disease stages [73].
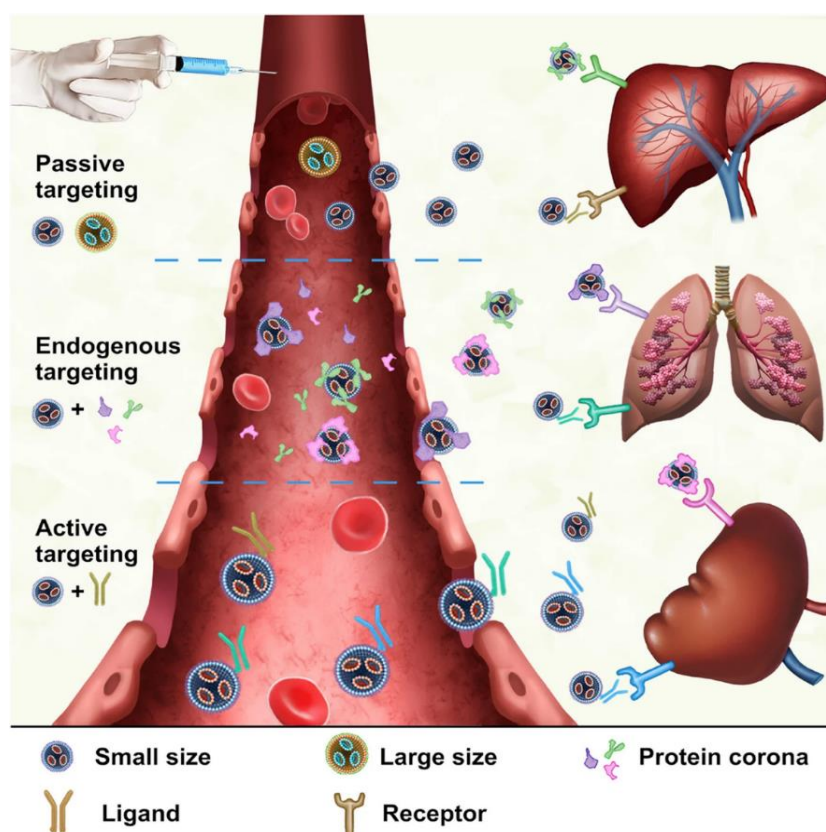
Figure 1.12 *Schematic illustration of targeting mechanisms of mRNA NPs. After intravenous injection, NPs achieve specific delivery to organs through passive, endogenous and active targeting. Passive targeting involves adjusting the size, structure and other physicochemical properties of NPs to achieve targeted delivery of mRNA. Endogenous targeting involves binding to different subsets of plasma proteins, guiding NPs to specific organs and being absorbed by target cells. Active targeting relies on modifying the NP surface with specific ligands that can specifically bind to the receptors highly expressed by target cells. The image*[70]

1.4 Aim and Objectives

At the onset of the COVID-19 pandemic, while studies on mRNA-LNPs existed, no studies specifically showed the *in vitro* and *in vivo* transfection efficiency of COVID-19 vaccine LNP formulations. This thesis initially focused on demonstrating the expression profile of the lipids used in the COVID-19 LNP vaccine formulations and comparing them to other ionisable/PEG lipids. This starting point provides an ideal foundation for further studies aiming to develop ionisable lipids.

In the meantime, the majority of studies concentrated on developing ionisable lipids, with only a few studies focused on the aqueous phase of LNPs, the buffer in which mRNA is diluted, and did not show *in vitro* and *in vivo* outcomes. To fill this gap in the literature, this thesis

aimed to investigate the effect of the molarity of the citrate buffer on the expression profile at the HEK-293 cells and BALB/c mice.

The next aim was to test the effect of microfluidic production and formulation parameters on *in vitro* and *in vivo* protein expression using a design of experiments (DoE) approach. This study is crucial as it shows the quadratic or interaction effect of these parameters *in vitro* and *in vivo*, which has not been widely covered in the literature.

Sex-specific immune response has been a persistent topic of debate. This thesis explored the expression and immune response differences in female and male BALB/c mice. This is a critical study, as no study has shown a difference in mRNA expression between biological sexes.

The following study aimed to improve the LNPs' efficiency, utilising the strong interaction between avidin and biotin. Biotinylated LNPs were injected into the mice before avidin injection. It was hypothesised that avidin would freely drain into the lymph nodes and form a complex with the biotinylated LNPs that had also drained into the lymph nodes. General objectives were examined for these studies:

1. Identifying the lipid compositions used in the COVID vaccines
2. Preparing these LNPs using Fluc-mRNA as model mRNA or using OVA-mRNA as model antigen,
3. Measuring particle critical quality attributes such as particle size, particle concentration, PDI, zeta potential, EE and recovery
4. Performing *in vitro* studies on the HEK-293 cell line, such as cellular toxicity, cellular uptake and cell expression
5. Testing these samples on BALB/c mice to assess either *in vivo* expression or immune response profile. The *in vivo* expression profile will be evaluated using an *in vivo* imaging system (IVIS), while the immune response will be tested by performing an Enzyme-Linked Immuno Sorbent Assay (ELISA).
6. Setting up DoE with FRR and TFR as microfluidic parameters and lipid concentration as formulation parameters. The main, quadratic and interaction effects of these parameters were tested by exploiting the Box-Behnken design.

Chapter 2: Exploring the Impact of Lipid Composition on the Transfection Efficiency of mRNA-LNPs: A combined *in vitro* and pre-clinical perspective.
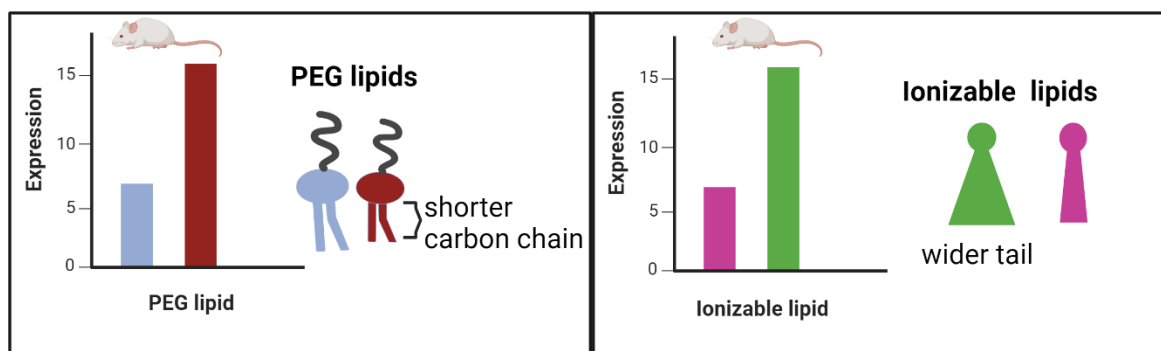
Th effect of the choice of PEG and ionisable lipids on mRNA-LNPs *in vivo* delivery

The work within this chapter has been submitted as a paper.

Author Credits

Burcu Binici (B.B.) Conceptualisation, methodology, formal analysis, investigation, data curation, writing – original draft preparation, writing- reviewing and editing, visualisation, project administration, funding acquisition.

Zahra Rattray (Z.R.) Conceptualisation, methodology, formal analysis, investigation, data curation, writing – original draft preparation, writing- reviewing and editing, visualisation, supervision.

Assaf Zinger (A.Z.) Conceptualisation, methodology, formal analysis, investigation, data curation, writing – original draft preparation, writing-reviewing and editing, visualisation,

Yvonne Perrie (Y.P.) Conceptualisation, methodology, formal analysis, investigation, data curation, writing – original draft preparation, writing- reviewing and editing, visualisation, supervision, project administration, funding acquisition.

2.1 Introduction

The recent development of messenger RNA (mRNA)-based vaccines has presented a highly encouraging approach to the rapid development of vaccines and immunisation against disease. The success of COVID mRNA vaccines relies on using lipid nanoparticles (LNPs) by encapsulating mRNA in a lipid shell. Naked mRNA is a polyanionic macromolecule rapidly degraded by extracellular RNases and cannot traverse cell membranes due to electrostatic repulsion. The encapsulation of mRNA into lipid vesicles enhances mRNA stability, facilitating cellular entry *via* endocytosis and improving expression in comparison to naked mRNA [75]. Moreover, LNPs have the potential to act as an adjuvant by augmenting the immune response [76]. Although the reason underlying the intrinsic adjuvant effect of LNPs is currently not fully understood, a study showed that inflammatory response from the mRNA-LNPs provides a basis for adjuvant activity, and ionisable lipids are likely responsible for this response. Also, it has been demonstrated that the adjuvant effect depends on the administration route of the LNPs [77].

LNPs are typically composed of four key lipids: an ionisable lipid, a PEGylated lipid, a phospholipid (often referred to as a helper lipid), and cholesterol. Helper lipids facilitate vesicle formation whilst reducing the cationic lipid concentration to a level that allows for effective encapsulation [78]. It has been reported that > 40 mol % is a likely threshold for such lipids to promote efficient and stable encapsulation [78]. DSPC is a commonly used phospholipid in nucleotide delivery; it is a structural lipid of mammalian cell membranes and enhances LNP stability due to its saturated carbon tail and high melting point. DOPE is another phospholipid considered for LNPs; it has a double bond in the acyl chains, making a bulky tail and smaller head group compared to DSPC, creating a cone-shaped structure [17,20]. This structural feature is reported to improve intracellular nucleotide delivery by promoting the Hii phase but also decreases LNP stability. Cholesterol is commonly used in LNPs for particle formation and stability, bridging the gap between lipids in LNPs and facilitating endosomal release [19]. Currently, three approved mRNA-LNP products contain DSPC and cholesterol, albeit with differing ionisable and PEG lipids [13].

Early nucleic acid delivery systems relied on permanently cationic-charged lipids, but their use was limited by cytotoxicity concerns [79]. Mainly as they activate several cellular pathways, such as pro-apoptotic and pro-inflammatory cascades [79]. This led to the development of

ionisable lipids, which switch from a positive charge in acidic pH (favouring their interaction with negatively charged mRNA) to neutral in physiological pH. Therefore, LNPs formed at acidic pH are buffer exchanged to achieve pH 7.4. Upon administration, LNPs are endocytosed, and the tertiary amine of the ionisable lipids is protonated into the quaternary amine in the acidic endosome (pH 4). Protonated ionisable lipids interact with anionic lipids of the endosome membrane, and this electrostatic interaction disrupts the endosomal membrane, releasing mRNA into the cytosol. The power of ionisable lipids is based on their pKa and 3D structural properties (Figure 2.1). The pKa of LNPs should be sufficiently high to achieve protonation in acidic environments and sufficiently low to carry a smaller positive surface charge at physiological pH, minimising toxicity [80]. The optimal pKa range of ionisable lipids to elicit an adaptive immune response via the intramuscular route was defined as 6.6-6.9; however, this decreased to 6.2-6.6 for optimum protein expression following intravenous injection [25]. Another critical factor dictating lipid efficacy in LNPs is the molecular shape of ionisable lipids. Branched-tailed ionisable lipids may lead to a cone-shaped structure, promoting endosomal escape [61]. Meanwhile, PEGylated lipids offer steric stability to LNPs, which is crucial for particle integrity. Typically, 1.5 mol% of PEGylated lipid is used in the clinically approved LNPs [21–23]. PEG content can affect LNP characteristics, such as LNP formation and the number of mRNA copies per LNP [81]. The length of the lipid tail of the PEG lipid further dictates the expression profile by affecting the desorption rate of the PEG chain [34,35]. After LNPs enter the body, it is proposed that the PEG needs to be released (via desorption) from the LNPs so that they can be internalised into the cells efficiently since the long hydrophilic PEG chain tends to hinder cellular uptake. The desorption rate of the PEG chain is driven by the quantity and length of hydrophobic chains in the molecule [34]. Given the impact of these changes in formulation and the link to LNP function, the overall aim of our study was to investigate how the choice of ionisable and PEGylated lipids alters LNP physio-chemical characteristics and their downstream effects on *in vitro* efficacy and *in vivo* potency. By considering this, our work aims to support more effective screening of LNPs.
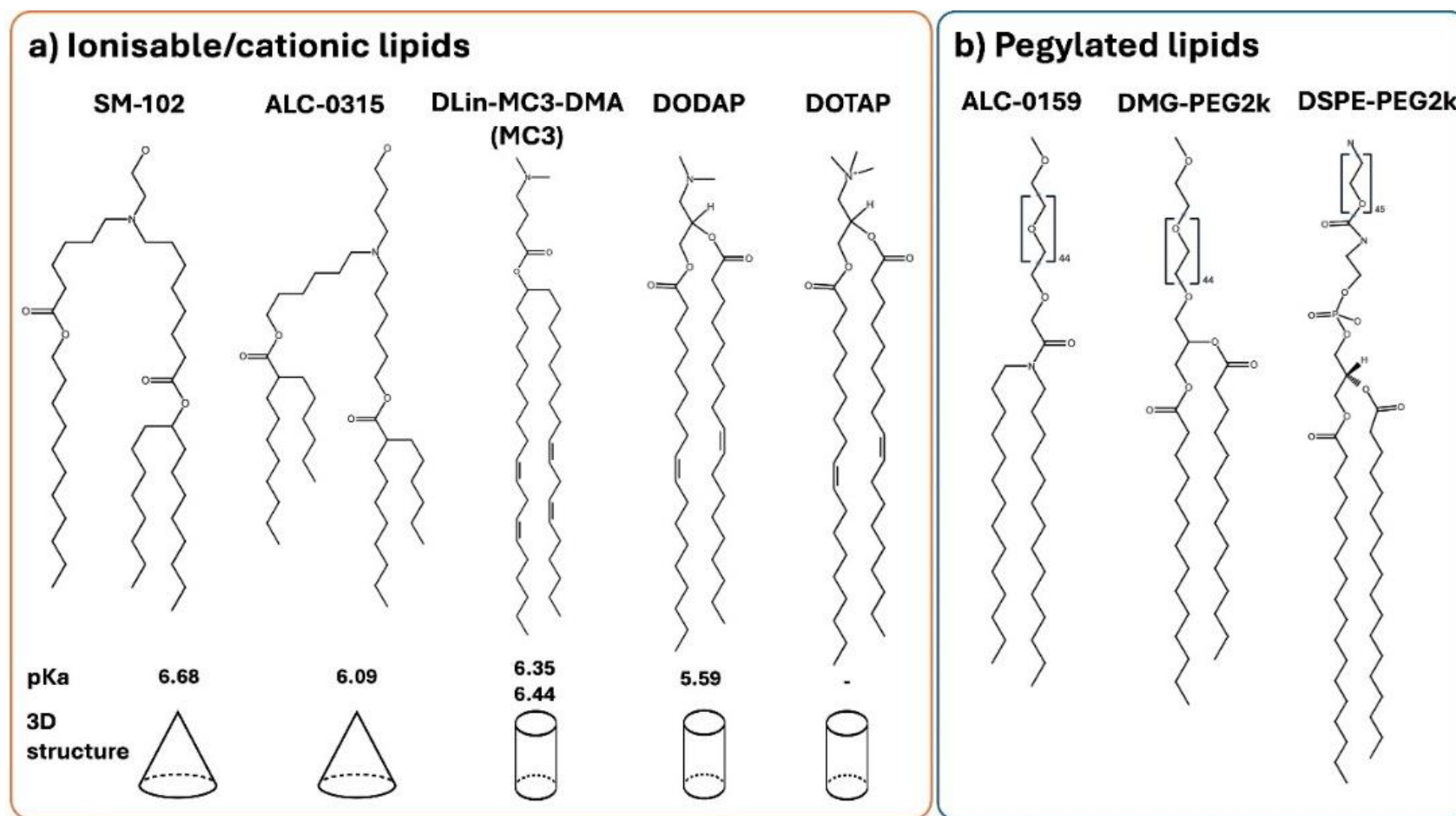
Figure 2.1 *The structures of the a) ionisable & cationic lipids and b) pegylated lipids used within this study. The structures were drawn using (Reaxys). The pKa for SM102, ALC-0315 and MC3 are from*[13] *and DODAP*[76]

2.2 Aim and Objectives

DSPC and cholesterol are well-established and approved helper lipids for LNP systems. Both have been used on three approved LNP-based products. Ionisable and PEGylated lipids are the focus of research. In this chapter, the choice of ionisable lipids, including ALC-0315, SM-102, MC3, DODAP and DOTAP and PEGylated lipids, including ALC-0159, DMG-PEG2k and DSPE-PEG2k tested *in vitro* and *in vivo*. The objectives for this aim were:

- Encapsulating Fluc mRNA into the ionisable lipids in a particle size aiming below 100 nm, monodisperse particle size distribution (below 0.2 PDI), neutral surface charge, high encapsulation (over 90%), and recovery efficiency (over 80%).

- Performing a-week stability study with these LNPs to confirm the stability of the formulation parameters such as the ratio between lipids, NP ratio,

- Evaluating the *in vitro* expression efficiency of the sample using the HEK-293 cell line and conforming if the LNPs are toxic to the cell in the concentration range used in the *in vitro* expression assay.

- Testing the sample *in vivo* using BALB/c mice and evaluating the expression and distribution profile.

2.3 Material and Method

2.3.1 Materials

1,2-distearoyl-sn-glycero-3-phosphocholine (DSPC), 1,2-dioleoyl-3-trimethylammoniumpropane (chloride salt) (DOTAP), 1,2-distearoyl-sn-glycero-3-phosphoethanolamine-N-[carboxy(polyethylene glycol)-2000] (sodium salt) (DSPE-PEG(2000)), 1,2-dimyristoyl-rac-glycero-3-methoxypolyethylene glycol-2000 (DMG-PEG2000), (1,2-dioleoyl-3-dimethylammonium propane) (DODAP), Polyadenylic acid (PolyA), Sodium citrate dihydrate, citric acid, Amicon® 10 kDa Ultra 15 mL Centrifugal Filters, dialysis membrane MWCO 12,000–14,000 Da, Cholesterol, Methoxypolyethyleneglycoloxy(2000)-N,N-ditetradecylacetamide (ALC-0159) were purchased from Merck (Gillingham, UK). 8-[(2-hydroxyethyl)[6-oxo-6-(undecyloxy)hexyl]amino]-octanoic acid, 1-octylnonyl ester (SM-102) was purchased from ABP Biosciences (Maryland, USA). 4 Hydroxybutyl)azanediyl)bis(hexane-6,1-diyl)bis(2-hexyldecanoate (ALC-0315) was purchased from MedChem Express (MedChemtronica AB, Sollentuna, Sweden). DLin-MC3-DMA (O-(Z,Z,Z,Z-heptatriaconta-

6,9,26,29-tetraen-19- yl)-4-(N,N-dimethylamino)) was gained from Biorbyt (Cambridge, UK). EZ Cap™ Firefly Luciferase mRNA was obtained from APExBIO Technology (Stratech Scientific Ltd, Cambridge, UK). Phosphate-buffered saline tablets (10 mM PBS pH 7.4) were acquired from Oxoid Ltd. (Basingstoke, UK). Minimum Essential Medium (MEM), Sodium Pyruvate (100 mM), UltraPure™ DNase/RNase-Free Distilled Water were purchased from Gibco™ (Paisley, UK). ONE-Glo™ Luciferase Assay System and VivoGlo luciferin were purchased from Promega (Southampton, UK). DiIC18(7) (1,1'-Dioctadecyl-3,3,3',3'-Tetramethylindotricarbocyanine Iodide (DIR), Quant-it™ RiboGreen RNA Assay Kit, TrypLE™ Express Enzyme (1X) were bought from ThermoFisher Scientific (Paisley, UK). BD Medical™ BD Micro-Fine™ Insulin Syringe was bought from Fisher Scientific (Loughborough, UK).

2.3.2 Methods

2.3.2.1 Preparation of Lipid Nanoparticles

Lipid nanoparticles (LNPs) were prepared using a staggered herringbone micromixer in the NanoAssemblr® Benchtop from Precision NanoSystems Inc. (Vancouver, BC, Canada). LNPs were prepared with NP6 (the molar ratio of amine groups (N) of the ionisable lipid to that of phosphate groups (P) of mRNA). The lipid phase was composed of DSPC:Chol:cationic/ionisable: PEG lipid (10:38.5:50:1.5 mol%), while the aqueous phase was prepared with Fluc mRNA in citrate buffer pH4. In the effect of the ionisable lipid study, cationic LNPs were prepared with DOTAP; ionisable LNPs were prepared with ALC-0315, SM-102, MC3, or DODAP, whilst DMG-PEG2k was the PEGylated lipid (Table 2.1). When testing the PEG lipids, ALC-0159, DMG-PEG2k, or DSPE-PEG2k were used as PEGylated lipids combined with ALC-0315 or SM-102 (Table 2.1). Lipids were dissolved in ethanol and mixed to the desired lipid ratio concentration. In the *in vivo* expression studies, DiR (1% molar of total lipid content), lipophilic dye, was included in the lipid phase to track the *in vivo* organ biodistribution of LNPs, using a DIR filter at an excitation level spectrum of 754 nm and emission spectrum of 778 nm. Fluc mRNA was dissolved in 50 mM citrate buffer (pH4) and 100 mM citrate buffer (pH6) for ionisable LNPs and cationic LNPs (DOTAP), respectively. Lipids dissolved in ethanol and aqueous phase containing FLuc mRNA were injected simultaneously in the micromixer at a 3:1 aqueous: organic flow rate ratio (FRR) and a 12 mL/min total flow rate (TFR). Initial and final waste volumes were set at 0.15 and 0.05 mL, respectively. 2 mL of LNPs were prepared.

Table 2.1 *Corresponding mRNA-LNP composition used in this study, equivalent to 5 µg Fluc mRNA/50 µL. All LNPs were prepared at NP6.*

LNPs	DSPC (µg)	CHOL (µg)	Ionisable Lipids (µg)	PEG lipid (µg)	mRNA (µg)	Lipid ratios (DSPC: Chol: ionisable: PEG lipid) (w/w)
ALC-0315	13.9	26.3	67.6	6.5	5	12:23:59:6
SM-102	13.9	26.3	62.7	6.6	5	13:24:57:6
MC3	13.9	26.2	56.7	6.6	5	13:25:55:6
DODAP	13.9	26.3	57.2	6.6	5	13:25:55:6
DOTAP	14.0	26.3	61.6	6.7	5	13:24:57:6

2.3.2.2 Down-stream Processing of LNPs

Dialysis (for cationic LNPs) or centrifugal filtration (for ionisable LNPs) was used to remove ethanol and adjust the formulation to physiologically relevant formulation conditions (pH 7.4). LNPs were dialysed (MWCO 14 kDa) against 10 mM PBS (pH 7.4) for one hour at ambient temperature under magnetic stirring. LNPs were diluted with 10 mM PBS (pH7.4) 40-fold and centrifuged (2,000x g acceleration:9 deceleration:9) at 4 °C in the centrifugal filter unit (10 kDa MWCO) until re-concentrating LNPs to the required volume.

2.3.2.3 LNP Characterization Using Dynamic Light Scattering

Following purification, particle size (z-average hydrodynamic diameter), polydispersity index (PDI), and zeta potential were measured by dynamic light scattering in Zetasizer Ultra (Malvern Panalytical Ltd, Worcestershire, UK), equipped with a 633 nm laser and a detection angle of 173°. Samples were diluted with 10 mM PBS pH 7.4 to a final lipid concentration of 0.1 mg/mL to measure particle size and polydispersity index (PDI). The same dilution with ultrapure water was used to measure zeta potential using electrophoretic mobility. Mean particle size, PDI, and zeta potential are expressed as the mean ± SD.

2.3.2.4 Entrapment Efficiency and mRNA Concentration within LNP Formulations

The encapsulation efficiency (EE%) and mass balance (MB%) of LNPs were determined using the Quant-iT™ RiboGreen® RNA quantification kit, referring to the amount of the encapsulated mRNA in the LNPs and total mRNA in the LNPs sample, respectively. LNPs were diluted to 3 µg/mL of mRNA with TE buffer. 50 µL of the diluted sample was incubated at 37 °C for 15 minutes with either 50 µL of TE or 50 µL of 2% Triton X-100 (extracting encapsulated mRNA by bursting LNPs), by referring to the amount of unencapsulated and total mRNA, respectively. 100 µL of Ribogreen fluorescent dye at 200 × and 500 × dilutions were added to the wells prepared with and without triton (only TE buffer), respectively. Fluorescence intensities were

measured at excitation and emission wavelengths of 480 nm/520 nm using the GloMax® Discover Microplate Reader. EE% (Equation 1.1) and mass balance% (Equation 1.2) were calculated according to the standard curves prepared with naked mRNA in the absence and presence of Triton.

2.3.2.5 *In vitro* Cell Viability and mRNA Expression Studies

HEK293 cells were cultivated in Minimum Essential Medium (MEM, Gibco) supplemented with 10% FBS, 1mM sodium pyruvate, 50U/mL penicillin-streptomycin at 37 °C in an environment containing 5% CO_2. HEK293 cells were sub-cultured at a density of 10,000 cells/well and incubated for 48 hours at 37 °C, 5% CO_2. For all *in vitro* studies, mRNA-LNPs were diluted with cell growth media to 1, 0.5, or 0.25 µg/mL (100, 50 or 25 ng mRNA /100 µL). To measure cell viability, 100 µL of each LNP formulation was added to the wells (quadruplicate) and incubated for 24 hours at 37 °C. The following day, 10 µL of Alamar blue was added to each well. Then, the plate was incubated for 4 hours, and the fluorescence intensity was measured (λem = 530-560 nm, λex = 590 nm) using a fluorimeter (Polarstar Omega, BMG Labtech). To measure mRNA expression, HEK-293 cells were treated with a serial dilution of mRNA-LNPs, as mentioned above. After 24 hours of incubation, One-Glo substrate (100 µL) was added, and luciferase expression was detected using a plate reader (Polarstar Omega, BMG Labtech) as luminescence.

2.3.2.6 *In vivo* LNP Retention at the Injection Site and mRNA Expression

All animals were handled in accordance with the UK Home Office Animals Scientific Procedures Act of 1986 (UK project license number PP1650440/ personal license number I52241434) in accordance with an internal ethics board. Groups of female 8-10-week-old BALB/c mice (n=5) were supplied by the Biological Procedure Unit at the University of Strathclyde, Glasgow. Pre-clinical imaging was performed using an *in vivo* imaging system (IVIS Spectrum, Perkin Elmer), and Living Image software ® 4.7.3 was used for image capture and data analysis, respectively.

Before starting this main study, a pilot kinetic study was performed to determine the time when luciferin activity peaked after administrating via the intraperitoneal (IP) route. Luciferin is rapidly eliminated from the blood circulation, and the level of luciferin delivery and elimination may vary. Therefore, a kinetic study was performed to determine the optimum time between D-luciferin injection and luminescence imaging; in other words, to define the

time when the luciferin level reached a stable plateau level after D-luciferin injection. A mouse was injected via intramuscular (IM) route with mRNA-LNPs (using pre-made Genvoy lipid and buffer). 6-hours later, d-luciferin was injected via the IP route, immediately mice were placed in the IVIS cabin under anaesthesia 16 images apart from 2.5 minutes were gained, and this imaging session was repeated at 24 h (day 1), 48 h (day 2), 120 h (day 5), and 168 h (day 7). Total flux was determined using imaging software, and the kinetic curve was plotted against time to assess luciferin activity.

In the main study, mice were injected with 5 µg of DiR-labelled Fluc mRNA LNPs per leg *via* IM injection and anaesthetised with 3% isoflurane and maintained at an isoflurane level of 2% in the IVIS chamber. Mice were imaged using the DiR filter (excitation/emission: 754/778 nm) to examine the biodistribution profile of DiR-labelled mRNA-LNPs. All mice subsequently received an IP injection of D-luciferin at 150 mg/kg. Following IP injection (20 minutes from the kinetic study), bioluminescence imaging was performed in an open filter using auto-exposure settings. Measuring DiR intensity and bioluminescence was conducted at 6 h, 24 h, 48 h and 192 h post-IM injection of LNPs. Images and data were exported using Living Image software ® 4.7.3. Average radiant efficiency and total flux were determined by region of interest tools for fluorescence and bioluminescence signals, respectively, by normalising according to the control mice. Average radiant efficiency and total flux were calculated for the fluorescence intensity and bioluminescence measurements and expressed mean ± SEM.

2.3.2.7 Statistical Analysis

Data is represented as a mean ± SD (Phyisco-chemical properties) or SEM (*in vitro* expression, cell toxicity, *in vivo* biodistribution and *in vivo* expression). GraphPad Prism was used to perform statistical analysis by performing ANOVA with post-hoc analysis wherever applicable. P-value < 0.05 was considered statistically significant.

2.4 Results

2.4.1 The Effect of Ionisable Lipids on LNP phyisco-chemical Properties

LNPs were prepared by mixing the lipid composition of DSPC: Chol: ionisable/cationic lipids: DMG-PEG2k (10:38.5:50:1.5 mol%) with Fluc mRNA at NP6 (Table 2.1), using a SHM and followed by purification with 10 mM PBS pH 7.4. All LNPs were < 100 nm in diameter, with low PDI (< 0.2) and near neutral zeta potential (Table 2.2). Irrespective of the choice of ionisable

(SM102, ALC-0315, MC3 or DODAP) or cationic (DOTAP) lipid, mRNA encapsulation was > 90%, and mRNA mass balance (total mRNA content) was high (>85%) (Table 2.2). The seven-day stability profile of these LNPs at storage temperature (2-8 ^{0}C) is shown in Table 2.2. LNPs prepared with ionisable lipids showed a stable profile, while the size of DOTAP-LNPs increased by approximately 15 nm (Table 2.2). The zeta potential of LNPs did not change significantly, nor did the encapsulation efficiency and mRNA mass balance (which remained >90% and 85%, respectively, for all formulations; Table 2.2).

Table 2.2 *The physicochemical properties of LNPs prepared with various ionisable/cationic lipids. LNPs comprised DSPC: Chol: ionisable/cationic lipid: DMG-PEG2k (10:38.5:50:1.5 molar ratio) and encapsulated Fluc mRNA at NP6. Ionisable lipids are ALC-0315, SM-102, MC3 (DLin-MC3-DMA) and DODAP, while cationic lipid is DOTAP. LNPs were stored in the fridge (2 − 8 ^{0}C). Characteristics were measured at 0 and 7 days. Results represent mean ± SD, n = 3 independent batches*

Cationic/Ionisable Lipids	Day	Diameter (nm)	PDI	Zeta Potential (mV)	EE (%)	Mass balance (%)
SM-102	0	64.9 ± 5.3	0.04 ± 0.03	-1.0 ± 0.9	97 ± 1	85 ± 16
	7	67.9 ± 6.8	0.03 ± 0.01	-1.5 ± 0.9	96 ± 0	84 ± 14
ALC-0315	0	55.2 ± 0.5	0.11 ± 0.02	-2.1 ± 1.1	93 ± 2	93 ± 11
	7	56.3 ± 1.0	0.12 ± 0.02	-3.7 ± 2.3	95 ± 1	100 ± 1
MC3	0	60.8 ± 1.3	0.11 ± 0.02	-1.6 ± 1.6	93 ± 2	93 ± 5
	7	60.6 ± 2.0	0.10 ± 0.02	-2.2 ± 0.5	93 ± 1	93 ± 6
DODAP	0	69.0 ± 2.8	0.04 ± 0.02	-1.4 ± 1.3	91 ± 1	97 ± 6
	7	66.1 ± 7.5	0.06 ± 0.02	-1.4 ± 1.0	87 ± 2	94 ± 2
DOTAP	0	49.8 ± 5.9	0.24 ± 0.04	2.4 ± 1.9	99 ± 0	89 ± 10
	7	68.7 ± 10.9	0.29 ± 0.03	4.8 ± 1.2	99 ± 1	87 ± 8

2.4.2 The Effect of Ionisable Lipid Composition on *in vitro* mRNA-LNP Expression

To investigate *in vitro* efficacy, HEK-293 cells were treated with Fluc-mRNA-LNPs for 24 h. Subsequently, cell viability and mRNA (luciferase) expression were also measured as a relative light unit (RLU) (Figure 2.2). Across all test concentrations, no notable impact on cell viability was observed (Figure 2.2a-e). Regarding mRNA expression (Figure 2.2f-j), expression levels were variable, with SM-102 levels 13-fold higher than MC3-LNPs, and 300-fold higher than ALC-0315. Notably, mRNA expression for DODAP and DOTAP was low (approx. 1500 and 500 lower than SM-102, respectively; Figure 2.2f-j).

SM102	ALC-0315	MC3	DODAP	DOTAP
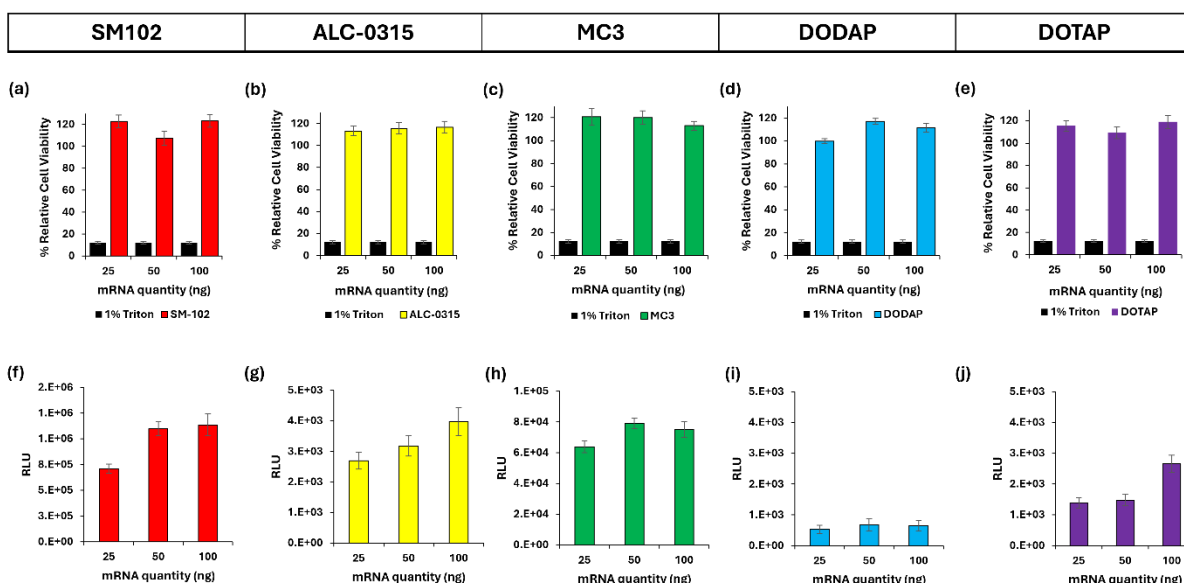
Figure 2.2 *In vitro transfection efficiency and toxicity profile of FLuc mRNA LNPs. HEK 293 cells were transfected with Fluc mRNA LNPs at mRNA of 25 ng, 50 ng, or 100 ng for all the formulations. 24-h post LNPs incubation a-e) HEK293 cell biocompatibility using Alamar blue, f-j) luminescence intensity was measured. LNPs comprised DSPC: Chol: ionisable/cationic lipid:DMG-PEG2k (10:38.5:50:1.5 molar ratio) and encapsulated Fluc mRNA at NP6. Ionisable lipids are ALC-0315, SM-102, MC3, and DODAP, while cationic lipid is DOTAP. Data is expressed as SEM (n=3) of three independent experiments.*

2.4.3 The Effect of Ionisable Lipid Composition on *in vivo* mRNA-LNPs Profile

2.4.3.1 Kinetic Profile of Luciferin

The time point (interval) when the D-luciferin reached the peak intensity and the plateau level was evaluated, performing a kinetic study with BALB/c mice injected via the IP route with 5 ug of Fluc mRNA-LNPs. The luminescence intensity was gained with 16 images in total with subsequent 2.5-minute intervals. 20 minutes was the most stable and plateau level for all time points (Figure 2.3).

2.4.3.2 The Effect of Ionisable Lipid Composition on *in vivo* mRNA-LNP Retention

To consider the *in vivo* expression and LNP retention at the injection site, BALB/c mice were intramuscularly injected in both hind legs with FLuc 5 µg mRNA formulated in the 5 different DiR-labelled LNPs (Figure 2.4). The results show that DiR-retention was only detected at the injection site as detecting the fluorescence intensity in internal organs with IVIS without organ extraction is difficult due to limited penetration depth in tissue (Figure 2.4a). Interestingly, whilst all mice received the same dose of DiR-labelled LNPs, after 6 hours, the fluorescent intensity at the injection site was higher for three out of the four ionisable LNPs (ALC-0315,

SM102 and MC3), whilst DODAP and DOTAP LNP DIR levels remained low (and remained low across the timescale of the study (Figure 2.4b).
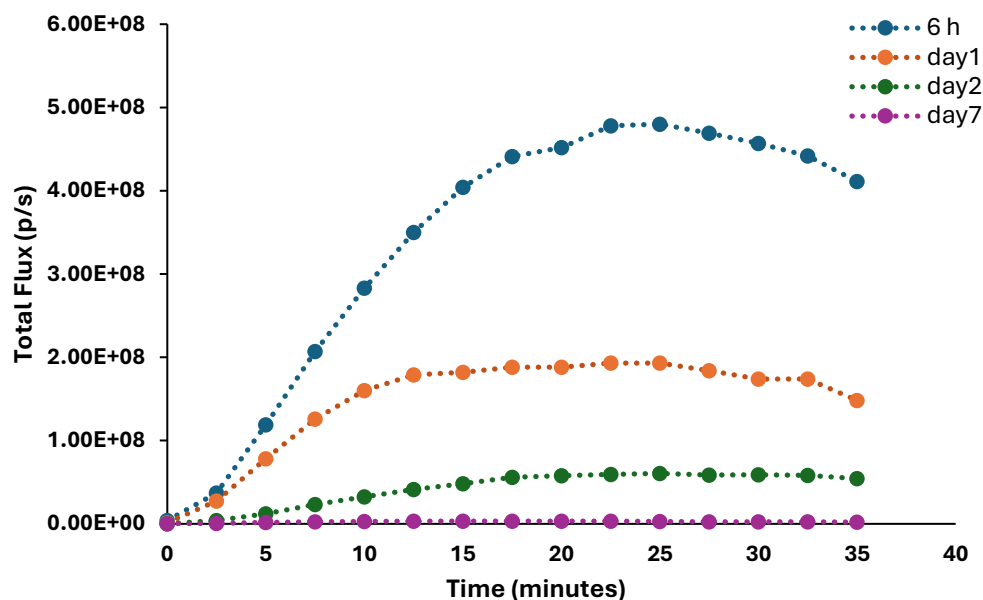
Figure 2.3 *The kinetic curve of d-luciferin in a BALB/c mouse. The mouse was injected with 5 ug of mRNA-LNPs. Six hours later, an intraperitoneal injection of d-luciferin was performed. Instantly, the mice were imaged with an open filter measuring luminescence intensity for almost 35 minutes at 2.5-minute intervals. Total flux was calculated from the injection site and plotted against time.*

After 6 h, SM-102 LNPs were cleared from the injection site more rapidly than LNPs containing either ALC-0315 or MC3 as the ionisable lipid (Figure 2.4 a and b). The difference in clearance rates from the injection site is exemplified in the AUC (Figure 2.4c), with LNPs composed of ALC-0315 and MC3 having similar AUC and significantly higher ($p<0.05$) than SM102 LNPs. Similarly, DODAP and DOTAP LNPs have a significantly lower ($p<0.05$) AUC than SM102. These results suggest the choice of ionisable/cationic lipids in LNPs affects their clearance rate from the injection site.

2.4.3.3 The Effect of Ionisable Lipid Composition on *in vivo* mRNA-LNP Expression

The same mice were analysed for mRNA protein (luciferase) expression (Figure 2.5). The results show distinct patterns over time and across different LNPs. At 6 h post-injection, the highest luciferase expression occurred at the injection site and the liver (Figure 2.5). The potency ranking for luciferase expression at the injection site for the LNPs was observed as ALC-0315 ≈ SM-102 >>MC3 >> DOTAP ≥ DODAP (Figure 2.5b). LNPs prepared using ALC-0315

and SM-102 showed comparable expression levels, with levels approximately 8-fold higher than MC3-LNPs and 180-fold higher compared to DODAP and DOTAP LNPs (which had similar levels of expression) (Figure 2.5b). Luciferase expression can also be seen in the liver for SM-102 and ALC-0315 LNPs (Figure 2.5c).
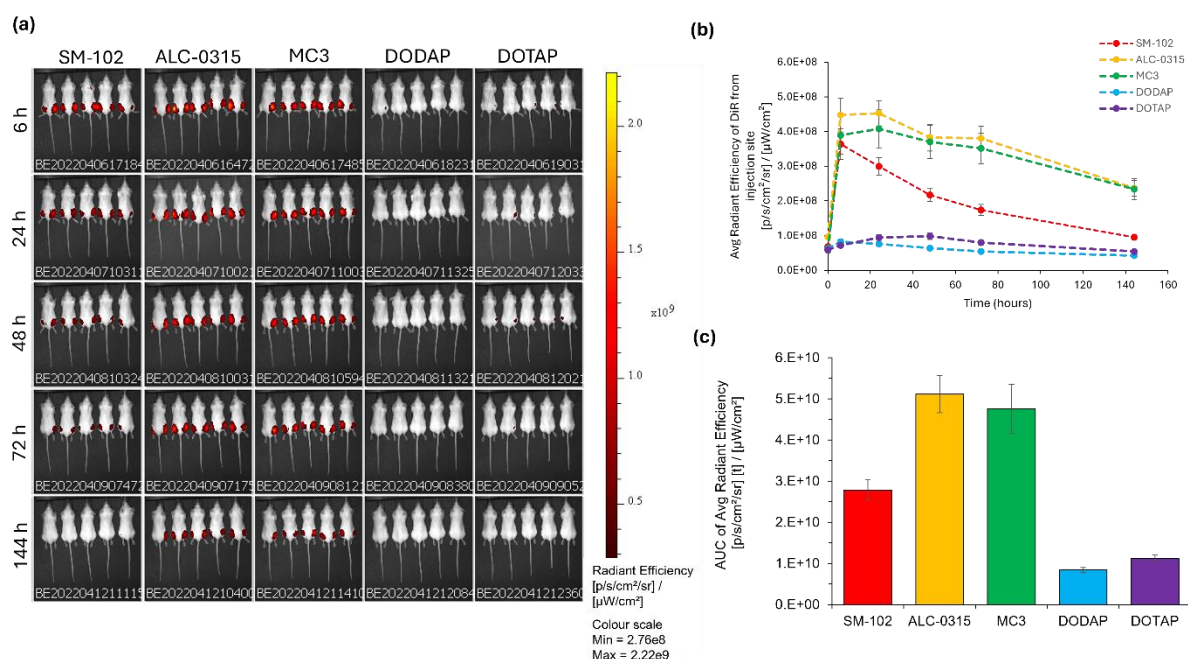
Figure 2.4 *LNP retention at the injection site. Female BALB/c mice were intramuscularly injected with DiR-labelled Fluc mRNA-LNPs, and the fluorescence intensity was measured at various time points (6 – 144 h). The injected dose was 5 μg mRNA encapsulated in LNPs composed of DSPC: Chol: ionisable/cationic lipids: DMG-PEG2k. The ionisable lipids are ALC-0315, SM-102, MC3, and DODAP, while cationic lipid is DOTAP. a) Representative IVIS images at selected time points after DiR-labelled mRNA-LNP injection. b) Fluorescence signal at the injection site over 144 h and c) the Area Under the Curve (AUC). Data are expressed by mean ± SEM (5 mice, 1 injection per hind leg; 10 data points). Connecting lines are for presentation purposes only.*

When considering the balance between expression at the injection site and the liver, ALC-0315 LNPs demonstrated significantly ($p < 0.05$) higher liver expression than SM102 LNPs (Figure 2.5d). These results suggest the choice of ionisable/cationic lipids in LNPs affects mRNA expression at the target site and the mRNA off-target effect in the liver.

2.4.4 The Impact of Pegylated Lipids on Fluc-mRNA LNP Characteristics and Potency

Given the effect of ionisable lipids *in vitro* and *in vivo*, we selected ALC-0315 and SM-102 as lead lipids and tested both lipids combined with three different PEG types used in the marketed products. These PEGylated lipids are ALC-0159, DMG-PEG2k and DSPE-PEG2k, used in Cominarity®, Spikevax® and Doxil®, respectively. DSPC and Cholesterol were included, as

reported in Table 2.1. LNPs were prepared using a microfluidic system, with all LNPs exhibiting a diameter <100 nm and a monodisperse particle size distribution (Table 2.3). All particles had neutral surface charge and > 90% mRNA entrapment efficiency and mass balance.
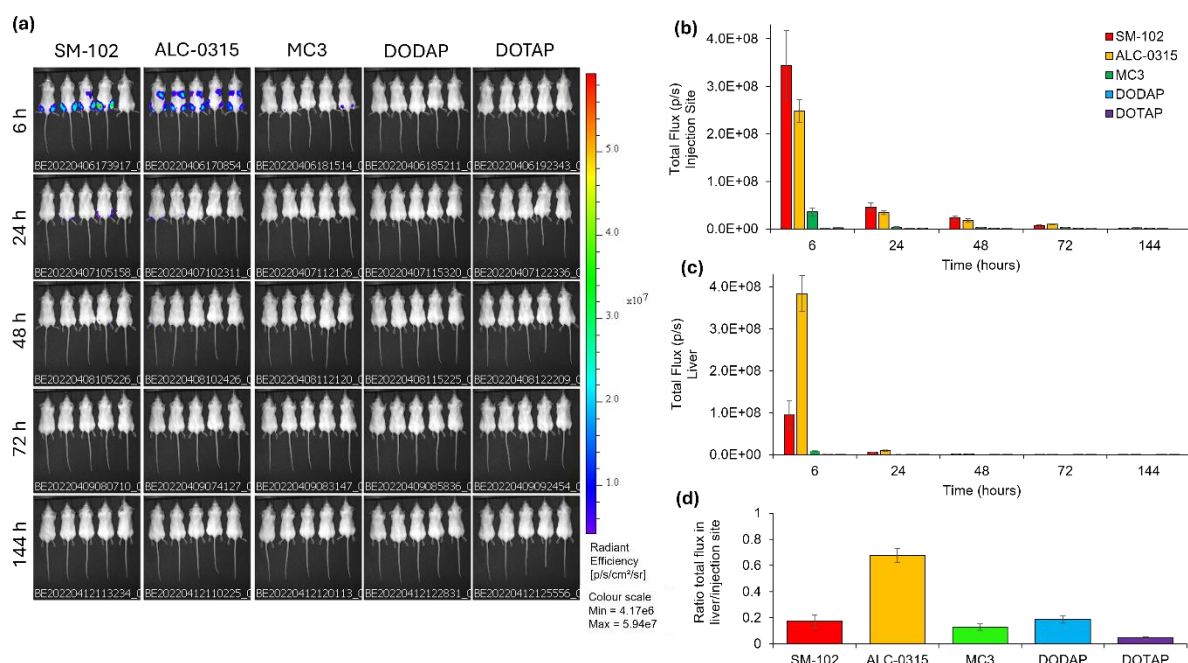
Figure 2.5 *Comparison of mRNA-encoded luciferase expression when formulated in different LNPs. The female BALB/c mice from Figure 3 were also imaged for luciferase expression. Mice were intramuscularly injected with DiR-labelled mRNA-LNPs, and the Flux was measured at various time points (6 – 144 h). The injected mRNA dose was 5 μg encapsulated in LNPs composed of DSPC: Chol: ionisable/cationic lipids: DMG-PEG2k. The ionisable lipids are ALC-0315, SM-102, MC3, and DODAP while the cationic lipid is DOTAP. a) Representative IVIS images at selected time points, b) Luminescence signal per injection site over 144 h, c) Luminescence signal per liver over 144 h, and d) ratio of total flux in liver/injection site (both legs). Data is expressed as mean ± SEM (5 mice, 1 injection per hind leg; 10 data points).*

Table 2.3 *Physicochemical properties of LNPs prepared with different PEGylated lipids. The LNPs comprised DSPC: Chol: ionisable/cationic lipid: PEG lipid (10:38.5:50:1.5 molar ratio) and encapsulated Fluc mRNA at NP6. Ionisable lipids are ALC-0315 and SM-102, while PEG lipids are ALC-0159, DMG-PEG2k and DSPE-PEG2k. They were manufactured using microfluidics at a 3:1 FRR and 12 mL/min TFR and purified by a spin column. After purification, average diameter, PDI and zeta potential were measured using DLS, while encapsulation efficiency and mass balance were measured using a Ribogreen kit. Results represent mean ± SD, n = 3 independent batches.*

ionisable lipid	Pegylated lipid	Diameter (nm)	PDI	Zeta Potential (mV)	EE (%)	Mass balance (%)
SM-102	ALC-0159	73.5 ± 2.5	0.05 ± 0.03	-1.7 ± 1.1	94 ± 3	91 ± 11
	DMG-PEG2k	66.4 ± 2.7	0.08 ± 0.01	-2.4 ± 0.7	91 ± 5	86 ± 12
	DSPE-PEG2k	63.4 ± 0.1	0.04 ± 0.02	-2.3 ± 2.2	97	92
ALC-0315	ALC-0159	74.5 ± 5.1	0.08 ± 0.03	-2.8 ± 1.1	92 ± 4	96 ± 8
	DMG-PEG2k	57.3 ± 3.0	0.11 ± 0.03	-3.0 ± 1.5	93 ± 2	92 ± 11
	DSPE-PEG2k	57.4 ± 0.4	0.04 ± 0.01	-2.5 ± 2.2	95	100

These mRNA-LNPs were tested in HEK-293 cells for their mRNA expression potency by measuring luciferase expression (Figure 2.6). Again, we see the same trend with LNPs prepared with ALC-0315 promoting significantly lower (p<0.05) expression than SM-102 LNPs. However, we also demonstrate that using ALC-0159 PEG lipid significantly (p<0.05) increased expression in comparison to DMG-PEG2k (Figure 2.6). Indeed, using ALC-0159 instead of DMG-PEG2k at the same 1.5% ratio within the formulations enhanced the mRNA expression 9-fold and 4-fold for ALC-0315 and SM-102-based LNPs, respectively (Figure 2.6).
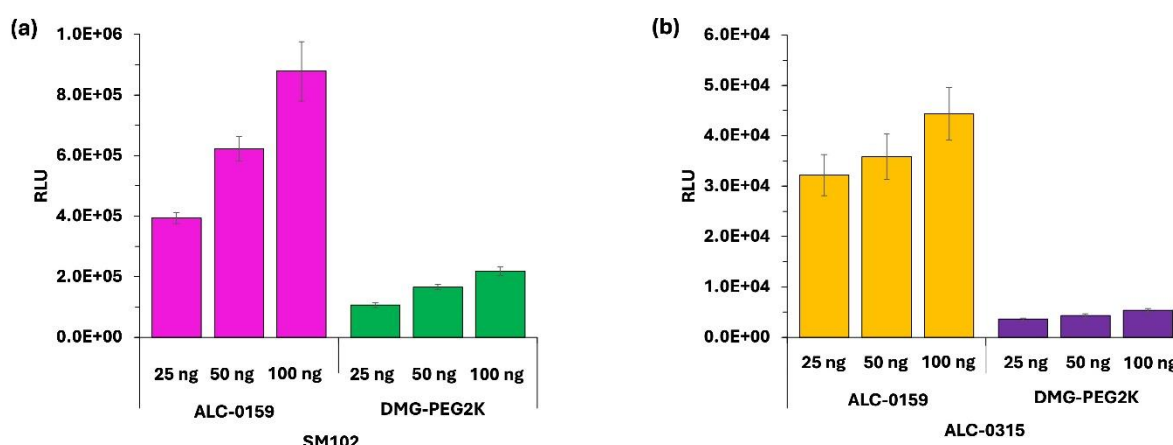
Figure 2.6 *The effect of PEGylated lipids on in vitro expression efficiency. HEK 293 cells were transfected with Fluc mRNA LNPs at mRNA levels of 25 ng, 50 ng, and 100 ng for all the formulations. 24-h post LNPs incubation luminescence intensity was measured. The LNPs comprised DSPC: Chol: ionisable: PEG lipid (10:38.5:50:1.5 molar ratio) and encapsulated Fluc mRNA at NP6. Ionisable lipids are a) SM102 with ALC-0159 or DMG-PEG2k and b) ALC-315 with ALC-0159 or DMG-PEG2k. Results represent mean ± SEM, n= 3 independent batches*

2.4.5 The Effect of PEGylated Lipid Choice on *in vivo* mRNA-LNP Distribution and Expression

To consider the impact of the choice of PEGylated lipid within the LNPs on the biodistribution and potency *in vivo*, BALB/c mice were injected with 5 µg of DiR-labelled LNPs encapsulated Fluc mRNA prepared with SM-102 (Figure 2.7 and 2.8) or ALC-0315 (Figure 2.9 and 2.10) as the ionisable lipid. Our results demonstrate that the choice of PEGylated lipid (DSPE-PEG2k vs DMG-PEG2k vs ALC-0159) has no notable impact on SM-102 LNP retention at the injection site (Figures 2.7a and b) and the calculated AUC (Figures 2.7c). However, the choice of PEGylated lipid has a major impact on protein expression (Figures 2.8a), with the use of DSPE-PEG2k within the LNPs significantly (p<0.05) reducing expression compared to LNPs prepared with ALC-0159 or DMG-PEG2k (which are not significantly different) both at the injection site

(Figures 2.8b and c) and the liver (Figures 2.8d and e). Therefore, the different expression levels measured at the injection site do not result from differences in clearance.
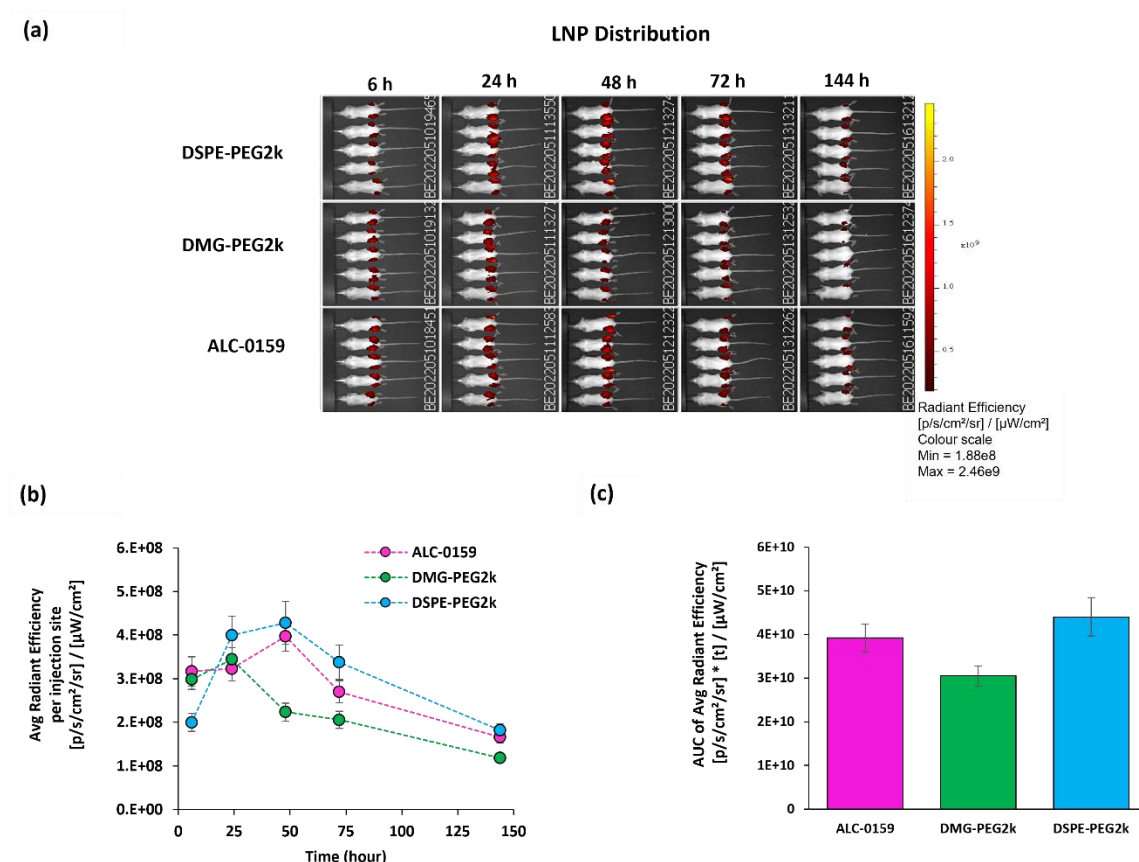
Figure 2.7 *Biodistribution of SM-102 Fluc mRNA-LNPs labelled with DiR prepared with three different PEGylated lipids (ALC-0159, DMG-PEG2k and DSPE-PEG2k), a) IVIS image representing the biodistribution profile of DiR labelled LNPs and b) the quantification of DIR intensity from the injection site over the time and c) the Area Under the Curve (AUC). The LNPs comprised DSPC: Chol: SM-102: PEG lipid (10:38.5:50:1.5 molar ratio) and encapsulated Fluc mRNA at NP6. PEG lipids are ALC-0159, DMG-PEG2k and DSPE-PEG2k. Female BALB/c mice were injected with 5 ug of Fluc mRNA-LNPs. Data is expressed as mean ± SEM (5 mice, 1 injection per hind leg; 10 data points).*

In the case of ALC-0315 LNPs (Figure 2.9 and Figure 2.10), the choice of pegylated lipid again had no impact on LNPs clearance (Figure 2.9a) from the injection site, with similar LNP retention for ALC-0315 LNPs prepared with DSPE-PEG2k, DMG-PEG2k and ALC-0159 (Figures 2.9b and c). However, again similar to SM-102, FLuc protein expression was significantly (p<0.05) lower for LNPs prepared with DSPE-PEG2k both at the injection site (Figures 2.10a, b and c) and liver (Figures 2.10a, d and e) compared to LNPs prepared with ALC-0159 and DMG-PEG2k. However, unlike the SM-102 LNPs, LNPs prepared with the ionisable lipid ALC-0315 in combination with the pegylated lipid ALC-0159 gave significantly (p<0.05) higher expression

both at the injection site (Figures 2.10b and c) and the liver (Figures 2.10d and e) than LNPs prepared with ALC-0315 and DMG-PEG2k.
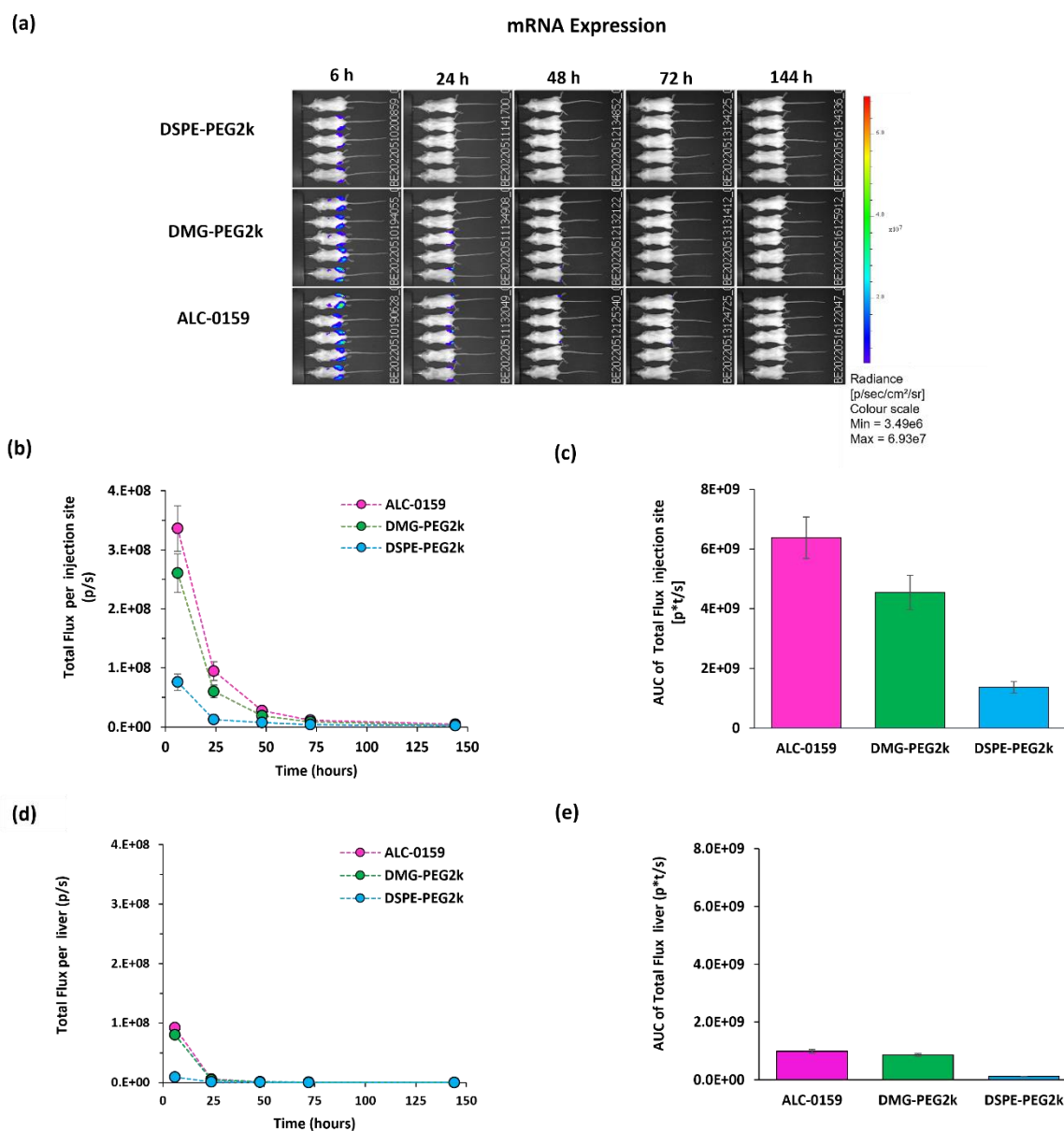
Figure 2.8 *Expression profile of SM-102 Fluc mRNA-LNPs labelled with DiR prepared with three different PEGylated lipids (ALC-0159, DMG-PEG2k and DSPE-PEG2k), a) Representative IVIS image of the expression profile of the LNPs formulated with mRNA-encoded and quantification of the luminescence signal as the light emitted from b) the injection site and corresponding c) Area Under the Curve (AUC) d) liver and e) corresponding the Area Under the Curve (AUC). The LNPs comprised DSPC: Chol: SM-102: PEG lipid (10:38.5:50:1.5 molar ratio) and encapsulated Fluc mRNA at NP6. PEG lipids are ALC-0159, DMG-PEG2k and DSPE-PEG2k. Female BALB/c mice were injected with 5 ug of Fluc mRNA-LNPs. Data is expressed as mean ± SEM (5 mice, 1 injection per hind leg; 10 data points).*

2.5 Discussion

In this study, we have compared mRNA-LNPs formulated from five different ionisable/cationic lipids and three different PEGylated lipids. All formulations had a fixed molar ratio of DSPC:

Chol: Ionisable/cationic lipid: PEG lipid (10:38.5:50:1.5%), and we systematically measured their physical-chemical characteristics, *in vitro* expression, *in vivo* expression, and injection site clearance.

Physico-chemical characterisation demonstrated that the choice of ionisable or cationic lipids (Figure 2.1) had no notable impact on LNP physico-chemical attributes measured, which is likely driven by the manufacturing process rather than the choice of lipid. Given the similarity in these physico-chemical attributes but differences in potency, this highlights that these characteristics are a good indicator of quality (and hence useful critical quality attributes) but not necessarily potency indicating. This was confirmed by first investigating the choice of ionisable lipids on *in vitro* (Figure 2.2) and *in vivo* expression efficacy (Figure 2.5) in HEK-293 cells and BALB/c mice, respectively.
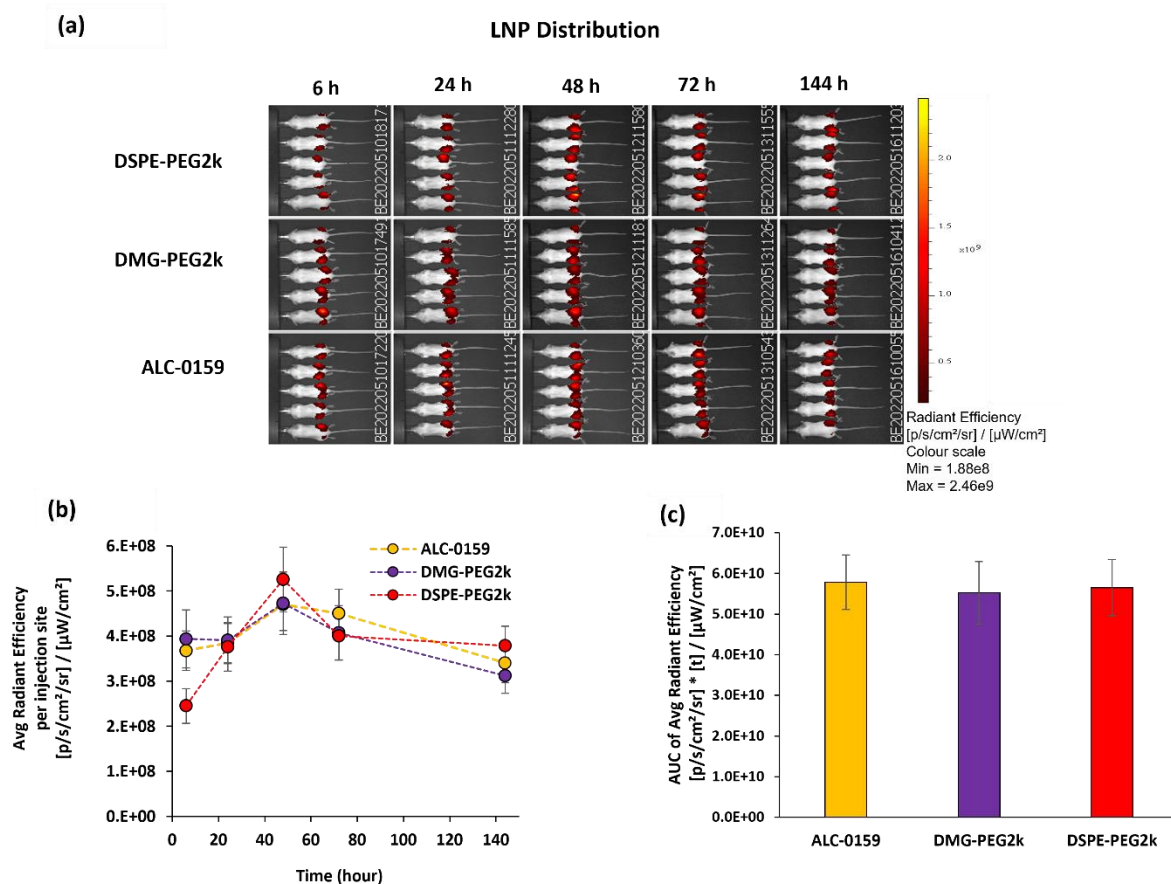
Figure 2.9 *Biodistribution profile of ALC-0315 Fluc mRNA-LNPs labelled with DiR prepared with three different PEGylated lipids (ALC-0159, DMG-PEG2k and DSPE-PEG2k), a) IVIS image representing the biodistribution profile of DiR labelled LNPs and b) the quantification of DIR intensity from the injection site over the time and c) the Area Under the Curve (AUC). The LNPs comprised DSPC: Chol: SM-102: PEG lipid (10:38.5:50:1.5 molar ratio) and encapsulated Fluc mRNA at NP6. PEG lipids are ALC-0159, DMG-PEG2k and DSPE-PEG2k. Female BALB/c mice were injected with 5 ug of Fluc mRNA-LNPs. Data is expressed as mean ± SEM (5 mice, 1 injection per hind leg; 10 data points).*
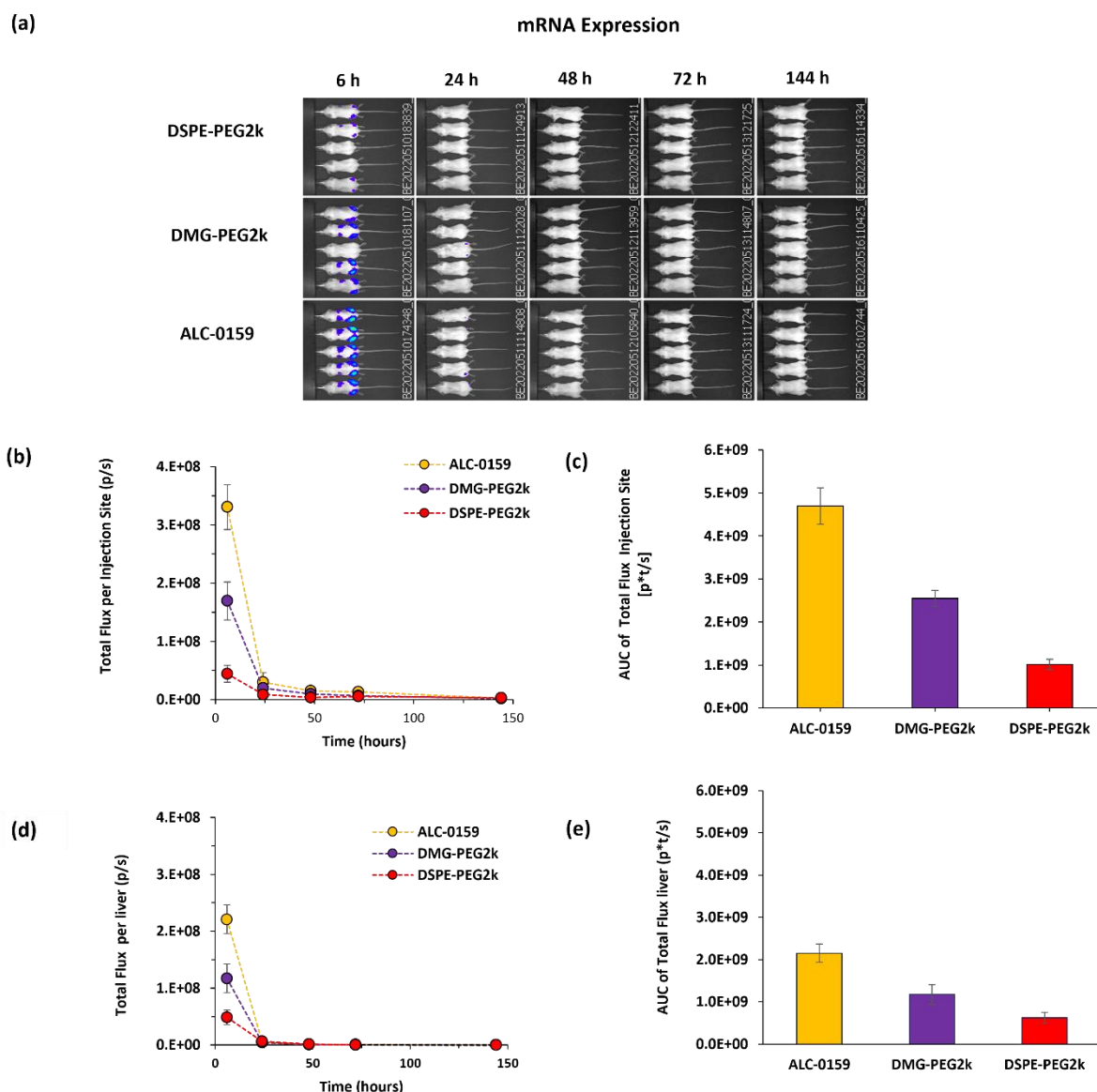
Figure 2.10 *Expression profile of ALC-0315 Fluc mRNA-LNPs labelled with DiR prepared with three different PEGylated lipids (ALC-0159, DMG-PEG2k and DSPE-PEG2k), a) Representative IVIS image of the expression profile of the LNPs formulated with mRNA-encoded and quantification of the luminescence signal as the light emitted from b) the injection site and corresponding c) Area Under the Curve (AUC) d) liver and e) corresponding the Area Under the Curve (AUC). The LNPs comprised DSPC: Chol: SM-102: PEG lipid (10:38.5:50:1.5 molar ratio) and encapsulated Fluc mRNA at NP6. PEG lipids are ALC-0159, DMG-PEG2k and DSPE-PEG2k. Female BALB/c mice were injected with 5 ug of Fluc mRNA-LNPs. Data is expressed as mean ± SEM (5 mice, 1 injection per hind leg; 10 data points).*

All LNPs prepared with the various ionisable lipids were consistently <100 nm in size, with a low polydispersity (< 0.2 PDI), high (> 90%) encapsulation efficiency and mass balance. All LNPs had a near-neutral zeta potential (Table 2.2). The order of potency for in vitro transfection from high to low delivery was SM-102 >>>> MC3>>> DOTAP ≈ ALC-0315>DODAP (Figure 2.2); however, in vivo expression for SM-102 and ALC-0315 LNPs was comparable at the injection

site, yet ALC-0315 LNPs promoted significantly higher expression at the liver (Figure 2.6). The in vitro expression profile was not normalised according to total protein content as LNPs were relatively compared. Also, it was shown that all LNPs were not toxic to the HEK-293 cell line at the concentration range mRNA expression study performed (Figure 2.2).

The higher *in vivo* potency of SM-102 and ALC-0315 compared to MC3, DODAP, and DOTAP has been attributed to differences in the different lipid molecular shapes rather than their pKa[76]. The branched ester chains of SM-102 and ALC-0315 lipid tails (and hence cone shape) increased mRNA delivery compared to more cylindrical MC3, DODAP, and DOTAP lipids [82,83]. The branched-tail structure of SM-102 and ALC-0315 is reported to enable disruption of the endosomal membrane in a greater proportion and release of mRNA into the cytosol [61]. The highest *in vitro* expression, with SM-102 having the highest pKa and the lowest expression, with DODAP having the lowest pKa, highlighted the importance of pKa in *vitro* expression. However, why ALC-0315 has lower potency *in vitro* despite higher *in vivo* potency is unclear and emphasises the issues in effectively down-selecting LNP formulations when progressing from *in vitro* to pre-clinical studies. The hepatic tropism of ALC-0315 LNPs compared with SM-102 LNPs after IM injection shown in our studies has also been demonstrated by Zhang *et al.* investigating the expression kinetics of LNPs [84]. It has been published that lower pKa is related to the expression in the liver for IM injection[85]. Among the ionisable lipids, ALC-0315 has the lowest pKa and the highest expression in the liver. Regarding the biodistribution profile of LNPs, DiR intensity was similar for all LNPs after LNP injection. However, ALC-0315, SM-102, and MC3 had higher fluorescence intensity than DODAP and DOTAP at 6 h. Whilst the use of the DiR-label to track LNP distribution following injection is a commonly used approach [86], tracking LNPs beyond the injection site is a challenge as detecting the fluorescence intensity in internal organs with IVIS without organ extraction is difficult due to limited penetration depth in tissue, explaining why bioluminescence can only be detected in the liver [60].

Differences in the ratio of expression between the injection site and the liver for LNPs and nanoparticles, in general, could be related to 1) LNP physico-chemical characteristics, which in turn affect clearance to the liver, 2) particle uptake and metabolism in the liver. Given the similarities in the LNP physico-chemical attributes (Table 2.2), this suggests differences in metabolism and/or immunogenicity of the ionisable lipids drive these differences and given

that *in vitro* studies lacking metabolic and immune functionality, they do not adequately predict *in vivo* performance [87].

Given the potency of SM-102 and ALC-0315 LNPs, we then focused on these formulations and considered the impact of the choice of PEGylated lipid used within the formulation. Again, physico-chemically, the particles were similar (Table 2.3), and SM-102 LNPs outperformed ALC-0315 LNPs in HEK293 cells, irrespective of the PEGylated lipid used (ALC-0159 vs DMG-PEG2k). However, with both ionisable lipids, using ALC-0159 in the LNP composition resulted in higher *in vitro* expression. These LNPs were then progressed for *in vivo* evaluation along with the consideration of a third PEGylated lipid – DSPE-PEG2k, which has an 18-carbon tail compared to ALC-0159 and DMG-PEG2k, which both have 14 carbon tails. While the choice of PEG-lipid did not influence clearance from the injection site (Figure 2.7 and Figure 2.9), luciferase expression was impacted, with both SM-102 LNPs (Figure 2.8) and ALC-0315 LNPs (Figure 2.10) showing luciferase expression in the order of ALC-0159>DMG-PEG2k>DSPE-PEG2k, with the difference between ALC-0159 and DMG-PEG2k being more notable when combined with ALC-0315 (Figure 2.10).

PEGylated lipids are incorporated into LNP formulations to provide stability through steric stabilisation both in the vial and within the biological milieu. The length of the lipid tail of these PEGylated lipids plays a crucial role in determining the fate of LNPs *in vivo*. Specifically, C18 acyl chains exhibit efficient anchoring in the membrane. On the other hand, shorter C14 lipids tend to rapidly desorb, leading to their replacement by a protein corona. This protein corona significantly influences the subsequent destiny of the LNPs, resulting in a distinctly different outcome [88]. For example, Mui *et al.* examined the desorption rate of various PEGylated lipids having 3-different alkyl chains after IV injection and showed PEG-lipid loss from LNPs *in vivo* to occur at >45%/hour, 1.3%/hour, and 0.2%/hour for C14, C16, and C18, respectively [34]. Thus, the steric barrier presented by C18 PEG-lipids could be considered permanent, which confirms our finding that DSPE-PEG reduces mRNA-LNP potency (Figures 7 and 8). However, the interaction between the ionisable lipid and the PEG-lipid must also be considered. Indeed, it has been shown that PEG desorption rates may be linked to the choice of ionisable lipid, as SM-102 LNPs were shown to lose their PEG chain more easily compared to other ionisable lipids [88]. This may explain why ALC-0159 and DMG-PEG2k had comparable protein expression levels for SM-102 LNPs but different profiles for ALC-0315 LNPs.

2.6 Conclusions

Overall, our studies confirm that for the development of mRNA LNP formulations, physicochemical characteristics are indicative of the manufacturing process product quality but not potency indicating, and the prudent selection of *in vitro* and *in vivo* models is a pivotal factor in bridging the translation gap even within pre-clinical studies. In vitro, transfection efficiency exhibited a potency order of SM-102 > MC3 > DOTAP ≈ ALC-0315 > DODAP, whilst *in vivo* expression in BALB/c mice showed ALC-0315 LNPs displaying comparable potency to SM-102. Considering the choice of PEGylated lipid component, this did not impact LNP clearance from the injection site, but in terms of potency, there is an intricate interplay between ionisable lipids and PEGylated lipids, with the combination of ALC-0315 as an ionisable lipid with ALC-0159 as the PEGylated lipid providing the highest protein expression.

In conclusion, SM-102 LNP was selected as a lead formulation for the next chapter to test the other parameters because it performed well *in vitro* and *in vivo* among the other lipids.

Chapter 3: Impact of Citrate Buffer Ionic Strength on the Characteristics and Efficacy of Lipid Nanoparticles
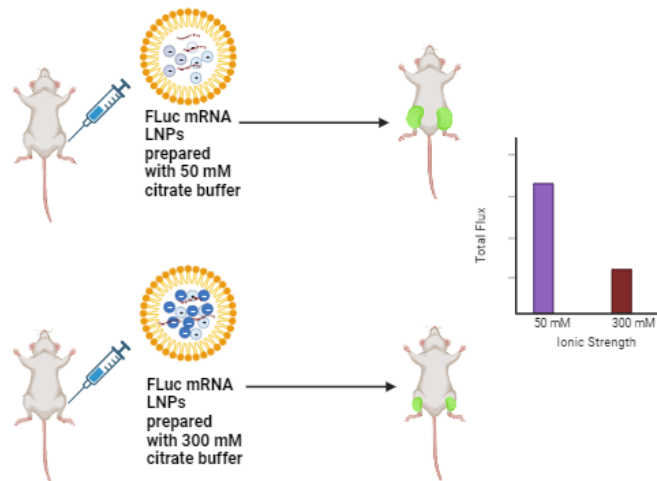
Formulation of Fluc-mRNA in higher ionic strength of citrate buffer impact transfection efficiency

The work within this chapter was submitted as a paper.

Author Credits

Burcu Binici (B.B.) Conceptualization, methodology, software, validation, formal analysis, investigation, data curation, writing—original draft preparation, writing—review and editing, visualisation, funding acquisition.

Ankita Borah (A.B.) Conceptualization, methodology, software, validation, formal analysis, investigation, data curation, writing—original draft preparation, writing—review and editing, visualisation.

Yvonne Perrie (Y.P.) Conceptualization, methodology, investigation, resources, visualisation, supervision, project administration, funding acquisition

3.1 Introduction

LNPs are recognised as the go-to platform for RNA-based therapeutics and vaccines. LNPs are versatile carriers that support the delivery of both small interfering RNA (siRNA) and longer messenger and self-amplifying RNA (mRNA and saRNA) owing to their ability to protect and deliver nucleic acids combined with their biocompatibility and bioavailability [89].

Whilst most studies have focused on the mixing process and the lipid phase, the other component of LNP production is the encapsulation buffer. Aqueous phase parameters such as the choice of buffer to dissolve the nucleic acids, its ionic strength, and the pH all influence the nucleic acids' overall state and can influence the self-assembly process in the LNP formulation. The aqueous phase used in this production process has two roles: It dissolves the RNA and should support its stability. In addition, the pH of the aqueous phase controls the charged state of the pH-sensitive ionisable lipids, which are designed to be protonated at lower pH (to support nucleic acid complexation and endosomal release) and neutral at physiological pH to avoid the related toxicity issues seen with cationic lipids [7,90]. At lower pH, in addition to imparting the positive charge on the ionisable lipids, it has also been demonstrated that in acidic pH conditions, the membrane packing density of the lipids in LNPs reduces due to the electrostatic repulsion between the lipid molecules, which helps the fusion of the LNPs with the endosomal membrane and can delineate the release of nucleic acids [91]. Thus, the pH of the aqueous phase is a crucial parameter dictated by the pKa of the ionisable lipid. Given that most ionisable lipids have a pKa around 6, a pH 4 is widely used to provide electrostatic interaction between anionic phosphate bond RNA and positive quaternary amine in the ionisable lipid [92]. Studies by Semple et al. demonstrated the effect of the pH of the aqueous phase on the encapsulation efficiency of LNPs, with results showing that increasing pH from 3.5 to 6.5 decreased encapsulation efficiency from 90 to almost 0 [93]. A similar study by Jeffs et al. showed that increasing pH from 4 to 10 decreased EE from 90% to almost 65% [94]. The pH of the aqueous buffer may also impact the particle size, given that Ly et al. showed that using acidic pH led to smaller particles. The authors hypothesised that ionisable lipids in lower pH were more highly charged and experienced more opportunity to interact with anionic saRNA, resulting in rapid particle formation and, hence, smaller particle [95]

In addition to the pH, different buffers such as malic acid buffer, acetate buffer, lactate buffer, and citric acid buffers have also been investigated in the LNPs formulation, and their effect on

the physicochemical characteristics of LNPs reported [96]; LNPs prepared in the acetate and lactate buffers had a smaller mean particle diameter compared to the LNPs prepared in malate and citrate buffers, with no obvious differences in the other physicochemical characteristics (PDI, zeta potential, and siRNA encapsulation). However, LNPs prepared in the malate and citrate buffers were less cytotoxic compared to those prepared with acetate and lactate buffers. Generally, citrate buffer has been the preferred choice to prepare RNA-based LNPs as it prevents RNA base hydrolysis, where chelating di- and trivalent ions in citric acid deactivates DNases/RNases [43]. It was shown that the citrate buffer offered the most stable environment to mRNA compared to the other buffers, such as sodium phosphate and HEPES (both 10 mM); however, this also depends on the pH [97]. For example, increasing pH from 4 to 6 improved the mRNA stability with citrate buffer; however, mRNA was more degraded with HEPES when the pH increased from 7 to 8. It is also reported that the buffers, including sodium ions such as citrate or sodium acetate, tend to yield relatively larger particles by making complex with payloads, whilst HEPES buffers, which do not contain metal ions, are not likely to make such heterogeneous particles [98]. Moreover. It was shown that the interaction between lipid and nucleic acid depends on the encapsulation buffer. For example, citrate buffers made the nucleic acid (NA) surface more negative than the HEPES buffer. This allows more electrostatic interaction between NA and lipid and hence increases the thickness of the NA layer adsorbed onto the lipid bilayer [99].

However, whilst the choice of buffer and its pH are key considerations, the ionic strength of the aqueous buffer is also an important parameter and overlooked compared to the other parameters. The citrate and acetate buffer are commonly used to encapsulate RNA into the LNPs, and the three clinically used RNA LNPs-based products employ these buffers, although they do not specifically mention it; it is revealed from their preclinical studies [21–23,40]. Increasing ionic strength likely led to an increase in the particle size [100,101]. The addition of sodium chloride (NaCl) was used as a strategy to improve the EE [102]. Moreover, it has been shown that increasing ionic strength affected the EE depending on the pH; for example, increasing ionic strength 25-fold decreased the EE by nearly 10 times at pH4, but it was only halved at pH5, while this did not affect the particle size with such dramatically, increased the size slightly [103]. Moreover, it was shown that increasing ionic strength from 20 mM to 300 mM of citrate buffer drastically diminished EE from 95% to 7% when encapsulating siRNA;

however, it did not affect EE for antisense oligonucleotides [104]. So far, as can be seen, many studies have focused on the effect of ionic strength on particle size and EE. Cheng et al. showed increasing ionic strength from 25 mM to 300 mM led to greater transfection efficiency both *in vitro* and *in vivo* [105]. The author associated this improvement with forming more bleb structures with higher ionic strength.

Given not much study considering the effect of ionic strength on *in vitro* and *in vivo* outcome, in this chapter, the influence of increasing ionic strengths of citrate buffer from 50 mM to 300 mM used in the manufacture of mRNA-LNPs on the resultant LNP physicochemical characteristics, *in vitro* transfection and *in vivo* efficiency and biodistribution was investigated.

3.2 Aim and Objectives

This chapter aimed to consider the effect of the ionic strength of citrate buffer on mRNA LNPs *in vitro* and *in vivo* efficiency. To achieve this, the objectives of this study were:

- Preparing Fluc-mRNA-LNPs with 50 mM, 100 mM, and 300 mM citrate buffer and characterise the LNPs.
- Analysing the particle size distribution and the particle concentration using a single particle-based technique called NTA.
- Determine the effect of ionic strength on pKa of LNPs using TNS assay,
- Demonstrating qualitative and quantitative cellular uptake profile of LNPs using HEK-293 cell line and transfection efficiency and toxicity profile.
- Considering the biodistribution profile of LNPs and the *in vivo* expression profile.

3.3 Material and Method

3.3.1 Materials

The ionisable lipid 8-[(2-hydroxyethyl) [6-oxo-6-(undecyloxy) hexyl]amino]-octanoic acid, 1-octylnonyl ester (SM-102) was purchased from BroadPharm, USA, and 1,2-distearoyl-sn-glycero-3-phosphocholine (DSPC), 1,2-dimyristoyl-rac-glycero-3-methoxypolyethylene glycol-2000 (DMG-PEG2000) were procured from Avanti Polar Lipids (Alabaster, AL, USA). Polyadenylic acid (PolyA), cholesterol (Chol), citric acid, sodium citrate tribasic dehydrate, and triton X-100 were acquired from Sigma-Aldrich (St. Louis, MO, USA). EZ-Cap-modified firefly luciferase-mRNA is procured from APExBIO (USA). Quant-it Ribogreen RNA assay, 1,1'-

Dioctadecyl-3,3,3',3'-tetramethylindocarbocyanine perchlorate (DilC),1,1-dioctadecyl-3,3,3,3-tetramethylindotricarbocyanine iodide (DiR), Nuc Blue nuclear stain, and DPBS (Ca2+ and Mg 2+ free), methanol free formaldehyde, and BCA protein assay kit from Thermo Fisher Scientific, MA, (USA). Minimal Essential Medium (MEM), fetal bovine serum (FBS), sodium pyruvate, and penicillin/streptomycin were acquired from Gibco technologies. Phalloidin-iFlour 488 was from Abcam, ONE-Glo luciferase assay system, Vivo Glo luciferin substrate from Promega. All other solvents were of analytical grade and were supplied in-house.

3.3.2 Preparation of LNPs

LNPs were prepared in NanoAssemblr Benchtop from Precision NanoSystem Inc (Vancouver, BC, Canada) using a herringbone microfluidic chip. LNPs were composed of DSPC: Cholesterol: SM-102:DMG-PEG2k at 10:38.5:50:1.5% molar ratio dissolved in absolute ethanol as the organic phase at 5 mg/mL, corresponding to 1.25 mg/mL after microfluidic production. The aqueous phase comprises the firefly luciferase (Fluc-mRNA) dissolved in citrate buffer at different ionic strengths (50 mM, 100 mM or 300 mM) at an N/P ratio 6. The flow rate ratio (aqueous to ethanol) and total flow rate were adjusted to 3:1 and 12 mL/min, respectively. For the *in vivo* experiments, DiR was added to the organic phase to prepare the DiR-labelled Fluc-mRNA LNPs. PolyA was used as a surrogate for mRNA in cellular uptake studies, where DilC was added to the organic phase to prepare DilC-labelled LNPs. Both the fluorescent dyes were used at a concentration of 1 % of the total molarity of the lipid mixture.

3.3.3 Removal of Ethanol Content and Buffer Exchange with Centrifugal Filter Unit

Following the preparation of the LNPs, they were purified by a spin column centrifugal filter unit to remove ethanol content and increase pH to physiological conditions through buffer exchange. The LNPs were diluted 1:40 times in 10 mM PBS pH 7.4 and then centrifuged at 2,000 g at 4 ^{0}C till the desired volume of the LNPs was recovered. The LNPs were concentrated twice using the spin column centrifugal unit, with the final mRNA concentration being 130 µg/mL and lipid concentration 2.5 mg/mL.

3.3.4 LNPs Characterization by Using Dynamic Light Scattering: Particle Size, Polydispersity and Zeta Potential

Particle size (z-average hydrodynamic diameter), PDI (polydispersity index), and zeta potentials were measured by dynamic light scattering using a Zetasizer Ultra (Malvern

Panalytical Ltd, Worcestershire, UK) equipped with a 633 nm laser and a detection angle of 173°. Particle size and PDI were measured in 10 mM PBS pH 7.4, and ultrapure water was used for zeta potential. The samples were diluted at 1:10 for all the measurements. Mean particle size and PDI are expressed as the mean $\pm$ SEM.

3.3.5 Entrapment Efficiency

The encapsulation efficiency of PolyA/Fluc mRNA was determined using Ribogreen Assay according to the manufacturer's instructions. Briefly, 50 µL of samples were added to the 96-well black plates in the presence or absence of 0.1 w/v% Triton X-100, referring to the total and unencapsulated mRNA, respectively. The plate was incubated at 37 °C for 15 minutes, followed by adding Ribogreen fluorescent dye. To the Triton (+) wells, Ribogreen dye was added at a concentration of 1:200 and to the Triton (-) 1:500. The fluorescence intensity was quantified using GloMax® Discover Microplate Reader at excitation and emission wavelength of 480 nm/520 nm respectively. The encapsulation efficiency (%) (Equation 1.1) and recovery (%) (Equation 1.2) were calculated according to the standard curve of Triton (+) and Triton (-).

3.3.6 Nanoparticle Tracking (NTA) Analysis of LNPs

The estimated particle concentration of LNPs, hydrodynamic diameter and distribution were analysed using the Nano Sight NS300 system (Malvern Panalytical, Worcestershire, UK) equipped with a 488 nm laser module and a high-sensitivity camera. All samples were diluted with PBS pH7.4. Camera levels of 9 and 5 of the detection thresholds were set to acquire five 60-second videos. All samples were analysed under constant flow conditions (flow setting 100) and at an ambient temperature (~25 °C). A detection threshold of 3 was selected for post-processing analyses. Data were analysed using the NTA software (v3.4.0.0.3).

3.3.7 Cryogenic transmission electron microscopy (cryo-TEM) of mRNA LNPs

The effect of the citrate buffer molarity on Fluc-mRNA SM-102 LNP morphology was evaluated using cryo-transmission electron microscopy (cryo-TEM). mRNA-LNP (5 µL) was drop cast onto a 400-mesh lacey carbon-coated grid using single-sided blotting for 2s, then immersed in 100 % nitrogen-cooled ethane. Images were recorded using a JEOL 2100F FEG-TEM at liquid nitrogen temperature and 200 kV.

3.3.8 TNS Assay

20 mM citrate buffer pH ranged from 3.0 to 6.0, sodium phosphate buffer pH ranged from 6.5 to 8.0, and tris buffer pH 8.5 to 9.0 were prepared. 0.6 mM of the fluorogenic probe, 6-(p-toluidine)-2-naphthalene sulfonic acid sodium salt (TNS) was prepared by dissolving in the distilled water. LNPs were diluted to 0.5 mM of lipid concentration. Then, diluted LNPs were added to each well with each buffer in triplicate. TNS reagent was added to all wells, and the plate was incubated at room temperature for 10 minutes in a dark environment. Then, the fluorescence intensity was measured at the excitation and emission levels of 355 and 460, respectively. The blank value was subtracted from each reading. The data was normalised by dividing each fluorescence intensity by the maximum fluorescence intensity, and an average of these normalised values was calculated. A scatter graph of these normalised values against each pH was plotted, using polynomial order 3. pKa is defined as the pH at which the normalised value is 0.5, corresponding to 50% fluorescence.

3.3.9 Cell Culture Maintenance

Human embryonic kidney (HEK 293) cells were used for the *in vitro* experiments, including nanoparticle uptake and transfection experiments. The cell line was maintained in Minimum Eagle's medium (MEM) supplemented with 10 % fetal bovine serum, sodium pyruvate, and 1 % penicillin/streptomycin in a humidified environment (37 °C, 5 % CO_2) till confluent. The media was replaced after 2-3 days and passaged for the experiments while they were at 80-90 % confluency.

3.3.10 Qualitative Nanoparticle Uptake Study

The internalisation of the LNPs was investigated using HEK 293 cells by confocal laser scanning microscopy. HEK 293 cells were seeded at a density of 10,000 cells in a glass-bottom confocal dish and grown till 70-80 % confluency was achieved. The monolayer of cells was then incubated with poly A-Dil C labelled LNPs (100 µg/mL) for 24 hours. The LNPs were then aspirated gently to avoid dislodging the cells after incubation. The cells were washed with 10 mM PBS (pH 7.4) three times gently to remove non-internalized LNPs. The cells were fixed using 4 % formaldehyde for 10-15 minutes, then washed with 10 mM PBS (pH 7.4) and treated with 0.1 % Triton X-100 in 10 mM PBS to aid cell membrane permeabilisation. After the Triton X-100 treatment, the cells were stained with phalloidin-iFluor 488 reagent (1 hour) for actin filaments co-localization. The cells were given a final wash with 10 mM PBS followed by

staining the nucleus with NucBlue Live Ready Probes for 20 minutes. The cells were then observed under the confocal microscope (Leica) at 40 X magnification. The poly A-Dil C labelled LNPs fluoresces at an excitation/emission wavelength of 549 nm/565 nm, while the phalloidin-iFluor 488 fluoresces under the FITC channel. The images were analysed using ImageJ software.

3.3.11 Quantitative Nanoparticle Uptake Study

HEK 293 cells were seeded at a density of 10,000 cells/mL in a 24-well plate and grown till 70-80 % confluency was achieved. Dil C labelled Poly A-LNPs suspended in MEM were added to the cells at a concentration of 44 µg/mL and 2 µg/mL and left for 24 hours of incubation. Following the incubation period, the LNPs were aspirated, and the cells were washed in cold 10 mM PBS pH 7.4 twice to thrice to remove the non-internalized LNPs. The cells were then lysed by 1 % v/v Triton X-100 in 10 mM PBS pH 7.4 for 30 minutes. The cell lysates were centrifuged at 10,000 rpm for 10 minutes. The supernatant was used to measure the concentration of the internalised LNPs using a fluorescence microplate reader (Promega, GloMax® Discover Microplate Reader) at an excitation/emission of 549/565 nm. The unknown concentration of the fluorescent LNPs was analysed from the standard curve of the Dil C labelled LNPs. The cell lysates were also subjected to the BCA protein assay kit to determine the protein content. The nanoparticle uptake was expressed as by the following Equation 3.1[106]

$$NPs\ uptake = \frac{\text{µg of nanoparticles calculated from the standard curve of nanoparticles}}{\text{mg of total cell protein calculated from BCA assay}}$$

Equation 3.1

3.3.12 Transfection Study

The *in vitro* mRNA transfection assay was conducted using the ONE-Glo Luciferase assay system. Prior to the transfection experiment, HEK 293 cells were passaged and seeded in a white 96-well plate at a cell density of 10,000 cells/100 µL and left to grow in the appropriate humidified environment to achieve 75-80 % confluency. Fluc-mRNA SM-102 LNPs were serially diluted in MEM media at concentrations ranging from 2 µg/mL, 1 µg/mL, 0.5 µg/mL, and 0.25

µg/mL. Upon reaching confluency, the media was aspirated from the cells, and the LNPs (100 µL) were added to the cells at the above concentrations and incubated for 24 hours. The following day, 100 µL of ONE-Glo luciferase reagent was added to the cells containing the LNPs, mixed well to aid lysis, and luminescence was measured using a plate reader (Promega, GloMax® Discover Microplate Reader).

3.3.13 Cell Viability Study

Cell viability of the LNPs was carried out in HEK293 cells using Alamar blue assay. Briefly, 10,000 cells/100 µL were seeded in a 96-well plate and grown till confluent. LNPs were added to the cells at the lipid concentrations 44 µg/mL, 22 µg/mL, 11 µg/mL, and 5.5 µg/mL and incubated for 24 hours. 1% Triton in MEM media was used as a positive control. The next day, the LNPs were aspirated, and fresh MEM media was added to the cells, followed by the addition of 10 µL Alamar blue reagent. The fluorescence is measured in the cells after 4 hours of incubation using a microplate reader (Promega, GloMax® Discover Microplate Reader) with the excitation/emission wavelength 590 nm/ 560 nm. The relative cell viability was calculated as a percentage.

3.3.14 Fluorescence and Bioluminescence of DiR labelled Fluc-mRNA LNPs by IVIS

For *in vivo* studies, female BALB/c mice, 8-10 weeks old, an average weight of 22 grams, were divided into 3 different groups. All the experiments were conducted three times independently, with three mice in each group per experiment (a total of 9 mice per formulation). All animals were handled in accordance with the UK Home Office Animals Scientific Procedures Act of 1986 in accordance with an internal ethics board and a UK government-approved project and personal license.

LNPs were labelled with DiR, a lipophilic dye, and loaded with Fluc mRNA to track the biodistribution of LNPs and to assess the expression profile, respectively. The fluorescence of DiR was imaged at the excitation wavelength of 710 nm and an emission filter of 780 nm, while Fluc mRNA expression was imaged on the luminescent filter to analyse bioluminescence. A medium binning and f/stop of 2 was used, and acquisition times were defined using auto-exposure settings.

In terms of the experimental plan, mice were injected 5 µg / 50 µL of mRNA-LNPs per leg via IM route. They were anaesthetised using 3 % isoflurane. Anaesthesia was maintained (2% isoflurane) during imaging in the IVIS imaging chamber. Mice were imaged first for the biodistribution of the LNPs under the DiR filter and then following subcutaneous (SC.) injection of D-luciferin at a dose rate of 150 mg/kg. D-luciferin was prepared at a working concentration of 30 mg/mL in sterile DPBS (In this chapter, the injection route was changed from IP (Chapter 2) to SC. In subsequent chapters, it was applied as SC). 10 minutes after SC luciferin injection, mice were imaged for bioluminescence. These imaging sessions for both fluorescence and bioluminescence were repeated at 6-, 24-, and 48-hours post-IM injection of LNPs. D-luciferin was injected at the same dose rate at every time point before bioluminescence measurements. Mice were terminated at the end of the 48-hour study using a Schedule 1 method. Image capture and data analysis were carried out using Living Image software. Total radiant efficiency and total flux were gained by region of interest for fluorescence and bioluminescence, respectively, and normalised to the control mice (The fluorescence and luminescence intensities were divided by those of the control mouse). Average radiant efficiency and average total flux were calculated for the fluorescence intensity and bioluminescence measurements, respectively.

3.3.15 Statistical Analysis

Data is represented as a means of three independently conducted separate experiments and GraphPad Prism was used to perform statistical analysis by performing ANOVA with post-hoc analysis wherever applicable. *P-value < 0.05* was considered statistically significant.

3.4 Results

3.4.1 The Impact of Citrate Buffer Concentration on the Physicochemical Properties of LNPs

LNPs were prepared with the lipid composition of DSPC:Chol:SM-102:DMG-PEG2k (10:38.5:50:1.5% molar ratio) encapsulating Fluc mRNA prepared in 50 mM, 100 mM or 300 mM of citrate buffer at pH 4.0. LNPs were subject to buffer exchange with 10 mM PBS at pH 7.4. The results in Table 3.1 show that increasing the concentration of citrate buffer corresponded to an increase in particle size, with LNPs prepared using 50 mM citrate buffer being 88 ± 7 nm, increasing to 111 ± 15 nm and 116 ± 8 nm for 100- and 300-mM citrate buffer respectively. However, irrespective of the buffer concentration, all LNPs had a polydispersity

index below 0.2, with no significant difference in zeta potential (Table 1). When considering the ability of the LNPs to load nucleic acids dissolved in the different citrate buffer concentrations, all LNPs had an encapsulation efficiency (EE%) of over 95% and a nucleic acid recovery of over 90% (Table 1).

Table 3.1 *The effect of concentration of citrate buffer concentration 50 mM, 100 mM or 300 mM on LNPs z-average size, PDI, zeta potential, Encapsulation Efficiency (%) and recovery (%). (EE) and recovery % refers to the percentage of encapsulated RNA and the total RNA present in the LNPs during the manufacturing process, respectively. LNPs composed of DSPC: Chol: SM-102:DMG-PEG2k (10:38.5:50:1.5 molar ratio) and encapsulated Fluc mRNA (or PolyA for uptake study) at NP6. They were manufactured using microfluidics at a 3:1 FRR and 12 mL/min TFR and purified by spin column. Results represent mean ± SEM, n= 3 independent batches.*

Citrate buffer concentration (mM)	Average diameter (nm)	PDI	Zeta Potential (mV)	EE (%)	Recovery (%)
50	88 ± 7	0.13 ± 0.04	-1.6 ± 0.9	97 ± 2	110 ± 14
100	111 ± 15	0.17 ± 0.06	1.5 ± 0.9	97 ± 1	96 ± 12
300	116 ± 8	0.13 ± 0.04	5.5 ± 1.8	98 ± 1	93 ± 6

The particles were analysed with NTA (Figure 3.1). Particle concentration decreased slightly with increasing the concentration of citrate buffer. Also, a small second peak appeared with 100 and 300 mM of citrate buffer, although all LNPs had monodisperse size distribution.
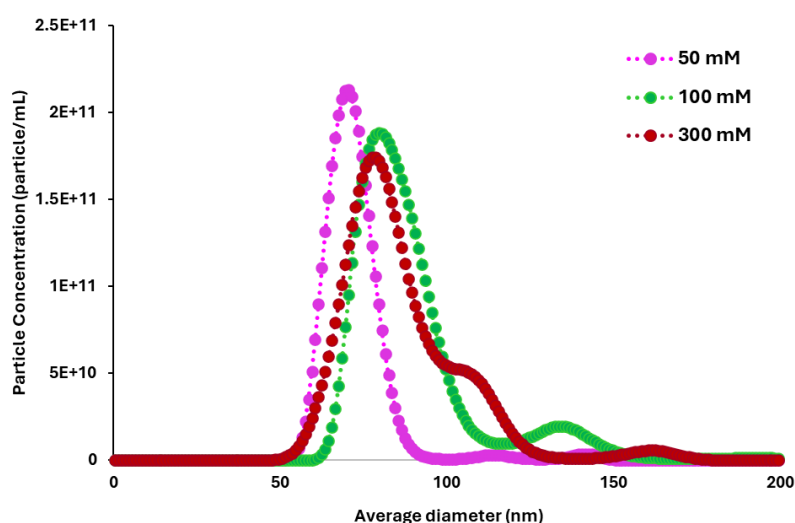
Figure 3.1 *NTA size distribution of mRNA-LNPs prepared with 50 mM, 100 mM and 300 mM of citrate buffer. One sample was measured for each concentration with five technical replicates.*

Also, particles were imaged using Cryo-TEM to investigate further the effect of the molarity of citrate buffer on the particle morphology (Figure 3.2). This figure shows the presence of two types of structures. LNPs with well-defined, spherical or near-spherical morphology and a smooth, continuous outer layer can be seen. Their internal structure appears as a dense, homogeneous core, which suggests an electron-dense core containing mRNA. Within LNP formulations, 'Bleb' structures (previously described [9]) are seen (marked with white arrows; Figure 3.2). Bleb structures in LNPs refer to protruding vesicular or bud-like formulations and result from phase separation or instability within the lipid bilayer. These bleb structures can be seen in LNP formulations prepared using the three different citrate buffer molarities (Figure 3.2). However, at the higher 300 mM citrate buffer concentration (Figure 3.2E and F), these blebs can be seen budding off (denoted with the red arrows).
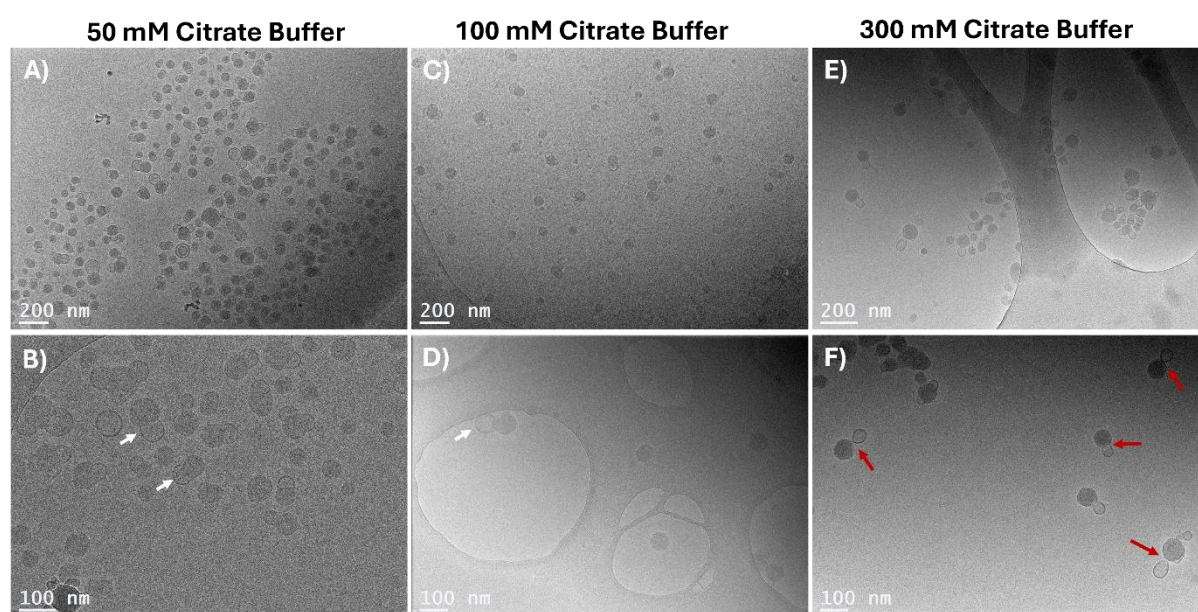
Figure 3.2 *Cryo-TEM images of mRNA-LNPs prepared with (A-B) 50 mM, (C-D) 100 mM and (E-F) 300 mM of citrate buffer. Red arrows show the bleb dissociation*

3.4.2 TNS Assay

The effect of the ionic strength of citrate buffer on the pKa of LNPs was tested using a TNS binding assay (Figure 3.3). The best sigmoidal curve was fitting to the data. All LNPs had similar pKa at around 6.5, irrespective of the citrate buffer molarity.
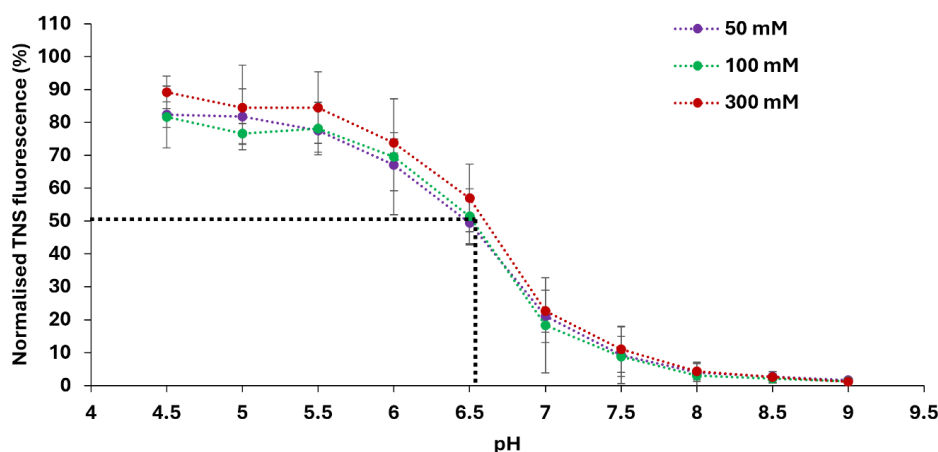
Figure 3.3 *Determination of pKa by TNS fluorescence titration. The four amino lipids shown are examples illustrating the full pKa range evaluated. Sigmoidal best-fit analyses were applied with pKa defined as the pH at half-maximal fluorescence intensity (n=3).*

3.4.3 *In vitro* Cellular Uptake of LNPs

The cell uptake of SM-102 LNPs was investigated in both a qualitative and quantitative manner by using a Dil fluorescent dye and employing confocal microscopy and fluorescence intensity measurements, respectively. Dil belongs to a family of fluorescent lipophilic carbo cyanic dyes, which have weak fluorescence but emit strong fluorescence intensity when incorporated into cellular membranes [107]. In this study, we used a Dil C18 dye to label the SM-102 LNPs and monitor the cellular internalisation inside the HEK 293 cells after 24 hours of incubation and observed under confocal microscopy as a part of the qualitative analysis of the uptake study. To mark the co-localization of the nucleus and the actin filaments, the cells were stained by a nuclear stain Nuc Blue (blue) and phalloidin-iFluor 488 conjugate (green). As observed from Figure 3.4a, the LNPs prepared using 50 mM citrate buffer had a relatively higher fluorescence intensity, demonstrating the increased uptake of LNPs compared to the LNPs prepared using 100 mM and 300 mM of citrate buffer. The HEK 293 cells were also stained with Dil C dye to demonstrate that the dye, when used alone to label the cells, stains only the cell membrane (Figure 3.4b), whereas when incorporated into LNPs, they are readily internalised by the cells via endocytic pathways to appear as endocytic bodies in the cytoplasm.

The quantitative analysis of the Dil C SM-102 LNPs was conducted by measuring the fluorescence intensity of the LNPs, and the nanoparticle uptake was expressed in terms of per milligram of protein. Following the cell lysis, the supernatant was used to measure the fluorescence intensity of the LNPs and to calculate the concentration. For the quantitative

analysis, HEK 293 cells were incubated with two different concentrations of Dil C LNPs (44 µg/mL and 2 µg/mL). 44 µg/ml of Dil C LNPs was chosen on account of the concentration of lipids estimated to be present when a 2 µg/mL of mRNA dose is used for the transfection experiment, where lipid to mRNA w/w ratio is maintained at 22:1. 2 µg/mL of Dil C LNPs was used as a lower limit of LNPs concentration for comparative analysis, As observed from the Figure 3.4c the cell uptake of the LNPs at 44 µg/mL is higher in all the three different formulations as would be expected. However, whilst at lower lipid concentrations (2 µg/mL), there are no notable differences in LNP uptake observed, at the higher lipid concentrations (44 µg/mL), differences in LNP update are seen (Figure 3.4); a trend of lower LNP uptake with LNPs prepared with higher citrate buffer concentrations is seen, with LNPs prepared with 50 mM citrate buffer concentrations showing significantly ($p<0.05$) high cell uptake compared to those LNPs prepared at 300 mM citrate buffer (Figure 3.4c).
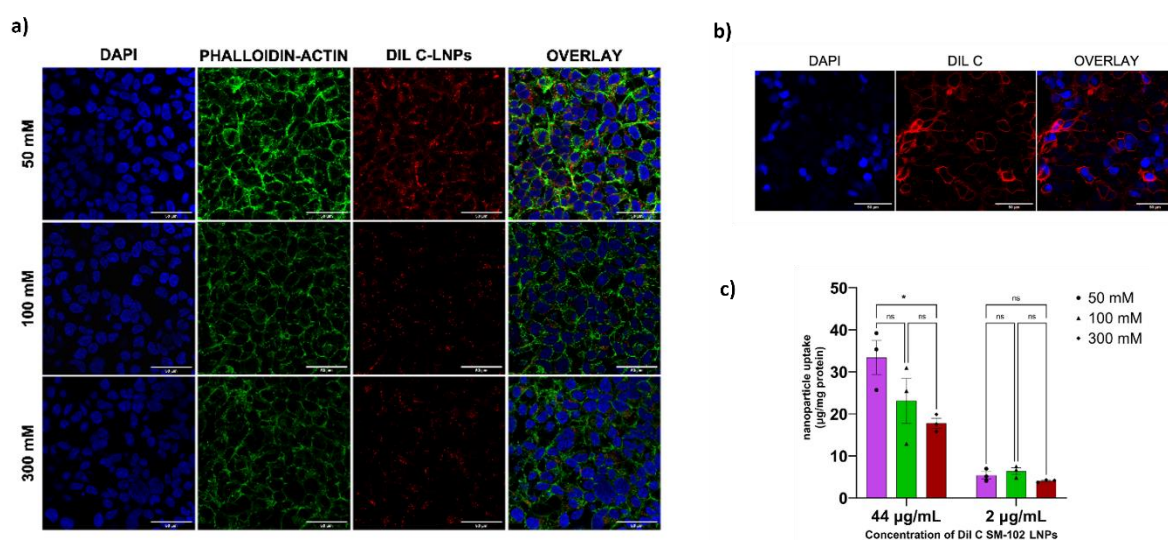
Figure 3.4 *Cellular Uptake of Dil C labelled LNPs. (a) Qualitative uptake of Dil C LNPs in HEK 293 cells prepared using 50 mM, 100 mM or 300 mM citrate buffer aqueous phase and incubated for 24 h and observed under confocal microscopy (on a scale of 50 µm). (b) Cellular membrane staining by Dil C only in HEK 293 cells (on a scale of 50 µm). (c) Quantitative uptake of Dil C LNPs in HEK 293 cells incubated for 24 h and measured by fluorescent spectrophotometer. Data is represented as SEM (n=3) of three independent experiments and statistical analysis done by GraphPad Prism (ns= not significant; *P< 0.05)*

3.4.4 *In vitro* Transfection Efficacy of LNPs Prepared Using Different Citrate Buffer Solutions.

In our study, HEK 293 cells were incubated with Fluc mRNA-based SM-102 lipid nanoparticles at four different mRNA concentrations (2 µg/mL, 1 µg/mL, 0.5 µg/mL, and 0.25 µg/mL) for 24 hours. Relative luminescence intensity was measured using an in vitro luciferase assay along

with cell viability (Figure 3.5). Figure 3.5a shows an mRNA dose-response curve for each of the 3-citrate buffer molarities. These results show that whilst there is no significant difference in transfection efficacy between LNPs prepared with 50- or 100-mM citrate buffer, the 300 mM citrate buffer LNP formulation tended to give lower luciferase expression levels compared to the LNPs prepared with 50- or 100-mM citrate buffer. These differences in transfection levels were not related to cell viability as a cell viability study of the three LNP formulations was conducted in a dose-dependent manner for 24 hours (Figure 3.5b). The concentrations were selected as equivalent to the lipid concentrations present in the LNPs used for the transfection experiment. From the cell viability data (Figure 3.5b), it is evident that all three LNP formulations did not induce any toxicity to the cells, maintaining cell viability greater than 90 % at all concentrations. The positive control cells treated with 1% Triton displayed only 15 % viability, confirming the lysis of the cell membrane.
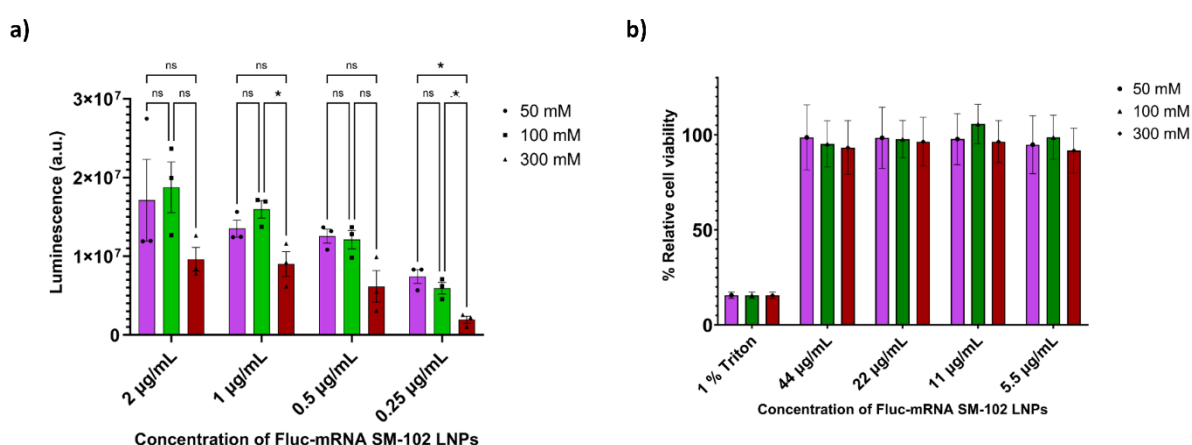
Figure 3.5 *In vitro mRNA a) transfection efficiency and b) cell viability: HEK 293 cells transfected with DiR-Fluc mRNA LNPs at mRNA concentrations of 2 µg/mL, 1 µg/mL, 0.5 µg/mL, and 0.25 µg/mL for all the formulations. 24-h post LNPs incubation luminescence intensity was measured. Fluc-mRNA SM-102 LNPs were prepared in different ionic strengths of citrate buffer 50 mM, 100 mM, or 300 mM and checked for biocompatibility in HEK293 cells for 24 hours. Data is expressed as Mean ± SEM (n=3) of three independent experiments followed by conducting ANOVA using GraphPad Prism (ns= not significant; *P< 0.05).*

3.4.5 Biodistribution and Bioluminescence Profile of DiR Fluc-mRNA LNPs

Before starting this study, a pilot study was performed to determine whether labelling LNPs with DiR affects the in vivo expression profile in the range of citrate buffer concentration. Figure 3.6 showed that DiR did not significantly affect the expression profile.
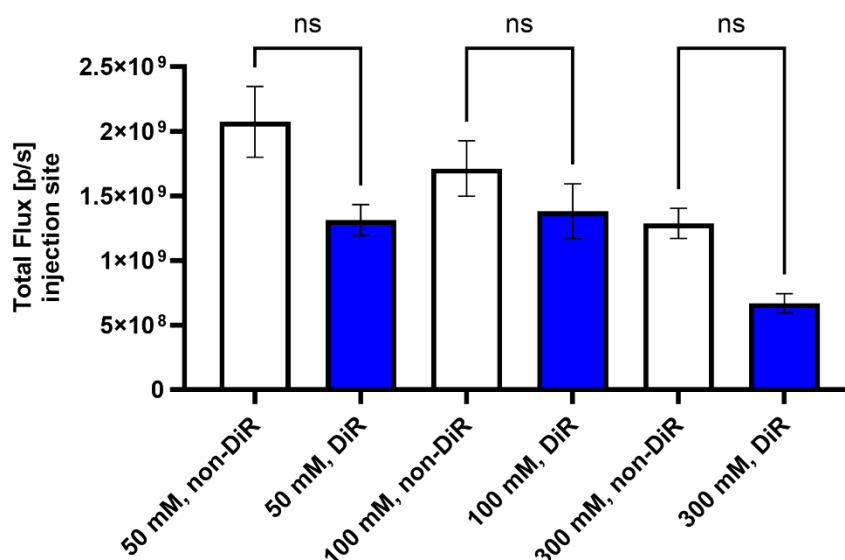
Figure 3.6 *The effect of DiR on the in vivo expression profile of mRNA-LNPs prepared with 50, 100, and 300 mm of citrate buffer (ns=nonsignificant). BALB/c mice were injected with 5 µg of Fluc mRNA-LNPs via the IM route. 6h later, the mice were injected with luciferin, and the bioluminescence was quantified from the injection site. Data is expressed mean ± SEM (3 mice in each group; each mouse was injected in each hind leg).*

The biodistribution and bioluminescence profile of the DiR-labelled Fluc-mRNA LNPs was analysed using the IVIS system at different time points (15 min, 6 h, 24 h, and 48 h) after injection of the LNPs (Figure 3.7 and 3.8). BALB/c mice were injected with 5 µg (mRNA) of DiR Fluc mRNA-LNPs into each leg via the IM route. The results in Figure 3.7 show similar distribution profiles for all three LNP formulations, with the majority of the LNPs being detected at the injection site (Figure 3.7b) and no observed levels of fluorescence measured at the liver (Figure 3.7c).

In line with the distribution data, luciferase expression was primarily focused on the injection site (Figure 3.8); however, luciferase expression was also noted at the liver after 6 h when the peak luciferase protein expression was measured for all three LNP preparations. Furthermore, similar to the *in vitro* expression, the LNPs prepared using 300 mM citrate buffer gave lower luciferase expression compared to those prepared with 50 mM or 100 mM citrate buffer both at the injection site (Figure 3.8b) and the liver (Figure 3.8c). These results confirm that adopting 50 mM or 100 mM citrate buffer concentrations in the preparation of mRNA-LNPs provides higher efficacy formulations compared to 300 mM citrate buffer, both *in vitro* and *in vivo*.
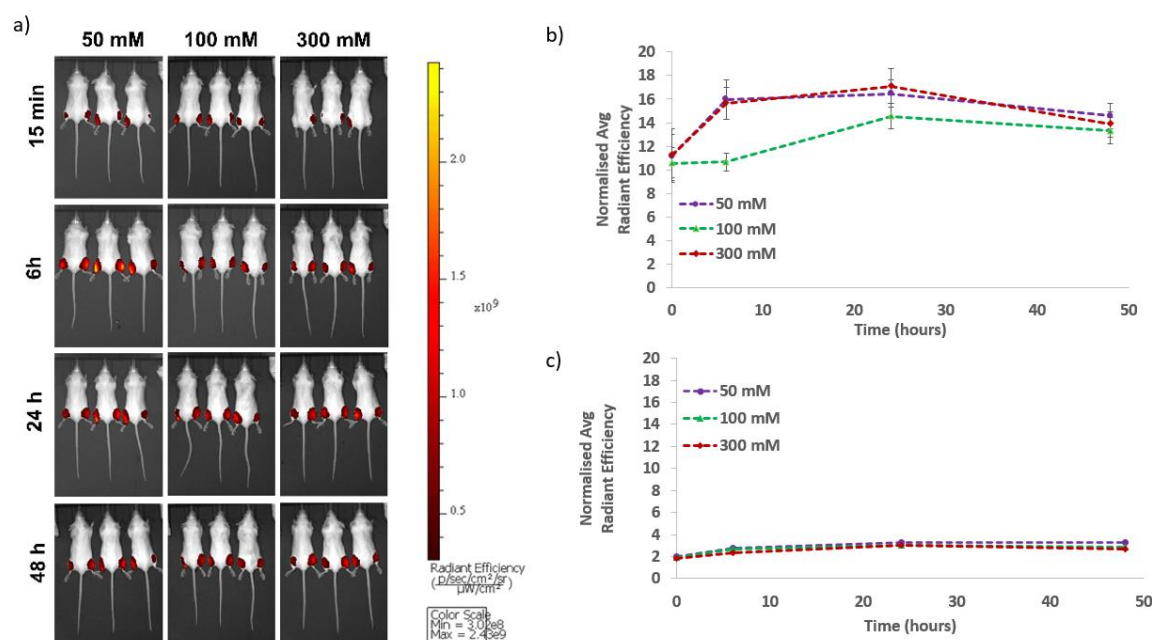
Figure 3.7 *Measurements of fluorescence DIR in mRNA-LNPs prepared using 50 mM, 100 mM or 300 mM citrate buffer (a) Representative IVIS images of groups of 3 BALB/c mice injected with DIR labelled mRNA-LNPs via the intramuscular route and imaged at specific time points (15 min, 6 h, 24 h and 48 h). Quantitative analysis of the fluorescence intensity in the b) injection site and c) liver after labelled LNP injection. Data is expressed as mean ± SEM (a total of 9 mice per formulation split over 3 independent studies).*

3.5 Discussion

LNP preparation via microfluidics is based on the nanoprecipitation of lipids and simultaneously encapsulating nucleic acids driven by electrostatic interaction between the positive amine group of ionisable lipid and anionic mRNA phosphate group. This study investigated the effect of citrate buffer ionic strength used as an aqueous phase to prepare LNPs composed of DSPC: Chol: SM-102: DMG-PEG2k (molar ratio 10:38.5:50:1.5%). Overall, increasing the ionic strength of citrate buffer led to an increase in LNP particle size, from 88 nm for LNPs prepared with 50 mM citrate buffer to 110 nm and 116 nm for 100 mM and 300 mM LNPs, respectively (Table 3.1). However, in all cases, the LNPs maintained a low polydispersity profile (PDI < 0.2) and a near-neutral zeta potential (Table 3.1). Similarly, the encapsulation efficiency and the recovery of mRNA within these LNPs were not affected by the changes in citrate buffer ionic strength (Table 3.1). Analysing the samples with NTA showed that increasing the ionic strength decreased the particle concentration and tended to appear as a second small peak (Figure 3.1). Cryo-TEM images showed that LNPs produced using 300 mM citrate buffers had increased bleb structures (Figure 3.2). In terms of potency, both *in*

vitro (Figure 3.4 and 3.5) and *in vivo* (Figure 3.8), the 50 mM and 100 mM citrate buffer formulations showed enhanced mRNA-luciferase expression compared to the 300 mM citrate buffer formulations.
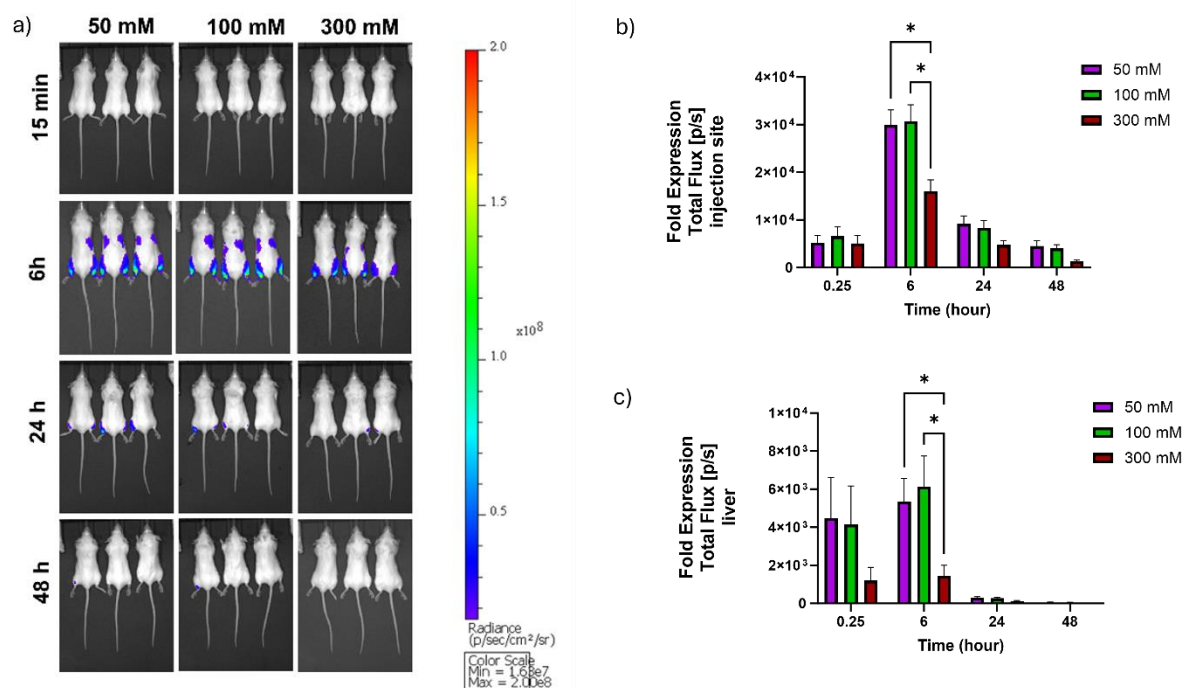
Figure 3.8 *In vivo expression profile of LNPs encapsulated Fluc mRNA prepared with 50 mM, 100 mM or 300 m of citrate buffer (a) Representative IVIS images of groups of 3 BALB/c mice injected with 5 µg Fluc mRNA-LNP intramuscularly. Quantification of the bioluminescent signal at specific time points at (b) the injection site and (c) the liver, Data is expressed mean ± SEM (a total of 9 mice per formulation split over 3 independent studies).*

At a fundamental level, these findings could suggest that increasing the size of LNPs may reduce their effectiveness. However, when considering the particle sizes presented in Table 3.1, the differences, although potentially noteworthy from a critical quality attribute standpoint, are relatively small (40 nm) between 50 mM and 100 mM buffer, and there is no significant difference between the 100 mM and 300 mM citrate buffer LNP formulations. However, the link between manufacturing conditions and particle size is an important consideration. For example, Lou et al. investigated the role of TRIS buffer concentration on liposomes produced by microfluidics. These studies showed that neutral liposomes, comprising DSPC and cholesterol, maintained a consistent size of approximately 80 nm across TRIS buffer concentrations ranging from 0 to 1000 mM. In contrast, cationic liposomes showed a stepwise increase in size from 40 to over 600 nm across the same TRIS concentration range. Despite variations in size, all formulations exhibited narrow and unimodal size distributions,

as evidenced by low polydispersity index (PDI) values (0.05–0.25) and Cryo-TEM characterisation [101]. This buffer-induced size control was attributed to the packing parameter of lipids based on the effective area of the head group, the length of the alkyl chain, and the alky chain volume. Similarly, Cheung and Al-Jamal also showed that when manufacturing liposomes using microfluidics, including ions (saline or PBS) in the aqueous phase led to an increase in particle size of liposomes and made a more monodisperse particle size distribution [108]. Nakamura et al. also showed the impact of buffer choice on LNP particle size[96]. Within their studies, to investigate the effect of salt concentration in acidic aqueous buffer, NaCl was added to 20 mM acetate buffer (pH 4.0) at concentrations of 20, 50, or 150 mM, and in their studies, they demonstrated that the addition of NaCl to acetate buffer increased the size of LNPs from approx. 100 to 160 nm as the NaCl concentration increased from 0 to 150 mM, and this was attributed to the salt-out effect [96]. Similarly, within our studies, by increasing the ionic strength of the citrate buffer 6-fold (from 50 mM to 300 mM), we may induce an osmotic imbalance, altering the LNP structure. Indeed, Zhigaltsev et al., showed that osmotic stress can drive the formation of bilamellar lipid structures [109]. In their study, they increased the ionic strength by adding NaCl to liposomes and LNPs, creating an osmotic pressure gradient that causes water efflux from the particle's aqueous interior. These changes may be an obstacle to releasing mRNA into the cytosol due to different lamellar structures, thereby resulting in lower mRNA expression, as seen in Figures 3.5 and 3.8.

It has also been proposed that bleb structures can be induced in mRNA-LNP systems by preparing them in the presence of high concentrations of pH 4 buffer (including citrate buffer) and that these systems can exhibit enhanced transfection properties both *in vitro* and *in vivo* [105]. The formation of a bleb has been reported to involve the production of protrusions from the particles, consistent with areas enriched with DSPC and with an aqueous core that may or may not contain mRNA [110]. These bleb structures form due to the segregation of the different lipids within the LNP composition upon dilution of the lipids in ethanol into the aqueous media during manufacture. Indeed, molecular simulation studies also suggest that LNP structures may include solvent pockets, and experimental findings reveal non-spherical morphologies linked to the segregation of the bilayer-forming component DSPC, resulting in pronounced blebs [110]. However, bleb formation may be interlinked to the choice of ionisable lipid used; Cheng et al. noted that the high concentration buffer induced fusion and

formation of larger structures including blebs was more pronounced DLin-KC2-DMA (KC2) compared to SM-102[105]. Through the optimisation of pH 4 buffer concentration and type, LNP mRNA systems encoding firefly luciferase with KC2 achieved *in vivo* transfection potencies comparable to or better than those obtained with LNPs containing SM-102. This enhanced transfection efficiency was credited to the improved stability of mRNA, particularly when it is sequestered into bleb structures within the LNPs [105]. This underpins the importance of considering the citrate buffer concentration in conjunction with the lipid composition in producing LNPs.

In general, the success of any nanoparticle system in biomedical applications is established when it reaches the target tissue, followed by its internalisation, and effectively carries out the intended functions [111]. The internalisation of the LNPs by the cells is governed by multiple uptake mechanisms, for example, clathrin and caveolae-mediated endocytosis [112] and macro pinocytosis that is further dependent on the nanoparticle physicochemical characteristics and the cell type [112,113]. In our studies, it was observed that LNPs prepared using 50 mM citrate buffer as the aqueous phase displayed an increased nanoparticle uptake both qualitatively and quantitatively compared to LNPs prepared with 300 mM citrate buffer (Figure 3.4). One can expect a higher uptake of the nanoparticles in a concentration-dependent manner depending on the cell type; however, it is also anticipated that saturation at a certain concentration would occur. Indeed, Peñaloza et al. investigated this phenomenon, demonstrating a higher percentage of nanoparticle uptake in three different cell lines in a concentration-dependent manner, ultimately showing a saturation effect beyond a particular concentration [114].

The transfection efficiency of the LNPs is the downstream activity investigated by encapsulating an mRNA encoding firefly luciferase inside SM-102-based LNPs. Human embryonic kidney (HEK 293) is a popular mammalian cell line widely used due to its high transfection efficiency [115], protein production, rapid doubling time, ease of culture conditions, and maintenance [116,117]. Similarly, for *in vivo* testing, BALB/c mice are commonly used for mRNA-LNP protein expression and vaccine studies. It was demonstrated that the 300 mM citrate buffer LNP formulation shows lower protein expression both *in vitro* (Figure 3.4 and 3.5) and *in vivo* (Figure 3.8). However, generally, the lack of in vitro-*in vivo* correlation in LNP testing is a well-recognized issue, as is the difference between mouse and

non-human primate performance. For example, Whitehead et al. studied a large library of nanoparticles in multiple *in vitro* systems and mice, and they noted that when the diameter of LNPs is less than 200 nm, size does not correlate with *in vivo* efficacy [118]. Similarly, Hassatt et al. designed a series of studies to systematically change LNP particle size without altering lipid composition and evaluated the biophysical properties and immunogenicity of the resulting LNPs [46]. The authors showed that whilst small diameter LNPs were substantially less immunogenic in mice, all particle sizes tested ((small (64 nm), medium (81 nm), large (108 nm) and extra-large (146 nm)) yielded a robust immune response in non-human primates.

In this chapter, in addition to testing the transfection efficiency of the different LNP formulations we also considered their biodistribution in BALB/c mice. LNPs were loaded with Fluc mRNA and labelled with DiR to assess their expression and biodistribution profile simultaneously. The incorporation of DiR into the lipid bilayer of LNPs did not affect luminescence intensity (Figure 3.6). Mice were injected intramuscularly with 5 µg Fluc mRNA-LNPs per leg and imaged for fluorescence (DiR) and bioluminescence (luciferase). Our results (Figure 3.7) showed high levels of LNPs retained at the injection site, with DiR fluorescence intensity increasing to a maximum at 24 h after dosing all formulations. No notable fluorescence intensity was measured at the liver or spleen. It's important to acknowledge that detecting the fluorescence intensity of internal organs is difficult with IVIS without extracting the organs due to the limited penetration depth in tissue. When considering luciferase expression (Figure 3.8), we see mRNA expression at the intramuscular injection site and the liver. At both sites, the LNPs prepared with high (300 mM) citrate buffer promoted lower luciferase expression. The expression and biodistribution of FLuc-LNPs were also studied by Di et al. and they compared the use of DiR as an LNP marker with deuterium-labelled LNPs [119]. From their studies, the muscle signal from DiR-LNPs showed a gradual increase over time, peaking at 48 hours, while the liver signal reached its maximum at 7 hours but diminished considerably by 48 hours. The authors note that whilst fluctuation in signals at the injection site could be indicative of the potential leakage of DiR molecules incorporated in the LNPs over time, the generally consistent signals at the injection site suggest that such release may not be significant. Furthermore, the observed metabolism and excretion of LNPs in the liver (where the signal cannot be detected in live imaging) might explain the decrease in signal over time [119]. Indeed, the authors confirmed this using LC/MS for quantification of deuterium-

labelled LNPs [119]. Given the stability of deuterium-labelled cholesterols within the LNPs bilayer, the release of 2H-cholesterols in the plasma is expected to be minimal. Tissue concentration measurements for deuterium-labelled LNPs aligned well with fluorescence intensity data, with the muscle at the injection site exhibiting the highest and relatively constant LNP concentration within 24 hours. The liver and spleen displayed comparable LNP concentrations, but due to the larger volume of the liver, it can capture more LNPs. When normalised to LNPs% per tissue, the muscle accumulated 60–80%, the liver 10%–20%, and the spleen only 1%–2% [119]. These results correspond to our findings with IVIS imaging of the mice detecting the DiR-labelled LNPs at the injection site and mRNA expression at both the injection site and liver (Figures 3.3 and 2.4). Di et al. also used their protocols to investigate the impact of LNP size on biodistribution after intramuscular injection, and whilst all IM injected LNPs were found to migrate from the injection site, smaller (~100 nm) LNPs were cleared more quickly than larger (180 and 330 nm) LNPs, possibly via the draining lymph nodes. With reference to particle size, studies have indicated that nanoparticles with sizes below 200 nm can access lymphatic drainage through advection (the passive transport carried along by fluid flow). On the other hand, 200 to 500 nm particles might rely on dendritic cells (DCs) to circulate to the lymph [119]. However, in our studies, whilst we see lower expression levels at both the injection site and liver for our 300 mM citrate buffer LNPs compared to LNPs prepared with 50 and 100 mM, all three formulations were well below 200 nm. Furthermore, LNPs prepared at 100 or 300 mM were not significantly different in size (approx. 120 nm), again suggesting differences in expression are not a result of different sizes or clearance rates from the injection site. Notwithstanding, there does remain the potential for both the LNPs and their expressed luciferase to be taken up by the lymphatics and into the circulation and hence luciferase detection at the liver (particularly given the correlation of higher expression levels at both the injection site and liver).

Surface charge is also a critical quality attribute of LNPs and can impact their potency and biodistribution. The surface charge of LNPs is driven by the pKa of the ionisable lipids within LNPs and the pH of the buffer they are suspended in[120]. It is also reported that the biological performance of LNPs can depend on their interactions with blood proteins and cell membranes, and surface charge can affect cellular uptake, endosomal release, and biodistribution of nanoparticles[121,122]. For example, Carrasco et al. showed that

intramuscularly administered LNPs exhibit off-target systemic production of mRNA in the liver depending on the surface charge of nanoparticles [85] and neutral particles can move to the liver more easily than their charged counterparts [85,119,123,124]. These interactions are strongly influenced by the charge state of the LNP's amine headgroups [125]. It has also been reported that the ionic strength can affect the apparent pKa of LNPs [126]. Therefore, whilst in our studies, there is minimal difference in the zeta potential of the three formulations, and it is unlikely these small differences alone would have a biological impact, the zeta potential is an indirect measure of surface charge and changes in the apparent pKa may not be detected. Increasing the ionic strength of the citrate buffer 6-fold (from 50 mM to 300 mM) may lead to changes in the apparent pKa of LNPs, which thereby impacts the potency of LNPs, potentially through reducing ionisation during endosomal maturation[126]. However, ionic strength did not affect the pKa of LNPs (Figure 3.3).

3.6 Conclusion

In the current study, we have investigated the influence of ionic strengths of citrate buffer on the physicochemical characteristics of mRNA-based LNPs and its effect on the *in vitro* and *in vivo* transfection efficiency. Varying the ionic strength of citrate buffer from 50 to 300 mM was shown to impact the particle size of the LNPs (increasing it from approx. 90 to 120 nm). In all the formulations, the PDI was low (<0.2), and encapsulation efficacy was high (>85%). The choice of citrate molarity also influenced LNP cellular internalisation, with LNPs prepared using 50 mM citrate buffer exhibiting increased uptake compared to the LNPs prepared using 300 mM citrate buffer. Whilst there was no notable difference in the *in vitro* transfection efficiency between the 50 mM and 100 mM LNP formulations, LNPs prepared with 300 mM citrate promoted lower transfection levels. A similar trend was shown *in vivo* with similar expression levels in mice after IM injection for the 50 mM and 100 mM LNP formulations but lower expression for the 300 mM formulation, concluding that the ionic strength of the aqueous phase in the preparation of mRNA-based LNPs governs their physicochemical properties and potency.

Overall, the *in vitro* and *in vivo* effect of the ionic strength of encapsulation buffer, citrate buffer, was not known before this study. It is confirmed that citrate buffer ionic strength is a key material attribute in pre-clinical studies that must be controlled when manufacturing LNPs.

Chapter 4: Exploiting Design of Experiment Approach Using C12-200 Ionisable Lipid

4.1 Introduction

Design of experiments (DoE) is a pivotal research tool, investigating the interactions between multiple parameters simultaneously. Also, it is a component of quality-by-design, which is an approach ensuring the quality and safety of the product from the early stage of development during the product lifecycle [127]. It explores multiple critical factors of the process or the formulation parameters and then allows for improving product quality and process optimisation. It has been widely used in drug delivery platforms and has been used to optimise mRNA-LNP efficiency and efficacy [55,127–131]. DoE can evaluate multiple parameters simultaneously instead of testing one factor at a time. Understanding the critical parameters of formulation variables and process parameters, as well as their interactions, successfully initiates the development of the process or product. It can also reduce labour and cost whilst minimising the use of resources, including reagents and animals with fewer *in vivo* studies.

In this chapter, the effect of formulation parameters, such as lipid concentration and microfluidic process parameters (including FRR and TFR), on LNP attributes (defined as responses) presented in Table 4. 1 were investigated. C12-200 (Figure 4.1) was used as the ionisable lipid within the LNP.

Table 4.1 *The factors with levels evaluated in this study and their target responses.*

Factors	Level Coded		
	Low	Middle	High
FRR (aq: lipid v/v)	1 (1:1)	3 (3:1)	5 (5:1)
TFR (mL/min)	4	12	20
Lipid concentration (mM)	6	18	30

Responses	Target
Particle size (nm)	< 100 nm
PDI	< 0.2
Zeta Potential (mV)	NA
EE (%)	~ 100
mRNA Recovery (%)	~ 100
In vitro Transfection (RLU)	Highest
In vivo Transfection from Injection site	Highest
In vivo Transfection from Liver	Lowest
Biodistribution	NA

DoE predicts the output of any given data based on the regression equation generated from the design. Different designs are used depending on the stage of the research. For example, a screening design is applied in the initial stage of development to identify which factors among

many variables impact the response. Then, factorial design allows for the working of the main effects of the parameters and the interaction(s) between them.

In this study, a response surface design was applied, which offers the main effect, interaction, and quadratic effect. The quadratic effect allows for the exploration of the curvature in the model, namely, capturing the non-linear relationship between the variable and the response [55]. It is very useful in the optimisation process that shows a non-linear model. The curvature and the interaction may be overlooked when only working with main (linear) effects. The Box-Behnken design, a subgroup of the response surface design, was performed for this study.
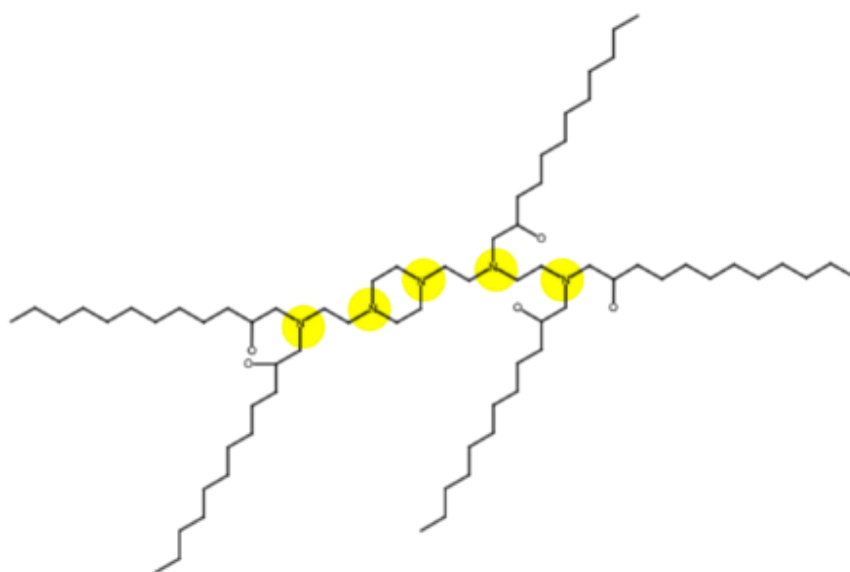
Figure 4.1 The chemical structure of C12-200, the yellow highlights the charged amine groups.

4.1.1 Box-Behnken DoE Approach – Background and Rationale.

The Box-Behnken is a type of response surface design used in DoE, and it is well suited for determining the optimal settings of input factors to achieve desired outputs while minimising variability. This design is characterised by its efficiency in fitting quadratic models and its ability to identify both linear and interaction effects among variables, and it was selected as it is suitable for the second-order model, which captures the curvature and non-linearity in the response surface (Figure 4.2) [132]. In a three-factor Box-Behnken design, all design points are at the same distance from the central point, which means the prediction error is the same for all points (Figure 4.2). Homogenously distributed design points prevent adding extreme and impractical experimental conditions to the model. Also, the Box-Behnken design allows for the

visualising of the relationship between the variables and responses by helping to understand the pattern behaviour and optimising the process [133]. It explores the quadratic effect and variable interaction with fewer experimental runs compared to the full factorial design [134]. The three-factor Box–Behnken design comprises 15 preparation runs, including 3 central runs. The factors and levels are shown in Table 4.2. For example, there would be 27 experimental (3 x 3 x 3) runs in case of using a general full factorial design. However, the Box-Behnken design almost halved the number of runs generated by the full factorial design. This offers more cost-effective and sustainable research and ethical considerations in terms of using fewer animals for studying LNPs.
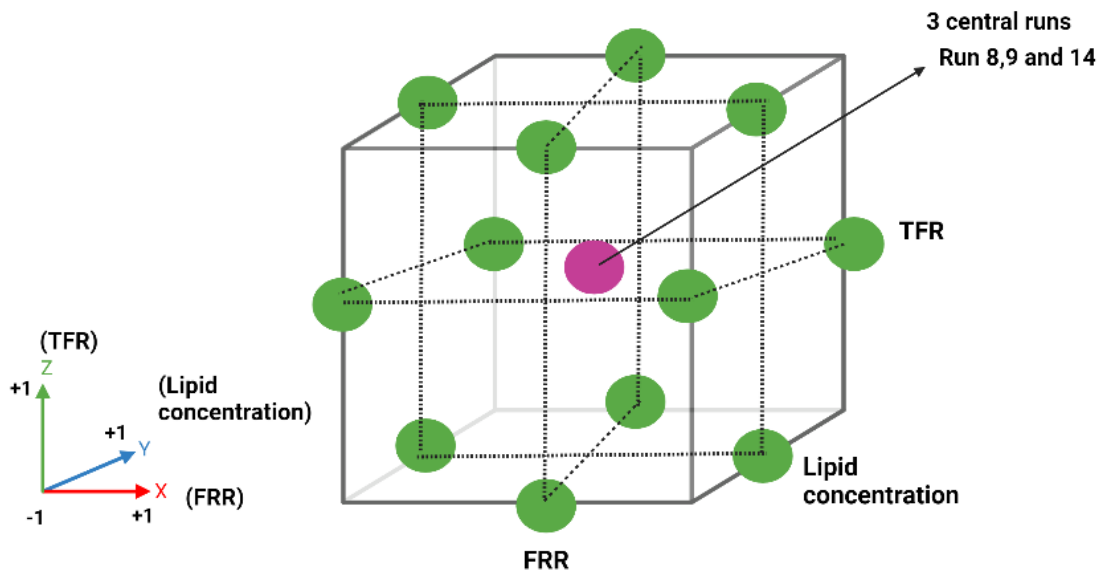
Figure 4.2 *Illustration of Box-Behnken Desing. There are three factors (FRR, TFR, and lipid concentration), with three levels: low, middle, and high. There are 18 runs in total, including 3 central runs for estimating error.*

This approach searches the main effect of the variables (x, y) and the interaction between the variables (xy) and quadratic effects (x^2, y^2). The quadratic model calculated using multiple regression analysis is described by the following Equation 4.1.

$$Y = a_0 + a_1X_1 + a_2X_2 + a_3X_3 + a_4X_1X_2 + a_5X_2X_3 + a_6X_1X_3 + a_7X_{12} + a_8X_{22} + a_9X_{32}$$

Equation 4.1

In Equation 4.1, Y is the particle size, PDI, zeta potential, encapsulation efficiency (EE), Recovery, *in vitro* expression, *in vivo* expression, and DiR intensity increment%. X is a preparation parameter where TFR, FRR and lipid concentration are, and α is a regression coefficient.

The accuracy of the model was evaluated by using the scatter plot of the experimental versus predicted values and adjusted R-sq value [55]. Using an experimental vs predicted scatter plot helps to visualise how well the model prediction aligns with the actual data points. A well-fitting model can be recognised by scattered data points along a diagonal line. This shows a strong fitting between the predicted and the observed values. Also, the distribution of the data points should be random. The existence of a pattern (such as a curve shape) in the distribution may indicate some limitations in the model that need to be addressed. In addition to the scatter plot, R-sq is an important parameter presenting the proportions of the variance in the response variables explained by predictor variables in the sample. Higher R-sq values indicate better prediction ability of the model across the actual data. However, the R-sq value tends to increase by adding the independent parameters to the model with multiple parameters, even if they do not improve the model. This R-sq value can be adjusted by considering the number of predictors and number of data points in the model, and this is called the adjusted R-sq. Therefore, the adjusted R-sq provides a more accurate conclusion than the R-sq. Another type of R-sq is the predicted R-sq, which evaluates the prediction ability of the model and provides information about the overfitting of the model. If the predicted R-sq is distinctly lower than R-sq, the model is likely overfitting, and some terms may be eliminated from the model to improve the accuracy. Also, the histogram graph of the frequency-residual should have a bell shape, as the expected prediction error is the same for all points in this design. ANOVA was conducted to identify the statistically significant terms of the model. Response surface factors were generated using this model to assess the relationship of the parameters. The estimation for the error was evaluated using central point runs performed at the same experimental conditions. Central runs are Runs 8, 19, and 14 (Table 4.2). The design details of all experiments are shown in Table 4.2.

Table 4.2 *Preparation parameters for DoE. Different lipid concentrations, FRR and TFR, were used to prepare DiR-labelled mRNA-LNPs. NP8 ratio remained for all runs.*

Runs	FRR	TFR (mL/min)	Lipid Concentration (mM)
1	1 (-1)	4 (-1)	18 (0)
2	1 (-1)	12 (0)	30 (1)
3	5 (1)	4 (-1)	18 (0)
4	5 (1)	12 (0)	30 (1)
5	3 (0)	4 (-1)	30 (1)
6	3 (0)	20 (1)	30 (1)
7	5 (0)	20 (1)	18 (0)
8	3 (0)	12 (0)	18 (0)
9	3 (0)	12 (0)	18 (0)
10	3 (0)	20 (1)	6 (-1)
11	5 (1)	12 (0)	6 (-1)
12	1 (-1)	12 (0)	6 (-1)
13	3 (0)	4 (-1)	6 (-1)
14	3 (0)	12 (0)	18 (0)
15	1 (-1)	20 (1)	18 (0)

4.2 Aim and Objectives

In this chapter, DOE was exploited to consider how manufacturing process parameters (TFR, FRR and lipid concentration) impacted LNP characteristics and potency *in vitro* and *in vivo*. To achieve this, the objectives were.

- Defining the most suitable design for the study. Then, decide the level for each parameter.

- Performing the DoE, collecting the data and analysing the DoE in the software.

- Optimise the models by trying methods such as model reduction (removing some parameters from the model to improve the accuracy).

- Evaluating the main, quadratic and interaction effect of FRR, TFR and lipid concentration over the particle physicochemical properties

- Performing validation runs to test the predictability of the models.

4.3 Materials and Methods

4.3.1 Materials

1,1'-[[2-[4-[2-[[2-[bis(2-hydroxydodecyl)amino]ethyl](2-hydroxydodecyl)amino]ethyl]-1-piperazinyl]ethyl]imino]bis-2-dodecanol (C12-200) was purchased from BroadPharm (Peterborough, UK). 1,2-distearoyl-sn-glycero-3-phosphocholine (DSPC), Cholesterol, 1,2-

dimyristoyl-sn-glycero-3-phosphoethanolamine-N-[methoxy(polyethylene glycol)-2000] (ammonium salt) (DMPE-PEG(2000)), Amicon® 100 kDa Ultra 15 mL Centrifugal Filters, Cholesterol were purchased from Merck (Gillingham, UK). Minimum Essential Medium (MEM), Sodium Pyruvate (100 mM), UltraPure™ DNase/RNase-Free Distilled Water were purchased from GibcoTM (Paisley, UK). ONE-Glo™ Luciferase Assay System and VivoGlo luciferin were purchased from Promega (Southampton, UK). DiIC18(7) (1,1'-Dioctadecyl-3,3,3',3'-Tetramethylindotricarbocyanine Iodide (DIR), Quant-it™ RiboGreen RNA Assay Kit, TrypLE™ Express Enzyme (1X), Sodium Acetate (3 M), pH 5.5, RNase-free, Sodium Chloride (5 M), RNase-free were bought from ThermoFisher Scientific (Paisley, UK). BD Medical™ BD Micro-Fine™ Insulin Syringe was bought from Fisher Scientific (Loughborough, UK).

4.3.2 Establishing the Design Space

The parameters were selected based on a literature search [55,95], considering which parameters can be altered (factors such as the molar ratio of the lipids and the ratio between lipid and mRNA need to be kept the same). The level of the parameter was decided according to the capability of the production facility (for process parameters) and based on the lab experience for formulation parameters. 18 mM was selected as a central level for the lipid concentration since it allows the preparation of 100 µg/mL of encapsulated mRNA to the LNPs (according to NP8 ratio). Then, 6 mM and 30 mM were decided for the low and high levels, respectively. For FRR, 3:1 (aq: lipid v/v) was selected as middle level due to being the common ratio to prepare mRNA-LNPs. Therefore, 1 (1:1) and 5 (5:1) were the low and high level, respectively. Given that the maximum speed of the microfluidic system is 20 mL/min, 4, 12 and 20 mL/min for the range of TFR were selected.

4.3.3 LNPs Preparation

Lipid nanoparticles (LNPs) were prepared using a staggered herringbone micromixer in the NanoAssemblr® Benchtop from Precision NanoSystems Inc. (Vancouver, BC, Canada). LNPs were prepared with NP8. The lipid phase was composed of DSPC:Chol:C12-200: DMPE-PEG lipid (16:46.5:35:2.5 mol%), while the aqueous phase was prepared with Fluc mRNA in 50 mM sodium acetate and 100 mM sodium chloride. DiR (1% molar of total lipid content) was included in the lipid phase to track the *in vivo* organ biodistribution of LNPs, using a DIR filter at an excitation level spectrum of 754 nm and emission spectrum of 778 nm. Microfluidic parameters (FRR and TFR) and lipid concentration are shown in table 4.2. mRNA concentration

was adjusted according to FRR, keeping all LNPs at NP8. Initial and final waste volumes were set at 0.15 and 0.05 mL, respectively.

For the validation run, FRR, TFR and lipid concentration were selected as 3 (3:1 v/v aq/lipid), 15 ml/min and 20 mM lipid stock, respectively. The relative error is calculated with Equation 4.2.

$$Relative\ Error\% = \frac{Measured\ value - Predicted\ value}{Measured\ value} \times 100$$

Equation 4.2

4.3.4 Down-stream Processing of LNPs and Characterisations

The samples were diluted 40x in TRIS/Sucrose pH7.4 (300 mM Sucrose in 10 mM TRIS) and centrifuged (2,000x g acceleration:9 deceleration:9) at 18 °C with centrifugal filter unit (MWCO 100 kDa) to remove ethanol and to raise pH to 7.4). LNPs were concentrated to the required concentration.

After purification, physicochemical properties of LNPs were characterised using Zetasizer Ultra (Malvern Panalytical Ltd, Worcestershire, UK). Briefly, samples were diluted with TRIS to 0.1 mg/mL of lipid concentration to measure particle size and PDI. Then, zeta potential was measured with the samples diluted to 0.1 mg/ml of lipid stock with ultrapure water. EE and recovery were evaluated using Ribogreen kit. Briefly, diluted samples (3 ug/mL mRNA-LNPs) were added to the black plate in the absence and presence of Triton, referring to the unencapsulated and total mRNA, respectively. EE and recovery were calculated according to equations 1.2 and 1.3.

4.3.5 In vitro mRNA Expression Studies

LNPs serial diluted (2, 1, 0.5 and 0.25 µg/mL with cell media) were added to the plate having a density of 10000 cells per well. 24-hour incubation at 37^{0}C, 100 µL of One-glo luciferin reagent was added to each well and the luminescence was measured using a plate reader (Glomax®, Promega).

4.3.6 *In vivo* LNP Retention at the Injection Site and mRNA Expression

Female BALB/c mice (8-12 weeks old) were injected with 5 µg of DiR labelled mRNA-LNPs per leg. They were imaged with a DiR filter (excitation peak at 710 nm and an emission peak at 780 nm) using IVIS Spectrum (Pekin Elmer) under anaesthesia. 6-hours later, the mice were imaged again under the DiR filter and injected with luciferin (at a dose rate of 150 mg/kg) via the SC route. 10-minutes later, they were imaged with an open filter. Mice were terminated using the Schedule 1 method. The data were analysed using Living Imaging Software to quantify the DiR and bioluminescence intensity. The fold expression was calculated by dividing the luciferin intensity by the luciferin intensity gained from the control mouse (1.8E+06 and 4.5E+06 are for the injection site and liver, respectively) (Equation 4.3). DiR increment% refers to the % increment of DiR intensity from 0h to 6h in both the injection site and liver (Equation 4.4).

$$Fold\ expression = \frac{Luc_a}{Luc_{control}}$$

Equation 4.3

$$DiR\ increment\ \% = \frac{DiR_{6h} - DiR_{0h}}{DiR_{0h}}$$

Equation 4.4

4.3.7 Statistical Analysis

Data are expressed as mean. Minitab 20 software was used to analyse the polynomial model. ANOVA with post-hoc analysis was performed to test the model fit. $p < 0.05$ was considered statistically significant. Fisher's Least Significant Difference (LSD) post-hoc test was performed where applicable.

4.4 Results

The results from the Box-Behnken experimental design were used to create, through response-surface methodology, a model to predict z-average, PDI, zeta potential, EE, recovery, *in vitro* expression, *in vivo* expression, and biodistribution. Table 4.3 shows all data, and the corresponding statistical outcomes of the data are shown in Table 4.4.

Table 4.3 Evaluation of DoE results for DiR-labelled Fluc-mRNA LNPs. The result represents mean (n=1)

Runs	FRR	TFR	Lipid Conc. (mM)	z-average diameter (nm)	PDI	Zeta Potential (mV)	EE (%)	Recovery (%)	in vitro expression (RLU)	Fold in vivo expression injection site	Fold in vivo expression liver	DiR increment % injection site	DiR increment % liver
1	1	4	18	152.0	0.23	22.7	100	62	94210	74	85	87	49
2	1	12	30	177.9	0.44	15.1	90	100	216954	147	70	89	58
3	5	4	18	75.9	0.16	14.1	100	100	103973	133	78	333	110
4	5	12	30	58.8	0.15	1.9	100	100	62259	108	136	339	142
5	3	4	30	101.2	0.12	14.1	99	100	210410	85	115	325	141
6	3	20	30	64.3	0.20	1.6	100	100	78973	111	78	205	141
7	5	20	18	64.6	0.20	13.8	100	100	97067	94	326	450	234
8	3	12	18	56.4	0.15	7.6	99	91	59446	123	220	407	208
9	3	12	18	59.5	0.22	14.5	100	100	50202	89	114	459	232
10	3	20	6	70.7	0.21	0.6	94	100	137629	127	111	385	217
11	5	12	6	86.1	0.25	12.9	100	100	212321	168	159	301	166
12	1	12	6	161.4	0.22	5.8	100	100	64846	59	32	152	117
13	3	4	6	75.1	0.21	13.6	100	100	127602	115	52	435	104
14	3	12	18	56.8	0.17	3.2	100	100	55014	94	131	507	127
15	1	20	18	150.9	0.09	14.1	99	63	53351	54	56	138	65

Table 4.4 *Effect of each factor for z-average diameter, PDI, zeta potential, encapsulation efficiency (EE), recovery, in vitro expression, in vivo expression and DiR increment p-values of the responses generated by Box-Behnken design.*

<table>
<tr><td></td><td colspan="9" align="center">p-value</td></tr>
<tr><td>Source</td><td>z-average diameter</td><td>PDI</td><td>Zeta Potential</td><td>EE</td><td>Recovery</td><td>In vitro expression</td><td>In vivo expression Injection site</td><td>In vivo expression liver</td><td>DiR increment % Injection site</td></tr>
<tr><td>Model</td><td>0.000</td><td>0.323</td><td>0.149</td><td>0.548</td><td>0.436</td><td>0.002</td><td>0.174</td><td>0.115</td><td>0.060</td></tr>
<tr><td>Linear</td><td>0.000</td><td>0.703</td><td>0.141</td><td>0.526</td><td>0.313</td><td>0.052</td><td>0.190</td><td>0.065</td><td>0.033</td></tr>
<tr><td>FRR</td><td>0.000</td><td>0.285</td><td>0.294</td><td>0.242</td><td>0.084</td><td>0.347</td><td>0.047</td><td>0.021</td><td>0.008</td></tr>
<tr><td>TFR</td><td>0.074</td><td>0.868</td><td>0.043</td><td>0.554</td><td>0.976</td><td>0.013</td><td>0.766</td><td>0.143</td><td>0.992</td></tr>
<tr><td>Lipid Concentration (mM)</td><td>0.725</td><td>0.921</td><td>0.988</td><td>0.569</td><td>1.000</td><td>0.582</td><td>0.786</td><td>0.758</td><td>0.218</td></tr>
<tr><td>Square</td><td>0.001</td><td>0.278</td><td>0.130</td><td>0.643</td><td>0.218</td><td>0.002</td><td>0.355</td><td>0.343</td><td>0.040</td></tr>
<tr><td>FRR*FRR</td><td>0.000</td><td>0.360</td><td>0.108</td><td>0.790</td><td>0.277</td><td>0.103</td><td>0.926</td><td>0.875</td><td>0.011</td></tr>
<tr><td>TFR*TFR</td><td>0.301</td><td>0.243</td><td>0.241</td><td>0.790</td><td>0.277</td><td>0.110</td><td>0.352</td><td>0.595</td><td>0.335</td></tr>
<tr><td>Lipid Conc (mM)*Lipid Con (mM)</td><td>0.018</td><td>0.208</td><td>0.142</td><td>0.261</td><td>0.150</td><td>0.000</td><td>0.160</td><td>0.100</td><td>0.125</td></tr>
<tr><td>2-Way Interaction</td><td>0.100</td><td>0.175</td><td>0.238</td><td>0.333</td><td>1.000</td><td>0.001</td><td>0.105</td><td>0.127</td><td>0.852</td></tr>
<tr><td>FRR*TFR</td><td>0.569</td><td>0.245</td><td>0.400</td><td>0.963</td><td>0.966</td><td>0.331</td><td>0.719</td><td>0.037</td><td>0.694</td></tr>
<tr><td>FRR*Lipid Conc (mM)</td><td>0.048</td><td>0.068</td><td>0.075</td><td>0.142</td><td>1.000</td><td>0.000</td><td>0.024</td><td>0.564</td><td>0.551</td></tr>
<tr><td>TFR*Lipid Conc (mM)</td><td>0.111</td><td>0.588</td><td>0.956</td><td>0.302</td><td>1.000</td><td>0.006</td><td>0.778</td><td>0.375</td><td>0.677</td></tr>
<tr><td>Error</td><td></td><td></td><td></td><td></td><td></td><td></td><td></td><td></td><td></td></tr>
<tr><td>Lack-of-Fit</td><td>0.024</td><td>0.154</td><td>0.779</td><td>0.003</td><td>0.111</td><td>0.051</td><td>0.362</td><td>0.692</td><td>0.228</td></tr>
<tr><td>Pure Error</td><td></td><td></td><td></td><td></td><td></td><td></td><td></td><td></td><td></td></tr>
<tr><td>Total</td><td></td><td></td><td></td><td></td><td></td><td></td><td></td><td></td><td></td></tr>
</table>

4.4.1 Physico-chemical Properties of LNPs

4.4.1.1 Considering the impact of Process Parameters on LNP Particle Size.

The particle size of the LNPs ranged from 56 nm to 178 nm (Table 4.3), showing the model was significant (p=0.000) (Table 4.3). The adjusted R-sq of the regression model (Equation 4.5) was high (96.3%).

z-average diameter = 238.4 - 84.55 FRR - 0.73 TFR - 1.33 Lipid Conc. + 12.06 FRR*FRR + 0.0790 TFR*TFR + 0.1057 Lipid Conc. *Lipid Conc. - 0.160 FRR*TFR - 0.456 FRR*Lipid Conc. - 0.0847 TFR*Lipid Conc.

Equation 4.5

The scatter plot of the predicted fitted, as an indicator for the accuracy of the model, showed a narrow distribution around the regression line in the 95% confidence level (Figure 4.3). Also, the mean of the actual data fell outside the 95% confidence area, showing that the regression model is significant. However, the model suffered from a lack-of-fit with a 0.024 p-value (Table 4.4); this is likely due to a very narrow distribution of estimated error generated by the central point runs. LNPs produced under the same experimental condition (Central runs; runs 8, 9 and 14) showed a maximum standard deviation of 1.9 nm in size and a minimum of 0.7 nm (data not shown), showing a very narrow error.
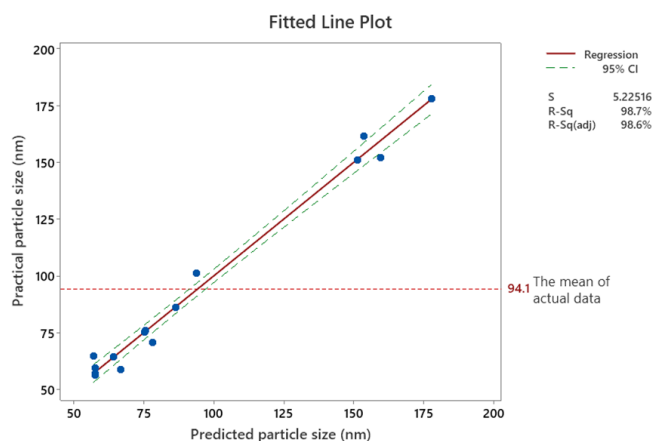
Figure 4.3 *Scatterplots of observed versus predicted values modelled by multiple regression based on DoE for particle size. The red continuous line and the area between the green dashed line and the dashed red line represent the fitted regression line, the 95% confidence area, and the mean of actual data, respectively.*

Equation 4.5 suggests that FRR, TFR, and Lipid Conc. all have a negative main effect, meaning increasing any of these factors tends to decrease particle size. The negative interaction terms suggest that combining certain factors (FRR with TFR, FRR with Lipid Conc., and TFR with Lipid Conc.) tends to have a synergistic effect in reducing the z-average diameter. However, the

	R-sq	R-sq(adj)
	98.7%	96.3%

	R-sq	R-sq(adj)
	73.8%	26.7%

	R-sq	R-sq(adj)
	82.6%	51.3%
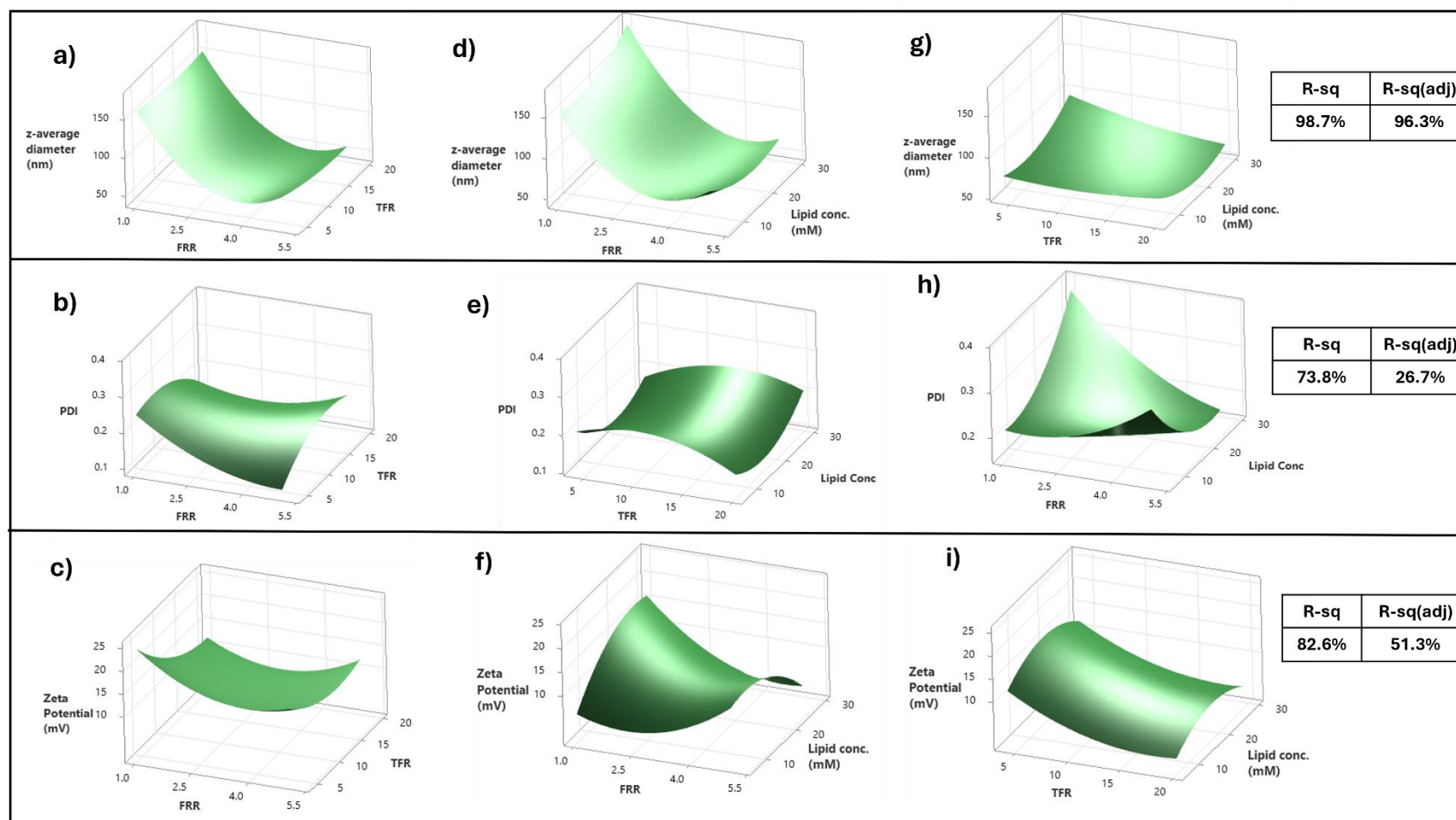
Figure 4.4 Response surface factors against particle size, PDI and zeta potential of LNPs. The effect of FRR (vol/vol) and TFR (mL/min) on the a) particle size, b) PDI and c) zeta potential at 18 mM of lipid concentration. The effect of TFR and lipid concentration (mM) on the d) particle size, e) PDI and f) zeta potential at TFR (mL/min) =12. The effect of TFR (mL/min) and lipid concentration (mM) on the g) particle size, h) PDI and i) zeta potential at FRR=3. The result represents n=1.

significance level of these factors was considered according to Table 4.4. Thus, it was visualised through a response-surface graph to further elucidate these trends and interactions (Figure 4.4). A significant quadratic effect of the FRR (p=0.000) and lipid concentration (p=0.018), in addition to the significant main effect of FRR (p=0.00), was seen in the model (p≤0.05) (Table 4.4). A significant interaction between FRR and lipid concentration was also seen (p=0.048). Moreover, the interaction plots and Fischer LSD test for pairwise comparison revealed that LNPs prepared with 1:1 FRR had a distinct particle size over 100 nm compared to the other FRR (Figure 4.5).
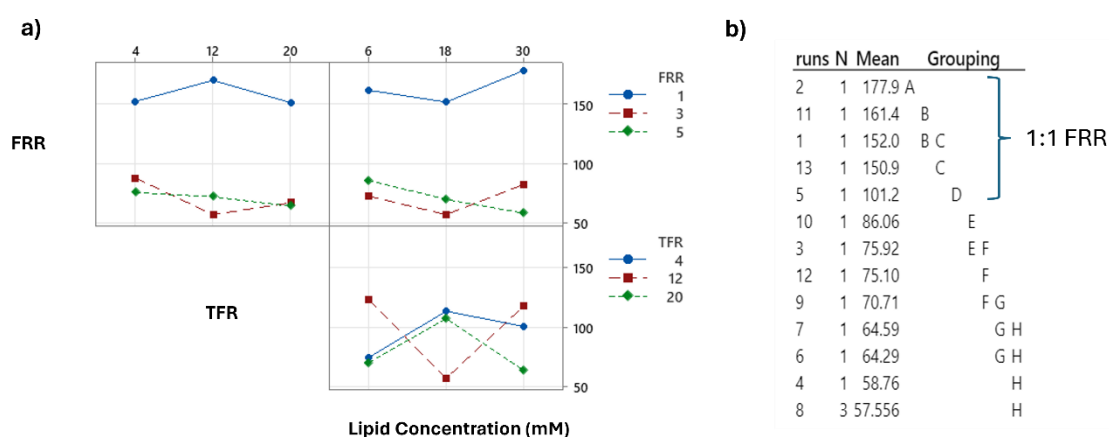
Figure 4.5 *a) interaction plots for mean particle size between FRR and TFR at lipid concentration=18 mM, FRR and lipid concentration at TFR=12 mL/min, TFR and lipid concentration at FRR=3. b) Pairwise comparison of particle sizes. Fischer Least Significant Difference (LSD) test was performed and means that do not share a letter are significantly different.*

4.4.1.2 Considering the Impact of Process Parameters on LNP PDI

PDI fluctuated between 0.09 (monodispersed) to 0.44 (polydisperse) for all runs, with most of the PDI around 0.2 and only one response at 0.44 (Table 4.3). Adjusted R-sq of the regression equation (Equation 4.6) was low (27%). Also, the predictability of the model was low, as seen from the prediction-fitted line graph (Figure 4.6). The data points were not distributed diagonally. Therefore, the model cannot be used to predict PDI. The response surface factors against the PDI of the LNPs are shown in Figure 4.4. LNPs produced under the same experimental conditions (run 8, 9 and 14) showed a maximum standard deviation of 0.04 in PDI and a minimum of 0.01, showing a very narrow error. However, overall, the model did not show a significant profile (p=0.323), highlighting that the parameters tested did not affect the particle size distribution significantly. Therefore, the interaction plot and pairwise comparison are not shown.

*PDI = 0.280 - 0.0415 FRR + 0.0049 TFR - 0.0051 Lipid Conc + 0.00875 FRR*FRR - 0.000718 TFR*TFR + 0.000348 Lipid Conc*Lipid Conc + 0.00275 FRR*TFR - 0.00323 FRR*Lipid Conc + 0.000201 TFR*Lipid Conc.*
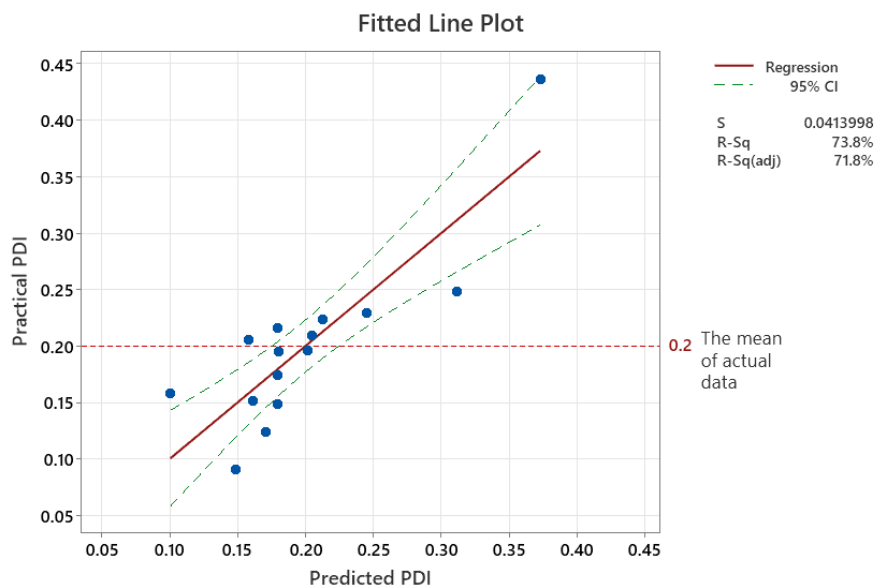
Figure 4.6 *Scatterplots of observed versus predicted values modelled by multiple regression based on DoE for PDI. The red continuous line, the area between the green dashed line, and the dashed red line represent the fitted regression line, the 95% confidence area, and the mean of actual data, respectively.*

4.4.1.3 Considering the Impact of Process Parameters on LNP Zeta Potential

The zeta potential varied from 0.55 mV to 22.7 mV (Table 4.3). The predictability of the model equation (Equation 4.7) for the zeta potential was low (Adjusted R-sq=51%, Figure 4.4). Also, the predicted-fitted line plot indicated the low predictability of the zeta potential based on the parameters. The model for zeta potential also did not exhibit a significant interaction and quadratic effect (Table 4.4 and Figure 4.4). From Equation 4.7, a negative coefficient for TFR and FRR and a positive coefficient for lipid concentration were noted. Only the significant level of the main effect of TFR was observed (p=0.043) (Table 4.4). This means there is a significant difference between the mean of the zeta potential of LNPs prepared in the different levels of TFR (4, 12 and 20 mL/min).

*Zeta Potential= 19.5 - 5.57 FRR - 2.13 TFR + 1.639 Lipid Conc + 1.147 FRR*FRR + 0.0489 TFR*TFR - 0.0284 Lipid Conc*Lipid Conc + 0.130 FRR*TFR - 0.2111 FRR*Lipid Conc + 0.0014 TFR*Lipid Conc*
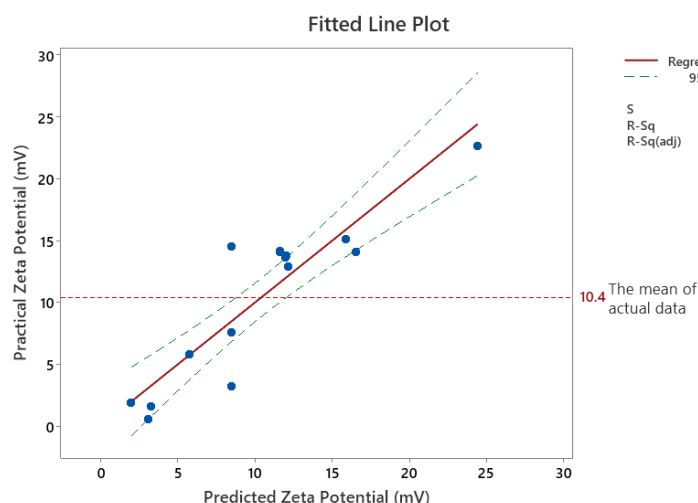
Figure 4.7 *Scatterplots of observed versus predicted values modelled by multiple regression based on DoE for zeta potential. The red continuous line and the area between the green dashed line and the dashed red line represent the fitted regression line, the 95% confidence area, and the mean of actual data, respectively.*

The effect of TFR on zeta potential can be visualised better with an interaction plot (Figure 4.8); for example, LNPs prepared at 4 mL/min showed slightly higher zeta potential irrespective of lipid concentration at 3:1 FRR (Figure 4.8a). However, the Fischer LSD test showed only one pair for all runs, meaning all zeta potentials are non-significant (Figure 4.8b).
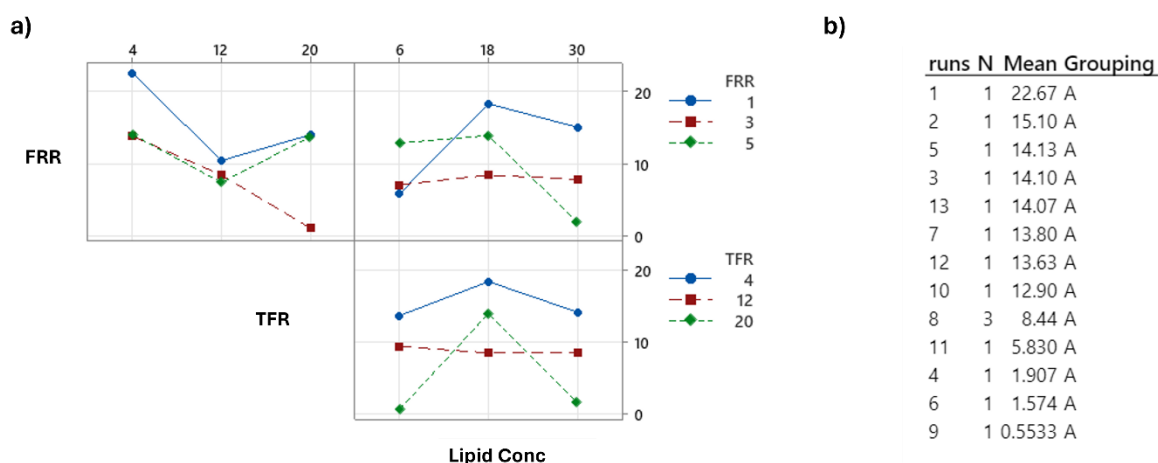
Figure 4.8 *a) interaction plots for zeta potential between FRR and TFR at lipid concentration=18 mM, FRR and lipid concentration at TFR=12 mL/min, TFR and lipid concentration at FRR=3. b) Pairwise comparison of particle sizes. Fischer Least Significant Difference (LSD) test was performed and means that do not share a latter are significantly different.*

4.4.1.4 Considering the Impact of Process Parameters on LNP Encapsulation Efficiency and Recovery

EE for all LNPs was almost 100% (Table 4.3), meaning that TFR, FRR and lipid concentration did not affect the EE. Therefore, the model (p=0.548) has no prediction ability since all LNPs had very similar EE efficiency, irrespective of lipid conc., TFR and FRR. Similarly, recovery (the total mRNA concentration of the sample) was approx. 100% for most samples, with only two LNPs having low recovery (approx. 62%; Table 4.3), and the model was not significant (p=0.436). However, FRR can influence recovery, as evidenced by the fact that these two LNPs were prepared at 1:1 FRR. Also, this can be confirmed with the lowest p-value (p=0.084) among the other p-values.

4.4.2 The Effect on In vitro Expression Profile

All samples were tested with the HEK-293 cell line to assess their *in vitro* expression profile. The predicted-practical graph (Figure 4.9) showed a good confidence interval along with the fitted line plot. The model (Equation 4.8) was significant (p=0.002, Table 4.4), and the closeness of adjusted R-sq (93.2%) and R-sq (97.6) indicated the goodness of the model (Figure 4.10). Therefore, the model can be used to predict *in vitro* expression profiles. The p values for FRR*lipid concentration and TFR*lipid concentration were significant at 0.000 and 0.006, respectively. This means the effect of the lipid concentration on the *in vitro* expression profile depends on both FRR (Figure 4.10 c, d) and TFR (Figure 4.10 e, f), and this interaction tends to decrease the *in vitro* expression according to Equation 4.6. Moreover, a non-linear relationship between lipid concentration and *in vitro* expression appeared (p=0.000, Table 4.4)

In vitro expression= 67842 + 28654 FRR - 3570 TFR - 2827 Lipid Conc + 4088 FRR*FRR + 249 TFR*TFR + 471.2 Lipid Conc*Lipid Conc + 531 FRR*TFR - 3148 FRR*Lipid Conc - 368.4 TFR*Lipid Conc

Equation 4.8

4.4.3 *In vivo* Expression

The samples were tested on BALB/c mice injected with 5 µg of mRNA-LNPs intramuscularly at both hind legs (Figure 4.11). The expression was quantified from the injection site and the liver. The model for the injection site (Equation 4.9) and the liver (Equation 4.10) showed a lack of fit with low R-sq and adjusted R-sq values (Figure 4.12).
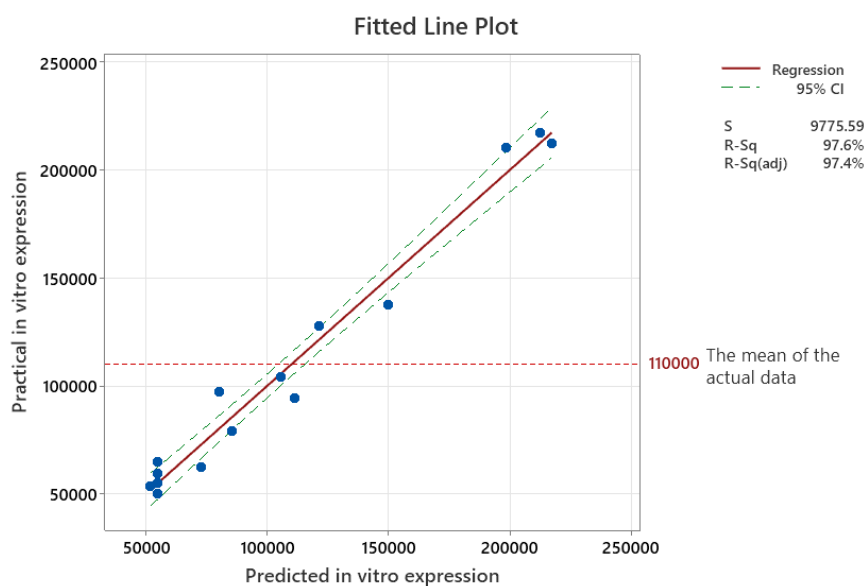
Figure 4.9 *Scatterplots of observed versus predicted values modelled by multiple regression based on DoE for in vitro expression. The red continuous line, the area between the green dashed line and dashed red line represent the fitted regression line, the 95% confidence area.*

g)		R-sq	R-sq (adjusted)
	In vitro expression	97.6%	93.2%
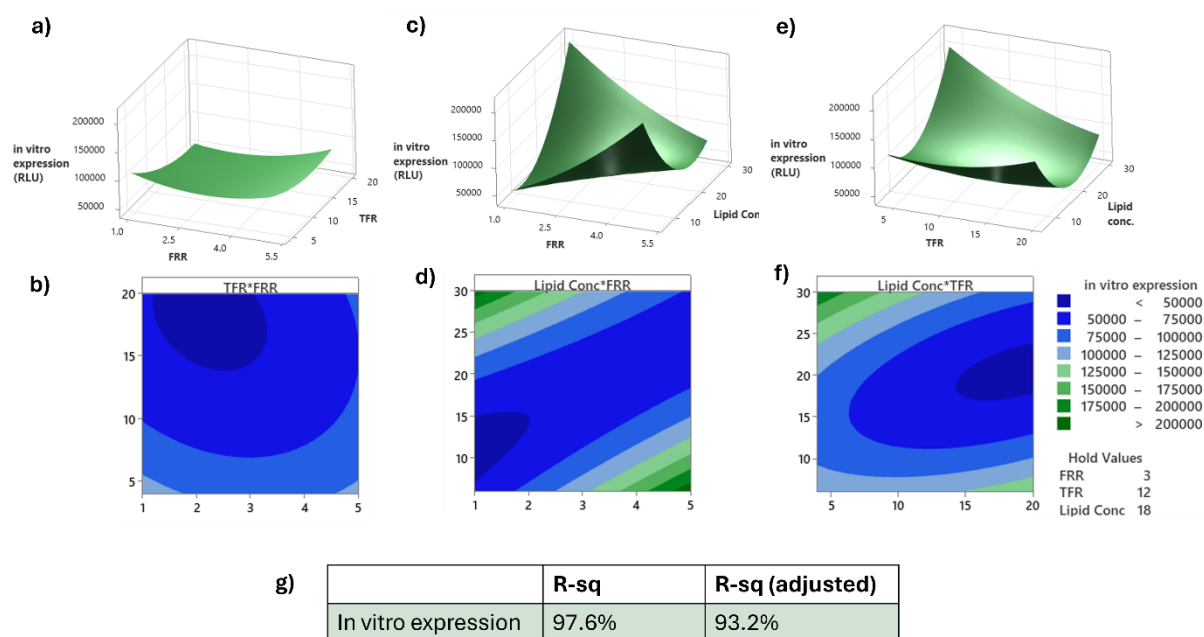
Figure 4.10 *Response surface factors against in vitro expression profile of LNPs on HEK-293 cell line. At 18 mM of lipid concentration, the effect of FRR (vol/vol) and TFR (mL/min) on the a) in vitro expression profile and b) corresponding contour plot. At TFR (mL/min) =12, the effect of FRR (vol/vol) and lipid concentration (mM) on the c) in vitro expression profile and d) corresponding contour plot. At FRR=3, the effect of TFR (mL/min) and lipid concentration (mM) on the e) in vitro expression profile and f) corresponding contour plot, g) R-sq and adjusted R-sq values.*

The model was not significant for the injection site (p=0.174, table 4.4) and liver (p=0.115, table 4.4). Therefore, the models cannot be used to predict the in vivo expression profile of mRNA-LNPs. To improve the models, model reduction was applied by removing lipid concentration from the model as the lipid concentration was the same for all samples for injecting. However, it did not result in a better fit (data was not shown). Regarding the effect of the parameters, the interaction between lipid concentration and FRR was significant (p=0.024) for the injection site (Figure 4.12 c). This interaction tended to decrease the expression in the injection site (Equation 4.9). The expression in the liver was affected by a positive interaction between TFR and FRR (p=0.037) (Figure 4.12 b).

in vivo expression (injection site) = 6.8 + 43.2 FRR + 4.45 TFR - 0.95 Lipid Conc - 0.29 FRR*FRR - 0.191 TFR*TFR + 0.1368 Lipid Conc*Lipid Conc - 0.273 FRR*TFR + 0.036 TFR*Lipid Conc

Equation 4.9

in vivo expression (liver)=-74 - 5.6 FRR + 0.7 TFR + 18.15 Lipid Conc - 1.05 FRR*FRR - 0.226 TFR*TFR - 0.356 Lipid Conc*Lipid Conc + 4.31 FRR*TFR- 0.63 FRR*Lipid Conc - 0.248 TFR*Lipid Conc

Equation 4.10
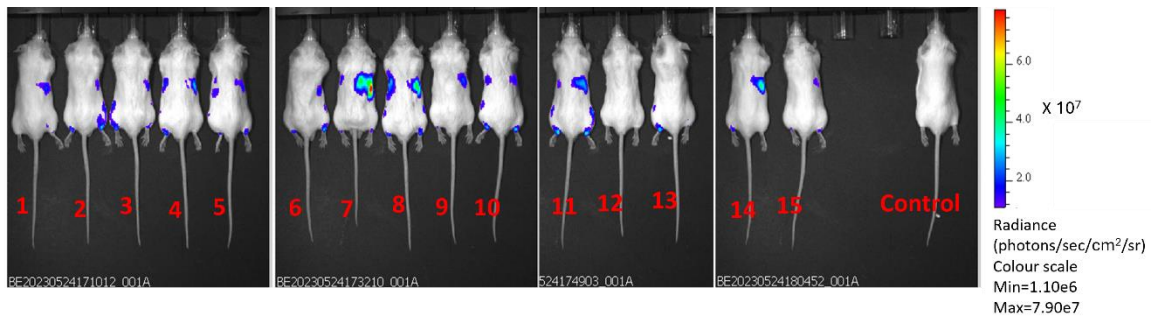
Figure 4.11 *Bioluminescence images of BALB/c mice 6h after* injected with DIR-labelled mRNA-LNPs via the intramuscular route. Red number refers to DoE runs specified on the table 4.2.

4.4.4 Biodistribution

The distribution of the DiR-labelled LNPs was evaluated by imaging mice under the DiR filter (Figure 4.13). Chapter 2 showed that DiR intensity increased (Figure 2.4b) 6 h after the IM injection of the LNPs, and this increment was higher for the LNPs having higher expression (Figure 2.5b). Therefore, the DiR% increment (Equation 4.4) in the injection site was calculated for each LNP to assess the possible relationship between the DiR increment and the expression.
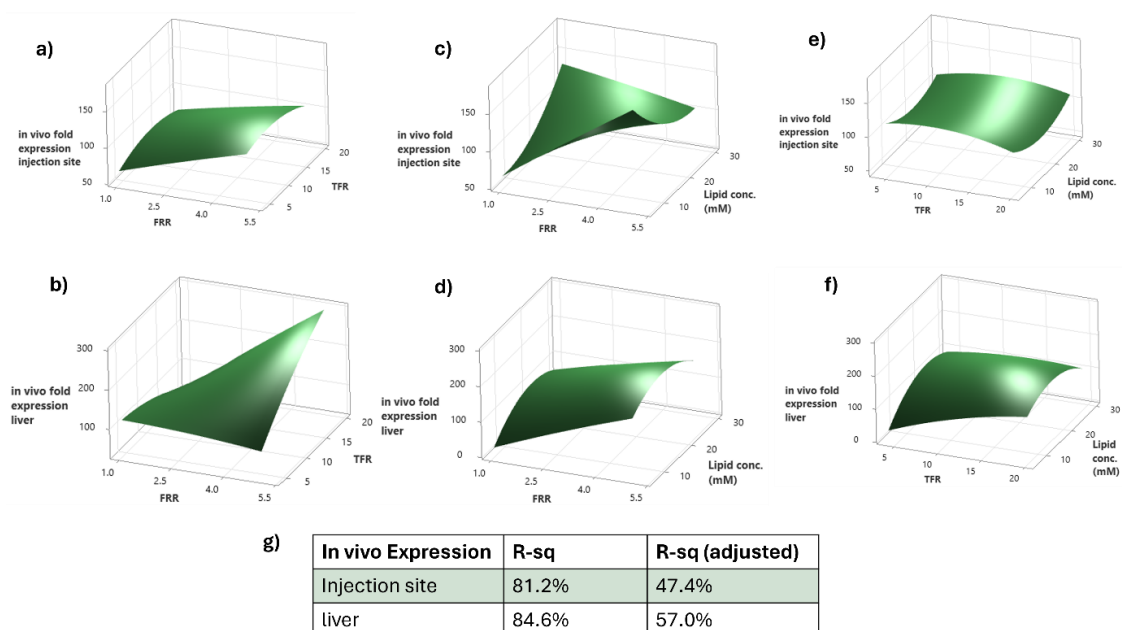
Figure 4.12 Response surface factors against in vivo expression profile of LNPs on BALB/c mice. At 18 mM of lipid concentration, the effect of FRR (vol/vol) and TFR (mL/min) on the in vivo expression profile from the a) injection site and b) liver. At TFR (mL/min) =12, the effect of FRR (vol/vol) and lipid concentration (mM) on the in vivo expression profile from the c) injection site and d) liver. At FRR=3, the effect of TFR (mL/min) and lipid concentration (mM) on the in vivo expression profile from the e) injection site and f) liver, g) corresponding R-sq and R-sq (adjusted) for the expression in the injection site and the liver

The models were not significant (Table 4.4); however, removing lipid concentration from the model (as all LNPs were diluted to the same lipid concentration for *in vivo* studies) improved the accuracy of the equation. The R-sq and adjusted R-sq for the injection site were around 75% and 60%, respectively (Figure 4.14). According to Equation 4.11, FRR and TFR had a positive effect on DiR% increment, but their quadratic effect was negative. FRR and DiR% increment had a non-linear relationship, and TFR positively affected DiR% increment, but their quadratic effect was negative. FRR and DiR% increment had a non-linear relationship (p=0.007, Figure 4.14 b).

% Dir increment in the injection site = -167 + 280.8 FRR + 11.1 TFR - 38.9 FRR*FRR - 0.594 TFR*TFR + 1.03 FRR*TFR

Equation 4.11
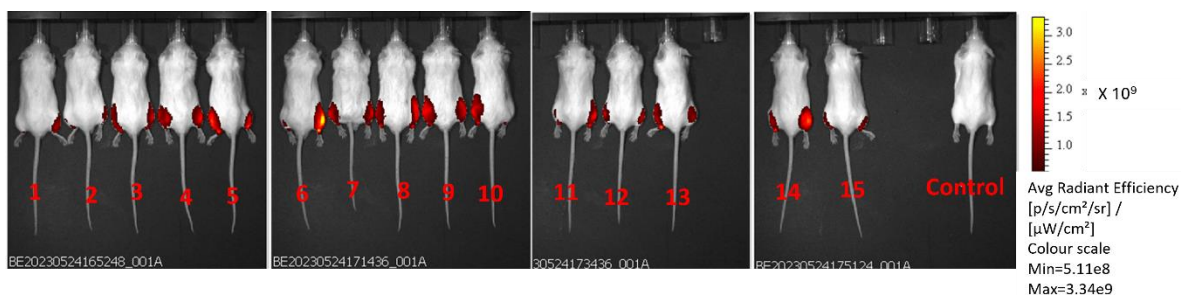
Figure 4.13 *Fluorescence images of BALB/c mice 6h after* injected with DiR-labelled mRNA-LNPs via the intramuscular route. The red number refers to the DoE runs specified in Table 4.2.
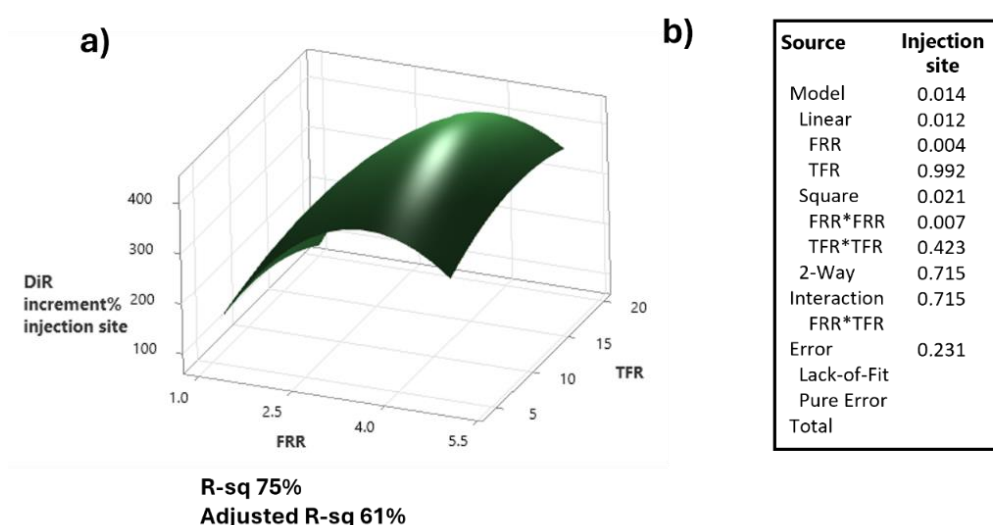
Figure 4.14 *Response surface factors against DiR increment profile of LNPs on BALB/c mice. At 18 mM of lipid concentration, the effect of FRR (vol/vol) and TFR (mL/min) from the a) injection site and b) ANOVA result showing the effect of TFR and FRR against the DiR increment% in the injection site.*

4.4.5 Validation Runs

Validation runs were performed to test the accuracy of the models. 3:1 FFR, 12 mL/min TFR and 20 mM of lipid stock were selected as they are the parameters commonly used when making LNPs. Relative errors% (Equation 4.2) from this validation run are shown in Table 4.5. Surprisingly, the model predicted the expression in the liver with only a 1% error, even if the model accuracy was low for the expression profile in the liver (Figure 4.12). Another surprising result was the lack of predictability of in vitro expression, although the model fits well (Figures 4.9 and 4.10).

Table 4.5 *Relative error (%) from the validation run for particle size, PDI, zeta potential, EE (%), Recovery (%) in vitro expression and in vivo expression. The parameters for FFR, TFR and lipid concentration were selected as 3, 5 mL/min, and 20 mM for the validation run, respectively.*

Response	Relative Error (%)
Particle size	17
PDI	29
Zeta Potential	25
EE (%)	0
Recovery (%)	15
In vitro expression	632
In vivo Expression (injection site)	208
In vivo Expression (liver)	1

4.5 Discussion

In these studies, the impact of microfluidics production parameters (impact of FRR, TFR, and lipid concentration) on the physicochemical properties, *in vitro*, and *in vivo* profiles of LNPs were evaluated using a DoE approach. For the physicochemical properties, particle size, PDI, zeta potential, EE and recovery can be considered critical quality attributes and, hence, were tested. Among these parameters, the model was significant for only particle size (p=0.000, Table 4.4), and the predictability of the model was high (R-sq adjusted 96.3%, Figure 4.4). FRR had a linear and non-linear effect on the particle size (Table 4.4). The interaction plot clearly showed that the particles prepared with 1:1 FRR showed a distinct profile and size over 150 nm, irrespective of TFR and lipid concentration (Figure 4.5 a). Also, the effect of FRR on the particle size depends on the lipid concentration and vice versa (p $_{FRR*lipid conc}$ =0.048). Increasing lipid concentration from 6 mM to 18 mM showed a similar profile for all FRR ranges; however, increasing to 30 mM showed a concentration-dependent profile (Figure 4.5 a).

The case of increasing FRR (more aqueous phase) leading to a decrease in the particle size has been reported in numerous reports [43,55,130,135]. When the lipids and aqueous phases mix, lipids are spontaneously organised into the bilayer formation due to the decreasing solubility. Increasing FRR (more aqueous phase/less solvent lipid phase) allows lipids to diffuse faster into the aqueous phase, and this allows the lipid bilayer to decrease in size, ultimately forming smaller particles [43,108]. Moreover, it was reported that particle size could be adjusted precisely by controlling the flow conditions and the mixer design, size tuning at 10

nm intervals ranging from 20 to 100 nm [136]. Thus, the DoE model aligns with published knowledge, further validating its applicability. It has also been reported that a high total flow rate can lead to smaller particle sizes by applying higher shear stress [137]. However, in the range of this DoE, TFR did not affect the particle size. Given the small range in TFR for the microfluidic system used (5 to 20 mL/min), this is not surprising and aligns with previous work from our laboratory [43].

The developed models for PDI, EE and recovery were not significant. This aligns with current understanding of the LNP systems because microfluidic mixing is widely associated with low PDI and high EE [42,138,139]. However, the highest PDI values only appeared with 1:1 FRR (lowest level of FRR) and 30 mM of lipid concentration (highest level of lipid conc) (Table 4.4), and this is linked to a high particle size. FRR is a key parameter in controlling the PDI of LNPs since the diffusion rate in MF is reduced at low FRR [55]. Also, it was reported PDI can be modulated by FRR and chip geometry [140,141]. Even if there is no significant parameter in the model for PDI, the interaction between FRR and lipid concentration had the highest effect (with the lowest p-value). This means the effect of FRR depends on the lipid concentration for PDI. EE and recovery were almost 100% for all runs, so there are no assumptions based on these parameters for the EE of the nanoparticles. The preparation method can substantially affect EE; with traditional methods, such as thin film hydration and ethanol injection, giving more heterogeneous distributed particle sizes with low mRNA encapsulation efficiency [76]. However, EE is also dependent on factors such as the size of the mRNA molecule and the choice of lipids [17,142,143].

The model for zeta potential was non-significant. This is unsurprising as all formulations have an NP8 ratio, meaning the ratio between mRNA and lipid was the same. In other words, LNPs prepared with higher lipid concentrations had a proportionally higher amount of mRNA, which maintained the electrostatic interactions across the formulations. Zeta potential can be influenced by factors such as lipid composition, the head group of the lipids, the ligands, and ionic strength or the pH of the solution [144,145].

The *in vitro* expression profile was tested using the HEK-293 cell line. The model was statistically significant with high accuracy (93.3% adjusted R-sq). It was affected by the lipid concentration*FRR and lipid concentration*TFR. It is known that particle size and zeta potential can modulate the cell uptake and, hence, *in vitro* expression profile [146–148].

Therefore, it is hypothesised that in vitro expression can be modulated by particle size and zeta potential, considering the significant relationship between FRR and particle size. Indeed, it has been reported that HEK-293 cells can only take up particles below 100 nm efficiently [149]. If particles over 100 nm were removed from the model, and the regression analysis performed against (z-average diameter)^3 (as the volume of the particles) (Figure 4.15), the adjusted-R-sq of the regression equation was 85 and 88 for the z-average diameter and (z-average diameter) ^3. This explains why FRR likely affects the *in vitro* expression indirectly via the particle size.
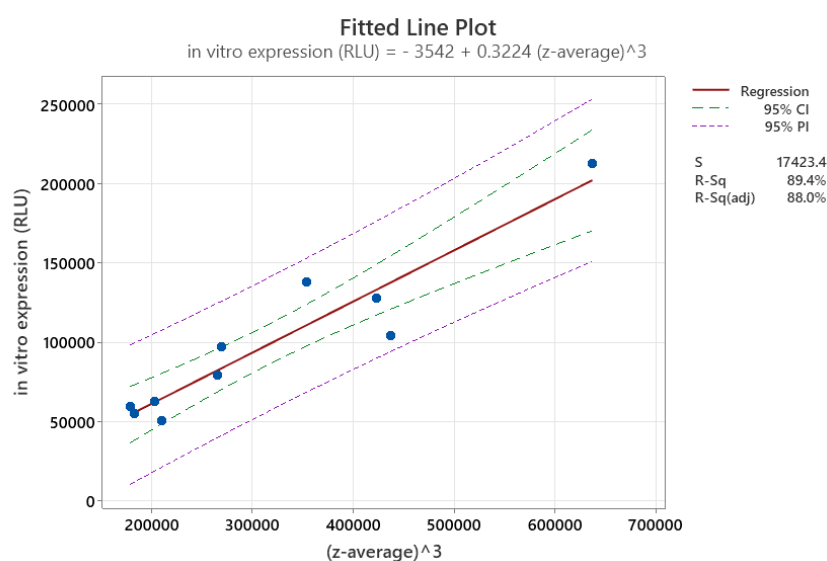
Figure 4.15 *Regression analysis between z-average^3 and the in vitro expression. The particles over 100 nm in size were removed from the model, and regression analysis was performed between z-average diameter^3 and the in vitro expression profile.*

The *in vivo* expression profile of LNPs was tested on BALB/c mice, and the expression occurred mostly in the injection site and the liver (Figure 4.11). FRR showed the main effect on the *in vivo* expression of both the injection site and the liver (Table 4.4). Also, the interaction between lipid concentration and FRR affected the *in vivo* expression in the injection site, although the model did not show good accuracy (47.4% adjusted R-sq, Figure 4.12).

Similar to in vitro expression, the link between the process variable (FRR) and the *in vivo* expression could well be driven by particle size. To test this, a regression analysis between the particle size and the *in vivo* expression was also performed (again, removing the data particle sizes over 100 nm). The adjusted R-sq was 58% with particle size^3 in the injection site. The model was improved slightly, but overall, *in vivo* expression model did not show good accuracy

against particle size. This suggests that *in vitro* can be effectively modelled, but *in vivo* performance cannot.

It is widely reported that in gene therapy in general and with LNPs, the field struggles with identifying strong *in vitro in vivo* correlation [87]. For example, the authors demonstrated the lack of correlation regarding the potency of LNPs prepared with various ionisable lipids such as ALC-0315, SM-102 and MC3. To consider this correlation based on the results from the DoE, regression analysis between *in vitro* and *in vivo* expression (total expression from the injection site and the liver) was performed, and no correlation was identified.

The same mice were imaged under the DiR filter to track the biodistribution of the LNPs. DiR intensity always increased 6 hours after IM injection of the LNPs and started to decrease over time, and the increment rate varied between formulations (Figure 2.5, Figure 2.9, Figure 3.7). Therefore, it was evaluated if there is a relationship between DoE parameters and DiR increment%. The model was significant for DiR increment in the injection (p=0.014, Figure 4.14 b). FRR (p=0.004) and FRR*FRR (p=0.007) were responsible for this significance level. This effect of FRR likely depends on the particle size, considering the relationship between FRR and particle size. Linear regression analysis between particle size and DiR increment showed an inverse trend (Figure 4.16) with good accuracy (adjusted R-sq 73.5% and R-sq 75.5%). DiR, a lipophilic dye bound to the LNP membrane, is likely to leak and spread at the injection site because the LNP membrane is disturbed in the endosomal escape step. IVIS maynot accurately detect this dispersion.

The accuracy was evaluated by validation runs. It was expected that particle size and in vitro expression would be predicted better, considering their adjusted R-sq value (Figure 4.3 and 4.3 for particle size. Figure 4.9 and 4.10 for *in vitro* expression) and practical-predicted line plot. Particle size was predicted with a 17% relative error (Table 4.5). The *in vitro* expression model was filled with a 632% relative error (Table 4.5). However, the expression in the liver was predicted with a 1% error (Table 4.5) even if the model accuracy was low (Figure 4.12).
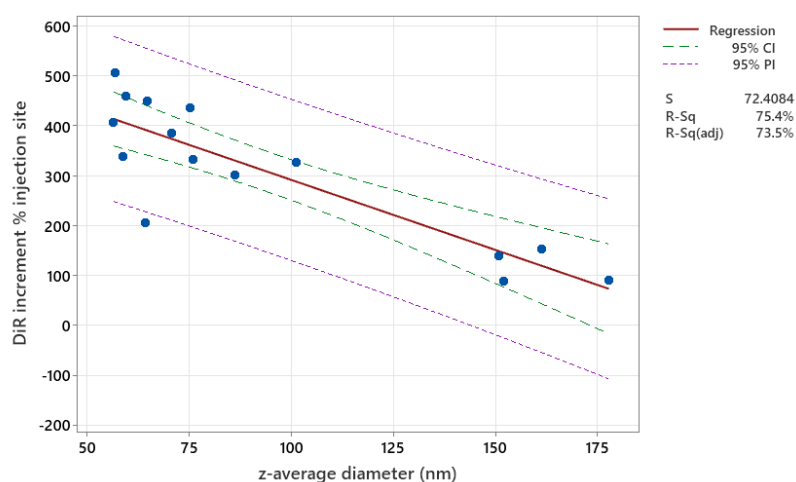
Figure 4.16 *Regression analysis of DiR increment in the injection site against z-average diameter*

DoE has been widely used in the LNP field. Kaufmann et al. used a definitive and fractional factorial design to optimise the *in vivo* mRNA delivery efficiency of LNPs composed of C12-200 developed for siRNA delivery [24]. They tested the parameters such as C12-200: mRNA weight ratio, phospholipid (DSPC, DOPE), and the molar composition of the lipids. They optimised the parameters, for example, using DOPE instead of DSPC, increasing C12-200: mRNA improved in vivo transfection efficiency. With the optimised formulation, mRNA expression in the liver followed by IV injection was improved over 7-fold. In another study, Qin et al. employed a mixture D-optimal design testing the molar ratio of the lipid of LNPs encapsulating either pDNA or siRNA on particle size, EE, *in vitro* and *in vivo* transfection efficiency in a tumour model [128]. They demonstrated that lipid composition influenced particle size and *in vitro* and *in vivo* outcomes; however, this effect depended on the choice of payload. Also, it presented the lack of *in vitro* and *in vivo* correlation. Another DoE using orthogonal design aimed to optimise the LNP composition for a potent mRNA delivery to T cells with low cellular toxicity. Initially, they utilised an orthogonal design with 16 runs testing the ratio of lipids and suggested that increasing the molarity of ionisable lipid and DOPE in combination with less cholesterol improved mRNA delivery to Jurkat cells. Then, the study continued with a second DoE, including 12 runs, and eventually, the transfection efficiency was improved 3-fold with less toxicity compared to the LNPs from the first DoE [150]. Another DoE approach was used to optimise delivering self-amplifying RNA (saRNA)[95]. The authors employed a two-step iterative approach. Initially, they utilised a definitive screening design to test a wide range of factors such as the choice of payload (mRNA vs saRNA), ionisable lipids and phospholipids,

temperature, and pH of aqueous phase over the response, including particle physicochemical properties. Optimised parameters were fixed, and then BBD was employed to test the defined critical process parameters, such as ionisable lipid type and buffer pH, from first DoE over the response, including protein expression and cellular activation, in addition to the physicochemical properties of LNPs. In the end, the study showed that higher pH was associated with smaller particle sizes, whereas an increased amount of phospholipid led to larger particle sizes, higher EE, and improved RNA integrity. The protein expression level was improved with higher ionisable lipids content. Another DoE approach focused on producing LNPs to deliver mRNA within a specific size range of 60 to 180 nm [151]. They tested the parameters, including the composition of the buffer, buffer pH and sonication time. Notably, both sonication time (ranging from 0 to 100 seconds) and pH levels (from 4.2 to 5) correlated with particle size, resulting in particles ranging from 50 to 200 nm. Additionally, the polydispersity index (PDI) was higher when the sonication time and pH were both low. The choice of buffer for dialysis, specifically PBS pH 7.4, PBS pH 7.2, HEPES pH 6.7, and HEPES acetate pH 6.7, also affected particle size, with larger particles observed in PBS pH 7.4 and HEPES pH 6.7. However, the buffer concentration did not significantly impact the final diameter of the particles.

4.6 Conclusion

In this chapter, the impact of manufacturing processes on C12-200 mRNA-LNPs was evaluated, exploiting the DoE platform. The main interaction and quadratic effect of FRR, TFR (as manufacturing parameter), and lipid concentration (as formulation parameter) on LNP critical quality parameters (size, PDI, zeta potential, EE, and recovery) were tested. Also, the samples were tested *in vitro* with the HEK-293 cell line and *in vivo* with BALB/c mice. Overall, the DoE showed the importance of considering the quadratic effect when designing the experiment. From these studies, using this LNP formulation, the optimised production parameters for C12-200 LNPs were 5:1 FRR, 4 mL/min TFR, and 6 mM lipid stock, giving the highest expression in the injection site and the lowest expression in the liver. In these parameters, particle size, PDI, zeta potential, EE, and recovery would be 92.4 nm, 0.24, 17.7 mV, 99.5 % and 100 %, respectively.

Chapter 5: The Role of Biological Sex in Pre-Clinical (Mouse) mRNA Vaccine Studies

This chapter has been published in Vaccines.

Credit for Authors

Burcu Binici (B.B.) methodology, validation, formal analysis, resources, data curation, conceptualisation, investigation, writing—original draft preparation, review and editing, visualisation.

Zahra Rattray (Z.R.) conceptualisation, investigation, writing—original draft preparation, review and editing, visualisation, supervision.

Avi Schroeder (A.V.) conceptualisation, investigation, writing—original draft preparation, review and editing, visualisation.

Yvonne Perrie (Y.P.) methodology, validation, formal analysis, resources, data curation, conceptualisation, investigation, writing—original draft preparation, review and editing, visualisation, supervision, project administration, funding acquisition.

5.1 Introduction

Both biological sex and gender influence vaccine uptake, responses, and outcomes [152]. A range of studies spanning animal models [153,154] and humans [155–157] have reported biological sex influences immune responses and vaccine efficacy. For instance, Klein et al., demonstrated that female mice, upon vaccination with inactivated influenza A virus, exhibited higher antibody responses and greater activation of germinal centre B cells and memory CD8+ T cells against influenza challenge compared to their male counterparts [153]. Whilst in humans, biological sex-specific responses against the seasonal influenza vaccine have been reported in older adults[158]. Reports also highlight higher adverse effects related to vaccines in females and may reflect a greater immune response in females compared to males [159,160] as could the differences in prevalence of anti-PEG antibodies in males and females [161]. However, when considering immune response to COVID-19 infections, the data is less clear with studies have reported higher immune responses in either females [155,162–164] or males [165–167], while other found no difference [168,169]. Similarly, whilst the initial reports on the safety and efficacy of two mRNA lipid nanoparticles (LNPs) based vaccines [22,23] did not fully provide sex-based data [170]. A review considering sex difference in efficacy of COVID-19 vaccines notes that no statistically significant differences between males and females were reported for the Moderna or Pfizer-BioNTech mRNA vaccines [160].

The factors mediating biological sex-dependent immune response could be age, sex hormones and/or genetics driven while the factors for gender differences could be behaviour, environmental and/or microbiome, when considering sex and gender as a biological variable and social construct, respectively [152,171]. For example, reports have suggested that COVID-19 vaccines can affect the duration and magnitude of the menstrual cycle [172] and mice intravenously injected with LNPs loaded with mRNA during the menstrual cycle demonstrated enhanced LNP accumulation and gene expression in the ovaries and uterus [171]. It has also been reported that elevated levels of estradiol provide a protective effect for young female individuals facing COVID-19 while the decline of estrogen levels in peri-menopausal women (~55 years) is associated with increased fatality rates in women [171,173]. Another factor is the gene dose of Toll-like receptor 7 (TLR-7), one of the pattern recognition receptors for SARS CoV-2 ssRNA, and females have biallelic TLR7 expression due to having two X chromosomes,

leading to the production of more type 1 interferon, resulting in stronger immune responses compared to males [174].

LNPs play a pivotal role in the formulation of mRNA COVID-19 vaccines developed by Pfizer/BioNTech and Moderna. These LNPs are composed of four lipids: a neutral phospholipid (in both vaccines this is distearoylphosphatidylcholine (DSPC)), cholesterol, an ionisable lipid and a pegylated lipid. Within the Pfizer-BioNTech formulation the ionisable lipid is ALC-0315 ([(4-hydroxybutyl)azanediyl]di(hexane-6,1-diyl)bis(2-hexyldecanoate)) and the pegylated lipid is ALC-0159 (2-[(polyethylene glycol)-2000]-N,N ditetradecylacetamide) and these are at the molar lipid ratio (%) of 9.4:42.7:46.3:1.6 (DSPC:Chol:Ionisable lipid:PEGylated lipid) [14]. Within the Moderna mRNA formulation the ionisable lipid is SM-102 (heptadecan-9-yl 8-((2-hydroxyethyl) (6-oxo-6-(undecyloxy) hexyl) amino) octanoate) and PEG2000-DMG (1,2-Dimyristoyl-sn-glycerol-3-methoxypolyethylene glycol) is the pegylated lipid. These are at the molar lipid ratio (%) of 10: 38.5:50:1.5 [14]. Within these LNPs, the DSPC and cholesterol is added to stabilise the particle. The ionisable lipid is used to complex the mRNA, at low pH these ionisable lipids are cationic and interact with the anionic mRNA during particle formation. The PEG-lipid is added to control particle and stabilize the particle during storage [14].

Following administration of mRNA-LNP vaccines, a dynamic cellular process ensues, where LNPs are taken up by cells through endosomal pathways, facilitating the release of mRNA into the cytosol. The released mRNA is then translated into the corresponding antigen protein within the ribosome, consequently initiating the activation of the immune system. Considering this interplay between mRNA-LNP vaccines and the immune system, it is crucial to explore potential variations in immune responses across different biological sexes. Discrepancies in immune responses after vaccination could be influenced by multiple factors. For instance, depending on the biological sex, LNPs may undergo different processing, encountering unique biological environments associated with each biological sex. Indeed, biological sex-dependent protein corona formation has been reported [175] suggesting that the biological sex of the host could impact the interaction between LNPs and proteins in the body. Any differences in the protein corona may change LNP surface properties, which in turn could impact cellular uptake and the processing of LNPs and hence affect biodistribution, clearance and expression profiles [176–179].

Given the significance of these factors, our study aimed to investigate biological sex-dependent immune responses by comparing antibody responses and protein expression in female and male BALB/c mice. These mice were intramuscularly injected with mRNA LNPs, typical of a standard vaccine mouse model. The primary objective was to investigate antibody response disparities across the biological sexes and determine whether these differences are driven by mRNA expression profiles or immunological responses. This research seeks to add valuable insights into designing pre-clinical mouse mRNA vaccine studies and understand the potential impact of biological sex on mRNA-LNP vaccination efficacy.

5.2 Aim and Objectives

The work in this chapter focused on evaluating the possible protein expression and immune response differences between female and male BALB/c mice. For this, LNPs were prepared using Fluc mRNA and OVA mRNA to evaluate the expression and the immune response, respectively. To achieve this, the objectives were:

- Initially, encapsulating two different mRNA (Fluc mRNA and OVA mRNA) into the LNPs with high loading and favouring similar size, PDI and zeta potential as the *in vivo* clinical outcome will be compared.
- Performing an IVIS study for quantifying the expression profile
- Injecting mice with OVA mRNA LNPs and performing ELISA to quantify the immune response.

5.3 Materials and Methods

5.3.1 Materials

The ionisable lipid 8-[(2-hydroxyethyl)[6-oxo-6-(undecyloxy)hexyl]amino]-octanoic acid, 1-octylnonyl ester (SM-102) was purchased from BroadPharm (USA). 1,2-distearoyl-sn-glycero-3-phosphocholine (DSPC), 1,2-dimyristoyl-rac-glycero-3-methoxypolyethylene glycol-2000 (DMG-PEG2000) were procured from Avanti Polar Lipids (Alabaster, AL, USA). Cholesterol (Chol), citric acid, sodium citrate tribasic dehydrate, sulfuric acid, hydrogen peroxide (H_2O_2), Tween 20, 3,3',5,5'-Tetramethylbenzidine dihydrochloride hydrate (TMB) were acquired from Merck (NJ, ABD). EZ Cap™ Firefly Luciferase mRNA (5-moUTP) is procured from APExBIO (TX, USA). Ovalbumin (OVA)-encoding mRNA modified with 5-methoxyuridine (5moU) (MRNA41) was purchased from OZ Bioscience (Marseille, France). Goat anti-Mouse IgG (H+L) Secondary

Antibody HRP (A16066) was bought from Invitrogen. Goat Anti-Mouse IgG2a-HRP (1081-05) and Goat Anti-Mouse IgG1-HRP (1071-05) were gained from Southern Biotech. Quant-it Ribogreen RNA assay kit, 1,1-dioctadecyl-3,3,3,3-tetramethylindotricarbocyanine iodide (DiR) were bought from Invitrogen (Massachusetts, USA). Minimal Essential Medium (MEM), fetal bovine serum (FBS), sodium pyruvate, and penicillin/streptomycin were acquired from Gibco, Thermo Fisher Scientific. ONE-Glo luciferase assay system, Vivo Glo luciferin substrate were from Promega (Wisconsin, USA). All other solvents were of analytical grade and were supplied in-house.

5.3.2 LNP Preparation

LNPs were prepared using the NanoAssemblr Benchtop from Precision Nanosystems Inc (Vancouver, BC, Canada). The lipid phase was composed of 6 mg/mL of DSPC: Cholesterol: SM-102: DMG-PEG2k molar ratio of 10:38.5:50:1.5% while the aqueous phase was prepared with 87 μg/mL of mRNA in 50 mM pH4 citrate buffer, corresponding to a N/P of 6 (the molar ratio of amine groups of the ionisable lipid to phosphate groups on mRNA). mRNA encoding ovalbumin (OVA) as a model antigen and mRNA encoding Firefly luciferase (Fluc) as a reporter gene were used in the immunisation study and expression study, respectively. DiR (1% mol), a lipophilic fluorescent dye, was included in the organic phase to track the *in vivo* organ biodistribution of LNPs in the *in vivo* expression study, using a DIR filter at an excitation level spectrum of 750 nm and emission spectrum of 780 nm. The microfluidic parameter was kept the same at a 3:1 flow rate ratio (FRR; ratios between the aqueous and organic phase) and 12 mL/min total flow rate (TFR). After self-assembling LNPs using microfluidics, they were purified using a spin column (Amicon® Ultra-15 Centrifugal Filter Unit, 100 kDa), by diluting the samples 40 times in 10 mM PBS pH7.4 and followed by centrifuging at 2,000 g at 4 °C until the required volume was recovered.

5.3.3 LNPs Characterization by Using Dynamic Light Scattering: Particle Size, Polydispersity and Zeta Potential

The z-average hydrodynamic diameter, polydispersity index (PDI) and zeta potential were assessed using dynamic light scattering using a Zetasizer Ultra (Malvern Panalytical Ltd, Worcestershire, UK). The instrument is equipped with a 633 nm laser and detection angle of 173°. To measure particle size and PDI, samples were diluted to 0.1 mg/mL lipid concentration

with 10 mM PBS pH 7.4. To measure zeta potential samples were diluted with ultrapure water for zeta potential. Mean particle size, PDI and zeta potential are expressed as the mean ± SD.

5.3.4 Entrapment Efficiency

The encapsulation efficiency of LNPs was determined using the Ribogreen kit. Briefly, 50 µL of the sample was added to the 96-well black plate in the presence and absence of 0.1 w/v% Triton X-100 to define total mRNA and unencapsulated mRNA, respectively. The plate was incubated at 37 ^{0}C for 15 minutes to allow LNP disruption to determine the total mRNA concentration. 100 µL of Ribogreen fluorescent dye was added to the wells with 200 x dilution and 500 x dilution for Triton (+) and Triton (-) wells, respectively. The fluorescence intensity was quantified using a GloMax® Discover Microplate Reader at excitation and emission wavelength of 480 nm/520 nm. The encapsulation efficiency (%) and recovery (%) were calculated according to the standard curve with and without Triton to quantify non-encapsulated and total mRNA concentration.

5.3.5 In vivo Studies

All animals were handled in accordance with the UK Home Office Animals Scientific Procedures Act of 1986 (UK project license number PP1650440/ personal license number I52241434) in accordance with an internal ethics board.

5.3.5.1 Biodistribution and In vivo mRNA Expression Study

To compare responses between male and female mice, two independent studies were conducted with groups of 2 females, 2 males, and 1 non-injected mouse. 8-10-week-old BALB/c mice were provided by the Biological Procedure Unit at the University of Strathclyde, Glasgow. LNPs were prepared with Fluc mRNA and labelled with DiR with the aim of assessing the expression profile of Fluc mRNA and tracking the biodistribution of LNPs, respectively. Mice imaging was gained using an *in vivo* imaging system (IVIS Spectrum, Perkin Elmer) and Living Image software was used for image capture and data analysis. Mice were intramuscularly injected in each hind leg with 5 µg of Fluc mRNA LNPs and then were anaesthetized with 3% isoflurane and transferred to the IVIS cabin, maintaining isoflurane level at 2%. Mice were imaged under a DiR filter at an excitation of 754 nm and an emission of 778 nm. Then, they received a subcutaneous (sc) injection of d-luciferin at a dose of 150 mg Luciferin/kg body weight. 10 minutes after the sc injection, mice were imaged for bioluminescence imaging in an open filter during the time defined by auto-exposure settings.

These imaging sessions with DiR filter and bioluminescence were repeated 6, 24, 48 and 192 h post-injection of LNPs. After the last time point, mice were terminated using a schedule 1 method. Image capture and data analysis were carried out using Living Image software. Average radiant efficiency and total flux were gained by region of interest for fluorescence and bioluminescence respectively and normalized with the control mice. Average radiant efficiency and average total flux were calculated for both the fluorescence intensity and bioluminescence measurements.

5.3.5.2 Immunization studies

Female and male BALB/c mice, 8-10 weeks old (average of 20 g), were split into 3 groups (1, 2.5 and 5 µg) of 3 mice which were obtained from the Biological Procedure Unit at the University of Strathclyde, Glasgow. Each group was tested in two independent studies (thus a total data set of 6 mice per group). In the first study, a control group was also included to confirm no background responses (data not reported). The mice were immunized two times with 4-week intervals between the two immunizations. Mice were primed with OVA mRNA LNPs intramuscularly at 1, 2.5 or 5 µg per dose, and the blood was collected on day 27. Then, they were boosted with the second matching dose on day 28. Two weeks after the booster dose (day 42), mice were terminated by cardiac puncture and the blood was collected.

5.3.5.3 Immunological readouts – Antibody Responses

A direct enzyme-linked immunosorbent assay (ELISA) was used to detect total IgG, IgG1 and IgG2a in the serum. The plates were coated overnight with 100 µL per well of 1 µg/mL OVA protein in 0.1 M carbonate buffer pH 9.6 at 4 °C. The plates were washed with washing buffer (10 mM PBS pH 7.4 with 0.05 % Tween 20) three times and then blocked with 200 µL of 10% v/v FBS diluted in PBS pH 7.4 for 2 hours at room temperature (RT) to eliminate any non-specific binding. During this time, the serum samples were diluted in 10 mM PBS containing 5 % *v/v* FBS. The plates were washed 5 times and then 100 µL of diluted serum samples were added to the wells for 1 hour at room temperature. After 5 washes in ELISA washing buffer, the plates were incubated for 1 h with 100 µL of horseradish peroxidase labelled goat anti-mouse total IgG (1:2500, Invitrogen), anti-mouse IgG1 (1:5000, Southern Biotech) and anti-mouse IgG2a (1:5000, Southern Biotech). After incubation, the plates were washed 5 times and 100 µL of 3,3',5,5'-Tetramethylbenzidine (TMB) substrate was added to each well and incubated in the dark at room temperature for up to 10 minutes. The reaction was stopped

by adding 100 µL of 0.2 M H_2SO_4. The absorbance was immediately measured at an optical density of 450 nm (OD450) using iMark™ Microplate Absorbance Reader (Bio-Rad, USA). The endpoint value was defined according to the dilutions and the reciprocal endpoint was calculated.

5.3.5.4 Re-stimulation of Splenocytes

The mice were terminated with a cardiac puncture on day 42 and the spleens were discarded and placed into the universal container including 5 mL of complete RPMI 1640 media and placed on ice until finished discarding all spleens. Then, spleens were smashed through a cell strainer and centrifuged 300 x g for 5 mins at 4 °C. Supernatant was discarded, and the 3 mL of Boyle solutions was added to the cell pellet to remove erythrocytes, allowing to incubate at RT for 5 minutes. Then, the suspension was centrifuged at 300 x g for 5 mins at 4 ^{0}C. The supernatant was removed, and the cell pellet was washed twice with complete media, centrifuging at 300 x g for 5 mins at RT. The cell pellet was removed and resuspended in 1 mL of complete media. Viable cells were counted using a cell counter (Thermo Invitrogen) by Trypan blue. The cells were diluted to 5×10^5 cells per 100 µL (5×10^6 cells/mL) and 100 µL of the cell suspension was added to the Nuclon 96-well plate (Fisher Scientific, Loughborough, UK). The cells were then stimulated with 100 µL of 1 µg/mL OVA protein as the antigen. Also, 100 µL of concanavalin A (ConA; 10 µg/mL) and 100 µL of media were added to the appropriate wells as positive and negative control, respectively. The cells were then incubated at 37 °C; 5% CO_2 and 95% humidity for 3 days. Then they were stored at -20 °C until performing cytokine ELISAs.

5.3.5.5 Cytokine ELISA

Sandwich ELISA was used to quantify IFN-γ and IL-5 in the restimulated spleens. The plate was coated with OVA antigen 50 µL/well of 2 µg/mL rat anti-mouse cytokine antibody in PBS, pH 9, and incubated at 4 ^{0}C overnight. After coating, the plates were washed 3 times with washing buffer and blocked with 200 µL/well using 10 mM PBS pH 7.4 containing 10% v/v FCS (heat-inactivated) for 1 hour at 37 ^{0}C to eliminate any non-specific binding. The plates were then washed 3 times and 30 µL of the cell supernatant added or 30 µL of IFN-γ or IL-5 standard diluted in 10 % v/v FCS in 10 mM PBS pH 7.4, followed by 2 hours incubation at RT. Then, plates, were washed three times using the washing buffer and 100 µL of rat anti-mouse biotin IFN-γ antibody was added to the wells at a concentration of 1 µg/mL diluted in 10% v/v FCS in

10 mM PBS pH 7.4. The plates were incubated for 1 hour at 37 ^{0}C 100 μL/well of HRP-streptavidin (diluted 1:4000 in 10 % v/v FCS in 10 mM PBS pH 7.4) to the wells and incubated for 1 hour as before. The plates were then washed five times in wash buffer and followed by the addition of 100 μL/well of TMB (room temperature) applied to the wells. The plates were then kept in the dark and the reaction was stopped by adding 100 μL/well of 0.2 M H_2SO_4 before reaching the endpoint.

5.3.6 Statistical Information

Data is represented as a means of separate experiments and GraphPad Prism was used to perform statistical analysis by performing ANOVA with post-hoc analysis wherever applicable. P-value < 0.05 was considered statistically significant.

5.4 Results

5.4.1 mRNA-LNP Physico-chemical Attributes

LNPs were prepared with OVA mRNA and Fluc mRNA for the vaccine and protein expression studies respectively (average molecular weights for OVA mRNA (451 kDa) and FLuc mRNA (672 kDa) are calculated based on the number of nucleotides of 1375 and 1921, respectively). However, given that the LNPs were formulated at N/P of 6, this accommodates any differences in the molecular weight of mRNA. The results in Table 5.1 show that LNPs formulated from DSPC: Cholesterol: SM-102: DMG-PEG2k molar ratio of 10:38.5:50:1.5% could effectively entrap both types of mRNA with encapsulation and recovery > 95% in LNPs which were 69 to 76 nm in z-average diameter, with a low Polydispersity Index (PDI) (<0.02) and near neutral zeta potential that was not significantly different between the two different mRNA payloads.

Table 5.1 *mRNA-LNPs physico-chemical attributes prepared with different mRNA payloads. Results are expressed as the mean ± SD, n = 3.*

LNP Physicochemical attributes		
mRNA payload	Ovalbumin (OVA)-encoding mRNA modified with 5-methoxyuridine (5moU)	EZ Cap™ Firefly Luciferase mRNA (5-moUTP)
z-average diameter (nm)	69 ± 6	76 ± 1
PDI	0.04 ± 0.03	0.04 ± 0.01
Zeta Potential (mV)	-1.6 ± 2	-4.5 ± 3
mRNA Encapsulation (%)	95 ± 2	99 ± 1
mRNA Recovery (%)	102 ± 12	106 ± 3

5.4.2 Immune responses in Female and Male Mice after mRNA-LNP Immunisation

BALB/c mice were immunised with 1, 2.5 or 5 µg of OVA mRNA LNPs as characterised in Table 5.1. Mice were dosed via intramuscular injection with a prime (day 0) and boosters (day 28). The serum was collected via tail bleeding 27 days after the first injection and two weeks after the second injection (day 42), and the antibody endpoint titres was detected by ELISA. When comparing the responses in the two different biological sexes of mice, the results in Figure 5.1a demonstrate that female mice mounted a significantly ($p<0.05$) stronger total IgG response than male mice after the primer dose across all three mRNA doses (1, 2.5 or 5 µg), which was up to 14 times higher in female than male mice when 1 µg OVA mRNA encapsulated in LNPs was administered. After a booster dose, total IgG titres increased for all mice, and again the female mice mounted significantly ($p<0.05$) higher IgG responses compared to male mice (figure 5.1b). Indeed, the female mice overall had 20, 8, and 5 times higher immune responses than male mice immunised with 1 µg, 2.5 µg or 5 µg of OVA mRNA encapsulated in LNPs, respectively (figure 5.1b). When considering IgG dose responses, a linear dose-response association is seen in male mice (R-sq≈1) but is not apparent in female mice (Figure 5.1a and 5.1b). With IgG1 (Figure 5.1c and d) and IgG2a (Figure 5.1e and f) responses, antibody titres were lower in all mice, more widely spread, and with no dose-response relationship. After the first injection, whilst generally there is a trend of higher antibody responses in female mice, significant differences were only noted after the first dose at 1 and 5 µg mRNA doses for IgG1 (Figure 5.1c and e). After the 2nd (booster) injection, IgG1 and IgG2a responses were similar in female and male mice except for a higher 5 µg mRNA dose, which stimulated significantly higher IgG2a titres in female mice (Figure 5.1d and f). Across the 3 doses, the ratio of IgG2a/1 was not significantly different between female and male mice (Figure 5.1g). Moreover, IFN- γ was stimulated very low (Figure 5.2).

5.4.3 mRNA-encoded Protein LNPs: Clearance and Expression in Female and Male Mice after Intramuscular Injection

Given female mice had stronger antibody responses compared to male mice when vaccinated with OVA-encoded mRNA-LNPs, we further investigated if these differences in response were the result of differences in mRNA protein expression profiles between the female and male mice or from different immune responses against the encoded protein.
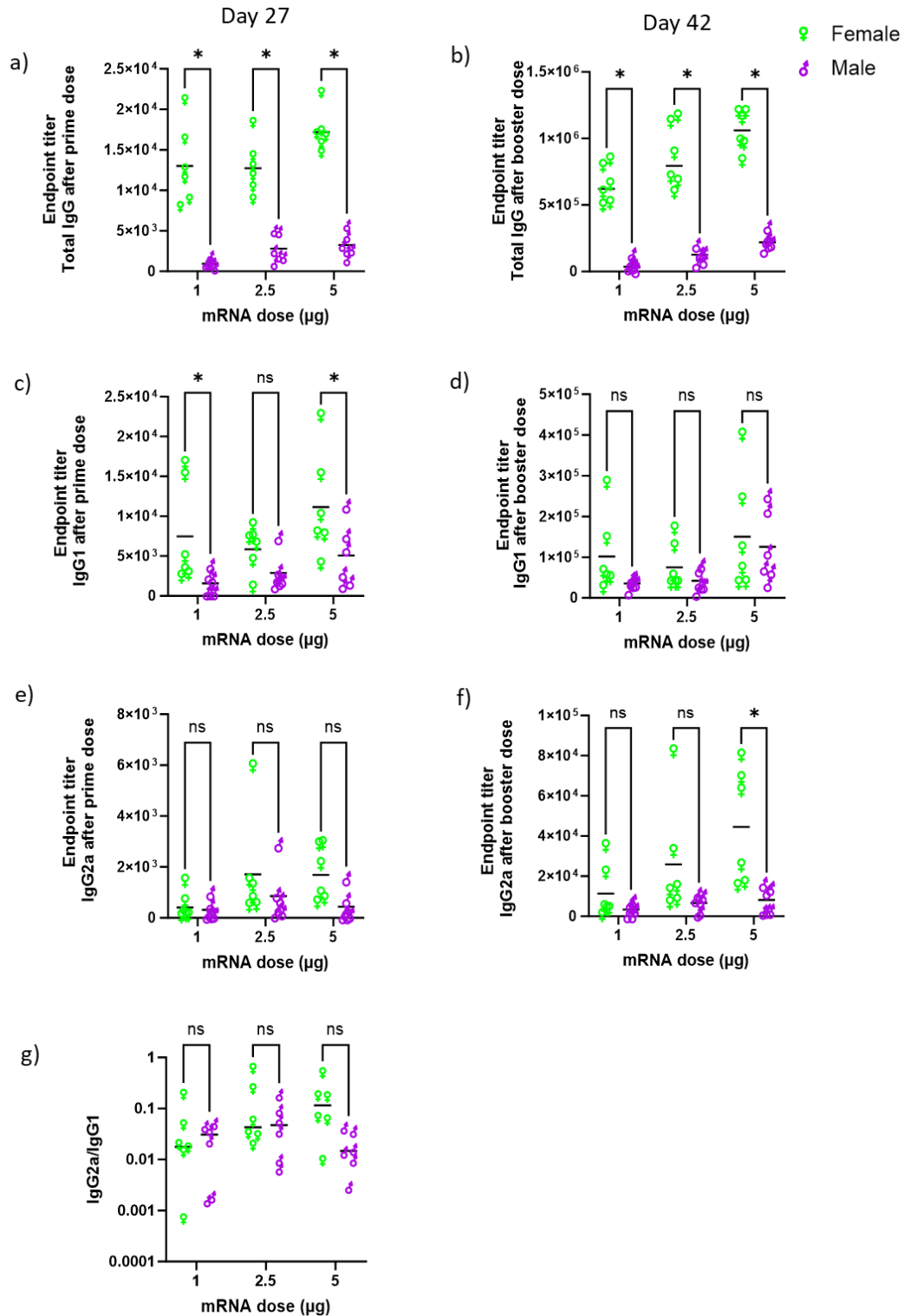
Figure 5.1 *Antibody responses in female and male BALB/c mice immunised with 1, 2.5, or 5 µg of OVA-mRNA encapsulated in LNPs on day 0 and 28. Serums were collected after the first and second doses via tail bleeding. Semi-quantitative ELISA was performed. Total anti-OVA IgG endpoint titres elicited by OVA mRNA LNPs after a) 1st and b) 2nd dose. Anti-OVA protein-directed-IgG1 after c) 1st and d) 2nd dose. Endpoint titter of IgG2a to OVA mRNA LNPs after e) prime, f) booster dose and g) show the IgG2a/1 ratio. Each point represents an individual mouse, and the black line represents the mean of each group. A total of 18 female mice and 18 male mice split over 2 independent studies) and statistical analysis done by GraphPad Prism (ns= not significant; *P< 0.05)*

To study this, BALB/c mice were intramuscularly injected with DiR labelled LNPs encapsulating 5 µg of mRNA encoding luciferase (Fluc). By using DiR-labelled mRNA-LNPs, we can track both the biodistribution of LNPs (by imaging the mice under a DIR fluorescence filter) and mRNA luciferase expression (via bioluminescence imaging)[119].
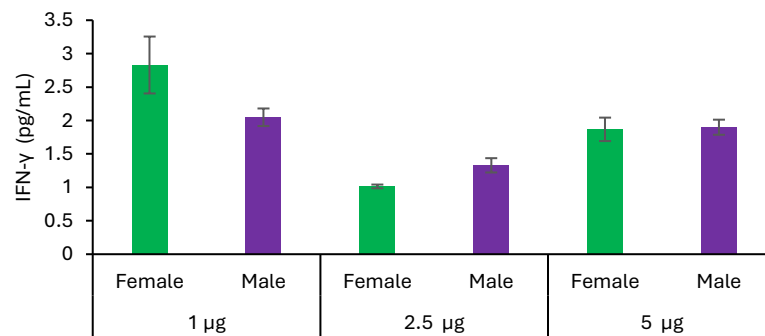
Figure 5.2 *IFN- γ level of female and male BALB/c mice immunised with 1, 2.5 and 5 ug of OVA mRNA-LNPs. Sandwich ELISA was performed.*

Figure 5.3 shows the fluorescence intensity profiles for both the male and female mice over the 196 h of the study, with Figure 5.3a representative IVIS images at 6, 24 and 48 h. Figure 5.3b shows the distribution profile and Figure 5.3c shows the Area Under the Curve (AUC). The results show that both males and females have similar clearance rates of the DiR-labelled LNPs from the intramuscular injection site, with peak fluorescence intensity (Cmax) being measured 6 h after mRNA-LNP injection gradually (Figure 5.3b) with no significant difference in the AUC between female and male mice (Figure 5.3c).

In line with the distribution data, luciferase expression was primarily focused on the injection site and was not significantly different between female and male mice (Figure 5.4) with peak luciferase expression measured at the 6 h timepoint (Figure 5.4a and b). Luciferase expression was also detected in the liver (Figures 5.4a and c). The results presented in Figure 5.4c indicated that at 6 h there are significantly ($p < 0.05$) higher luciferase expression levels in the liver in female mice. However, at all other time points, no statistically significant difference is observed between the expression levels in the female and male mice. These results confirmed that the difference in immune responses between female and male mice is not due to differences in mRNA-protein expression or LNP distribution after intramuscular injection and is a result of differences between female and male mice to generate immune responses to mRNA-encoded antigens.
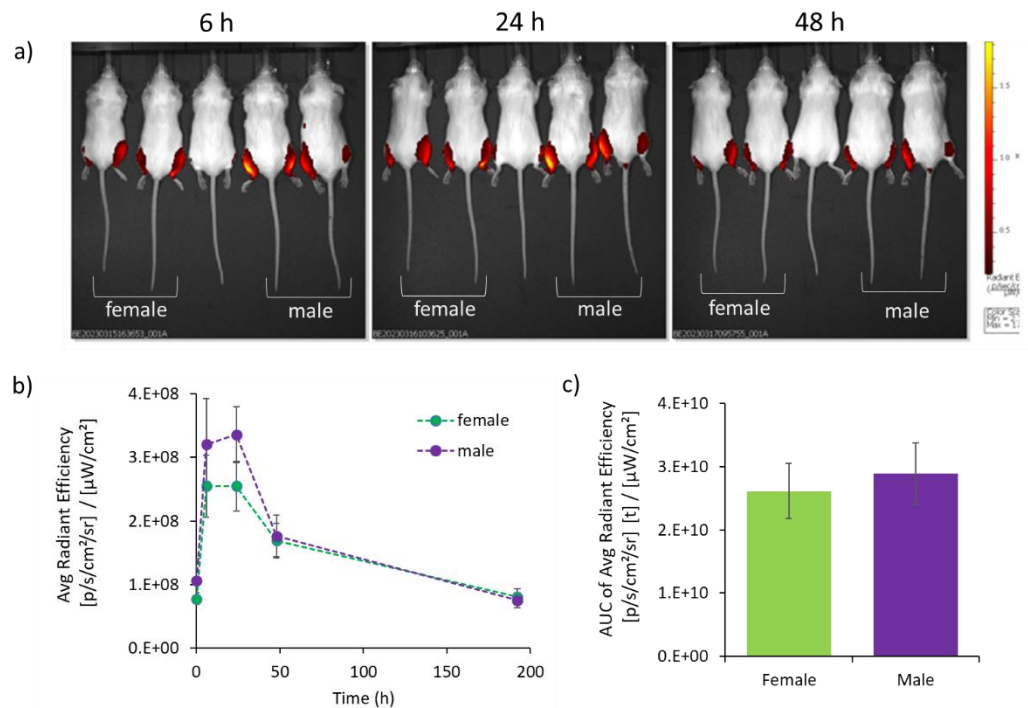
Figure 5.3 *mRNA-LNP fluorescence intensity after intramuscular injection in female and male mice. The injected mRNA dose was 5 µg mRNA encapsulated in LNPs. a) Representative IVIS images at selected time points after DiR labelled mRNA-LNP injection (left 2 mice are female; right 2 mice are male; middle mouse is not injected). b) Fluorescence signal at the injection site over 196 h and c) the Area Under the Curve (AUC). Data is expressed mean ± SEM (a total of 18 female mice and 18 male mice split over 2 independent studies).*
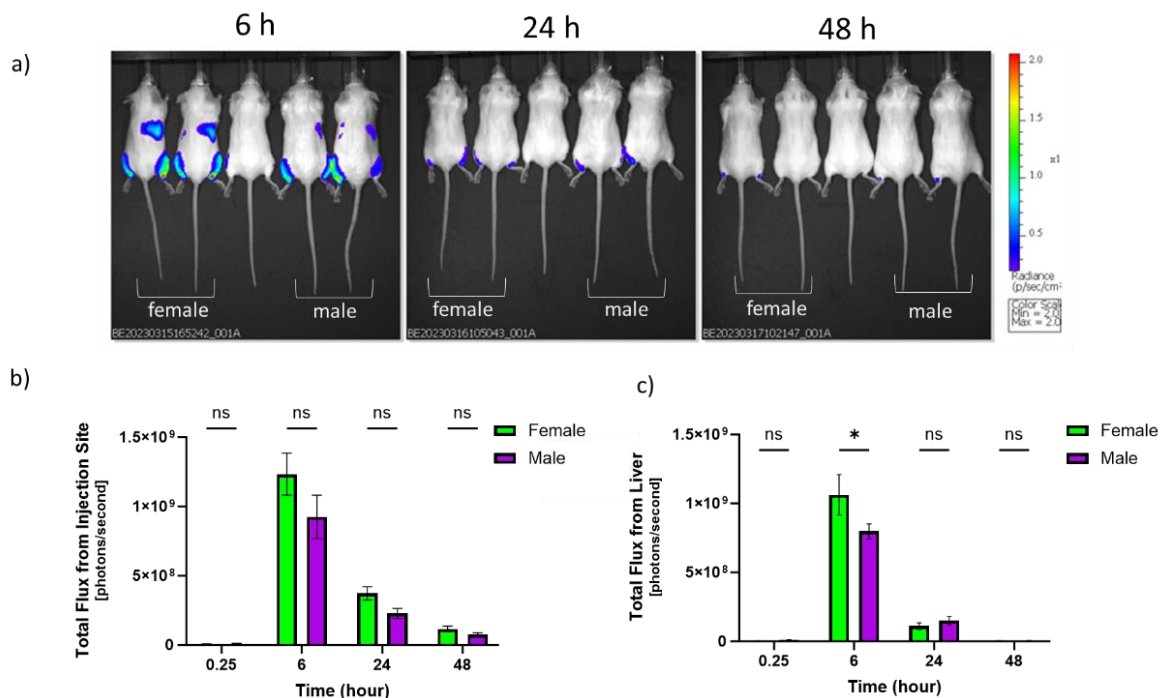
Figure 5.4 *Luciferase expression after Fluc-mRNA LNP intramuscular injection in female and male BALB/c mice. The injected mRNA dose was 5 µg mRNA encapsulated in LNPs. a) Representative bioluminescence IVIS images at selected time points after mRNA-LNP injection. b) Bioluminescence signal at the injection site at 0.25, 6, 24 and 48 h and c) Bioluminescence signal at the liver at 0.25, 6, 24 and 48 h. Data is expressed by mean ± SEM (a total of 18 female mice and 18 male mice split over 2 independent studies) and statistical analysis done by GraphPad Prism (ns= not significant; *P< 0.05).*

5.5 Discussion

In our research, we have confirmed that following intramuscular injection in BALB/c mice, females demonstrate significantly ($p < 0.05$) higher IgG immune responses against the mRNA-encoded antigen (OVA) compared to their male counterparts across the three doses tested (Figure 5.1). Additionally, we observed comparable mRNA-LNP clearance from the injection site (Figure 5.3) and protein (luciferase) expression at the injection site for both female and male mice, but females did exhibit higher luciferase expression within the liver (Figure 5.4). However, it is important to recognise that the inherent properties and functions of the expressed protein (OVA and Fluc) could potentially influence various aspects of antigen trafficking, processing, and subsequent immune responses. A study investigating expression kinetics and immunogenicity of mRNA-LNPs considered the correlation between luciferase expression and anti-luciferase responses using a range of LNP formulations, including SM-102 LNPs, like the formulation used in our study. The authors note that LNPs that induced the highest total luciferase expression induced significant anti-luciferase serum antibody titres when compared to empty particles [84]. However, they also acknowledge that luciferase is reported to be a relatively weak immunogen, and it may not reflect the efficacy of other vaccine antigens [180]. Nonetheless, these disparities highlight the intricate interplay between biological sex and immune responses, emphasising the importance of considering these factors when designing pre-clinical mRNA-LNP vaccine studies.

The effectiveness of mRNA encoding therapeutic proteins and vaccines is influenced by factors such as the administration route and the location, duration, and magnitude of protein production. Depending on the injection site, localised protein, and disseminated expression in the liver can occur [60]. Moreover, following intramuscular administration, the depth of the injection can determine differential expression levels at the muscle versus the liver. Deep intramuscular injections of mRNA-LNPs lead to strong protein production in the liver, compared to superficial injections which predominately yield protein in the muscle [60]. Whilst we did not see discernible differences in protein expression levels in the muscle between female and male mice, variations in muscle density could potentially contribute to differences in luciferase expression measured in the liver (Figure 5.4). The mRNA-LNP luciferase location within the mouse tissue/body will also impact on the strength of the fluorescent and luminescent signals. Indeed, detecting the fluorescence intensity in internal

organs with IVIS is challenging without organ extractions due to the limited penetration depth in tissue, explaining why we detect mRNA-LNPs at the injection site and not at the liver (Figure 5.3).

When evaluating vaccine efficacy, numerous studies, including those in murine and human models, have previously highlighted the influence of biological sex on immunological responses [166,181], as we report in Figure 5.1. For instance, Breznik et al., explored the impact of biological sex and the female reproductive cycle on circulating leukocyte levels in C57BL/6J mice. Their investigation revealed that while biological sex significantly shapes the prevalence and variability of immune cells in peripheral blood, there is no substantial effect associated with the female reproductive cycle [182]. Another study showed that women elicited a greater immune response to inactivated influenza vaccination in women of all ages, regardless of dose or influenza strain, and women had an equivalent antibody response with half the dose of influenza vaccine compared to men[183]. Sex differences in immune responses to respiratory viruses have also been observed in both humans and experimental rodent models [184]. The influence of sex hormones on these responses may involve direct actions on innate immune cells or indirect modulation by other immune or non-immune cells responding to sex hormones [184]. The influence of hormones, specifically testosterone and oestrogens, has been shown to play a role in modulating immunological responses, leading to variations in adaptive immunity, T-lymphocyte function, and helper-inducer cell activity [185,186]. It has also been observed that male hormones promote a tendency towards cell-mediated immune responses, while female hormones tend to promote humoral immunity[187]. Within our studies, we tested IgG1 and IgG2a subclasses in addition to IgG (Figure 5.1), and both female and male mice had higher IgG1 than IgG2a titres, indicating a stronger T helper type 2 (Th2) immune response was activated upon OVA mRNA LNPs vaccination. This is perhaps not surprising as BALB/c mice have been reported to be biased towards Th2 immune responses [188]. Moreover, IFN-gamma, which is commonly associated with Th1 responses, was not stimulated (Figure 5.2); this absence further supports the observation that the mice tend to exhibit a Th2 response.

After intramuscular injection mRNA-LNPs can be taken up by tissue-resident dendritic cells and macrophages, eliciting a local immune response at the injection site [189]. Once taken up, mRNA needs to be released from both the endosome and their LNP carrier into the

cytosol. Once in the cytosol, the mRNA is translated into the corresponding antigenic protein in the ribosome. Subsequently, this antigen undergoes degradation in the cytosolic proteasomes, revealing antigenic epitopes that form complexes with MHC class I. These activated dendritic cells present the antigen to T cells, which become activated and differentiate into cytotoxic T cells or helper T cells [190]. Myocyte transfection by mRNA vaccines can also activate bone marrow-derived dendritic cells (DCs), contributing to T cell priming [191]. Based on this mechanism, this supports our finding that there is no major biological difference in the expression profiles for mRNA-encoded protein, rather the differences become apparent during the down-stream processing of the antigen to create the immune responses.

Within research, there is a growing acceptance for the need for males and females to be equally represented in research. This includes pre-clinical research. Indeed, using both sexes, in this context defined by a set of biological attributes, when designing research experiments is now the default for many grant funders and this is long overdue. Previously, using male models in research was a default approach, and male animals were used six times more often than females[192]. However, anecdotally, female mice are often used in pre-clinical vaccine studies due to lower levels of aggression towards each other and thus are easier to be socially housed in stable groups with compatible cage mates in line with the National Centre for the Replacement, Refinement, and Reduction of Animals in Research (NC3R) guidance. Through our investigations, we show that the biological sex of mice does not impact on mRNA-LNP protein expression at the injection site but does impact on mRNA-LNP vaccine immune responses, and thus in designing studies, this is an important factor. Nonetheless, it is crucial to consider the specific research question and the contextual nuances of the study when designing pre-clinical investigations. Whilst, using a mix of male and female subjects to test vaccine safety and efficacy is key, consideration of data handling is also important. For instance, when evaluating the impact of formulation on vaccine efficacy, averaging responses from a mix of male and female mice may lead to a broad data spread, as highlighted in Figure 5.5; when the IgG responses are pooled, higher variation in the data is noted (Fig 5.5a). In contrast, in Fig 5.5b and c, where no significant differences between males and females were observed, the variability is low. Thus, the pooling of data from both sexes might obscure important distinctions in responses to formulations. Equally, designing studies with

appropriate mouse numbers and study replicates using both male and female mice may result in higher animal usage than needed to address the research question, particularly when considering the limitations of the mouse model in vaccine studies generally. In such instances, it is important to report the sex and age of the animals used in preclinical experiments.
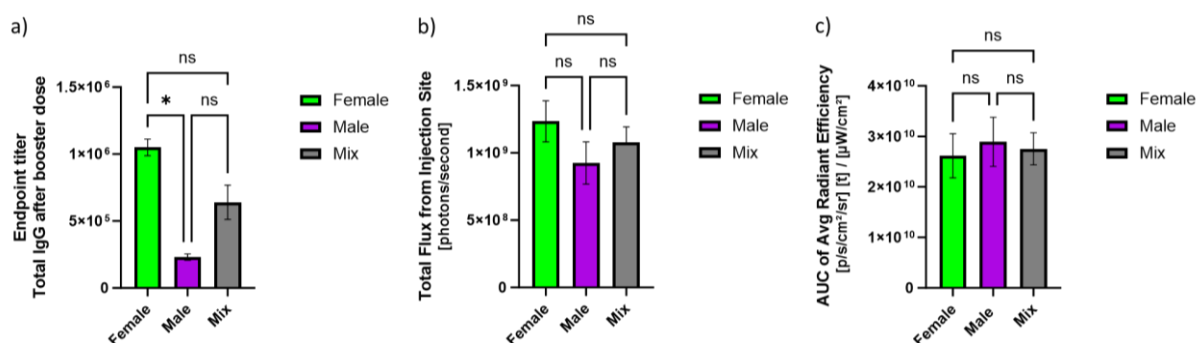
Figure 5.5 *Comparison of responses from female mice, male mice, and the average across all mice for a) IgG responses, b) luciferase expression and c) AUC. Mice were intramuscularly injected with 5 µg mRNA encapsulated in LNPs with mRNA encoded with either OVA ((a) vaccine study) or Fluc ((b) expression studies) and labelled with DiR for c) investigating clearance. Data is expressed mean ± SEM (a total of 18 female mice and 18 male mice split over 2 independent studies) and statistical analysis done by GraphPad Prism (ns= not significant; *P< 0.05).*

5.6 Conclusions

When testing mRNA-LNP vaccine (OVA) responses, female BALB/c mice showed a stronger immune response than male mice, whilst mRNA-LNP protein (luciferase) expression was not notably different. Given these immune response differences, consideration should be given to this in experimental study plans, and averaging across different biological sexes should be discouraged. In all studies, the sex and age of the animals used in preclinical experiments should be reported.

Overall, the difference in immune responses between females and males has been widely debated in the literature. However, since mRNA-LNP vaccines have only recently been approved, this topic has not yet been a focus of research. This study is the first to reveal differences in mRNA-LNP expression profiles between the biological sexes. In conclusion, it showed females had higher immune responses than males even if they expressed the mRNA at a similar level.

Chapter 6: Investigating avidin-biotin interactions as a potential for targeting LNPs
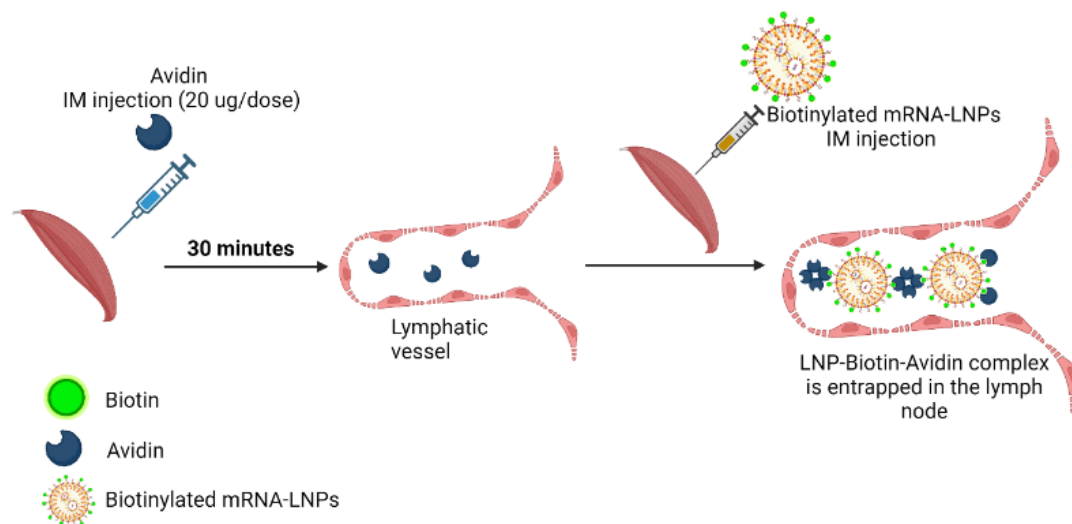
Introduction

At the beginning of the thesis, it is mentioned that encapsulating mRNA into the LNPs improves the transfection efficiency of mRNA; however, this improvement is accomplished once mRNA-LNPs reach the target cells/tissues. Also, the accumulation of LNPs in the target area does not necessarily ensure efficient cellular uptake, intracellular trafficking, endosomal escape, and translation efficiency [193]. However, the first step is to ensure that mRNA-LNPs reach the target area. Targeting the specific cells or tissues improves the efficiency and specificity of mRNA-LNP systems. It was shown, especially in Chapter 2, that LNPs injected via the IM route had an off-target effect on the liver in various ratios depending on the choice of the ionisable lipid used in the formulation. Extrahepatic delivery of LNPs remains challenging due to the inherent tropism of LNPs to the liver [194]. However, the targeting area depends on the therapeutic applications. For example, the liver is a critical target for gene silencing and regulation [7], while targeting the lymph node or antigen-presenting cells (APCs) may be a desired target for vaccination purposes [195]. Specific targeting of mRNA-LNPs can also improve their safety profile by reducing the off-target effect and minimising the dose required. For example, targeting APCs increases the magnitude of antigen synthesised by the cells and can potentially reduce the proportion of non-APCs transfected, and this may mitigate local side effects such as swelling [196].

Particle size and charge may play a role in the accumulation of LNPs in the different organs. Coating the LNP surface with phosphatidylserine was used for targeting the lymph nodes [193]. Using supplementary excipients in addition to the usual LNP composition (Helper: structural: ionisable: PEG lipid) can manipulate the biodistribution of LNPs and promote selective organ targeting [58,197]. The expression profile of LNPs in various tissues may also be based on the ionisation and structural properties of LNPs [85].

To consider targeting LNPs to enhance the potency of mRNA-LNP vaccines, the strong interaction between avidin and biotin. This approach has been implemented for liposomes investigated by considering the application of pre-dosing of avidin followed by injecting biotinylated mRNA-LNPs [50,51]. The principle behind this is that pre-dosed avidin drains to the lymph node as it is a small molecule. Then, subsequent injection of biotin-coated particles will drain to the lymph node. When both encounter in the lymph node, they will form a complex, leading to trapping them in the lymph nodes and thus potentially improving immune

responses (Figure 6.1a). Due to the intramuscular injection route, the popliteal and inguinal lymph nodes were targeted (Figure 6.1B).
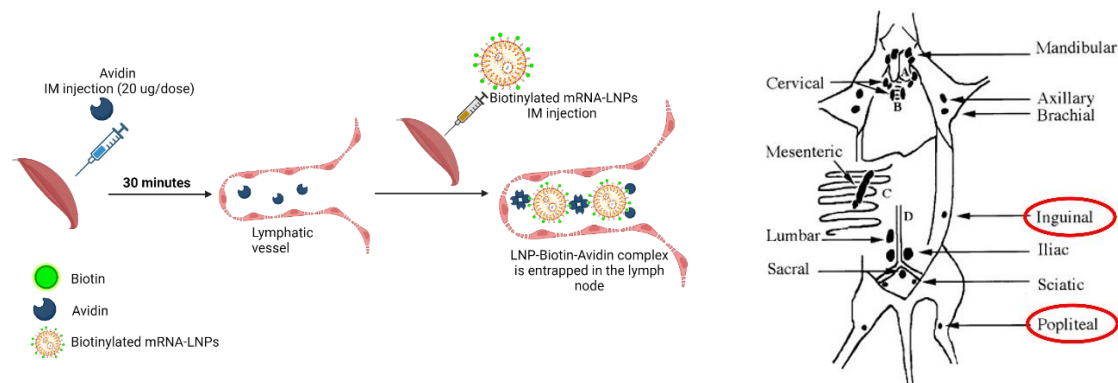
Figure 6.1 a) The rationale behind targeting the lymph node using Biotinylated LPs with pre-avidin injection. Created with Biorender and b) The Lymph nodes of the mice [198] and the lymph nodes focused on were shown with red circles.

6.1 Aim and Objectives

In this chapter, the aim was to develop LNPs that would target local lymph nodes after IM injection by using a combination of pre-dosing with avidin and biotinylated LNPs. To achieve this, the objectives were:

- Testing the effect of adding biotin (DMG-PEG2k-biotin) gradually from 0% to 1.5% on the particle size, PDI, zeta potential, EE, and recovery.

- Testing these samples on HEK-293 cells to evaluate whether biotin content impacts the particles' *in vitro* transfection efficiency and select the lead formulation.

- Evaluating lead biotinylated LNP formulation *in vivo* and comparing it to non-targeted LNPs.

6.2 Material and Method

6.2.1 Materials

1,2-distearoyl-sn-glycero-3-phosphocholine (DSPC), 1,2-dimyristoyl-rac-glycero-3-methoxypolyethylene glycol-2000 (DMG-PEG2000), Sodium citrate dihydrate, citric acid, Amicon® 100 kDa Ultra 15 mL Centrifugal Filters, Cholesterol were purchased from Merck (Gillingham, UK). DMG-PEG2k-biotin was gained from Nanocs (Macclesfield, UK). 8-[(2-hydroxyethyl)[6-oxo-6-(undecyloxy)hexyl]amino]-octanoic acid, 1-octylnonyl ester (SM-102) was purchased from ABP Biosciences (Maryland, USA). EZ Cap™ Firefly Luciferase mRNA (5-

moUTP) is procured from APExBIO Technology (Stratech Scientific Ltd, Cambridge, UK). Minimum Essential Medium (MEM), Sodium Pyruvate (100 mM), UltraPure™ DNase/RNase-Free Distilled Water were purchased from GibcoTM (Paisley, UK). ONE-Glo™ Luciferase Assay System and VivoGlo luciferin were purchased from Promega (Southampton, UK). DiIC18(7) (1,1'-Dioctadecyl-3,3,3',3'-Tetramethylindotricarbocyanine Iodide (DIR), Quant-it™ RiboGreen RNA Assay Kit, TrypLE™ Express Enzyme (1X) were bought from ThermoFisher Scientific (Paisley, UK). BD Medical™ BD Micro-Fine™ Insulin Syringe was bought from Fisher Scientific (Loughborough, UK).

6.2.2 LNPs Preparation

LNPs were composed of DSPC: Chol:SM-102: DMG-PEG2k (10:38.5:50:1.5 mol%) and encapsulating Fluc mRNA at NP6. Biotinylated LNPs were prepared using DMG-PEG2k-biotin. It is dissolved in the ethanol and added the required amount, and the total PEG ratio was kept at 1.5% of DMG-PEG2k and DMG-PEG2k-biotin. Only one pilot study was carried out using 4% PEG-biotin. In the text, plain LNPs refer to unbiotinylated LNPs. For *in vivo* studies, LNPs were labelled with DiR, including in the lipid phase.

6.2.3 Down-stream Processing of LNPs and Characterisations

The samples were diluted 40x in 10 mM PBS pH7.4 and centrifuged (2,000x g acceleration:9 deceleration:9) at 4 °C with a centrifugal filter unit (MWCO 100 kDa) to remove ethanol and to raise pH to 7.4). LNPs were concentrated to the required concentration.

After purification, the physicochemical properties of LNPs were characterised using Zetasizer Ultra (Malvern Panalytical Ltd, Worcestershire, UK). Briefly, samples were diluted with 10 mM PBS pH 7.4 to 0.1 mg/mL of lipid concentration to measure particle size and PDI. Then, zeta potential was measured with the samples diluted to 0.1 mg/ml of lipid stock with ultrapure water. EE and recovery were evaluated using Ribogreen kit. Briefly, diluted samples (3 ug/mL) were added to the black plate in the absence and presence of Triton, referring to the unencapsulated and total mRNA, respectively. EE and recovery were calculated according to equations 1.2 and 1.3.

6.2.4 In vitro mRNA expression studies

LNPs serial diluted (2, 1, 0.5 and 0.25 µg/mL with cell media) were added to the plate with a 10000 cells per well density. 24-hour incubation at 37 ^{0}C, 100 µL of One-glo luciferin reagent

was added to each well, and the luminescence was measured using a plate reader (Glomax®, Promega).

6.2.5 *In vivo* LNP Retention at the injection site and mRNA expression

Female BALB/c mice (8-12 weeks old) were injected with 5 µg of DiR labelled mRNA-LNPs per leg. They were imaged with a DiR filter (excitation peak at 710 nm and an emission peak at 780 nm) using IVIS Spectrum (Pekin Elmer) under anaesthesia. Later on (depends on the time point, see Figure 6.4), the mice were imaged again under the DiR filter and injected with luciferin (at a dose rate of 150 mg/kg) via the SC route. 10-minutes later, they were imaged with an open filter to gain luminescence intensity. Mice were terminated using the Schedule 1 method, and the organs were discarded and placed in a petri dish. Luminescence and DiR intensity were measured again (the time between luciferin injection and measuring the bioluminescence intensity from the discarded organs were tried to keep accurate between mice, and it was around 20 minutes). The data were analysed using Living Imaging Software to quantify the DiR and bioluminescence intensity.

6.2.6 Statistical analysis

Data is represented as a means of separate experiments and GraphPad Prism was used to perform statistical analysis by performing ANOVA with post-hoc analysis wherever applicable. P-value < 0.05 was considered statistically significant.

6.3 RESULTS

6.3.1 Evaluating the addition of PEG2k-biotin on the particle size and *in vitro* expression profile

Fluc mRNA-LNPs were prepared with various ratios of DMG-PEG2k/DMG-PEG2k-biotin to a total molar lipid content of 1.5 % (DSPC 10%: Cholesterol 38.5.%: SM-102 50%: DMG-PEG2k / DMG-PEG2k-biotin 1.5% mol). Increasing the PEG2k-biotin content from 0 to 1.5% mol (corresponding decrease in PEG2k molarity) increased the particle size gradually from 60 nm to 140 nm whilst all particles had monodispersed size distribution (PDI<0.2) and neutral zeta potential (Figure 6.2). EE and recovery of mRNA were high, above 90% and around 70%, respectively, for all formulations (Figure 6.2).

EE (%)	97 ± 1	96 ± 0	96 ± 1	96 ± 1	93 ± 0
Recovery (%)	73 ± 15	76 ± 15	72 ± 13	73 ± 20	68 ± 7
Zeta Potential (mV)	-0.3 ± 1.0	-4.6 ± 3.2	-0.1 ± 0.5	-2.2 ± 3.0	-1.8 ± 4.7
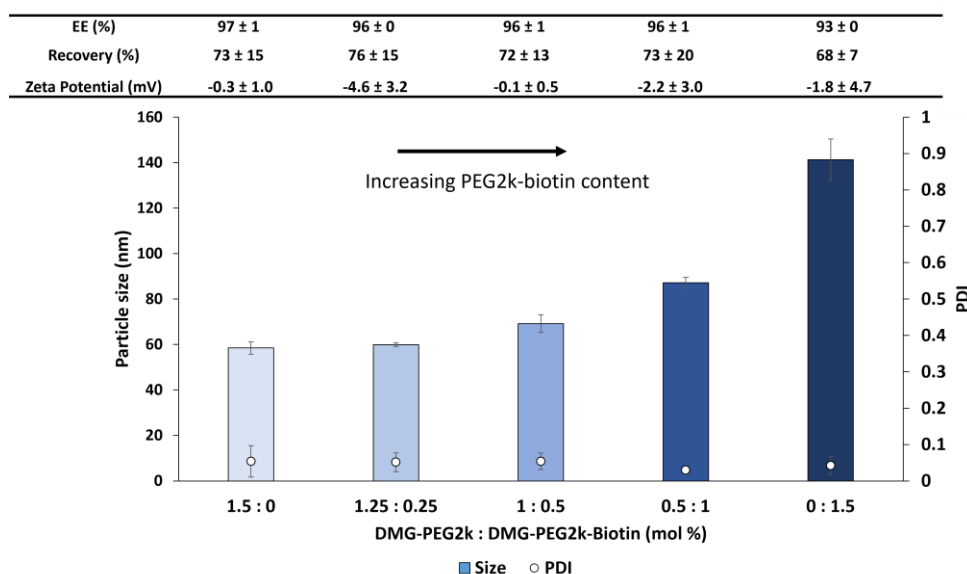
Figure 6.2 *The physicochemical properties of the LNPs prepared with different proportions of the DMG-PEG2k and DMG-PEG2k-biotin. LNPs were composed of DSPC: Cholesterol: SM-102: DMG-PEG2k/DMG-PEG2k-biotin at the molar ratio of 10:38.5:50:1.5%. Results represent mean ± SD, n = 2 independent batch*

These formulations were tested using the HEK-293 cell line to examine the effect of the biotin quantity on the *in vitro* mRNA expression profile (Figure 6.3). The results in Figure 6.3 show no clear biotin concentration-dependent expression. The substitution of DMG-PEG2k with DMG-PEG2k-biotin at the molar ratio of 0.25 % mol made no significant difference in expression across all concentrations tested (Figure 6.3). Increasing the molar % of DMG-PEK2k-biotin to 0.5% significantly (p<0.05) increased luciferase expression at higher mRNA concentrations (200 and 100 ng) (Figure 6.3). However, further increases in the biotin content resulted in reduced expression levels similar to or below the usual LNP formulation (only with DMG-PEG2k) (Figure 6.3). Thus, overall, combining DMG-PEG2k and DMG-PEG2k-biotin with the molar ratio of 1:0.5 % had the highest expression on HEK-293 cells, and from these results, LNP prepared with DMG-PEG2k: DMG-PEG2k-biotin (1:0.5 % mol) was selected as the lead formulation for the in vivo study.

6.3.2 *In vivo* Expression Profile of Biotinylated LNPs in the injection site and the lymph node.

Given the highest *in vitro* expression profile with DMG-PEG2k: DMG-PEG2k-biotin (1:0.5 % mol), an *in vivo* pilot study was performed with this formulation compared to the plain LNPs (1.5 mol % of PEG2k). The injection scheme is shown in Figure 6.4.
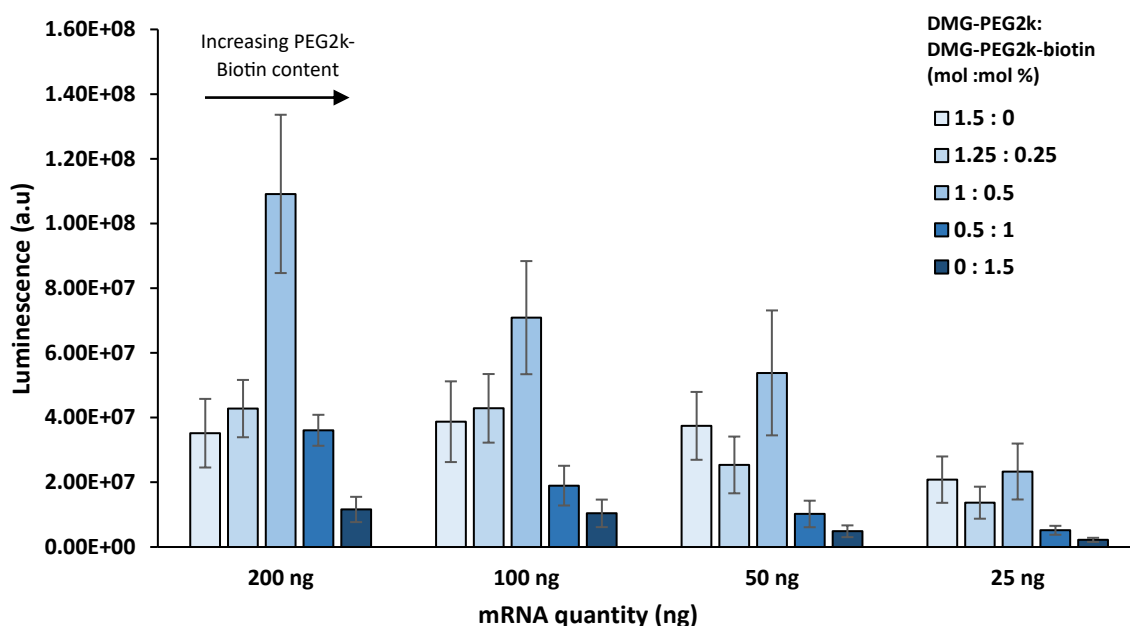
Figure 6.3 *In vitro mRNA transfection efficiency of LNPs (shown in figure 3) prepared various contents of DMG-PEG2k and DMG-PEG2k-biotin on HEK-293 cells. The samples were incubated with HEK-293 cells for 24 h at 37 ^{0}C, and the luminescence intensity was measured. LNPs were composed of DSPC: Cholesterol: SM-102: DMG-PEG2k/DMG-PEG2k-biotin at the molar ratio of 10:38.5:50:1.5%. Results represent mean ± SD, n = 2 independent batch.*

The accumulation profile of the biotinylated LNPs in the lymph node was tested by imaging mice and extracted lymph nodes at different time points. Three mice received a dose of avidin (20 μg per dose) via the IM route; 30 minutes later, all mice were injected with the LNP formulations specified in Figure 6.4. 1 h later, IM injection of LNPs, the mice injected with avidin and Biotinylated LNPs were imaged to measure DiR and luminescence intensity on the injection site and the discarded lymph nodes. The same procedure was carried out at 2.5 h for the mice injected with avidin and LNPs-biotin. 6 h later, the remaining mice were imaged with the same procedure. The physicochemical properties of DiR-labelled LNPs used in this *in vivo* pilot study are shown in Table 6.1. All parameters were very similar, with an average diameter of 60 nm of the size and monodispersed particle size distribution and neutral surface charge. EE and recovery were approximately 98 % and 82% on average for both formulations.

Biotinylated LNPs (with pre-dose of avidin) had a comparable expression in the injection site irrespective of the time points, with only a slight increment at 2.5 h (blue column in Figure 6.5a). Also, the mice not injected with avidin showed similar expressions for plain or biotinylated LNPs (blue column in Figure 6.5a).
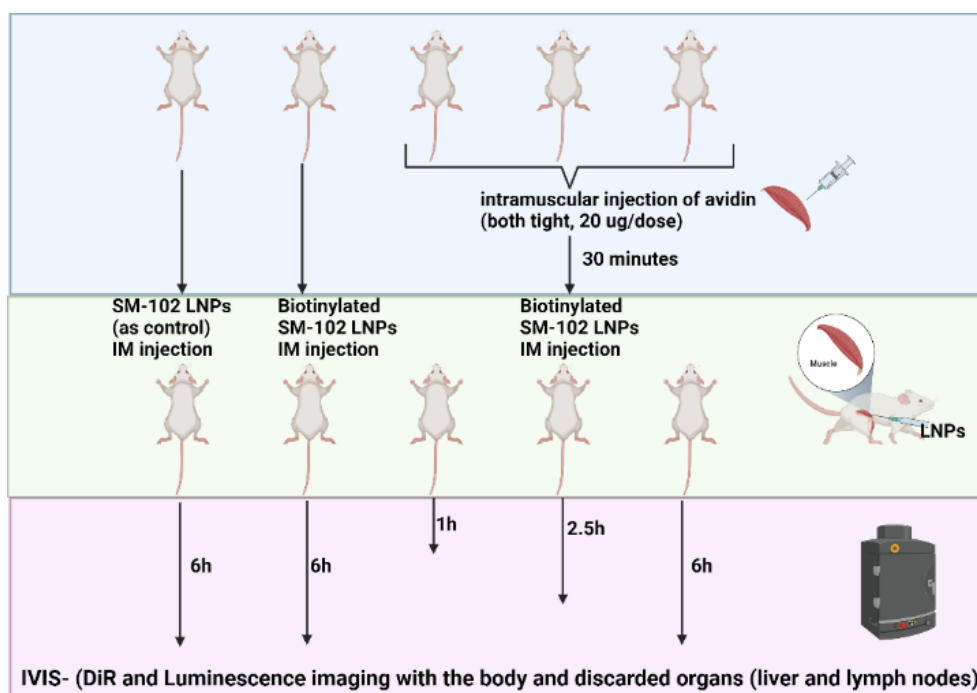
Figure 6.4 *Outline of the in vivo pilot study testing the effect of the biotin and avidin injection on the in vivo expression profile of BALB/c mice (The image created by Biorender)*

Overall, the *in vivo* expression had a very similar profile among LNPs irrespective of the time points in the injection site (p>0.05). However, the IM injection of avidin increased the expression gradually in the liver for the biotinylated LNPs over time (Figure 6.5a). Overall, avidin injection increased the expression in the liver threefold. The biodistribution of all LNPs was very similar among mice, with similar levels at the injection sites (Figure 6.5b). Discarded lymph nodes were imaged for luminescence intensity. Overall, injection of avidin decreased the expression in the lymph node fourfold, irrespective of avidin injection (Figure 6.5c), and there was a comparable expression between plain and biotinylated LNPs (without avidin injection) (Figure 6.5c).

Table 6.1 *Physicochemical characterisation of the DiR labelled LNPs used in the pilot IVIS study. LNPs were composed of DSPC: Cholesterol: SM-102 (10:38.5:50 % mol) and with the molar ratio of DMG-PEG2k/DMG-PEG2k-biotin shown in the table. Results represent mean ± SD, n = 1 batch.*

DMG-PEG2k : DMG-PEG2k-biotin (mol : mol %)	Diameter (nm)	PDI	Zeta Potential (mV)	EE (%)	Recovery (%)
1.5:0	58.8 ± 0.5	0.07 ± 0.01	0.3 ± 0.0	99	87
1:0.5	63.1 ± 0.5	0.07 ± 0.01	4.2 ± 1.2	98	78
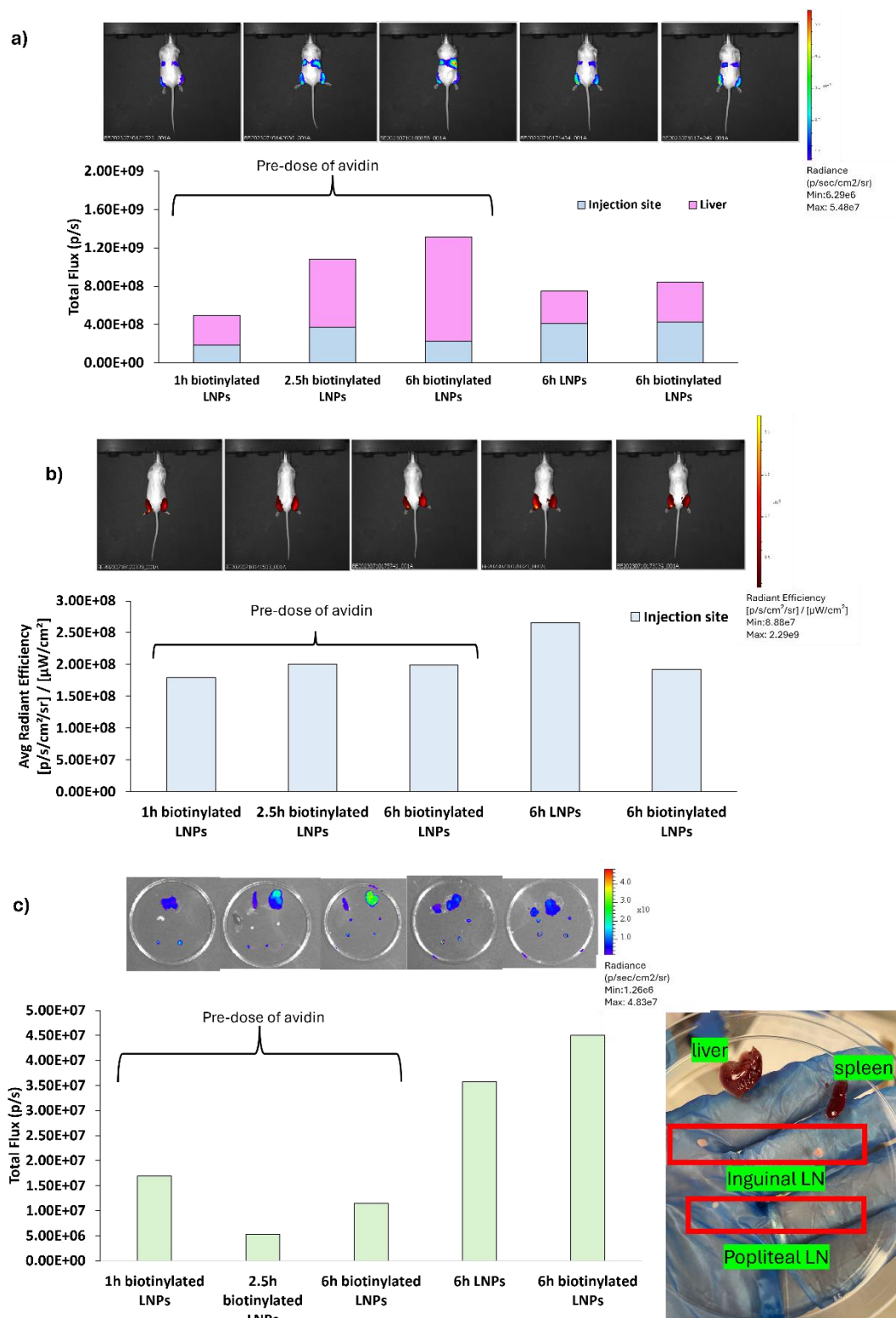
Figure 6.5 The expression and biodistribution profile of the LNPs according to the pilot study scheme shown in Figure 4. a) representative IVIS images for bioluminescence imaging and corresponding quantification signal from per the injection site and liver, b) representative IVIS images for DiR fluorescence imaging and corresponding the signal quantified from the per injection site, c) Representative IVIS images of the luminescence imaging of lymph nodes discarded from BALB/c mice injected with DiR-labelled mRNA-LNPs are characterised in Table 1. The quantification of the bioluminescence signal from the popliteal lymph node was presented in the graph. Results

represent mean, n = 1 independent batch. 1 mouse, 1 injection per hind leg; 2 data points. Each bar represents each mouse.

6.3.3 Testing the quantity of DMG-PEG2k-biotin content in vivo

After this pilot study, a dose escalation study was undertaken in a second pilot study. The PEG2k-biotin molarity was increased to 4% and tested against PEG2k-PEK2k-biotin (1:0.5%). The characterisation results are shown in Table 6.2. Increasing the PEG2k-biotin molarity increased the particle size (from 72 to 120 nm) but did not affect the PDI, zeta potential EE, or recovery efficiency (Table 6.2).

Table 6.2 Physicochemical characterisation of the DiR labelled LNPs used in the pilot IVIS study to test the biotin quantity. LNPs were composed of DSPC: Cholesterol: SM-102 (10:38.5:50 % mol) and with the molar ratio of DMG-PEG2k/DMG-PEG2k-biotin shown in the table. Results represent mean ± SD, n = 1 batch.

DMG-PEG2k : DMG-PEG2k-biotin (mol%)	Diameter (nm)	PDI	Zeta Potential (mV)	EE (%)	Recovery (%)
1:0.5	72 ± 0.4	0.03 ± 0.02	-2.5 ± 1.1	98	62
0:4	120 ± 1.8	0.03 ± 0.03	-1.2 ± 0.6	96	104

In vivo, increasing biotin content from 0.5% to 4% decreased the expression at the injection site and liver to near background levels, with expression at the injection site reducing 3-fold (blue column in Figure 6.6a). The expression in the liver (pink column in Figure 6.6a) was proportional to the expression in the injection site. 0.5% PEG-biotin LNPs showed higher DiR intensity than 4% PEG-biotin in the injection site (Figure 6.6b). The expression in the lymph node was decreased dramatically (over five-fold) by increasing biotin content (Figure 6.6c).

6.1 Discussion

This study investigated the strong non-covalent interaction between biotin and avidin as a targeting strategy. To achieve this, mRNA-LNPs were coated with biotin using DMG-PEG2k-biotin while avidin was administered intramuscularly 30 minutes before LNP injection. Avidin was injected before LNPs, as it has been shown this was a more efficient way to accumulate the particles than injecting LNPs before avidin [215].

Initially, the effect of DMG-PEG2k-biotin quantity on the physicochemical properties of LNPs was tested (Figure 6.2). Particle size increased gradually with the addition of biotin while keeping the particles neutral and mono-dispersed size distribution (Figure 6.2).
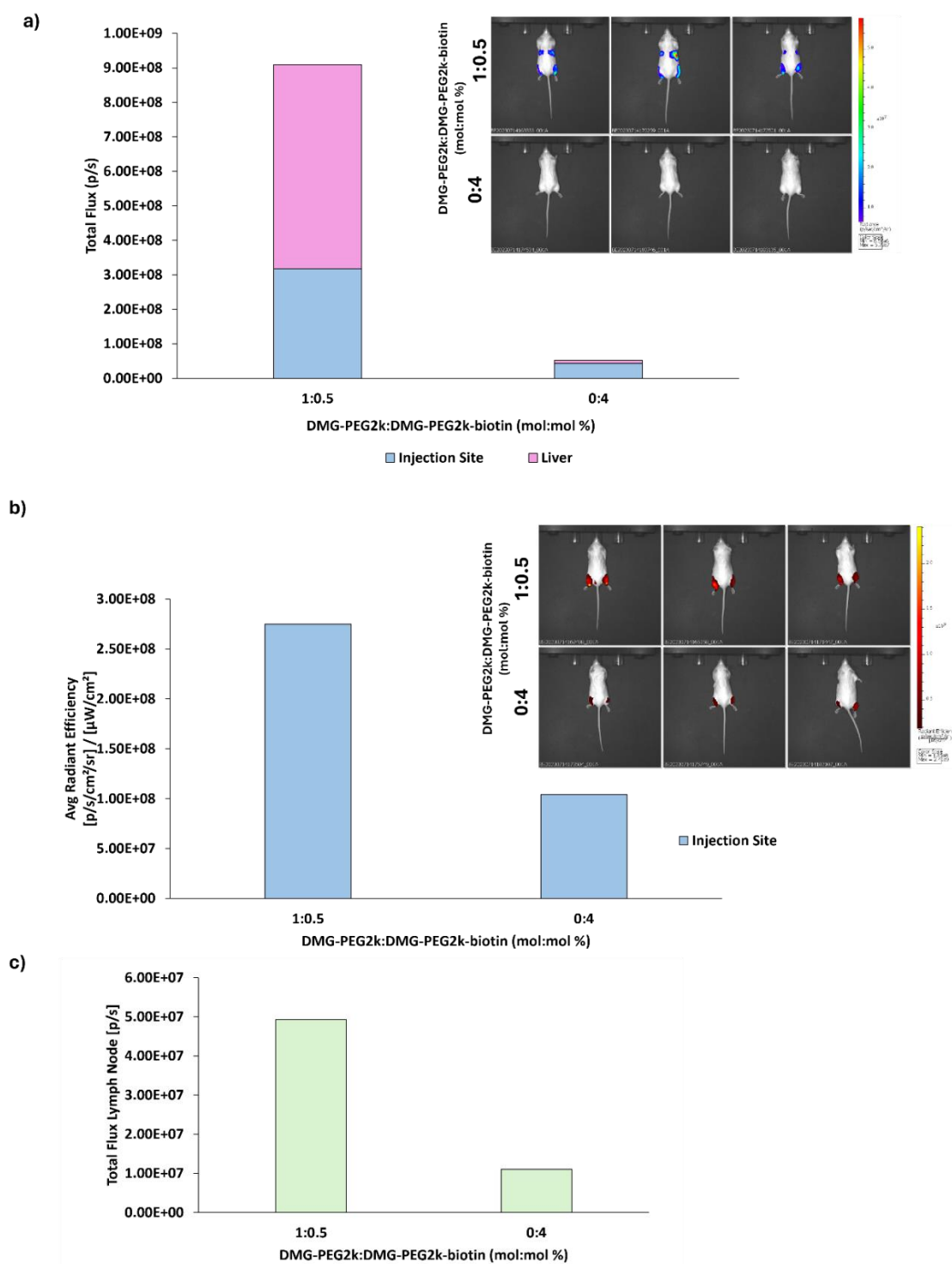
Figure 6.6 *The expression and biodistribution profile of the LNPs (table 6.2) according to the pilot study testing the biotin dose. a) representative IVIS images for DiR fluorescence imaging and corresponding the signal quantified from the per injection site and per liver, b) representative IVIS images for bioluminescence imaging and corresponding quantification signal from per the injection site and per liver, c) The in vivo transfection profile of the LNP (shown in the table2) in the lymph node. Results represent mean, n = 1 independent batch. One mouse, one injection per hind leg; 2 data points.*

Then, the samples were tested on the HEK-293 cell line to evaluate the *in vitro* expression profile (Figure 6.3). Coating the particles with biotin at the molar ratio of 0.25 and 0.5% improved the *in vitro* expression profile. Further coating decreased expression dramatically, specifically with the lowest expression at 1.5% mol of PEG2k-biotin (Figure 6.3). The combination of DMG-PEG2k: DMG-PEG2k-biotin (1:0.5 % mol) was selected as the lead formulation. Overall, coating LNPs with biotin and pre-dose of avidin did not affect the *in vivo* expression (Figure 6.5a; blue column) nor distribution (Figure 5b) at the injection site but did increase the expression at the liver (Figure 6.5a; pink column).

Biotin has been commonly used as a targeting ligand in the cancer cell due to overexpression of the biotin receptor in tumour cells [199,200]. It also can be used as a protein-repellent ligand to prevent protein corona formation [201]. Moreover, it has been shown that internalising biotin and biotinylated complexes depend on the cell line, and the uptake is mainly by passive diffusion on the HEK-293 cell line as it does not have sodium-dependent multivitamin receptors [202]. This is also confirmed by the study showing higher cellular uptake of biotinylated particles in the cancer cell line compared to the HEK-293 cells [199]. Therefore, the standard HEK293 model used for *in vitro* analysis of LNP expression can test expression potency but would highlight any advantages of biotin-medicated uptake. Thus, the changes in expression seen with the different biotin concentrations in the LNPs may be due to differences in the physicochemical characteristics, particularly particle size. HEK-293 cell line uses clathrin-mediated endocytosis, suitable for particles below 100 nm [149]. Therefore, LNPs prepared with 1.5% mol of DMG-PEG2k-biotin had a size of around 140 nm (Figure 6.2), and this likely hindered cellular uptake, leading to lower *in vitro* transfection efficiency. However, increasing biotin content from 0.5 to 1% mol decreased the *in vitro* expression despite both LNP formulations below 100 nm (Figure 6.2). Thus, the impact of the DMG-PEG2k-biotin on cell expression may be due to the biotin obstructing cellular uptake due to the denser biotin content. Modifying the PEG chain by biotin may change the cellular uptake mechanism [203]. Also, ligand density on the particle surface can affect the cellular uptake profile [204].

It is also important to note that the LNPs were tested without being crossed-linked with avidin. With the proposed targeting strategy, the LNPs would get trapped in the lymphatics because of cross-linking [205–207] which would inherently increase the total aggregate size further.

Particle size also has a major impact on lymphatic targeting, and optimum size ranges depending on the administration route, the injection site, injection volume and rate [208,209]. For example, the particles injected subcutaneously accumulated higher in the lymph nodes compared to the intravenous injection [210]. It was reported that small particles (25 nm) had higher lymph node accumulation than 100 nm when injected via the interstitial tail vein route [211]. Another study reported that particles 10-80 nm had higher lymphatic uptake [212]. Moreover, the valves mediating entrance into lymphatic vessels may mechanically expand due to injection volume and rate, and this may need to be emphasised for small animal models as they have a smaller volume than the injection volume [208,213]. Also, it needs to be mentioned that smaller particles can freely be drained to the lymph node. However, big particles are excluded by the tight junction in the endothelial cells of the lymphatic vessels taken up by the dendritic cells and drained to the lymph nodes [214].

Particle charge and surface chemistry also play roles in lymphatic entry [208]. For example, anionic particles had rapid clearance to the lymph node, and cationic particles had a depot effect by interaction with the residence proteins [51,215]. Surface-modified LNPs were used to target APCs, mediately lymphatic delivery with such ligands as mannose, hyaluronic acid [216]. A study reported that increasing PEG concentration from 1.5% to 3% with DSPE-PEG2k diminished the expression in the lymph nodes, while PEGylation with Tween-20 improved the expression in the lymph nodes from 1.5% to 3% Twenn-20. This study confirmed that the quantity and the structure of the PEG chain affected the expression profile in the lymph nodes [217].

It was also reported that protein and small hydrophilic particles can enter the systemic circulation by passing through the entire lymphatic chain and the thoracic duct [208]. Avidin is rapidly cleared from the blood circulation and accumulates in the liver, spleen, and kidney [218]. Therefore, avidin may mediate the accumulating LNPs in the liver by passing through the lymphatic chain, which can correspond to decreasing the expression in the lymph node (Figure 6.5c).

Given the low dose of biotin employed to test the LNPs within Figure 6.5, it was thought that the biotin quantity might not be enough for the targeting lymph node as the studies used 20% mol of DSPE-PEG2k-biotin [50,51]. Thus, the biotin quantity was increased to 4%. However, this diminished the *in vivo* expression (Figure 6.6). This could be again a result of

physicochemical attributes (e.g. particle size of the LNPs (120 nm) Table 6.2) and/or failure to promote expression after internalisation. The inability to promote expression can result from a range of factors, including inefficient endosomal escape; if the change in the PEG-headgroup changes interactions with the endosomal membranes, the LNPs may not escape from the endosome into the cytoplasm efficiently, the mRNA payload will not be released to the site of action. Similarly, the biotinylated-LNPs may trigger an immune response, activating innate immune pathways, which could result in mRNA degradation or interference with its translation. Indeed, adding the biotin at this concentration could affect the stability, uptake, and release properties, all of which can impact mRNA expression.

While new insights have been developed within this chapter, there were some limitations in this study that can be addressed in future studies. Initially, the results suggest that quantifying the emitted light from lymph nodes using IVIS may not be the most efficient method. Also, given the proximity of the popliteal lymph node to the injection site (Figure 6.1), when removing the lymph node, there is the potential for contamination of luciferase from the injection site to the lymph node, which could lead to false positive results. Also, draining avidin to the lymph node could be further confirmed to ensure alignment with previous studies [205–207]. This could be achieved by performing the imaging session in different time frames and maybe using fluorescence-labelled avidin (however, the issue of limited tissue penetration with the IVIS is also acknowledged). Moreover, the expression level decreased over time after culling the mice. Hence, the lymph nodes need to be removed quickly to image, and more importantly, the time between injection of the luciferin reagent and the imaging of the lymph node must be consistent for each mouse. Finally, it was reported that the particles size over 50-100 nm are trapped in the extracellular matrix [208]. Therefore, clearance of the LNPs may be an issue; however, data has shown that after IM injection, LNPs do move, so movement from the injection site to the draining lymph nodes may be achievable [60]. Whilst, in clinical practice, a two-step vaccination method (pre-dose with avidin, followed by vaccination with biotin-LNPs) is of limited value, the investigations within this chapter lay the foundation for further investigations into this strategy as a tool to provide further insights into the benefits of redirecting LNPs to draining lymphatics via a range of strategies.

6.2 Conclusion

This chapter describes a potential targeting approach using avidin-biotin interaction to deliver mRNA-LNPs to the lymph node. The rationale is based on the migration of previously administered avidin to the lymph node, where it is retained through the formation of a complex with biotinylated LNPs. The study initially focused on assessing the concentration of the biotin. Increasing biotin content improved the *in vitro* expression up to some level and further increment diminished it. Biotinylated LNPs had comparable *in vivo* expression compared to non-biotinylated LNPs. However, pre-dosing with avidin injection increased the expression in the liver. These studies suggest that alternative strategies should be considered for the redirecting of mRNA-LNPs to the lymphatics. Whilst it has been previously shown that cationic liposomal adjuvants can be redirected to the lymphatics using this biotin-avidin targeting strategy and this increased cytokine responses to the loading sub-unit antigen, the results from the studies conducted here suggest further modifications of the strategy are needed for it to be applied to LNPs [50].

Chapter 7: General Discussion

7.1 Introduction

This thesis aimed to optimise the *in vitro* and *in vivo* efficacy of mRNA-LNPs prepared with the MF system. LNPs comprise helper lipids (DSPC and Cholesterol), ionisable lipids and PEGylated lipids. Each lipid has a unique role in encapsulating mRNA into the LNPs and releasing it into the cytosol to be translated into the corresponding antigen protein. The other component is the encapsulation buffer used to dilute mRNA in a buffer at pH4. After self-assembling, LNPs are purified to remove ethanol content and raise pH to the physiological conditions (pH 7.4). In this stage, the LNP buffer is exchanged for the storage buffer, generally PBS or TRIS. The parameters in each step have potentially affected the LNPs' efficiency *in vitro* and *in vivo*. This thesis focused on investigating the LNP delivery efficiency, testing the different parameters such as the choice of ionisable lipid and the ionic strength of encapsulation buffer (citrate buffer) in HEK-293 cell lines and BALB/c mice. Moreover, it addressed a gap in existing research by focusing on sex-based disparities in mRNA-LNP expression profile and the immune response in BALB/c mice, highlighting the importance of biological sex in mRNA vaccine research. The thesis continued with a targeting strategy to the lymph node, exploiting the strong interaction between avidin and biotin.

7.2 Evaluating LNPs Efficiency Considering Lipid Composition and Buffer Ionic Strength

Ionisable lipids are the most critical part of the LNPs due to the responsibility of encapsulation mRNA and releasing it into the cytosol. ALC-0315 and SM-102 are the ionisable lipids used in both mRNA COVID vaccines. *In vitro* (Figure 2.2), *in vivo* expression (Figure 2.5), and clearance (Figure 2.4) profiles were tested compared to MC3, DODAP and DOTAP. SM-102 had the best profile among the other lipids in terms of expression and clearance. Surprisingly, ALC-0315 drew attention with exceptionally low *in vitro* expression and the highest expression in the liver, although it had a comparable expression in the injection with SM-102. As mentioned in the introduction section, the efficiency of mRNA LNPs is driven by two factors: pKa and the shape of ionisable lipids. Considering the very similar structure of SM-102 and ALC-0315, this very low *in vitro* expression with ALC-0315 is likely associated with pKa. The close relationship between pKa and *in vitro* expression can be confirmed with a similar order for pKa and *in vitro* expression. pKa of the ionisable lipids and *in vitro* expression profile were in this order: SM-102 > MC3 > ALC-0315 > DODAP (DOTAP does not have a pKa as it is a permanent cationic

lipid). When considering the branched tail structure of SM-102 and ALC-0315 compared to the cylindrical structure of MC3, DODAP and DOTAP, the *in vivo* expression is likely driven by the shape of ionisable lipids if they are in the pKa range for an optimum protein expression via IM route[25]. As an overall experience from the studies, the expression in the injection site is correlated with expression in the liver (For example, as seen in Figure 3.8, LNPs prepared with 50, 100 and 300 mM of citrate buffer had a very similar trend in the injection site and the liver). However, when comparing, ALC-0315 had significantly higher expression in the liver than SM-102, even if they had a very similar expression at the injection site (Figure 2.5). This can be based on the pKa difference as SM-102's pKa is higher than ALC-0315 (Figure 2.1). Also, it is reported that the expression in the liver is related to the pKa of the ionisable lipids [85]. Adsorption of apoE onto the LNP surface will likely direct LNPs to the liver because apoE serves as a ligand for LDLR. The interaction rate between LNPs and apoE may be influenced by the pKa, as previously discussed regarding liver tropism and its association with pKa. This can be explained according to the Henderson-Hasselbalch equation (Equation 1.1); in the same pH, lower pKa needs to be balanced with a higher ratio of [tertiary amine]/[quaternary amine]. This means LNPs with lower pKa have a higher proportion of tertiary amine (neutral form) or less proportion of quaternary amine (protonated). Given that tertiary amine is more lipophilic than the quaternary counterpart, blood protein interacts with lipophilic molecules more (because proteins have hydrophobic regions). Overall, LNPs with lower pKa (which means more tertiary amine form, namely, more lipophilic characteristic) interact with the protein (apoE in this case) more in the blood circulation. Then, apoE-adsorbed LNPs will be internalised by LDL receptors in the liver. This would be the rationale behind the relationship between pKa and liver tropism.

Also, PEGylation affected the expression profile in the liver (Figure 2.8 and Figure 2.10). After losing the PEG chain from the particle surface, LNPs are a good target for apoE, leading to enhanced expression in the liver. Here, the desorption rate of the PEG chain gains importance. This depends on the number of carbon chains of PEG lipids. DSPE-PEG2k had the lowest expression (both injection site and liver) due to a longer carbon tail (18 C). Comparing ALC-0159 and DMG-PEG2k, which had the same carbon chain length (14 C), ALC-0159 improved the expression *in vitro* (Figure 2.6) and *in vivo* (Figure 2.8 and Figure 2.10). It was shown that DMG-PEG2k desorption from the LNP surface was faster compared to the ALC-0159 [88]. The

expression order was ALC-0159 > DMG-PEG2k > DSPE-PEG2k irrespective of the ionisable lipids; however, the difference between ALC-0159 and DMG-PEG2k was more pronounced when ALC-0315 used as an ionisable lipid. Therefore, it can be concluded that the combination of ionisable lipids and PEG lipids is also important. The other important conclusion from the results is the *in* vitro and *in vivo* correlation. For example, ALC-0159 PEG lipid improved the *in vitro* expression when combined with SM-102 but not with ALC-0315. However, when these samples were evaluated *in vivo*, such a difference disappeared. This shows the importance of improving the *in vitro* models for predicting *in vivo* outcomes. In this context, protein corona appears to be a critical aspect because LNP characteristics can be changed in the body after injection by interacting with the body protein, which can change the accumulation of the particles and release properties.

Then, this thesis focused on the ionic strength of the citrate buffer when encapsulating mRNA into the LNPs. The ionic strength of the buffers is overlooked in the literature as more research focuses on developing lipids. Chapter 3 demonstrated the importance of ionic strength; increasing the strength from 50 mM to 300 mM decreased the *in vitro* (Figure 3.4 and 3.5) and *in vivo* (Figure 3.8) transfection efficiency, although 50 and 100 mM had a similar profile. Also, increasing the ionic strength of the encapsulation buffer did not affect the pKa of LNPs (Figure 3.3). Morphology analysis demonstrated that the bleb structures (Figure 3.2). Considering the similar size, PDI, zeta potential (Table 3.1) and pKa of the LNPs, the bleb structure seems responsible for the expression profile.

7.3 Exploiting Desing of Experiment Approach

DoE is a great tool for testing many factors over various responses. It has many benefits, such as cost-effective research and the capability to explore the interaction between the factors. Box-Behnken design (Figure 4.2) was used to evaluate the effect of FRR, TFR and lipid concentration over particle size, PDI, zeta potential, EE, recovery, *in vitro* and *in vivo* expression and biodistribution (Table 4.1). Overall, FRR had the dominant effect on the parameters. For example, increasing FRR decreased the particle size (Figure 4.4). The *in vitro* expression (Figure 4.9) was closely related to FRR, but this was likely about particle size. FRR influences particle size, and particle size influences *in vitro* expression profile. Therefore, FRR is related to the *in vitro* expression profile. From DoE, an important conclusion was the quadratic effect of the parameters. This can be easily ignored when only focused on the linear

relationship. For example, before conducting DoE, the hypothesis was that the particle size should not be affected by the lipid concentration, as higher lipid concentrations are accompanied by proportionally higher mRNA concentrations to keep the NP ratio the same. It was believed that higher lipid concentrations would result in more particles of a similar size to those produced at lower concentrations. However, DoE showed the importance of the quadratic effect of lipid concentration. This was the only example in the frame of this DoE design. Investigating the quadratic, even cubic effect, between the parameters and response would be very valuable in improving the prediction ability of the model and understanding the relationship between the parameters and the responses. This eventually helps to optimise the settings or parameters for improved results.

7.4 Importance of Biological Sex

In Chapter 5, attention was drawn to the importance of biological sex differences in mRNA-LNP studies. The presence of the inequivalent immune response between females and males is known. However, there was no study in the literature showing the presence of sex-dependent mRNA-LNP expression difference. It was presented that female and male BALC/c mice expressed mRNA at a similar level (Figure 5.4), but female mice mounted a stronger immune response (Figure 5.1). Considering the biological sex difference in the immunological studies and when developing clinical products is very important. For example, the COVID-related death rate is likely higher in males, while the incidence associated with COVID-19 vaccines is likely higher in females. This health outcome can be improved by optimising the dose level according to the biological sex. For example, females can be immunised with a lower dose than the males need, which may reduce the anaphylaxis risk. For example, the total dose currently used to vaccinate 1,000 women could be used to vaccinate 2,000 women as the dose can be reduced for women. This means reducing the cost of the vaccine per person. This study also showed the importance of reporting the biological sex in vaccine studies. This will improve the quality and relevance of scientific findings. Presenting data by biological sex may improve the scientific understanding of the presence of sex-dependent disease mechanisms and immune function.

7.5 Future and Outlook

Overall, this thesis focused on investigating LNPs for efficient transfection efficiency *in vitro* and *in vivo*. A decision tree for new ionisable lipids from production to the pre-clinical

studies is summarised in Table 7.1. The biggest problem seen throughout the thesis was the lack of *in vitro* and *in vivo* correlation. This poses so many challenges in terms of the accuracy of the data and economic efficiency. The lipids that perform well *in vitro* can fail *in vivo* or vice versa. For example, ALC-0315 lipid failed *in vitro* but performed well *in vivo*. If this lipid had not been tested *in vivo* after failing the *in vitro* stage, this would have resulted in false negative results and led to losing money and misleading scientific knowledge. In the other case, if the product passed the *in vitro* stage but failed the *in vivo* stage, this led to ethical concerns related to animal usage in addition to again wasting money and time. If the product was successful *in vitro* and failed *in vivo*, the next step will be evaluating the product using more animals to find out why it failed *in vivo*. This leads to unnecessary usage of animals and raises ethical concerns. Another problem is that scaling up. The product, being successful *in vitro* and *in vivo* on the lab scale, can fail when produced on a big scale. This leads to losing more money, time, and resources.

Overall, the lack of *in vitro in vivo* correlation is currently a rising issue. There are studies to improve this, for example, by developing 3D cell culture models and organ-on-chips. The importance of pilot studies needs to be highlighted in the early stages. Evaluating the product early *in vivo* can prevent losing money and time. The collaboration between the scientific area needs to improve to understand the *in vitro* and *in vivo* structures regarding chemical, biological and physical views.
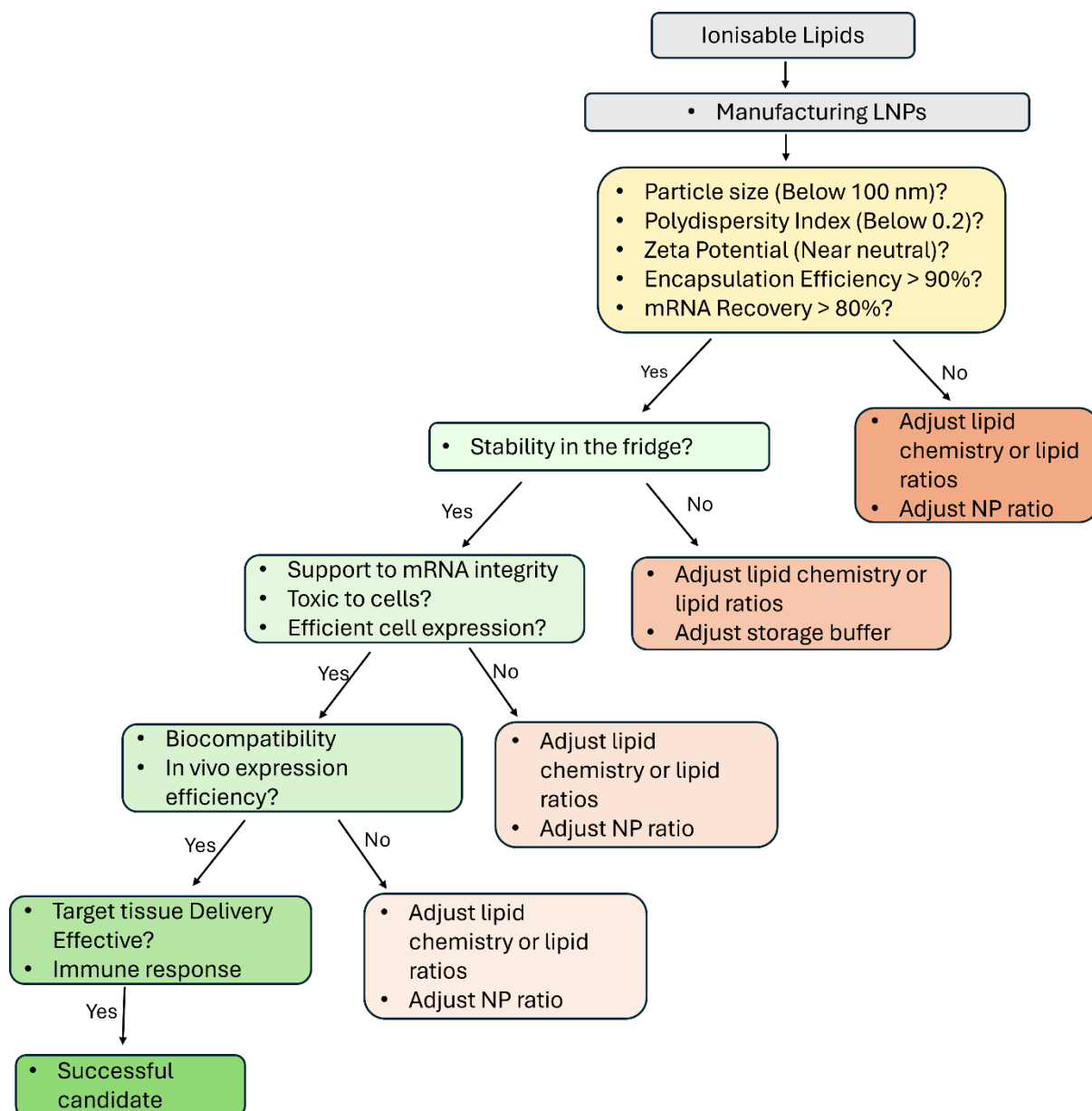
Figure 7.1 *A decision tree illustrating the development process of LNPs with new ionisable lipids, from production to in vivo studies. At each decision point, the outcome is based on the experimental results. A 'Yes' indicates progression to the next stage of studies, while a 'No' signifies the need to adjust formulation parameters before proceeding.*

References

[1]   A.D. Bangham, M.M. Standish, J.C. Watkins, Diffusion of univalent ions across the lamellae of swollen phospholipids, J Mol Biol 13 (1965) 238-IN27. https://doi.org/10.1016/S0022-2836(65)80093-6.

[2]   S. Joshi, M.T. Hussain, C.B. Roces, G. Anderluzzi, E. Kastner, S. Salmaso, D.J. Kirby, Y. Perrie, Microfluidics based manufacture of liposomes simultaneously entrapping hydrophilic and lipophilic drugs, Int J Pharm 514 (2016) 160–168. https://doi.org/10.1016/j.ijpharm.2016.09.027.

[3]   P.K. Working, A.D. Dayan, Pharmacological-toxicological expert report. CAELYX. (Stealth liposomal doxorubicin HCl)., Hum Exp Toxicol 15 (1996) 751–85.

[4]   M. Pisani, G. Mobbili, P. Bruni, Neutral Liposomes and DNA Transfection, in: Non-Viral Gene Therapy, InTech, 2011. https://doi.org/10.5772/21283.

[5]   M.J. OSTRO, D. GIACOMONI, D. LAVELLE, W. PAXTON, S. DRAY, Evidence for translation of rabbit globin mRNA after liposomemediated insertion into a human cell line, Nature 274 (1978) 921–923. https://doi.org/10.1038/274921a0.

[6]   R. Tenchov, R. Bird, A.E. Curtze, Q. Zhou, Lipid Nanoparticles—From Liposomes to mRNA Vaccine Delivery, a Landscape of Research Diversity and Advancement, ACS Nano (2021). https://doi.org/10.1021/acsnano.1c04996.

[7]   P.R. Cullis, M.J. Hope, Lipid Nanoparticle Systems for Enabling Gene Therapies, Molecular Therapy 25 (2017) 1467–1475. https://doi.org/10.1016/j.ymthe.2017.03.013.

[8]   M. Li, Y. Li, S. Li, L. Jia, H. Wang, M. Li, J. Deng, A. Zhu, L. Ma, W. Li, P. Yu, T. Zhu, The nano delivery systems and applications of mRNA, Eur J Med Chem 227 (2022) 113910. https://doi.org/10.1016/j.ejmech.2021.113910.

[9]   J.A. Kulkarni, D. Witzigmann, S.B. Thomson, S. Chen, B.R. Leavitt, P.R. Cullis, R. van der Meel, The current landscape of nucleic acid therapeutics, Nat Nanotechnol 16 (2021) 630–643. https://doi.org/10.1038/s41565-021-00898-0.

[10]   X. Hou, T. Zaks, R. Langer, Y. Dong, Lipid nanoparticles for mRNA delivery, Nat Rev Mater 6 (2021) 1078–1094. https://doi.org/10.1038/s41578-021-00358-0.

[11]   C. Webb, S. Ip, N. V Bathula, P. Popova, S.K. V Soriano, H.H. Ly, B. Eryilmaz, V.A. Nguyen Huu, R. Broadhead, M. Rabel, I. Villamagna, S. Abraham, V. Raeesi, A. Thomas, S. Clarke, E.C. Ramsay, Y. Perrie, A.K. Blakney, Current Status and Future Perspectives on MRNA Drug Manufacturing, Mol Pharm 19 (2022) 1047–1058. https://doi.org/10.1021/acs.molpharmaceut.2c00010.

[12]   X. Tang, Y. Zhang, X. Han, Ionizable Lipid Nanoparticles for mRNA Delivery, Adv Nanobiomed Res 3 (2023). https://doi.org/10.1002/anbr.202300006.

[13]   Y. Suzuki, H. Ishihara, Difference in the lipid nanoparticle technology employed in three approved siRNA (Patisiran) and mRNA (COVID-19 vaccine) drugs, Drug Metab Pharmacokinet 41 (2021) 100424. https://doi.org/10.1016/j.dmpk.2021.100424.

[14]   L. Schoenmaker, D. Witzigmann, J.A. Kulkarni, R. Verbeke, G. Kersten, W. Jiskoot, D.J.A. Crommelin, mRNA-lipid nanoparticle COVID-19 vaccines: Structure and stability, Int J Pharm 601 (2021) 120586. https://doi.org/10.1016/j.ijpharm.2021.120586.

[15]   https://www.ema.europa.eu/en/documents/product-information/spikevax-previously-covid-19-vaccine-moderna-epar-product-information_en.pdf, 2024.

[16]   https://www.ema.europa.eu/en/documents/product-information/comirnaty-epar-product-information_en.pdf, 2023.

[17]   C. Hald Albertsen, J.A. Kulkarni, D. Witzigmann, M. Lind, K. Petersson, J.B. Simonsen, The role of lipid components in lipid nanoparticles for vaccines and gene therapy, Adv Drug Deliv Rev 188 (2022) 114416. https://doi.org/10.1016/j.addr.2022.114416.

[18]   J.A. Kulkarni, M.M. Darjuan, J.E. Mercer, S. Chen, R. van der Meel, J.L. Thewalt, Y.Y.C. Tam, P.R. Cullis, On the Formation and Morphology of Lipid Nanoparticles Containing Ionizable Cationic Lipids and siRNA, ACS Nano 12 (2018) 4787–4795. https://doi.org/10.1021/acsnano.8b01516.

[19]   S. Patel, N. Ashwanikumar, E. Robinson, Y. Xia, C. Mihai, J.P. Griffith, S. Hou, A.A. Esposito, T. Ketova, K. Welsher, J.L. Joyal, Ö. Almarsson, G. Sahay, Naturally-occurring cholesterol analogues in lipid nanoparticles induce polymorphic shape and enhance intracellular delivery of mRNA, Nat Commun 11 (2020). https://doi.org/10.1038/s41467-020-14527-2.

[20]   X. Cheng, R.J. Lee, The role of helper lipids in lipid nanoparticles (LNPs) designed for oligonucleotide delivery., Adv Drug Deliv Rev 99 (2016) 129–137. https://doi.org/10.1016/j.addr.2016.01.022.

[21]   A. Akinc, M.A. Maier, M. Manoharan, K. Fitzgerald, M. Jayaraman, S. Barros, S. Ansell, X. Du, M.J. Hope, T.D. Madden, B.L. Mui, S.C. Semple, Y.K. Tam, M. Ciufolini, D. Witzigmann, J.A. Kulkarni, R. van der Meel, P.R. Cullis, The Onpattro story and the clinical translation of nanomedicines containing nucleic acid-based drugs, Nat Nanotechnol 14 (2019) 1084–1087. https://doi.org/10.1038/s41565-019-0591-y.

[22]   F.P. Polack, S.J. Thomas, N. Kitchin, J. Absalon, A. Gurtman, S. Lockhart, J.L. Perez, G. Pérez Marc, E.D. Moreira, C. Zerbini, R. Bailey, K.A. Swanson, S. Roychoudhury, K. Koury, P. Li, W. V. Kalina, D. Cooper, R.W. Frenck, L.L. Hammitt, Ö. Türeci, H. Nell, A. Schaefer, S. Ünal, D.B. Tresnan, S. Mather, P.R. Dormitzer, U. Şahin, K.U. Jansen, W.C. Gruber, Safety and Efficacy of the BNT162b2 mRNA Covid-19 Vaccine, New England Journal of Medicine 383 (2020) 2603–2615. https://doi.org/10.1056/NEJMOA2034577/SUPPL_FILE/NEJMOA2034577_PROTOCOL.PDF.

[23]   L.R. Baden, H.M. El Sahly, B. Essink, K. Kotloff, S. Frey, R. Novak, D. Diemert, S.A. Spector, N. Rouphael, C.B. Creech, J. McGettigan, S. Khetan, N. Segall, J. Solis, A. Brosz, C. Fierro, H. Schwartz, K. Neuzil, L. Corey, P. Gilbert, H. Janes, D. Follmann, M. Marovich, J. Mascola, L. Polakowski, J. Ledgerwood, B.S. Graham, H. Bennett, R. Pajon, C. Knightly, B. Leav, W. Deng, H. Zhou, S. Han, M. Ivarsson, J. Miller, T. Zaks, Efficacy and Safety of the mRNA-1273 SARS-CoV-2 Vaccine, New England Journal of Medicine 384 (2021) 403–416. https://doi.org/10.1056/NEJMOA2035389/SUPPL_FILE/NEJMOA2035389_DATA-SHARING.PDF.

[24]   K.J. Kauffman, J.R. Dorkin, J.H. Yang, M.W. Heartlein, F. Derosa, F.F. Mir, O.S. Fenton, D.G. Anderson, Optimization of Lipid Nanoparticle Formulations for mRNA Delivery in Vivo with

Fractional Factorial and Definitive Screening Designs, Nano Lett 15 (2015) 7300–7306. https://doi.org/10.1021/ACS.NANOLETT.5B02497/SUPPL_FILE/NL5B02497_SI_001.PDF.

[25]   K.J. Hassett, K.E. Benenato, E. Jacquinet, A. Lee, A. Woods, O. Yuzhakov, S. Himansu, J. Deterling, B.M. Geilich, T. Ketova, C. Mihai, A. Lynn, I. McFadyen, M.J. Moore, J.J. Senn, M.G. Stanton, Ö. Almarsson, G. Ciaramella, L.A. Brito, Optimization of Lipid Nanoparticles for Intramuscular Administration of mRNA Vaccines., Mol Ther Nucleic Acids 15 (2019) 1–11. https://doi.org/10.1016/j.omtn.2019.01.013.

[26]   Y. Eygeris, M. Gupta, J. Kim, G. Sahay, Chemistry of Lipid Nanoparticles for RNA Delivery, Acc Chem Res 55 (2022) 2–12. https://doi.org/10.1021/acs.accounts.1c00544.

[27]   X. Han, H. Zhang, K. Butowska, K.L. Swingle, M.-G. Alameh, D. Weissman, M.J. Mitchell, An ionizable lipid toolbox for RNA delivery, Nat Commun 12 (2021) 7233. https://doi.org/10.1038/s41467-021-27493-0.

[28]   M. Schlich, R. Palomba, G. Costabile, S. Mizrahy, M. Pannuzzo, D. Peer, P. Decuzzi, Cytosolic delivery of nucleic acids: The case of ionizable lipid nanoparticles, Bioeng Transl Med 6 (2021). https://doi.org/10.1002/btm2.10213.

[29]   M. Paloncýová, P. Čechová, M. Šrejber, P. Kührová, M. Otyepka, Role of Ionizable Lipids in SARS-CoV-2 Vaccines As Revealed by Molecular Dynamics Simulations: From Membrane Structure to Interaction with mRNA Fragments, J Phys Chem Lett 12 (2021) 11199–11205. https://doi.org/10.1021/acs.jpclett.1c03109.

[30]   R. Tenchov, J.M. Sasso, Q.A. Zhou, PEGylated Lipid Nanoparticle Formulations: Immunological Safety and Efficiency Perspective, Bioconjug Chem 34 (2023) 941–960. https://doi.org/10.1021/acs.bioconjchem.3c00174.

[31]   S.C. Semple, A. Akinc, J. Chen, A.P. Sandhu, B.L. Mui, C.K. Cho, D.W.Y. Sah, D. Stebbing, E.J. Crosley, E. Yaworski, I.M. Hafez, J.R. Dorkin, J. Qin, K. Lam, K.G. Rajeev, K.F. Wong, L.B. Jeffs, L. Nechev, M.L. Eisenhardt, M. Jayaraman, M. Kazem, M.A. Maier, M. Srinivasulu, M.J. Weinstein, Q. Chen, R. Alvarez, S.A. Barros, S. De, S.K. Klimuk, T. Borland, V. Kosovrasti, W.L. Cantley, Y.K. Tam, M. Manoharan, M.A. Ciufolini, M.A. Tracy, A. De Fougerolles, I. MacLachlan, P.R. Cullis, T.D. Madden, M.J. Hope, Rational design of cationic lipids for siRNA delivery, Nat Biotechnol 28 (2010) 172–176. https://doi.org/10.1038/nbt.1602.

[32]   M.R. Sherman, L.D. Williams, M.A. Sobczyk, S.J. Michaels, M.G.P. Saifer, Role of the Methoxy Group in Immune Responses to mPEG-Protein Conjugates, Bioconjug Chem 23 (2012) 485–499. https://doi.org/10.1021/bc200551b.

[33]   Y. Li, M. Kröger, W.K. Liu, Endocytosis of PEGylated nanoparticles accompanied by structural and free energy changes of the grafted polyethylene glycol, Biomaterials 35 (2014) 8467–8478. https://doi.org/10.1016/j.biomaterials.2014.06.032.

[34]   B.L. Mui, Y.K. Tam, M. Jayaraman, S.M. Ansell, X. Du, Y.Y.C. Tam, P.J. Lin, S. Chen, J.K. Narayanannair, K.G. Rajeev, M. Manoharan, A. Akinc, M.A. Maier, P. Cullis, T.D. Madden, M.J. Hope, Influence of Polyethylene Glycol Lipid Desorption Rates on Pharmacokinetics and Pharmacodynamics of siRNA Lipid Nanoparticles., Mol Ther Nucleic Acids 2 (2013) e139. https://doi.org/10.1038/mtna.2013.66.

[35]   T. Suzuki, Y. Suzuki, T. Hihara, K. Kubara, K. Kondo, K. Hyodo, K. Yamazaki, T. Ishida, H. Ishihara, PEG shedding-rate-dependent blood clearance of PEGylated lipid nanoparticles in mice: Faster

PEG shedding attenuates anti-PEG IgM production, Int J Pharm 588 (2020) 119792. https://doi.org/10.1016/j.ijpharm.2020.119792.

[36]   H. Tanaka, R. Miyama, Y. Sakurai, S. Tamagawa, Y. Nakai, K. Tange, H. Yoshioka, H. Akita, Improvement of mRNA Delivery Efficiency to a T Cell Line by Modulating PEG-Lipid Content and Phospholipid Components of Lipid Nanoparticles, Pharmaceutics 13 (2021) 2097. https://doi.org/10.3390/pharmaceutics13122097.

[37]   L.Y. Song, Q.F. Ahkong, Q. Rong, Z. Wang, S. Ansell, M.J. Hope, B. Mui, Characterization of the inhibitory effect of PEG-lipid conjugates on the intracellular delivery of plasmid and antisense DNA mediated by cationic lipid liposomes, Biochimica et Biophysica Acta (BBA) - Biomembranes 1558 (2002) 1–13. https://doi.org/10.1016/S0005-2736(01)00399-6.

[38]   K. Hong, W. Zheng, A. Baker, D. Papahadjopoulos, Stabilization of cationic liposome-plasmid DNA complexes by polyamines and poly(ethylene glycol)-phospholipid conjugates for efficient in vivo gene delivery, FEBS Lett 400 (1997) 233–237. https://doi.org/10.1016/S0014-5793(96)01397-X.

[39]   R.C. Ryals, S. Patel, C. Acosta, M. McKinney, M.E. Pennesi, G. Sahay, The effects of PEGylation on LNP based mRNA delivery to the eye, PLoS One 15 (2020) e0241006. https://doi.org/10.1371/journal.pone.0241006.

[40]   Md.A. Sufian, M.A. Ilies, Lipid-based nucleic acid therapeutics with in vivo efficacy, WIREs Nanomedicine and Nanobiotechnology 15 (2023). https://doi.org/10.1002/wnan.1856.

[41]   N.M. Belliveau, J. Huft, P.J. Lin, S. Chen, A.K. Leung, T.J. Leaver, A.W. Wild, J.B. Lee, R.J. Taylor, Y.K. Tam, C.L. Hansen, P.R. Cullis, Microfluidic synthesis of highly potent limit-size lipid nanoparticles for in vivo delivery of siRNA, Mol Ther Nucleic Acids 1 (2012) e37. https://doi.org/10.1038/mtna.2012.28.

[42]   M.J.W. Evers, J.A. Kulkarni, R. van der Meel, P.R. Cullis, P. Vader, R.M. Schiffelers, State-of-the-Art Design and Rapid-Mixing Production Techniques of Lipid Nanoparticles for Nucleic Acid Delivery, Small Methods 2 (2018) 1700375. https://doi.org/10.1002/smtd.201700375.

[43]   C.B. Roces, G. Lou, N. Jain, S. Abraham, A. Thomas, G.W. Halbert, Y. Perrie, Manufacturing Considerations for the Development of Lipid Nanoparticles Using Microfluidics, Pharmaceutics 12 (2020) 1095. https://doi.org/10.3390/pharmaceutics12111095.

[44]   G. Anderluzzi, Y. Perrie, Microfluidic Manufacture of Solid Lipid Nanoparticles: A Case Study on Tristearin-Based Systems, Drug Deliv Lett 10 (2020) 197–208. https://doi.org/10.2174/2210303109666190807104437.

[45]   S. Chen, Y.Y.C. Tam, P.J.C. Lin, M.M.H. Sung, Y.K. Tam, P.R. Cullis, Influence of particle size on the in vivo potency of lipid nanoparticle formulations of siRNA, Journal of Controlled Release 235 (2016) 236–244. https://doi.org/10.1016/j.jconrel.2016.05.059.

[46]   K.J. Hassett, J. Higgins, A. Woods, B. Levy, Y. Xia, C.J. Hsiao, E. Acosta, Ö. Almarsson, M.J. Moore, L.A. Brito, Impact of lipid nanoparticle size on mRNA vaccine immunogenicity, Journal of Controlled Release 335 (2021) 237–246. https://doi.org/10.1016/j.jconrel.2021.05.021.

[47]   T. Nakamura, M. Kawai, Y. Sato, M. Maeki, M. Tokeshi, H. Harashima, The Effect of Size and Charge of Lipid Nanoparticles Prepared by Microfluidic Mixing on Their Lymph Node

Transitivity and Distribution, Mol Pharm 17 (2020) 944–953.
https://doi.org/10.1021/acs.molpharmaceut.9b01182.

[48]   M. Danaei, M. Dehghankhold, S. Ataei, F. Hasanzadeh Davarani, R. Javanmard, A. Dokhani, S. Khorasani, M. Mozafari, Impact of Particle Size and Polydispersity Index on the Clinical Applications of Lipidic Nanocarrier Systems, Pharmaceutics 10 (2018) 57. https://doi.org/10.3390/pharmaceutics10020057.

[49]   F. Szoka, D. Papahadjopoulos, Comparative Properties and Methods of Preparation of Lipid Vesicles (Liposomes), Annu Rev Biophys Bioeng 9 (1980) 467–508. https://doi.org/10.1146/annurev.bb.09.060180.002343.

[50]   C.B. Roces, S. Khadke, D. Christensen, Y. Perrie, Scale-Independent Microfluidic Production of Cationic Liposomal Adjuvants and Development of Enhanced Lymphatic Targeting Strategies, Mol Pharm 16 (2019) 4372–4386. https://doi.org/10.1021/acs.molpharmaceut.9b00730.

[51]   S. Khadke, C.B. Roces, A. Cameron, A. Devitt, Y. Perrie, Formulation and manufacturing of lymphatic targeting liposomes using microfluidics, Journal of Controlled Release 307 (2019) 211–220. https://doi.org/10.1016/j.jconrel.2019.06.002.

[52]   C. Webb, S. Khadke, S.T. Schmidt, C.B. Roces, N. Forbes, G. Berrie, Y. Perrie, The Impact of Solvent Selection: Strategies to Guide the Manufacturing of Liposomes Using Microfluidics, Pharmaceutics 11 (2019). https://doi.org/10.3390/pharmaceutics11120653.

[53]   ASTM E3247-20 Standard Test Method for Measuring the Size of Nanoparticles in Aqueous Media Using Dynamic Light Scattering, FDA (2020).

[54]   V. Filipe, A. Hawe, W. Jiskoot, Critical Evaluation of Nanoparticle Tracking Analysis (NTA) by NanoSight for the Measurement of Nanoparticles and Protein Aggregates, Pharm Res 27 (2010) 796–810. https://doi.org/10.1007/s11095-010-0073-2.

[55]   T. Terada, J.A. Kulkarni, A. Huynh, S. Chen, R. van der Meel, Y.Y.C. Tam, P.R. Cullis, Characterization of Lipid Nanoparticles Containing Ionizable Cationic Lipids Using Design-of-Experiments Approach, Langmuir 37 (2021) 1120–1128. https://doi.org/10.1021/acs.langmuir.0c03039.

[56]   A. Pratsinis, Y. Fan, M. Portmann, M. Hammel, P. Kou, A. Sarode, P. Ringler, L. Kovacik, M.E. Lauer, J. Lamerz, G.L. Hura, C.-W. Yen, M. Keller, Impact of non-ionizable lipids and phase mixing methods on structural properties of lipid nanoparticle formulations, Int J Pharm 637 (2023) 122874. https://doi.org/10.1016/j.ijpharm.2023.122874.

[57]   S. Bhattacharjee, DLS and zeta potential – What they are and what they are not?, Journal of Controlled Release 235 (2016) 337–351. https://doi.org/10.1016/j.jconrel.2016.06.017.

[58]   Q. Cheng, T. Wei, L. Farbiak, L.T. Johnson, S.A. Dilliard, D.J. Siegwart, Selective organ targeting (SORT) nanoparticles for tissue-specific mRNA delivery and CRISPR–Cas gene editing, Nat Nanotechnol 15 (2020) 313–320. https://doi.org/10.1038/s41565-020-0669-6.

[59]   X. Wang, S. Liu, Y. Sun, X. Yu, S.M. Lee, Q. Cheng, T. Wei, J. Gong, J. Robinson, D. Zhang, X. Lian, P. Basak, D.J. Siegwart, Preparation of selective organ-targeting (SORT) lipid nanoparticles (LNPs) using multiple technical methods for tissue-specific mRNA delivery, Nat Protoc 18 (2023) 265–291. https://doi.org/10.1038/s41596-022-00755-x.

[60]   N. Pardi, S. Tuyishime, H. Muramatsu, K. Kariko, B.L. Mui, Y.K. Tam, T.D. Madden, M.J. Hope, D. Weissman, Expression kinetics of nucleoside-modified mRNA delivered in lipid nanoparticles to mice by various routes, Journal of Controlled Release 217 (2015) 345–351. https://doi.org/10.1016/j.jconrel.2015.08.007.

[61]   E. Kon, U. Elia, D. Peer, Principles for designing an optimal mRNA lipid nanoparticle vaccine, Curr Opin Biotechnol 73 (2022) 329–336. https://doi.org/10.1016/j.copbio.2021.09.016.

[62]   L. Zheng, S.R. Bandara, Z. Tan, C. Leal, Lipid nanoparticle topology regulates endosomal escape and delivery of RNA to the cytoplasm, Proceedings of the National Academy of Sciences 120 (2023). https://doi.org/10.1073/pnas.2301067120.

[63]   S. Chatterjee, E. Kon, P. Sharma, D. Peer, Endosomal escape: A bottleneck for LNP-mediated therapeutics, Proceedings of the National Academy of Sciences 121 (2024). https://doi.org/10.1073/pnas.2307800120.

[64]   M. Ramezanpour, D.P. Tieleman, Computational Insights into the Role of Cholesterol in Inverted Hexagonal Phase Stabilization and Endosomal Drug Release, Langmuir 38 (2022) 7462–7471. https://doi.org/10.1021/acs.langmuir.2c00430.

[65]   S.K. Patel, M.M. Billingsley, C. Frazee, X. Han, K.L. Swingle, J. Qin, M.-G. Alameh, K. Wang, D. Weissman, M.J. Mitchell, Hydroxycholesterol substitution in ionizable lipid nanoparticles for mRNA delivery to T cells, Journal of Controlled Release 347 (2022) 521–532. https://doi.org/10.1016/j.jconrel.2022.05.020.

[66]   L.M.P. Vermeulen, S.C. De Smedt, K. Remaut, K. Braeckmans, The proton sponge hypothesis: Fable or fact?, European Journal of Pharmaceutics and Biopharmaceutics 129 (2018) 184–190. https://doi.org/10.1016/j.ejpb.2018.05.034.

[67]   J. Kim, Y. Eygeris, M. Gupta, G. Sahay, Self-assembled mRNA vaccines, Adv Drug Deliv Rev 170 (2021) 83–112. https://doi.org/10.1016/j.addr.2020.12.014.

[68]   N. Chaudhary, D. Weissman, K.A. Whitehead, mRNA vaccines for infectious diseases: principles, delivery and clinical translation, (n.d.). https://doi.org/10.1038/s41573-021-00283-5.

[69]   J.W. Park, P.N.P. Lagniton, Y. Liu, R.-H. Xu, mRNA vaccines for COVID-19: what, why and how, Int J Biol Sci 17 (2021) 1446–1460. https://doi.org/10.7150/ijbs.59233.

[70]   M. Yuan, Z. Han, Y. Liang, Y. Sun, B. He, W. Chen, F. Li, mRNA nanodelivery systems: targeting strategies and administration routes, Biomater Res 27 (2023). https://doi.org/10.1186/s40824-023-00425-3.

[71]   M.-G. Alameh, I. Tombácz, E. Bettini, K. Lederer, S. Ndeupen, C. Sittplangkoon, J.R. Wilmore, B.T. Gaudette, O.Y. Soliman, M. Pine, P. Hicks, T.B. Manzoni, J.J. Knox, J.L. Johnson, D. Laczkó, H. Muramatsu, B. Davis, W. Meng, A.M. Rosenfeld, S. Strohmeier, P.J.C. Lin, B.L. Mui, Y.K. Tam, K. Karikó, A. Jacquet, F. Krammer, P. Bates, M.P. Cancro, D. Weissman, E.T. Luning Prak, D. Allman, B.Z. Igyártó, M. Locci, N. Pardi, Lipid nanoparticles enhance the efficacy of mRNA and protein subunit vaccines by inducing robust T follicular helper cell and humoral responses, Immunity 54 (2021) 2877-2892.e7. https://doi.org/10.1016/j.immuni.2021.11.001.

[72] S.A. Dilliard, Q. Cheng, D.J. Siegwart, On the mechanism of tissue-specific mRNA delivery by selective organ targeting nanoparticles, Proceedings of the National Academy of Sciences 118 (2021). https://doi.org/10.1073/pnas.2109256118.

[73] E. Kon, N. Ad-El, I. Hazan-Halevy, L. Stotsky-Oterin, D. Peer, Targeting cancer with mRNA–lipid nanoparticles: key considerations and future prospects, Nat Rev Clin Oncol 20 (2023) 739–754. https://doi.org/10.1038/s41571-023-00811-9.

[74] Z. Li, N. Zhong, L. Cao, Z. Cai, Y. Xiao, G. Wang, B. Liu, C. Xu, L. Bu, Nanoparticles Targeting Lymph Nodes for Cancer Immunotherapy: Strategies and Influencing Factors, Small (2024). https://doi.org/10.1002/smll.202308731.

[75] N. Pardi, M.J. Hogan, M.S. Naradikian, K. Parkhouse, D.W. Cain, L. Jones, M.A. Moody, H.P. Verkerke, A. Myles, E. Willis, C.C. LaBranche, D.C. Montefiori, J.L. Lobby, K.O. Saunders, H.-X. Liao, B.T. Korber, L.L. Sutherland, R.M. Scearce, P.T. Hraber, I. Tombácz, H. Muramatsu, H. Ni, D.A. Balikov, C. Li, B.L. Mui, Y.K. Tam, F. Krammer, K. Karikó, P. Polacino, L.C. Eisenlohr, T.D. Madden, M.J. Hope, M.G. Lewis, K.K. Lee, S.-L. Hu, S.E. Hensley, M.P. Cancro, B.F. Haynes, D. Weissman, Nucleoside-modified mRNA vaccines induce potent T follicular helper and germinal center B cell responses, Journal of Experimental Medicine 215 (2018) 1571–1588. https://doi.org/10.1084/jem.20171450.

[76] M.D. Buschmann, M.J. Carrasco, S. Alishetty, M. Paige, M.G. Alameh, D. Weissman, Nanomaterial Delivery Systems for mRNA Vaccines, Vaccines (Basel) 9 (2021) 65. https://doi.org/10.3390/vaccines9010065.

[77] S. Ndeupen, Z. Qin, S. Jacobsen, A. Bouteau, H. Estanbouli, B.Z. Igyártó, The mRNA-LNP platform's lipid nanoparticle component used in preclinical vaccine studies is highly inflammatory, IScience 24 (2021) 103479. https://doi.org/10.1016/j.isci.2021.103479.

[78] J.A. Kulkarni, D. Witzigmann, J. Leung, Y.Y.C. Tam, P.R. Cullis, On the role of helper lipids in lipid nanoparticle formulations of siRNA, Nanoscale 11 (2019) 21733–21739. https://doi.org/10.1039/C9NR09347H.

[79] S. Cui, Y. Wang, Y. Gong, X. Lin, Y. Zhao, D. Zhi, Q. Zhou, S. Zhang, Correlation of the cytotoxic effects of cationic lipids with their headgroups, Toxicol Res (Camb) 7 (2018) 473–479. https://doi.org/10.1039/C8TX00005K.

[80] J.A. Kulkarni, P.R. Cullis, R. van der Meel, Lipid Nanoparticles Enabling Gene Therapies: From Concepts to Clinical Utility, Nucleic Acid Ther 28 (2018) 146–157. https://doi.org/10.1089/nat.2018.0721.

[81] S. Li, Y. Hu, A. Li, J. Lin, K. Hsieh, Z. Schneiderman, P. Zhang, Y. Zhu, C. Qiu, E. Kokkoli, T.-H. Wang, H.-Q. Mao, Payload distribution and capacity of mRNA lipid nanoparticles, Nat Commun 13 (2022) 5561. https://doi.org/10.1038/s41467-022-33157-4.

[82] K. Hashiba, Y. Sato, M. Taguchi, S. Sakamoto, A. Otsu, Y. Maeda, T. Shishido, M. Murakawa, A. Okazaki, H. Harashima, Branching Ionizable Lipids Can Enhance the Stability, Fusogenicity, and Functional Delivery of mRNA, Small Science 3 (2023). https://doi.org/10.1002/smsc.202200071.

[83] K.A. Hajj, R.L. Ball, S.B. Deluty, S.R. Singh, D. Strelkova, C.M. Knapp, K.A. Whitehead, Branched-Tail Lipid Nanoparticles Potently Deliver mRNA In Vivo due to Enhanced Ionization at Endosomal pH, Small 15 (2019). https://doi.org/10.1002/smll.201805097.

[84]   W. Zhang, A. Pfeifle, C. Lansdell, G. Frahm, J. Cecillon, L. Tamming, C. Gravel, J. Gao, S.N. Thulasi Raman, L. Wang, S. Sauve, M. Rosu-Myles, X. Li, M.J.W. Johnston, The Expression Kinetics and Immunogenicity of Lipid Nanoparticles Delivering Plasmid DNA and mRNA in Mice, Vaccines (Basel) 11 (2023) 1580. https://doi.org/10.3390/vaccines11101580.

[85]   M.J. Carrasco, S. Alishetty, M.-G. Alameh, H. Said, L. Wright, M. Paige, O. Soliman, D. Weissman, T.E. Cleveland, A. Grishaev, M.D. Buschmann, Ionization and structural properties of mRNA lipid nanoparticles influence expression in intramuscular and intravascular administration, Commun Biol 4 (2021) 956. https://doi.org/10.1038/s42003-021-02441-2.

[86]   S. Roussel, P. Grenier, V. Chénard, N. Bertrand, Dual-Labelled Nanoparticles Inform on the Stability of Fluorescent Labels In Vivo, Pharmaceutics 15 (2023) 769. https://doi.org/10.3390/pharmaceutics15030769.

[87]   O. Escalona-Rayo, Y. Zeng, R.A. Knol, T.J.F. Kock, D. Aschmann, B. Slütter, A. Kros, In vitro and in vivo evaluation of clinically-approved ionizable cationic lipids shows divergent results between mRNA transfection and vaccine efficacy, Biomedicine & Pharmacotherapy 165 (2023) 115065. https://doi.org/10.1016/j.biopha.2023.115065.

[88]   M. Berger, M. Degey, J. Leblond Chain, E. Maquoi, B. Evrard, A. Lechanteur, G. Piel, Effect of PEG Anchor and Serum on Lipid Nanoparticles: Development of a Nanoparticles Tracking Method, Pharmaceutics 15 (2023) 597. https://doi.org/10.3390/pharmaceutics15020597.

[89]   G. Anderluzzi, G. Lou, S. Woods, S.T. Schmidt, S. Gallorini, M. Brazzoli, R. Johnson, C.W. Roberts, D.T. O'Hagan, B.C. Baudner, Y. Perrie, The role of nanoparticle format and route of administration on self-amplifying mRNA vaccine potency, Journal of Controlled Release 342 (2022) 388–399. https://doi.org/10.1016/j.jconrel.2021.12.008.

[90]   H. Lv, S. Zhang, B. Wang, S. Cui, J. Yan, Toxicity of cationic lipids and cationic polymers in gene delivery, Journal of Controlled Release 114 (2006) 100–109. https://doi.org/10.1016/j.jconrel.2006.04.014.

[91]   K. Koitabashi, H. Nagumo, M. Nakao, T. Machida, K. Yoshida, K. Sakai-Kato, Acidic pH-induced changes in lipid nanoparticle membrane packing, Biochimica et Biophysica Acta (BBA) - Biomembranes 1863 (2021) 183627. https://doi.org/10.1016/j.bbamem.2021.183627.

[92]   Y.Y.C. Tam, S. Chen, P.R. Cullis, Advances in Lipid Nanoparticles for siRNA Delivery, Pharmaceutics 5 (2013) 498. https://doi.org/10.3390/PHARMACEUTICS5030498.

[93]   S.C. Semple, S.K. Klimuk, T.O. Harasym, N. Dos Santos, S.M. Ansell, K.F. Wong, N. Maurer, H. Stark, P.R. Cullis, M.J. Hope, P. Scherrer, Efficient encapsulation of antisense oligonucleotides in lipid vesicles using ionizable aminolipids: formation of novel small multilamellar vesicle structures, Biochimica et Biophysica Acta (BBA) - Biomembranes 1510 (2001) 152–166. https://doi.org/10.1016/S0005-2736(00)00343-6.

[94]   L.B. Jeffs, L.R. Palmer, E.G. Ambegia, C. Giesbrecht, S. Ewanick, I. MacLachlan, A scalable, extrusion-free method for efficient liposomal encapsulation of plasmid DNA, Pharm Res 22 (2005) 362–372. https://doi.org/10.1007/S11095-004-1873-Z/METRICS.

[95]   H.H. Ly, S. Daniel, S.K. V Soriano, Z. Kis, A.K. Blakney, Optimization of Lipid Nanoparticles for saRNA Expression and Cellular Activation Using a Design-of-Experiment Approach., Mol Pharm 19 (2022) 1892–1905. https://doi.org/10.1021/acs.molpharmaceut.2c00032.

[96]   K. Nakamura, K. Aihara, T. Ishida, Importance of Process Parameters Influencing the Mean Diameters of siRNA-Containing Lipid Nanoparticles (LNPs) on the in Vitro Activity of Prepared LNPs, Biol Pharm Bull 45 (2022) 497–507. https://doi.org/10.1248/bpb.b21-01016.

[97]   U. Chheda, S. Pradeepan, E. Esposito, S. Strezsak, O. Fernandez-Delgado, J. Kranz, Factors Affecting Stability of RNA – Temperature, Length, Concentration, pH, and Buffering Species, J Pharm Sci 113 (2024) 377–385. https://doi.org/10.1016/j.xphs.2023.11.023.

[98]   M.A. Younis, I.A. Khalil, Y.H.A. Elewa, Y. Kon, H. Harashima, Ultra-small lipid nanoparticles encapsulating sorafenib and midkine-siRNA selectively-eradicate sorafenib-resistant hepatocellular carcinoma in vivo, Journal of Controlled Release 331 (2021) 335–349. https://doi.org/10.1016/j.jconrel.2021.01.021.

[99]   M. Mura, B. Humphreys, J. Gilbert, A. Salis, T. Nylander, Cation and buffer specific effects on the DNA-lipid interaction, Colloids Surf B Biointerfaces 223 (2023) 113187. https://doi.org/10.1016/j.colsurfb.2023.113187.

[100]   R.N. Kularatne, R.M. Crist, S.T. Stern, The Future of Tissue-Targeted Lipid Nanoparticle-Mediated Nucleic Acid Delivery, Pharmaceuticals 15 (2022). https://doi.org/10.3390/PH15070897.

[101]   G. Lou, G. Anderluzzi, S. Woods, C.W. Roberts, Y. Perrie, A novel microfluidic-based approach to formulate size-tuneable large unilamellar cationic liposomes: Formulation, cellular uptake and biodistribution investigations, European Journal of Pharmaceutics and Biopharmaceutics 143 (2019) 51–60. https://doi.org/10.1016/j.ejpb.2019.08.013.

[102]   J.P. Han, M. Kim, B.S. Choi, J.H. Lee, G.S. Lee, M. Jeong, Y. Lee, E.-A. Kim, H.-K. Oh, N. Go, H. Lee, K.J. Lee, U.G. Kim, J.Y. Lee, S. Kim, J. Chang, H. Lee, D.W. Song, S.C. Yeom, In vivo delivery of CRISPR-Cas9 using lipid nanoparticles enables antithrombin gene editing for sustainable hemophilia A and B therapy, Sci Adv 8 (2022). https://doi.org/10.1126/sciadv.abj6901.

[103]   D. Shirane, H. Tanaka, Y. Nakai, H. Yoshioka, H. Akita, Development of an Alcohol Dilution–Lyophilization Method for Preparing Lipid Nanoparticles Containing Encapsulated siRNA, Biol Pharm Bull 41 (2018) 1291–1294. https://doi.org/10.1248/bpb.b18-00208.

[104]   L.S. Mendonça, F. Firmino, J.N. Moreira, M.C. Pedroso de Lima, S. Simões, Transferrin Receptor-Targeted Liposomes Encapsulating anti- BCR-ABL siRNA or asODN for Chronic Myeloid Leukemia Treatment, Bioconjug Chem 21 (2010) 157–168. https://doi.org/10.1021/bc9004365.

[105]   M.H.Y. Cheng, J. Leung, Y. Zhang, C. Strong, G. Basha, A. Momeni, Y. Chen, E. Jan, A. Abdolahzadeh, X. Wang, J.A. Kulkarni, D. Witzigmann, P.R. Cullis, Induction of Bleb Structures in Lipid Nanoparticle Formulations of mRNA Leads to Improved Transfection Potency, Advanced Materials 35 (2023). https://doi.org/10.1002/adma.202303370.

[106]   J. Sun, C. Bi, H.M. Chan, S. Sun, Q. Zhang, Y. Zheng, Curcumin-loaded solid lipid nanoparticles have prolonged in vitro antitumour activity, cellular uptake and improved in vivo bioavailability, Colloids Surf B Biointerfaces 111 (2013) 367–375. https://doi.org/10.1016/j.colsurfb.2013.06.032.

[107]   N. Yektaeian, D. Mehrabani, M. Sepaskhah, S. Zare, I. Jamhiri, G. Hatam, Lipophilic tracer Dil and fluorescence labeling of acridine orange used for Leishmania major tracing in the fibroblast cells, Heliyon 5 (2019) e03073. https://doi.org/10.1016/J.HELIYON.2019.E03073.

[108] C.C.L. Cheung, W.T. Al-Jamal, Sterically stabilized liposomes production using staggered herringbone micromixer: Effect of lipid composition and PEG-lipid content, Int J Pharm 566 (2019) 687–696. https://doi.org/10.1016/j.ijpharm.2019.06.033.

[109] I. V Zhigaltsev, P.R. Cullis, Morphological Behavior of Liposomes and Lipid Nanoparticles, (2023). https://doi.org/10.1021/acs.langmuir.2c02794.

[110] M.L. Brader, S.J. Williams, J.M. Banks, W.H. Hui, Z.H. Zhou, L. Jin, Encapsulation state of messenger RNA inside lipid nanoparticles, Biophys J 120 (2021) 2766–2770. https://doi.org/10.1016/j.bpj.2021.03.012.

[111] K.A. Hajj, K.A. Whitehead, Tools for translation: non-viral materials for therapeutic mRNA delivery, (2017). https://doi.org/10.1038/natrevmats.2017.56.

[112] B. Li, X. Zhang, Y. Dong, Nanoscale platforms for messenger RNA delivery, Wiley Interdiscip Rev Nanomed Nanobiotechnol 11 (2019) e1530. https://doi.org/10.1002/WNAN.1530.

[113] L. Miao, J. Lin, Y. Huang, L. Li, D. Delcassian, Y. Ge, Y. Shi, D.G. Anderson, M. Wai, Synergistic lipid compositions for albumin receptor mediated delivery of mRNA to the liver, (n.d.). https://doi.org/10.1038/s41467-020-16248-y.

[114] J.P. Peñaloza, V. Márquez-Miranda, M. Cabaña-Brunod, R. Reyes-Ramírez, F.M. Llancalahuen, C. Vilos, F. Maldonado-Biermann, L.A. Velásquez, J.A. Fuentes, F.D. González-Nilo, M. Rodríguez-Díaz, C. Otero, Intracellular trafficking and cellular uptake mechanism of PHBV nanoparticles for targeted delivery in epithelial cell lines, J Nanobiotechnology 15 (2017) 1–15. https://doi.org/10.1186/S12951-016-0241-6/FIGURES/13.

[115] F.M. Wurm, Production of recombinant protein therapeutics in cultivated mammalian cells, Nature Biotechnology 2004 22:11 22 (2004) 1393–1398. https://doi.org/10.1038/nbt1026.

[116] G. Backliwal, M. Hildinger, S. Chenuet, S. Wulhfard, M. De Jesus, F.M. Wurm, Rational vector design and multi-pathway modulation of HEK 293E cells yield recombinant antibody titers exceeding 1 g/l by transient transfection under serum-free conditions, Nucleic Acids Res 36 (2008) 96. https://doi.org/10.1093/nar/gkn423.

[117] P. Thomas, T.G. Smart, HEK293 cell line: A vehicle for the expression of recombinant proteins, J Pharmacol Toxicol Methods 51 (2005) 187–200. https://doi.org/10.1016/J.VASCN.2004.08.014.

[118] K.A. Whitehead, J. Matthews, P.H. Chang, F. Niroui, J.R. Dorkin, M. Severgnini, D.G. Anderson, In vitro-in vivo translation of lipid nanoparticles for hepatocellular siRNA delivery., ACS Nano 6 (2012) 6922–9. https://doi.org/10.1021/nn301922x.

[119] J. Di, Z. Du, K. Wu, S. Jin, X. Wang, T. Li, Y. Xu, Biodistribution and Non-linear Gene Expression of mRNA LNPs Affected by Delivery Route and Particle Size, Pharm Res 39 (2022) 105–114. https://doi.org/10.1007/s11095-022-03166-5.

[120] C.A. Alabi, K.T. Love, G. Sahay, H. Yin, K.M. Luly, R. Langer, D.G. Anderson, Multiparametric approach for the evaluation of lipid nanoparticles for siRNA delivery, Proceedings of the National Academy of Sciences 110 (2013) 12881–12886. https://doi.org/10.1073/pnas.1306529110.

[121] C.A. Fromen, T.B. Rahhal, G.R. Robbins, M.P. Kai, T.W. Shen, J.C. Luft, J.M. DeSimone, Nanoparticle surface charge impacts distribution, uptake and lymph node trafficking by

pulmonary antigen-presenting cells, Nanomedicine 12 (2016) 677–687.
https://doi.org/10.1016/j.nano.2015.11.002.

[122] L.M. Kranz, M. Diken, H. Haas, S. Kreiter, C. Loquai, K.C. Reuter, M. Meng, D. Fritz, F. Vascotto, H. Hefesha, C. Grunwitz, M. Vormehr, Y. Hüsemann, A. Selmi, A.N. Kuhn, J. Buck, E. Derhovanessian, R. Rae, S. Attig, J. Diekmann, R.A. Jabulowsky, S. Heesch, J. Hassel, P. Langguth, S. Grabbe, C. Huber, Ö. Türeci, U. Sahin, Systemic RNA delivery to dendritic cells exploits antiviral defence for cancer immunotherapy, Nature 534 (2016) 396–401. https://doi.org/10.1038/nature18300.

[123] M. Jayaraman, S.M. Ansell, B.L. Mui, Y.K. Tam, J. Chen, X. Du, D. Butler, L. Eltepu, S. Matsuda, J.K. Narayanannair, K.G. Rajeev, I.M. Hafez, A. Akinc, M.A. Maier, M.A. Tracy, P.R. Cullis, T.D. Madden, M. Manoharan, M.J. Hope, Maximizing the Potency of siRNA Lipid Nanoparticles for Hepatic Gene Silencing In Vivo, Angew Chem Int Ed Engl 51 (2012) 8529. https://doi.org/10.1002/ANIE.201203263.

[124] M. Kawaguchi, M. Noda, A. Ono, M. Kamiya, M. Matsumoto, M. Tsurumaru, S. Mizukami, H. Mukai, S. Kawakami, Effect of Cholesterol Content of Lipid Composition in mRNA-LNPs on the Protein Expression in the Injected Site and Liver After Local Administration in Mice, J Pharm Sci (2023). https://doi.org/10.1016/J.XPHS.2022.12.026.

[125] J. Zhang, H. Fan, D.A. Levorse, L.S. Crocker, Ionization behavior of amino lipids for siRNA delivery: determination of ionization constants, SAR, and the impact of lipid pKa on cationic lipid-biomembrane interactions., Langmuir 27 (2011) 1907–14. https://doi.org/10.1021/la104590k.

[126] P. Patel, N.M. Ibrahim, K. Cheng, The Importance of Apparent pKa in the Development of Nanoparticles Encapsulating siRNA and mRNA, (2021). https://doi.org/10.1016/j.tips.2021.03.002.

[127] L. Gurba-Bryśkiewicz, W. Maruszak, D.A. Smuga, K. Dubiel, M. Wieczorek, Quality by Design (QbD) and Design of Experiments (DOE) as a Strategy for Tuning Lipid Nanoparticle Formulations for RNA Delivery, Biomedicines 11 (2023) 2752. https://doi.org/10.3390/biomedicines11102752.

[128] Y. Qin, A.A. Walters, N. Rouatbi, J.T.-W. Wang, H.M. Abdel-Bar, K.T. Al-Jamal, Evaluation of a DoE based approach for comprehensive modelling of the effect of lipid nanoparticle composition on nucleic acid delivery, Biomaterials 299 (2023) 122158. https://doi.org/10.1016/j.biomaterials.2023.122158.

[129] R. Rampado, D. Peer, Design of experiments in the optimization of nanoparticle-based drug delivery systems, (2023). https://doi.org/10.1016/j.jconrel.2023.05.001.

[130] E. Kastner, R. Kaur, D. Lowry, B. Moghaddam, A. Wilkinson, Y. Perrie, High-throughput manufacturing of size-tuned liposomes by a new microfluidics method using enhanced statistical tools for characterization, Int J Pharm 477 (2014) 361–368. https://doi.org/10.1016/j.ijpharm.2014.10.030.

[131] R.R. López, I. Ocampo, L.-M. Sánchez, A. Alazzam, K.-F. Bergeron, S. Camacho-León, C. Mounier, I. Stiharu, V. Nerguizian, Surface Response Based Modeling of Liposome Characteristics in a Periodic Disturbance Mixer, Micromachines (Basel) 11 (2020) 235. https://doi.org/10.3390/mi11030235.

[132] R.T. Johnson, D.C. Montgomery, Designing experiments for nonlinear models—an introduction, Qual Reliab Eng Int 26 (2010) 431–441. https://doi.org/10.1002/qre.1063.

[133] K. Yetilmezsoy, S. Demirel, R.J. Vanderbei, Response surface modeling of Pb(II) removal from aqueous solution by Pistacia vera L.: Box–Behnken experimental design, J Hazard Mater 171 (2009) 551–562. https://doi.org/10.1016/j.jhazmat.2009.06.035.

[134] S.L.C. Ferreira, R.E. Bruns, H.S. Ferreira, G.D. Matos, J.M. David, G.C. Brandão, E.G.P. da Silva, L.A. Portugal, P.S. dos Reis, A.S. Souza, W.N.L. dos Santos, Box-Behnken design: An alternative for the optimization of analytical methods, Anal Chim Acta 597 (2007) 179–186. https://doi.org/10.1016/j.aca.2007.07.011.

[135] C.B. Roces, E.C. Port, N.N. Daskalakis, J.A. Watts, J.W. Aylott, G.W. Halbert, Y. Perrie, Rapid scale-up and production of active-loaded PEGylated liposomes, Int J Pharm 586 (2020) 119566. https://doi.org/10.1016/j.ijpharm.2020.119566.

[136] N. Kimura, M. Maeki, Y. Sato, Y. Note, A. Ishida, H. Tani, H. Harashima, M. Tokeshi, Development of the iLiNP Device: Fine Tuning the Lipid Nanoparticle Size within 10 nm for Drug Delivery, ACS Omega 3 (2018) 5044–5051. https://doi.org/10.1021/acsomega.8b00341.

[137] A. Jahn, S.M. Stavis, J.S. Hong, W.N. Vreeland, D.L. DeVoe, M. Gaitan, Microfluidic Mixing and the Formation of Nanoscale Lipid Vesicles, ACS Nano 4 (2010) 2077–2087. https://doi.org/10.1021/nn901676x.

[138] N. Forbes, M.T. Hussain, M.L. Briuglia, D.P. Edwards, J.H.T. Horst, N. Szita, Y. Perrie, Rapid and scale-independent microfluidic manufacture of liposomes entrapping protein incorporating in-line purification and at-line size monitoring, Int J Pharm 556 (2019) 68–81. https://doi.org/10.1016/j.ijpharm.2018.11.060.

[139] J.B. You, K. Kang, T.T. Tran, H. Park, W.R. Hwang, J.M. Kim, S.G. Im, PDMS-based turbulent microfluidic mixer, Lab Chip 15 (2015) 1727–1735. https://doi.org/10.1039/C5LC00070J.

[140] A. Ghazal, M. Gontsarik, J.P. Kutter, J.P. Lafleur, D. Ahmadvand, A. Labrador, S. Salentinig, A. Yaghmur, Microfluidic Platform for the Continuous Production and Characterization of Multilamellar Vesicles: A Synchrotron Small-Angle X-ray Scattering (SAXS) Study, J Phys Chem Lett 8 (2017) 73–79. https://doi.org/10.1021/acs.jpclett.6b02468.

[141] L. Zhang, J.M. Chan, F.X. Gu, J.-W. Rhee, A.Z. Wang, A.F. Radovic-Moreno, F. Alexis, R. Langer, O.C. Farokhzad, Self-Assembled Lipid–Polymer Hybrid Nanoparticles: A Robust Drug Delivery Platform, ACS Nano 2 (2008) 1696–1702. https://doi.org/10.1021/nn800275r.

[142] P.S. Kowalski, A. Rudra, L. Miao, D.G. Anderson, Delivering the Messenger: Advances in Technologies for Therapeutic mRNA Delivery, Molecular Therapy 27 (2019) 710–728. https://doi.org/10.1016/j.ymthe.2019.02.012.

[143] M. Cornebise, E. Narayanan, Y. Xia, E. Acosta, L. Ci, H. Koch, J. Milton, S. Sabnis, T. Salerno, K.E. Benenato, Discovery of a Novel Amino Lipid That Improves Lipid Nanoparticle Performance through Specific Interactions with mRNA, Adv Funct Mater 32 (2022). https://doi.org/10.1002/adfm.202106727.

[144] D. Guimarães, A. Cavaco-Paulo, E. Nogueira, Design of liposomes as drug delivery system for therapeutic applications, Int J Pharm 601 (2021) 120571. https://doi.org/10.1016/j.ijpharm.2021.120571.

[145] S. Bhattacharjee, DLS and zeta potential – What they are and what they are not?, Journal of Controlled Release 235 (2016) 337–351. https://doi.org/10.1016/j.jconrel.2016.06.017.

[146] R. Manchanda, S. Nimesh, Controlled size chitosan nanoparticles as an efficient, biocompatible oligonucleotides delivery system, J Appl Polym Sci 118 (2010) 2071–2077. https://doi.org/10.1002/app.32508.

[147] F. Zhao, Y. Zhao, Y. Liu, X. Chang, C. Chen, Y. Zhao, Cellular Uptake, Intracellular Trafficking, and Cytotoxicity of Nanomaterials, Small 7 (2011) 1322–1337. https://doi.org/10.1002/smll.201100001.

[148] S.D. Conner, S.L. Schmid, Regulated portals of entry into the cell, Nature 422 (2003) 37–44. https://doi.org/10.1038/nature01451.

[149] J.J. Rennick, A.P.R. Johnston, R.G. Parton, Key principles and methods for studying the endocytosis of biological and nanoparticle therapeutics, Nat Nanotechnol 16 (2021) 266–276. https://doi.org/10.1038/s41565-021-00858-8.

[150] M.M. Billingsley, A.G. Hamilton, D. Mai, S.K. Patel, K.L. Swingle, N.C. Sheppard, C.H. June, M.J. Mitchell, Orthogonal Design of Experiments for Optimization of Lipid Nanoparticles for mRNA Engineering of CAR T Cells, Nano Lett 22 (2022) 533–542. https://doi.org/10.1021/acs.nanolett.1c02503.

[151] K. Nag, Md.E.H. Sarker, S. Kumar, H. Khan, S. Chakraborty, Md.J. Islam, J.C. Baray, M.R. Khan, A. Mahmud, U. Barman, E.H. Bhuiya, M. Mohiuddin, N. Sultana, DoE-derived continuous and robust process for manufacturing of pharmaceutical-grade wide-range LNPs for RNA-vaccine/drug delivery, Sci Rep 12 (2022) 9394. https://doi.org/10.1038/s41598-022-12100-z.

[152] K.L. Flanagan, A.L. Fink, M. Plebanski, S.L. Klein, Sex and Gender Differences in the Outcomes of Vaccination over the Life Course, (n.d.). https://doi.org/10.1146/annurev-cellbio-100616.

[153] A.L. Fink, K. Engle, R.L. Ursin, W.Y. Tang, S.L. Klein, Biological sex affects vaccine efficacy and protection against influenza in mice, Proc Natl Acad Sci U S A 115 (2018) 12477–12482. https://doi.org/10.1073/PNAS.1805268115/SUPPL_FILE/PNAS.1805268115.SAPP.PDF.

[154] S.L. Klein, K.L. Flanagan, Sex differences in immune responses, Nature Publishing Group (2016). https://doi.org/10.1038/nri.2016.90.

[155] E.P. Scully, J. Haverfield, R.L. Ursin, C. Tannenbaum, S.L. Klein, Considering how biological sex impacts immune responses and COVID-19 outcomes, (n.d.). https://doi.org/10.1038/s41577-020-0348-8.

[156] S.L. Klein, R. Morgan, The impact of sex and gender on immunotherapy outcomes, Biol Sex Differ 11 (2020). https://doi.org/10.1186/s13293-020-00301-y.

[157] Y. Avnir, C.T. Watson, J. Glanville, E.C. Peterson, A.S. Tallarico, A.S. Bennett, K. Qin, Y. Fu, C.-Y. Huang, J.H. Beigel, F. Breden, Q. Zhu, W.A. Marasco, IGHV1-69 polymorphism modulates anti-influenza antibody repertoires, correlates with IGHV utilization shifts and varies by ethnicity., Sci Rep 6 (2016) 20842. https://doi.org/10.1038/srep20842.

[158] R. El Ridi, R.A. Albrecht, G. Leroux-Roels, R. Nachbagauer, G.A. Poland, E.A. Voigt, I.G. Ovsyannikova, R.B. Kennedy, D.E. Grill, K.M. Goergen, D.J. Schaid, Article 180 GA (2019) Sex Differences in Older Adults' Immune Responses to Seasonal Influenza Vaccination, Front. Immunol 10 (2019) 180. https://doi.org/10.3389/fimmu.2019.00180.

[159] M.S. Green, V. Peer, A. Magid, N. Hagani, E. Anis, D. Nitzan, Gender Differences in Adverse Events Following the Pfizer-BioNTech COVID-19 Vaccine, Vaccines (Basel) 10 (2022). https://doi.org/10.3390/VACCINES10020233.

[160] A. Jensen, M. Stromme, S. Moyassari, A.S. Chadha, M.C. Tartaglia, C. Szoeke, M.T. Ferretti, COVID-19 vaccines: Considering sex differences in efficacy and safety, Contemp Clin Trials 115 (2022) 106700. https://doi.org/10.1016/j.cct.2022.106700.

[161] B.-M. Chen, Y.-C. Su, C.-J. Chang, P.-A. Burnouf, K.-H. Chuang, C.-H. Chen, T.-L. Cheng, Y.-T. Chen, J.-Y. Wu, S.R. Roffler, Measurement of Pre-Existing IgG and IgM Antibodies against Polyethylene Glycol in Healthy Individuals, Anal Chem 88 (2016) 10661–10666. https://doi.org/10.1021/acs.analchem.6b03109.

[162] T. Takahashi, M.K. Ellingson, P. Wong, B. Israelow, C. Lucas, J. Klein, J. Silva, T. Mao, J. Eun Oh, M. Tokuyama, P. Lu, A. Venkataraman, A. Park, F. Liu, A. Meir, J. Sun, E.Y. Wang, A. Casanovas-Massana, A.L. Wyllie, C.B. F Vogels, R. Earnest, S. Lapidus, I.M. Ott, A.J. Moore, Y. IMPACT Research Team, A. Shaw, J.B. Fournier, C.D. Odio, S. Farhadian, C. Dela Cruz, N.D. Grubaugh, W.L. Schulz, A.M. Ring, A.I. Ko, S.B. Omer, A. Iwasaki, Sex differences in immune responses that underlie COVID-19 disease outcomes Overview of the study design, Nature 588 (2020) 315. https://doi.org/10.1038/s41586-020-2700-3.

[163] C. Gebhard, V. Regitz-Zagrosek, H.K. Neuhauser, R. Morgan, S.L. Klein, Impact of sex and gender on COVID-19 outcomes in Europe, (n.d.). https://doi.org/10.1186/s13293-020-00304-9.

[164] F. Zeng, C. Dai, | Pengcheng Cai, J. Wang, | Lei Xu, J. Li, G. Hu, Z. Wang, | Fang Zheng, | Lin Wang, L. Wang, A comparison study of SARS-CoV-2 IgG antibody between male and female COVID-19 patients: A possible reason underlying different outcome between sex COVID-19 patients, SARS-CoV-2 IgG antibody, sexual discrepancy, J Med Virol 92 (2020) 2050–2054. https://doi.org/10.1002/jmv.25989.

[165] A.J. Markmann, N. Giallourou, D.R. Bhowmik, Y.J. Hou, A. Lerner, D.R. Martinez, L. Premkumar, H. Root, D. van Duin, S. Napravnik, S.D. Graham, Q. Guerra, R. Raut, C.J. Petropoulos, T. Wrin, C. Cornaby, J. Schmitz, J. Kuruc, S. Weiss, Y. Park, R. Baric, A.M. de Silva, D.M. Margolis, L.A. Bartelt, Sex Disparities and Neutralizing-Antibody Durability to SARS-CoV-2 Infection in Convalescent Individuals, MSphere 6 (2021). https://doi.org/10.1128/MSPHERE.00275-21.

[166] S.L. Klein, A. Pekosz, H.S. Park, R.L. Ursin, J.R. Shapiro, S.E. Benner, K. Littlefield, S. Kumar, H.M. Naik, M.J. Betenbaugh, R. Shrestha, A.A. Wu, R.M. Hughes, I. Burgess, P. Caturegli, O. Laeyendecker, T.C. Quinn, D. Sullivan, S. Shoham, A.D. Redd, E.M. Bloch, A. Casadevall, A.A.R. Tobian, Sex, age, and hospitalization drive antibody responses in a COVID-19 convalescent plasma donor population, Journal of Clinical Investigation 130 (2020) 6141–6150. https://doi.org/10.1172/JCI142004.

[167] J. Mehew, R. Johnson, D. Roberts, H. Harvala, M. Jennifer, J. Rachel, R. David, H. Heli, Rapid communication Convalescent plasma for COVID-19: male gender, older age and hospitalisation associated with high neutralising antibody levels, England, 22 April to 12 May 2020, (n.d.) 1. https://doi.org/10.2807/1560-7917.

[168] T.J. Gniadek, J.M. Thiede, W.E. Matchett, A.R. Gress, K.A. Pape, J.K. Fiege, M.K. Jenkins, V.D. Menachery, R.A. Langlois, T.D. Bold, SARS-CoV-2 neutralization and serology testing of COVID-

19 convalescent plasma from donors with nonsevere disease, Transfusion (Paris) 61 (2021) 17–23. https://doi.org/10.1111/TRF.16101.

[169] C. Kodde, S. Tafelski, E. Balamitsa, I. Nachtigall, M. Bonsignore, Factors Influencing Antibody Response to SARS-CoV-2 Vaccination, Vaccines (Basel) 11 (2023). https://doi.org/10.3390/vaccines11020451.

[170] G. Sulis, J.Y. Kim, V. Rodrigue, G. Gore, A. Peebles, A.K. Ulrich, M. Horn, N.E. Basta, Sex-disaggregated effectiveness data reporting in COVID-19 vaccine research: a systematic review Plain Language Summary, (n.d.). https://doi.org/10.1038/s43856-023-00297-7.

[171] M. Poley, P. Mora-Raimundo, Y. Shammai, M. Kaduri, L. Koren, O. Adir, J. Shklover, J. Shainsky-Roitman, S. Ramishetti, F. Man, R.T.M. de Rosales, A. Zinger, D. Peer, I. Ben-Aharon, A. Schroeder, Nanoparticles Accumulate in the Female Reproductive System during Ovulation Affecting Cancer Treatment and Fertility, ACS Nano 16 (2022) 5246–5257. https://doi.org/10.1021/acsnano.1c07237.

[172] A. Alvergne, E. Von Woon, V. Male, Effect of COVID-19 vaccination on the timing and flow of menstrual periods in two cohorts., Frontiers in Reproductive Health 4 (2022) 952976. https://doi.org/10.3389/frph.2022.952976.

[173] F. Li, A.C.M. Boon, A.P. Michelson, R.E. Foraker, M. Zhan, P.R.O. Payne, Estrogen hormone is an essential sex factor inhibiting inflammation and immune response in COVID-19, (123AD). https://doi.org/10.1038/s41598-022-13585-4.

[174] A.E. Spiering, T.J. de Vries, Why Females Do Better: The X Chromosomal TLR7 Gene-Dose Effect in COVID-19, Front Immunol 12 (2021). https://doi.org/10.3389/FIMMU.2021.756262.

[175] A.A. Ashkarran, H. Gharibi, J.W. Grunberger, A.A. Saei, N. Khurana, R. Mohammadpour, H. Ghandehari, M. Mahmoudi, Sex-Specific Silica Nanoparticle Protein Corona Compositions Exposed to Male and Female BALB/c Mice Plasmas, ACS Bio and Med Chem Au 3 (2023) 62–73. https://doi.org/10.1021/ACSBIOMEDCHEMAU.2C00040/SUPPL_FILE/BG2C00040_SI_001.PDF.

[176] Y. Yan, K.T. Gause, M.M.J. Kamphuis, C.-S. Ang, N.M. O'brien-Simpson, J.C. Lenzo, E.C. Reynolds, E.C. Nice, F. Caruso, Differential Roles of the Protein Corona in the Cellular Uptake of Nanoporous Polymer Particles by Monocyte and Macrophage Cell Lines, (2013). https://doi.org/10.1021/nn404481f.

[177] E. Vulpis, F. Giulimondi, L. Digiacomo, A. Zingoni, R. Safavi-Sohi, S. Sharifi, G. Caracciolo, M. Mahmoudi, The Possible Role of Sex As an Important Factor in Development and Administration of Lipid Nanomedicine-Based COVID-19 Vaccine, Mol. Pharmaceutics 18 (2021). https://doi.org/10.1021/acs.molpharmaceut.1c00291.

[178] L. Guo, Q. Zhang, X. Ma, J. Wang, T. Liang, miRNA and mRNA expression analysis reveals potential sex-biased miRNA expression, (n.d.).

[179] C.M. Lopes-Ramos, C.Y. Chen, M.L. Kuijjer, J.N. Paulson, A.R. Sonawane, M. Fagny, J. Platig, K. Glass, J. Quackenbush, D.L. DeMeo, Sex Differences in Gene Expression and Regulatory Networks across 29 Human Tissues, Cell Rep 31 (2020). https://doi.org/10.1016/j.celrep.2020.107795.

[180] S.P. Petkov, F. Heuts, O.A. Krotova, A. Kilpelainen, G. Engström, E.S. Starodubova, M.G. Isaguliants, Evaluation of immunogen delivery by DNA immunization using non-invasive bioluminescence imaging., Hum Vaccin Immunother 9 (2013) 2228–36. https://doi.org/10.4161/hv.25561.

[181] S. Fischinger, C.M. Boudreau, A.L. Butler, H. Streeck, G. Alter, Sex differences in vaccine-induced humoral immunity, (n.d.). https://doi.org/10.1007/s00281-018-0726-5.

[182] J.A. Breznik, C. Schulz, J. Ma, D.M. Sloboda, D.M.E. Bowdish, Biological sex, not reproductive cycle, influences peripheral blood immune cell prevalence in mice, J Physiol 599 (2021) 2169–2195. https://doi.org/10.1113/JP281198.

[183] R.J.M. Engler, M.R. Nelson, M.M. Klote, M.J. Vanraden, C.-Y. Huang, N.J. Cox, A. Klimov, W.A. Keitel, K.L. Nichol, W.W. Carr, J.J. Treanor, Half-vs Full-Dose Trivalent Inactivated Influenza Vaccine (2004-2005) Age, Dose, and Sex Effects on Immune Responses, n.d. https://jamanetwork.com/.

[184] V. Rider, J. Leffler, B. Thyagarajan, C. Seillet, E. Hall, S. Kovats, S. Kadel, Article 1653 1 Citation: Kadel S and Kovats S (2018) Sex Hormones Regulate Innate Immune Cells and Promote Sex Differences in Respiratory Virus Infection, Front. Immunol 9 (2018) 1653. https://doi.org/10.3389/fimmu.2018.01653.

[185] J. Roved, H. Westerdahl, D. Hasselquist, Sex differences in immune responses: Hormonal effects, antagonistic selection, and evolutionary consequences, (2016). https://doi.org/10.1016/j.yhbeh.2016.11.017.

[186] M. Poley, G. Chen, N. Sharf-Pauker, A. Avital, M. Kaduri, M. Sela, P.M. Raimundo, L. Koren, S. Arber, E. Egorov, J. Shainsky, J. Shklover, A. Schroeder, Sex-Based Differences in the Biodistribution of Nanoparticles and Their Effect on Hormonal, Immune, and Metabolic Function, Adv Nanobiomed Res 2 (2022). https://doi.org/10.1002/anbr.202200089.

[187] B. Spellberg, J.E. Edwards, Type 1/Type 2 Immunity in Infectious Diseases, n.d.

[188] A. Fukushima, T. Yamaguchi, W. Ishida, K. Fukata, T. Taniguchi, F.-T. Liu, H. Ueno, Genetic background determines susceptibility to experimental immune-mediated blepharoconjunctivitis: Comparison of Balb/c and C57BL/6 mice, Exp Eye Res 82 (2006) 210–218. https://doi.org/10.1016/j.exer.2005.06.010.

[189] M. Alberer, U. Gnad-Vogt, H.S. Hong, K.T. Mehr, L. Backert, G. Finak, R. Gottardo, M.A. Bica, A. Garofano, S.D. Koch, M. Fotin-Mleczek, I. Hoerr, R. Clemens, F. von Sonnenburg, Safety and immunogenicity of a mRNA rabies vaccine in healthy adults: an open-label, non-randomised, prospective, first-in-human phase 1 clinical trial., Lancet 390 (2017) 1511–1520. https://doi.org/10.1016/S0140-6736(17)31665-3.

[190] V. Gote, P.K. Bolla, N. Kommineni, A. Butreddy, P.K. Nukala, S.S. Palakurthi, W. Khan, A Comprehensive Review of mRNA Vaccines, Int J Mol Sci 24 (2023) 2700. https://doi.org/10.3390/ijms24032700.

[191] S. Lazzaro, C. Giovani, S. Mangiavacchi, D. Magini, D. Maione, B. Baudner, A.J. Geall, E. De Gregorio, U. D'Oro, C. Buonsanti, CD8 T-cell priming upon mRNA vaccination is restricted to bone-marrow-derived antigen-presenting cells and may involve antigen transfer from myocytes., Immunology 146 (2015) 312–26. https://doi.org/10.1111/imm.12505.

[192] A.K. Beery, I. Zucker, Sex bias in neuroscience and biomedical research, Neurosci Biobehav Rev 35 (2011) 565–572. https://doi.org/10.1016/j.neubiorev.2010.07.002.

[193] S. Luozhong, Z. Yuan, T. Sarmiento, Y. Chen, W. Gu, C. McCurdy, W. Gao, R. Li, S. Wilkens, S. Jiang, Phosphatidylserine Lipid Nanoparticles Promote Systemic RNA Delivery to Secondary Lymphoid Organs, Nano Lett 22 (2022) 8304–8311. https://doi.org/10.1021/acs.nanolett.2c03234.

[194] K.M. Tsoi, S.A. MacParland, X.-Z. Ma, V.N. Spetzler, J. Echeverri, B. Ouyang, S.M. Fadel, E.A. Sykes, N. Goldaracena, J.M. Kaths, J.B. Conneely, B.A. Alman, M. Selzner, M.A. Ostrowski, O.A. Adeyi, A. Zilman, I.D. McGilvray, W.C.W. Chan, Mechanism of hard-nanomaterial clearance by the liver, Nat Mater 15 (2016) 1212–1221. https://doi.org/10.1038/nmat4718.

[195] J. Chen, Z. Ye, C. Huang, M. Qiu, D. Song, Y. Li, Q. Xu, Lipid nanoparticle-mediated lymph node–targeting delivery of mRNA cancer vaccine elicits robust CD8 [+] T cell response, Proceedings of the National Academy of Sciences 119 (2022). https://doi.org/10.1073/pnas.2207841119.

[196] J. Huang, D. Yuen, J.D. Mintern, A.P.R. Johnston, Opportunities for innovation: Building on the success of lipid nanoparticle vaccines, Curr Opin Colloid Interface Sci 55 (2021) 101468. https://doi.org/10.1016/j.cocis.2021.101468.

[197] M. Qiu, Y. Tang, J. Chen, R. Muriph, Z. Ye, C. Huang, J. Evans, E.P. Henske, Q. Xu, Lung-selective mRNA delivery of synthetic lipid nanoparticles for the treatment of pulmonary lymphangioleiomyomatosis, Proceedings of the National Academy of Sciences 119 (2022). https://doi.org/10.1073/pnas.2116271119.

[198] P. Rennert, Selective disruption of lymphotoxin ligands reveals a novel set of mucosal lymph nodes and unique effects on lymph node cellular organization, Int Immunol 9 (1997) 1627–1639. https://doi.org/10.1093/intimm/9.11.1627.

[199] V.K. Yellepeddi, A. Kumar, S. Palakurthi, Biotinylated poly(amido)amine (PAMAM) dendrimers as carriers for drug delivery to ovarian cancer cells in vitro., Anticancer Res 29 (2009) 2933–43.

[200] M. Ramezani-Aliakbari, J. Varshosaz, H. Sadeghi-aliabadi, F. Hassanzadeh, M. Rostami, Biotin-Targeted Nanomicellar Formulation of an Anderson-Type Polyoxomolybdate: Synthesis and In Vitro Cytotoxicity Evaluations, Langmuir 37 (2021) 6475–6489. https://doi.org/10.1021/acs.langmuir.1c00623.

[201] M. Mahmoudi, M.P. Landry, A. Moore, R. Coreas, nature reviews materials The protein corona from nanomedicine to environmental science, Nature Reviews Materials | 8 (2023) 422–438. https://doi.org/10.1038/s41578-023-00552-2.

[202] S. Saha, R. Majumdar, A. Hussain, R.R. Dighe, A.R. Chakravarty, Biotin-conjugated tumour-targeting photocytotoxic iron(III) complexes, (n.d.). https://doi.org/10.1098/rsta.2012.0190.

[203] C. Brandenberger, C. Mühlfeld, Z. Ali, A. Lenz, O. Schmid, W.J. Parak, P. Gehr, B. Rothen-Rutishauser, Quantitative Evaluation of Cellular Uptake and Trafficking of Plain and Polyethylene Glycol-Coated Gold Nanoparticles, Small 6 (2010) 1669–1678. https://doi.org/10.1002/smll.201000528.

[204] V. Schubertová, F.J. Martinez-Veracoechea, R. Vácha, Influence of ligand distribution on uptake efficiency, Soft Matter 11 (2015) 2726–2730. https://doi.org/10.1039/C4SM02815E.

[205] L.A. Medina, S.M. Calixto, R. Klipper, W.T. Phillips, B. Goins, Avidin/biotin-liposome system injected in the pleural space for drug delivery to mediastinal lymph nodes, J Pharm Sci 93 (2004) 2595–2608. https://doi.org/10.1002/jps.20163.

[206] W.T. Phillips, R. Klipper, B. Goins, Novel method of greatly enhanced delivery of liposomes to lymph nodes., J Pharmacol Exp Ther 295 (2000) 309–13.

[207] C.L. Zavaleta, W.T. Phillips, A. Soundararajan, B.A. Goins, Use of avidin/biotin-liposome system for enhanced peritoneal drug delivery in an ovarian cancer model, Int J Pharm 337 (2007) 316–328. https://doi.org/10.1016/j.ijpharm.2007.01.010.

[208] P. Yousefpour, K. Ni, D.J. Irvine, Targeted modulation of immune cells and tissues using engineered biomaterials, Nature Reviews Bioengineering 1 (2023) 107–124. https://doi.org/10.1038/s44222-022-00016-2.

[209] H. Jiang, Q. Wang, X. Sun, Lymph node targeting strategies to improve vaccination efficacy, Journal of Controlled Release 267 (2017) 47–56. https://doi.org/10.1016/j.jconrel.2017.08.009.

[210] B.S. Doddapaneni, S. Kyryachenko, S.E. Chagani, R.G. Alany, D.A. Rao, A.K. Indra, A.W.G. Alani, A three-drug nanoscale drug delivery system designed for preferential lymphatic uptake for the treatment of metastatic melanoma, Journal of Controlled Release 220 (2015) 503–514. https://doi.org/10.1016/j.jconrel.2015.11.013.

[211] S.T. Reddy, A. Rehor, H.G. Schmoekel, J.A. Hubbell, M.A. Swartz, In vivo targeting of dendritic cells in lymph nodes with poly(propylene sulfide) nanoparticles, Journal of Controlled Release 112 (2006) 26–34. https://doi.org/10.1016/j.jconrel.2006.01.006.

[212] Y. Xie, T.R. Bagby, M. Cohen, M.L. Forrest, Drug delivery to the lymphatic system: importance in future cancer diagnosis and therapies, Expert Opin Drug Deliv 6 (2009) 785–792. https://doi.org/10.1517/17425240903085128.

[213] S. Kwon, E.M. Sevick-Muraca, Effect of lidocaine with and without epinephrine on lymphatic contractile activity in mice in vivo, J Anesth 30 (2016) 1091–1094. https://doi.org/10.1007/s00540-016-2260-8.

[214] V. Manolova, A. Flace, M. Bauer, K. Schwarz, P. Saudan, M.F. Bachmann, Nanoparticles target distinct dendritic cell populations according to their size, Eur J Immunol 38 (2008) 1404–1413. https://doi.org/10.1002/eji.200737984.

[215] S. Cai, Q. Yang, T.R. Bagby, M.L. Forrest, Lymphatic drug delivery using engineered liposomes and solid lipid nanoparticles, Adv Drug Deliv Rev 63 (2011) 901–908. https://doi.org/10.1016/j.addr.2011.05.017.

[216] K.J. Cho, Y.-E. Cho, J. Kim, Locoregional Lymphatic Delivery Systems Using Nanoparticles and Hydrogels for Anticancer Immunotherapy, Pharmaceutics 14 (2022) 2752. https://doi.org/10.3390/pharmaceutics14122752.

[217] D. Zukancic, E.J.A. Suys, E.H. Pilkington, A. Algarni, H. Al-Wassiti, N.P. Truong, The Importance of Poly(ethylene glycol) and Lipid Structure in Targeted Gene Delivery to Lymph Nodes by

Lipid Nanoparticles, Pharmaceutics 12 (2020) 1068.
https://doi.org/10.3390/pharmaceutics12111068.

[218]   G.A.F. van Tilborg, G.J. Strijkers, E.M. Pouget, C.P.M. Reutelingsperger, N.A.J.M. Sommerdijk, K. Nicolay, W.J.M. Mulder, Kinetics of avidin-induced clearance of biotinylated bimodal liposomes for improved MR molecular imaging, Magn Reson Med 60 (2008) 1444–1456. https://doi.org/10.1002/mrm.21780.